

Assessing Asphalt and Concrete Pavement Surface Texture in the Field

Saad I. Sarsam
Professor

College of Engineering/ University of Baghdad
E-Mail: saadisarsam@coeng.uobaghdad.edu.iq

Huda N. Al Shareef
MSc. Student

College of Engineering/ University of Baghdad
E-Mail: saadisarsam@coeng.uobaghdad.edu.iq

ABSTRACT

The incorporation of safety characteristics into the traditional pavement structural design or in the functional evaluation of pavement condition has not been established yet. The design has focused on the structural capacity of the roadway so that the pavement can withstand specific level of repetitive loading over the design life. On the other hand, the surface texture condition was neither included in the AASHTO design procedure nor in the present serviceability index measurements. The pavement surface course should provide adequate levels of friction and ride quality and maintain low levels of noise and roughness. Many transportation departments perform routine skid resistant testing, the type of equipment used for testing varies depending on the preference of each transportation department. It was felt that modeling of the surface texture condition using different methods of testing may assist in solving such problem. In this work, Macro texture and Micro texture of asphalt and cement concrete pavement surface have been investigated in the field using four different methods (The Sand Patch Method, Outflow Time Method, British Pendulum Tester and Photogrammetry Technique). Two different grain sizes of sand have been utilized in conducting the Sand Patch while the Micro texture was investigated using the British Pendulum tester method at wet pavement surface conditions. The test results of the four methods were correlated to the skid number. It was concluded that such modeling could provide instant data in the field for pavement condition which may help in pavement maintenance management.

Keywords: texture, pavement, surface condition, testing, modeling.

تقييم نسيجة السطح الاسفلتي والخرساني للرصفة موقعا

هدى نضر الشريف
طالبة ماجستير

جامعة بغداد، كلية الهندسة، قسم الهندسة المدنية

سعد عيسى سرسم
استاذ

جامعة بغداد، كلية الهندسة، قسم الهندسة المدنية

الخلاصة

مساهمة خصائص السلامة في تصميم الرصفة التقليدي او في التقييم الوظيفي لظروف الرصفة لم تعتمد لحد الآن. التصميم ركز على القدرة الهيكلية للطريق بحيث ان الرصفة يمكن ان تسند مستوى معين من التحميل المتكرر طيلة عمر الرصفة. من ناحية اخرى ظروف نسيجة السطح لم تضمن في خطوات تصميم (AASHTO) ولا في قياسات مؤشر خدمية الطريق. ان سطح الرصفة يجب ان يوفر مستويات كافية من الاحتكاك، نوعية القيادة، والحفاظ على مستويات منخفضة من الضوضاء والخشونة. اعتمدت العديد من اقسام النقل اختبار مقاومة انزلاق روتيني، نوع المعدات المستخدمة في الاختبار يختلف اعتمادا على المفضل لدى اقسام النقل. لقد تبين بأن نمذجة ظروف نسيج السطح باستخدام طرق مختلفة للاختبار يمكن ان تساعد في حل مثل هكذا مشكلة. في هذه الدراسة، اختبرت موقعا النسيجة الماكروية، والنسيجة المايكروية للرصفة الاسفلتية والرصفة الكونكريتية باستخدام اربع طرق (طريقة رقعة الرمل، زمن جريان الماء، جهاز البندول البريطاني، وتقنية الفوتوكرامتري). نوعين مختلفين من الرمل المنخول اعتمد في طريقة رقعة الرمل بينما النسيجة المايكروية اختبرت باستخدام طريقة جهاز البندول البريطاني على سطح الرصفة الرطبة. نتائج الاختبار للاربع طرق نمذجت وربطت في رقم انزلاق. ولقد استنتج ان مثل هكذا نمذجة تستطيع ان توفر بيانات لحظية موقعا لظروف التبليط التي يمكن ان تساعد في ادارة صيانة الرصفة.

الكلمات الرئيسية : نسجة السطح، الرصفة، حالة السطح، الفحص، النمذجة.

1. INTRODUCTION

1.1 General

Deterioration of the pavement surface (smoothing or polishing of the pavement surface), along with surface water accumulation in the form of rain, snow, or ice, can result in inadequate provision of skid resistance. Inadequate skid resistance can lead to higher incidences of skid related crashes, **Sarsam, 2009-a**. There is currently no agreement on what standards to use for optimizing skid resistance, or on a standardized testing procedure to adopt despite a significant amount of research conducted. Roadway pavements surface deteriorate with time as a result of traffic passes, environmental conditions, and poor pavement maintenance management. If this deterioration is not properly addressed, the amount of surface distress that can affect skid resistance will increase and be prejudicial to traffic, **Noyce et al, 2007**. In this sense, pavement surface characteristics are a significant issue because of its influence in preserving roadway safety. Maintaining these characteristics during pavement construction or rehabilitation may mitigate or even prevent crashes and incidents related to loss of vehicle control, hydroplaning, and/or excessive skidding, **Masad et al, 2010**. The surface quality of a pavement determines to a large degree the conditions under which safety can be maintained. Driver control of vehicles is strongly dependent upon pavement surface characteristics, geometrics, driver speed, and vehicle variables such as tire pressure, type of tread, and wheel loads. Important surface characteristics include pavement micro texture, macro texture, and drainage attributes, **Sarsam, 2009-b**. Loss of adhesion between vehicle`s tires and the road surface occurs in many road accidents whether or not it is the actual cause of the accident. Over the years, tire manufacturers have done a lot of research into different types of rubber and tread pattern to improve the safety of motor vehicles. The pavement- tire interaction is affected by the texture characteristics of the pavement such as the coefficient of friction, skid resistance, and hydroplaning effect on wet surface, **Noyce et al, 2005**. Until recently, the most common test methods for determining macro texture were labor intensive and time consuming. New developments in high resolution profiler have produced methods for estimating macro texture depth at different speeds, **Fuentes et al, 2010**. The fundamental questions that need to be addressed are:

- (1) How effectively and simply does such equipment characterize pavement micro and macro texture?
- (2) How this information could be used if it were available.

1.2 Research Objectives

The main objectives of this research work are:

- a.) Evaluating the cement concrete and asphalt concrete pavement surface condition from the skid resistance point of view using field tests. The micro and macro textures were evaluated using four different testing techniques.
- b.) Evaluating the significance, feasibility of using such different field tests to measure the skid resistance.

2. MATERIALS AND METHODS

This field work was conducted at University of Baghdad in Aljadriah campus roadway, and walkway network. Rigid pavement and flexible pavement were tested, 150 locations have been selected for each pavement type. The distance between one location and another was 1.2 meter minimum. Every test location was prepared for testing by thoroughly sweeping using a plastic brush. Then, the location was visually examined so that various pavement texture could be



included, and each test location does not contain any cracks or irregularities. Then, each location was subjected to the texture determination by using various testing procedures. Similar work was reported by **Sarsam, 2011**.

2.1 Sand Patch Test:

A specific volume of each type of graded sand prepared in the laboratory by sieving (passing sieve no. 25 and retained on sieve No. 52) was spread by using a specific plastic tool on the pavement surface in a circular motion. Two types of graded sand were used. **Table 1** shows the types of sand and their densities. Then, the mean texture depth (MTD) was calculated by using equation (4), **ASTM, 2009**.

2.2 Outflow Time:

The outflow time (OFT) was measured by using the outflow meter. Outflow meter was manufactured in local market by using plastic transparent jar of 1000 ml capacity rests on rubber annulus placed on the pavement. A valve at the bottom of the cylinder is closed and the cylinder is filled with water. The valve is then opened and the time required for cylinder to be empty is measured with a stopwatch and was reported as the outflow time (OFT). This test was conducted in accordance to **ASTM, 2009**, standard procedures for determining outflow time.

2.3 British Pendulum Test:

British Pendulum Tester is operated by releasing a pendulum from a height that is adjusted so that a rubber slider on the pendulum head contacts the pavement surface over a fixed length. Friction between the slider and the pavement surface reduces the kinetic energy of the head, and the reduced kinetic energy is converted to potential energy as the pendulum breaks contact with the surface and approaches its maximum recovered height. The pavement surface was wetted with 1000 ml of water to ensure that the surface voids are saturated, and the temperature was fixed at $(25\pm 3)^{\circ}\text{C}$ during the work to prevent the effect of temperature on the British Pendulum test results. The difference between the initial and recovered pendulum heights represents the loss in energy due to friction between the slider and the pavement surface. The BPT is equipped with a scale that measures the recovered height of the pendulum in terms of British Pendulum Number (BPN). The slip speed of the BPN is very slow (typically about 6 mph). This test was conducted in accordance to **ASTM, 2009**, standard procedures for determining British Pendulum Number.

2.4 Photogrammetry Technique

2.4.1 Direct Geo-referencing

Image orientation is a key element in any photogrammetric project, since the determination of three-dimensional coordinates from images require the image orientation to be known. In aerial Photogrammetry this task has been exclusively and very successfully solved by using aerial triangulation for many decades. Thus, aerial triangulation has become a key technology and an important cost factor in mapping and Geographic Information System (GIS), **Jasim, 2011**. In this work, there was two cameras their brand Panasonic fz50 orthogonally positioned on the pavement surface by using a frame designed and manufactured especially for this research work. Where Exterior Orientation Parameters (EOP) were defined such as height of flight and it was 1.2 m, and the rotation angles (ω , ϕ , κ), so there was no need to Differential Global Position System Receiver (DGPS), and Inertial Navigation System (INS) as they are used for determining EOP for direct geo-



reference. The distance between the centers of the cameras lenses was 53.4 cm. The overlap between the two shots was 45%. This technique was adopted for 15 shot locations on rigid pavement and 15 shot locations on flexible pavement. The camera properties were mentioned in **Table 2**. The stereo photo pair were fed to the ERDAS 8.4 software that has been used for image processing. This procedure was in agreement with the work reported by **Sarsam and AL Shareef, 2015**.

2.4.2 Image processing procedure adopted

Two overlap shots for each location were inserted in ERDAS 8.4 software. Pyramid layers were generated for every shot. Cameras properties, interior and exterior orientation such as height of flight and three rotation angles (ω , ϕ , κ). Such shots locations were the same for the previous testing techniques. The software convert the two overlap shots to a three dimensional photo and calculate the texture depth by selecting several tie points in every two shots, and aerial triangulation process was applied. Such procedure was in agreement with **Sarsam et al, 2015-a**.

3. MODELING OF PAVEMENT SURFACE TEXTURE

An effort has been made to find a direct relationship between micro and macro texture, using BPN, Outflow Time, Mean Texture Depth (Sand Patch Method and Photogrammetry Technique). Many statistics software have been tried including Statistica, SPSS, and ANN but the models were weak from the statistical point of view. So it was decided to examine the feasibility of using the indirect correlation using the well-known mathematical models of skid resistance and skid number (SN) as shown in equations 1, 2, and 3.

$$SN = SNo. \text{Exp}^{-(PNG / 100) V} \quad (1)$$

$$SNo = 1.32 \text{ BPN} - 34.9 \quad (2)$$

$$PNG = 0.157 (\text{MTD}) - 0.47 \quad (3)$$

Where:

SN: Skid Number.

SNo: Skid Number at Zero Speed.

PNG: Percent Normalized Gradient.

V: Vehicle Speed.

BPN: British Pendulum Number (percent).

MTD: Mean Texture Depth (cm).

MTD was calculated from sand patch method by using both river and silica sand. The mathematical equation used is illustrated below, **ASTM, 2009**:

$$\text{MTD} = \frac{4V}{\pi D^2} \quad (4)$$

Where:

V: volume of the sand (cm³).

D: diameter of the circular patch of the sand (cm).

Another mathematical expression (equation 5) was obtained from the literature, **Noyce et al., 2005**, which correlate OFT with MTD and implemented in the SN calculation. Two cases of such relation have been tried, the first one is to calculate MTD using the equation below:

$$\text{MTD} = \frac{3.114}{\text{OFT}} + 0.636 \quad (5)$$

Where:

MTD: Mean texture depth (cm).

OFT: Outflow time (seconds).

It was found that the relation could give MTD close to one cm, then the second case tried was to take MTD value equivalent to OFT. Such finding was further supported when plotting the OFT calculated using both calculation cases as demonstrated in **Fig.1** for asphalt concrete.

3.1 Asphalt Concrete Pavement

3.1.1 Effect of Sand Gradation Type on Skid Number

Fig. 2 illustrates the relationship between SN when using two different sand types in the sand patch test (fine and coarse sand). It shows that the effect of sand type on skid number was not significant for the range of sand types adopted, the coefficient of determination was 0.9997. Such results agrees well with the work of **Sarsam, 2009-a**.

3.1.2 Effect of Testing Technique on Skid Number

Fig. 3, 4, 5, and 6 show the variation of skid number when two testing techniques were implemented. The SN calculated using sand patch (natural sand) or (silica sand) was plotted on the x-axis, while the SN calculated using OFT equivalent to MTD or calculated from Equation 5 was plotted on y-axis. Both figures indicate very good statistical relationship, however, it was noticed that at high values of skid number, (above 30), the mode start to change, and the scatter of test results are away from the trend line. Such behavior correlates well with **Doty, 1974; and Sarsam, 2012** findings.

3.1.3 Effect of Photogrammetry testing technique on Skid Number

Fig. 7, 8, 9, and 10 shows the variation of skid number when three testing techniques were implemented, the SN calculated using MTD obtained from photogrammetry technique was plotted on the x-axis, while the SN calculated using sand patch (silica and natural) sand and OFT equivalent to MTD or calculated from Equation 5 were plotted on y-axis. Each figure indicates very good statistical relationship, however, it was noticed that at high values of skid number, (above 20) the mode start to change, and the scatter of test results are away from the trend line. **Table 3** shows summary of the statistical models developed for asphalt concrete pavement and **Table 4** illustrates other researchers' models and their coefficient of determination. Models are similar to those developed by **Sarsam, 2010; and Sarsam and Ali, 2015**.

3.2. Cement Concrete Pavement

3.2.1. Effect of Sand Gradation Type on Skid Number

Fig.11 exhibit OFT calculated using both calculation cases for cement concrete pavement. **Fig.12** illustrates the relationship between SN when using two different types of sand in the sand patch

test (silica and natural sand). It shows that the effect of sand types on skid number was not significant for the range of sand types adopted, the coefficient of determination was 0.9997.

3.2.2. Effect of Testing Technique on Skid Number

Fig.13, 14, 15, and 16 show the variation of skid number when two testing techniques were implemented, the SN calculated using sand patch (silica sand) or (natural sand) was plotted on the x-axis, while the SN calculated using OFT equivalent to MTD or calculated from Equation 5 was plotted on y-axis. Both figures indicate very good statistical relationship, however, it was noticed that at high values of skid number up to 40. Similar findings are reported by **Sarsam et al, 2015-b**.

3.2.3 Effect of Photogrammetry testing technique on Skid Number

Fig.17, 18, 19, and 20 show the variation of skid number when three testing techniques were implemented, the SN calculated using photogrammetry technique was plotted on the x-axis, while the SN was calculated using sand patch (silica and natural sand) and OFT equivalent to MTD or calculated from Equation 5 were plotted on y-axis. Each figure indicate very good statistical relationship, however, it was noticed that at high values of skid number,(above 25) the mode start to change , and the scatter of test results are away from the trend line. Such findings are in agreement with the work reported by **Table 5** shows summary of the statistical models developed for cement concrete pavement.

4. CONCLUSIONS

Based on the field work and the testing adopted, the following conclusions can be drawn:

1. The OFT (sec) and the sand patch (MTD-cm) correlates well with each other and can be substituted with each other when skid number is determined.
2. Both of silica and natural sand with types limits of (passing sieve No. 25 and retained on sieve No. 52) show equivalent MTD values when implemented in sand patch method.
3. MTD obtained from photogrammetry technique correlates well with MTD obtained from sand patch or OFT.
4. OFT as tested using outflow meter correlates well with MTD calculated from statistical model (Equation 5) when substitute OFT when SN is adopted.
5. The statistical models obtained for SN calculation for cement concrete pavement adopted for all the tested values of SN up to 40 while for asphalt concrete the model represents SN values up to an average SN values of 25 only.
6. Each of the testing techniques adopted (sand patch, outflow time, photogrammetry technique) for macro texture determination and British Pendulum Test for micro texture determination are considered good enough for evaluation of pavement surface texture for the limited site condition tested.

**REFERENCES**

- ASTM, 2009, *Road and Paving Materials*, Annual Book of ASTM Standards, Volume 04.03, American Society for Testing and Materials, USA.
- Doty R., 1974, *A Study of the Sand Patch and Outflow Meter Methods of Pavement Surface Texture Measurement*, ASTM Annual Meeting Symposium on Surface Texture and Standard Surfaces, Washington.
- Fuentes L., Gunaratne M., and Daniel H., 2010, *Evaluation of the Effect of Pavement Roughness on Skid Resistance*, Journal of Transportation Engineering, ASCE, Volume: 136, JULY.
- Henault J., 2011, *characterizing the Macro texture of Asphalt Pavement Designs in Connecticut*, Research Project: SPR-2243, Report 2, Report No. CT-2243-2-10-3.
- Jasim L. K. 2011, *Simulation Model for the Assessment of Direct and Indirect Geo-referencing Techniques in Analytical Photogrammetry*, University of Baghdad, Surveying Engineering.
- Masad E., Rezaei A., Chowdhury A., and Freeman T. 2010, *Field Evaluation of Asphalt Mixture Skid Resistance and its Relationship to Aggregate Characteristics*", Report No. FHWA/TX-10/0-5627-2.
- Noyce D. A., Bahia H. U., Yambo J., Chapman J., and Bill A. 2007, *Incorporating Road Safety into Pavement Management: Maximizing Surface Friction for Road Safety Improvements*, Report No. MRUTC 04-04.
- Noyce D., Bahia H., Yambó J., and Kim G. 2005, *Incorporating Road Safety into Pavement Management: Maximizing Asphalt Pavement Surface Friction for Road Safety Improvements*, Midwest Regional University Transportation Center, Traffic Operations and Safety (TOPS) Laboratory.
- Sarsam S. I. 2009-a, *Assessing Asphalt Concrete Deterioration Model from In-Service Pavement Data*, TRB Conference, Developing a Research Agenda for Transportation Infrastructure Preservation and Renewal Conference, TRB, Keck Center of the National Academies, November 12–13, Washington, D.C.
- Sarsam S. I. 2009-b, *Modeling Asphalt Pavement Surface Texture Using Field Measurements*, TRB Conference, Developing a Research Agenda for Transportation Infrastructure Preservation and Renewal Conference, TRB, Keck Center of the National Academies, November 12–13, Washington, D.C.
- Sarsam S. I., 2011, *Evaluating Asphalt Concrete Pavement surface texture characteristics*, 4TH International Scientific conference of Salah Alden University, Erbil, 18-20 October.
- Sarsam, S. I and AL Shareef H. N., 2015, *Assessment of texture and skid variables at pavement surface*, Applied Research Journal ARJ, Vol.1, Issue, 8, pp.422-432, October.



- Sarsam S., Daham A., Ali A., 2015-a, *Implementation of Close Range Photogrammetry to Evaluate Distresses at Asphalt Pavement Surface*, International Journal of Transportation Engineering and Traffic System IJTETS, Vol. 1: Issue 1, pp.31-44.
- Sarsam S. I., 2012, *Field evaluation of Asphalt Concrete Pavement surface texture and skid characteristics*, Proceedings, 5TH Euroasphalt & Eurobitume Congress, 13-15 / June, Istanbul.
- Sarsam S. I. 2010, *Visual evaluation of Asphalt Concrete surface condition using an expert system VEACPSC*, Indian Highways IRC Vol.38. No.9, India.
- Sarsam S. and Ali A., 2015, *Assessing Pavement Surface Macro-texture Using Sand Patch Test and Close Range Photogrammetric Approaches*, International Journal of Materials Chemistry and Physics, Public science framework, American institute of science Vol. 1, No. 2, pp. 124-131.
- Sarsam S., Daham A., Ali A., 2015-b, *Comparative Assessment of Using Visual and Close Range Photogrammetry Techniques to Evaluate Rigid Pavement Surface Distresses*, Trends in Transport Engineering and Applications. STM Journals, TTEA; 2(2): pp.28–36.

LIST OF Symbols

AASHTO: American Association of State Highway and Transportation Officials.
 ASTM: American Society for Testing and Materials.
 BPN: British Pendulum Number.
 DGPS: Differential Global Position System Receiver.
 EOP: Exterior Orientation Parameters.
 GIS: Geographic Information System.
 INS: Inertial Navigation System.
 MTD: Mean Texture Depth.
 OFT: Outflow Time.
 SN: Skid Number.

Table 1. Properties of Sand

Types of Sand	Density
Silica Sand (yellow)	1.44 gm./ cm ³
River Sand (gray)	1.31 gm./ cm ³

Table 2. Properties of the Digital Camera

Property	Specifications
Brand	Panasonic fz50
Focal Length	35 mm
Pixel Size	1.9 micron

**Table 3.** Summary of the Statistical Models Developed for asphalt concrete pavement

Mathematical Model	R ²	Y- axis SN	X-axis SN
$y = 0.9864x - 0.0153$	0.9997	MTD (cm),sand patch, silica sand	MTD (cm), sand patch, natural sand
$y = 1.1949x + 0.2705$	0.9977	OFT (sec)	MTD (cm), sand patch, natural sand.
$y = 1.2111x + 0.2923$	0.9976	OFT (sec)	MTD (cm),sand patch, silica sand
$y = 0.9373x + 0.2182$	0.9976	MTD (cm),OFT,eq.5	MTD (cm), sand patch, natural sand
$y = 0.95x + 0.2353$	0.9975	MTD (cm),OFT,eq.5	MTD (cm),sand patch, silica sand
$y = 0.7844x + 0.0054$	1	MTD (cm),OFT,eq.5	OFT (sec)
$y = 0.9952x - 0.1848$	0.9955	MTD (cm), sand patch, natural sand	MTD, photo. technique
$y = 0.9787x - 0.1745$	0.9942	MTD(cm),sand patch, silica sand	MTD, photo. technique
$y = 1.1918x - 0.1063$	0.9963	OFT (sec)	MTD, photo. technique
$y = 0.9366x - 0.0881$	0.9961	MTD (cm),OFT,eq.5	MTD, photo. technique

Table 4. Other Researchers Models

Tests	The thesis Models		Sarsam, 2009-a	
	Eq.	R ²	Eq.	R ²
SN sand patch (silica & natural)	$y = 0.9864x - 0.0153$	0.9997	$y = 1.002 x - 0.0123$	0.993
SN sand patch (silica sand) & OFT (tested)	$y = 1.2111x + 0.2923$	0.9976	$y = 1.279 x + 0.4541$	0.993
SN sand patch (natural sand) & OFT (tested)	$y = 1.1949x + 0.2705$	0.9977	$y = 1.277 x + 0.3195$	0.993

Table 5. Summary of the Statistical Models Developed for cement concrete pavement

Mathematical Model	R ²	Y- axis (SN)	X-axis (SN)
$y = 0.9946x - 0.0011$	0.9997	MTD(cm),sand patch, silica sand	MTD (cm), sand patch, natural sand
$y = 1.2134x - 0.0567$	0.9984	OFT tested (sec)	MTD (cm), sand patch, natural sand
$y = 1.2201x - 0.057$	0.9989	OFT tested (sec)	MTD(cm),sand patch, silica sand
$y = 0.9531x - 0.0486$	0.9984	MTD (cm),OFT,equation-5	MTD (cm), sand patch, natural sand
$y = 0.9583x - 0.0488$	0.9989	MTD (cm),OFT, equation-5	MTD(cm),sand patch, silica sand



$y = 0.7854x - 0.0038$	1	MTD (cm),OFT, equation-5	OFT tested (sec)
$y = 0.9977x - 0.1354$	0.9931	MTD (cm), sand patch, natural sand	MTD, photo. technique
$y = 0.9841x - 0.0881$	0.9908	MTD(cm),sand patch, silica sand	MTD, photo. technique
$y = 1.1802x - 0.1975$	0.9878	OFT tested (sec)	MTD, photo. technique
$y = 0.9274x - 0.1515$	0.9882	MTD (cm),OFT, equation-5	MTD, photo. technique

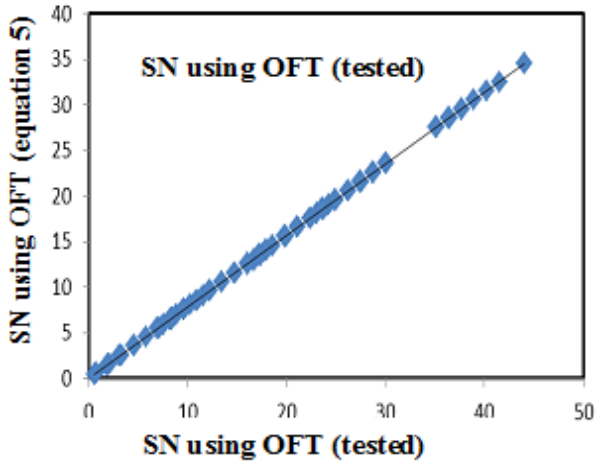


Figure 1. OFT Calculated Using Two Cases Sand type

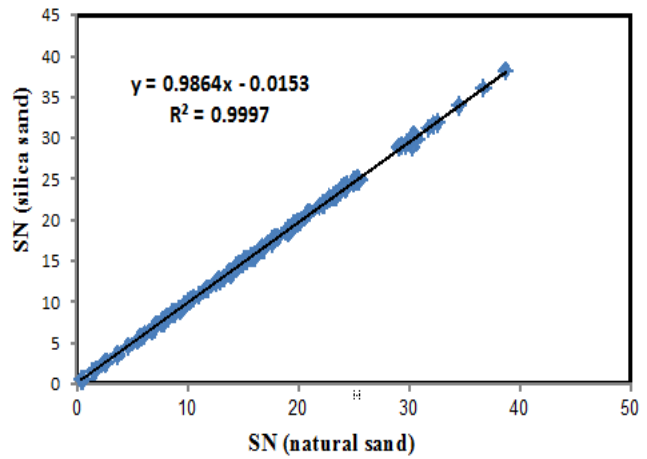


Figure 2. Variation of Skid Number with

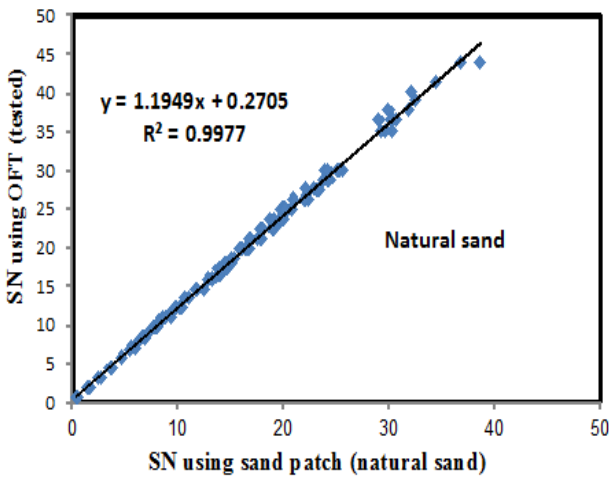


Figure 3: Effect of Testing Technique on SN

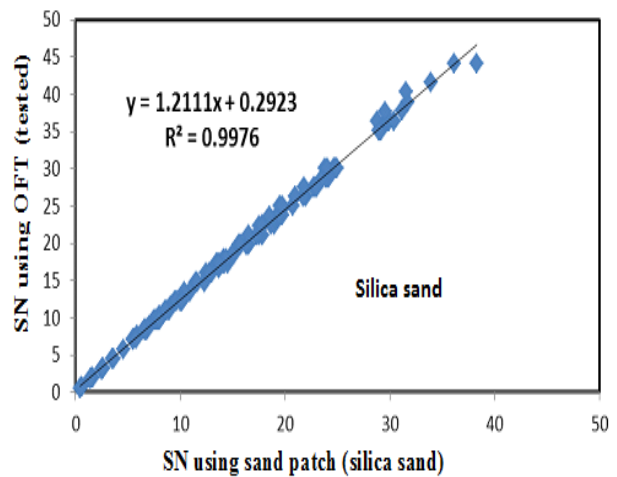


Figure 4: Effect of Testing Technique on SN

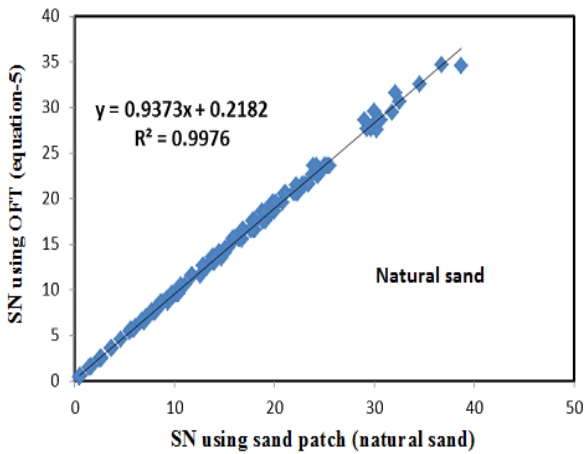


Figure 5. Effect of Testing Technique on SN

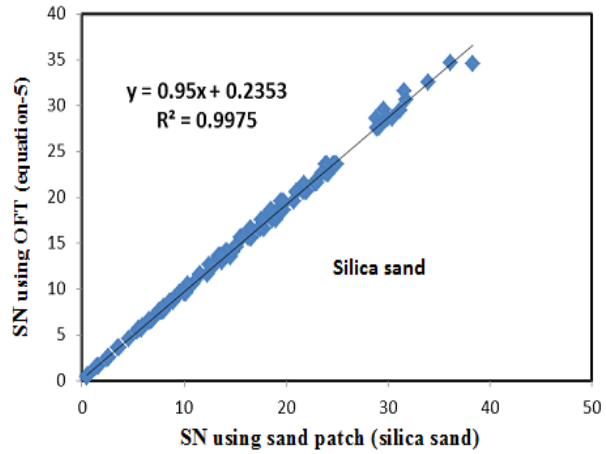


Figure 6: Effect of Testing Technique on SN

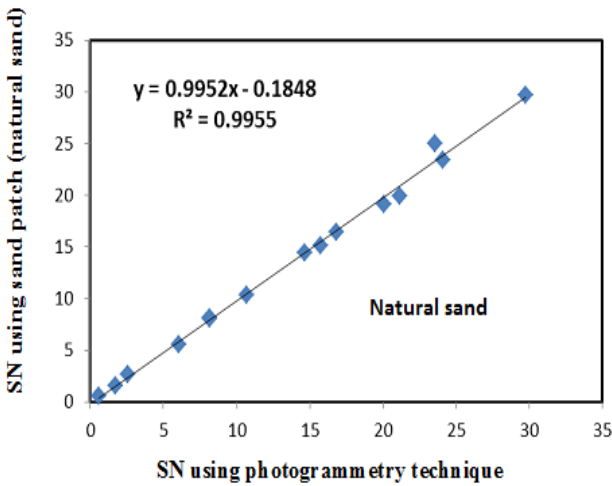


Figure 7. Variation of SN Using Photo technic

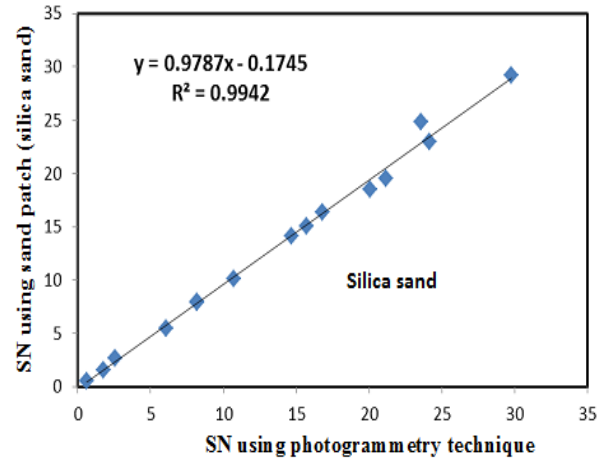


Figure 8. Variation of SN Using Photo technic

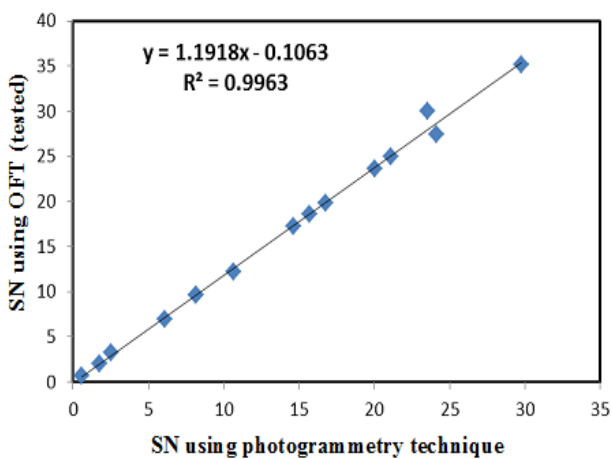


Figure 9. Variation of SN Using Photo and OFT

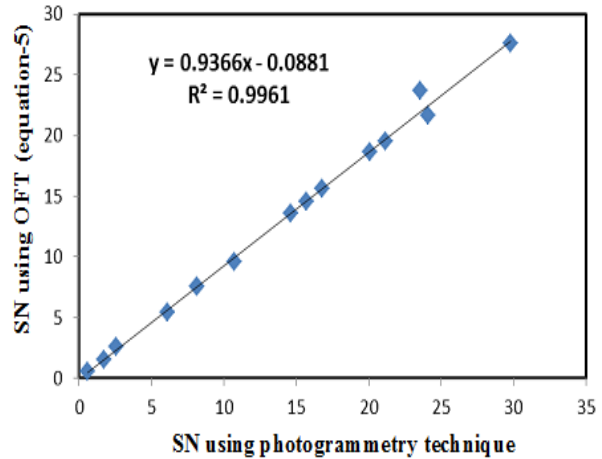


Figure 10. Variation of SN Using Photo and OFT

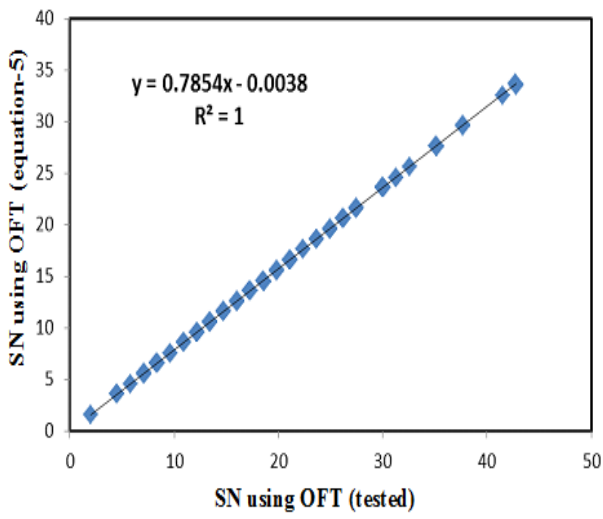


Figure11. OFT Calculated Using Two Cases

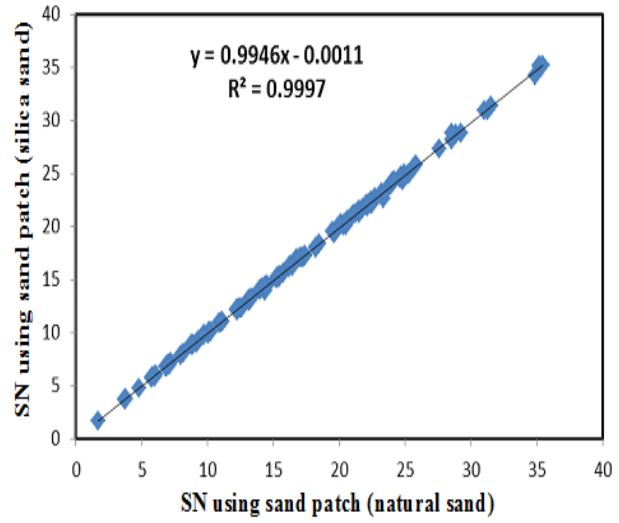


Figure12. Variation of Skid Number with Sand type

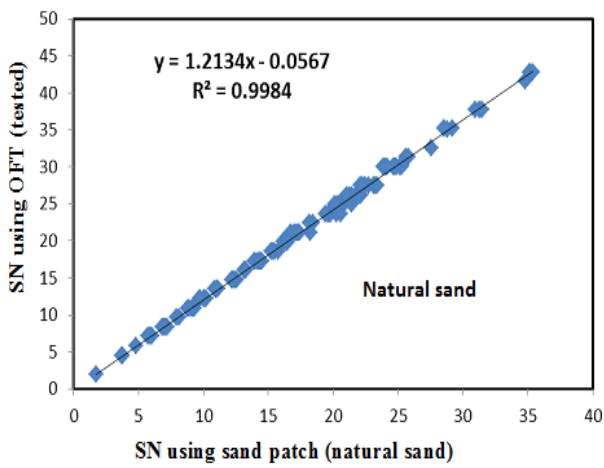


Figure 13. Effect of Testing Technique on SN

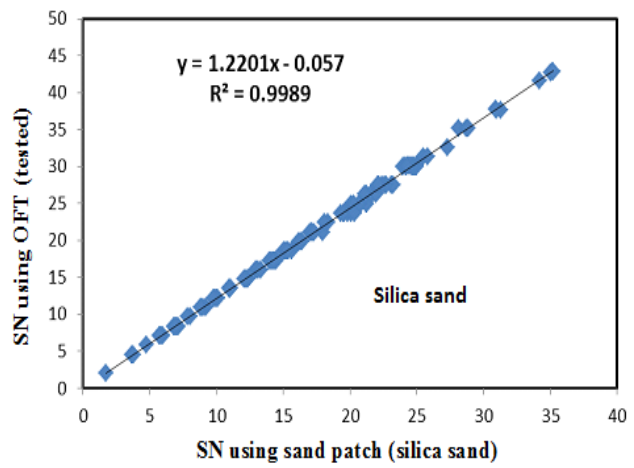


Figure14. Effect of Testing Technique on SN

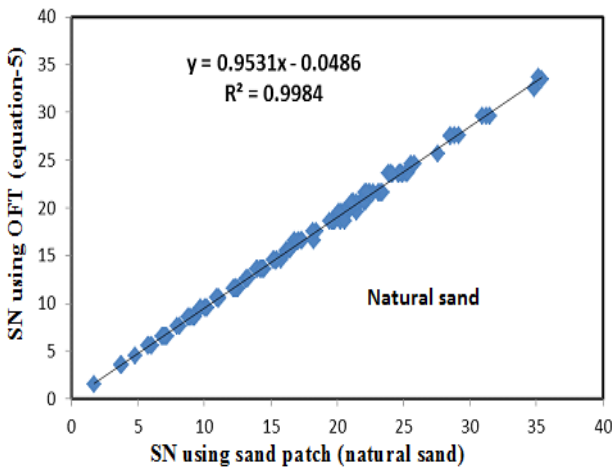


Figure 15. Effect of Testing Technique on SN

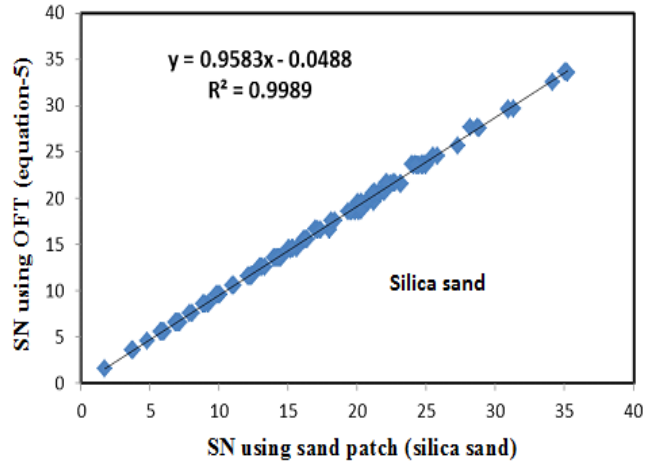


Figure 16. Effect of Testing Technique on SN

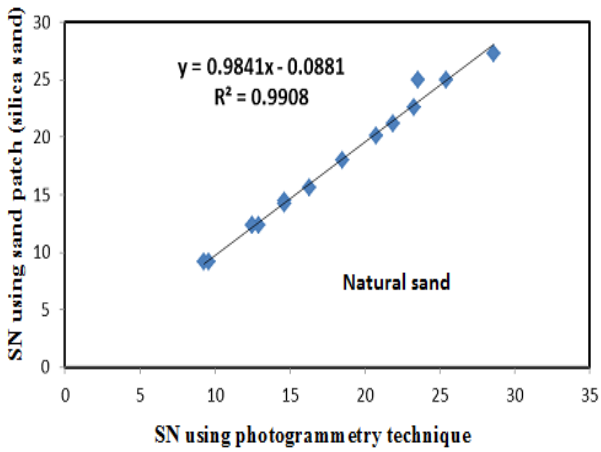


Figure 17. Variation of SN Using Photo

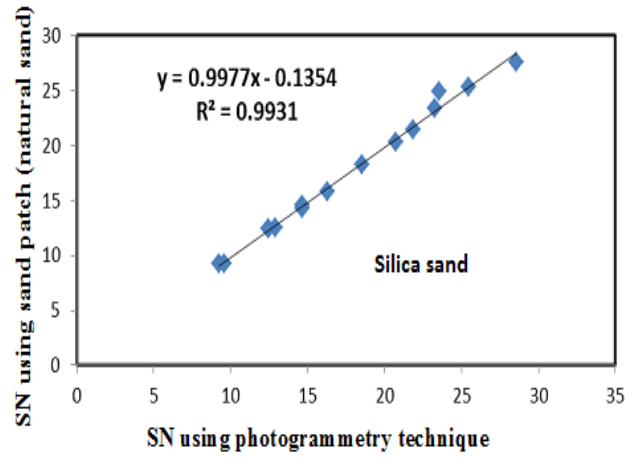


Figure 18. Variation of SN Using Photo .

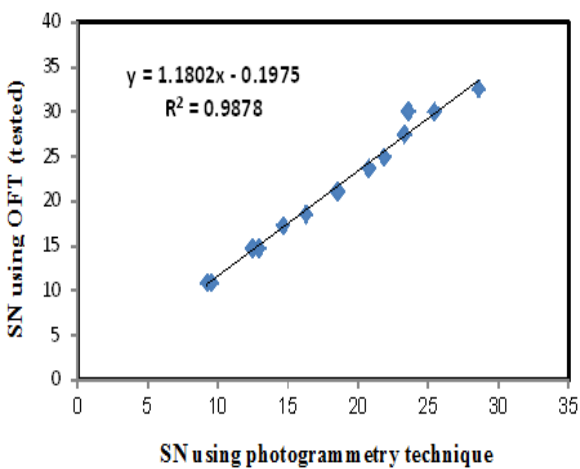


Figure 19. Variation of SN Using Photo and OFT

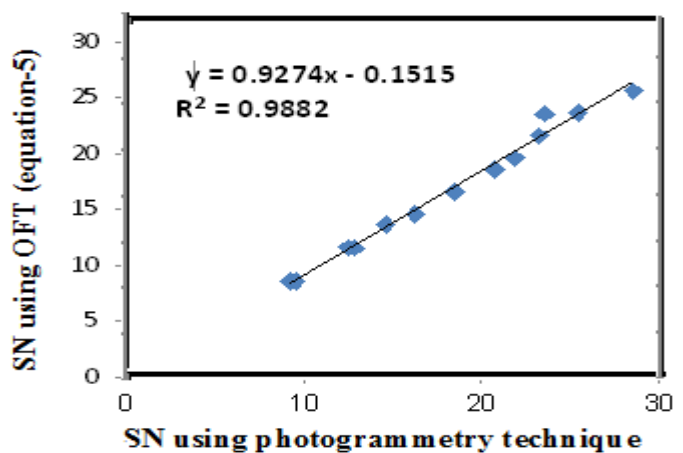


Figure 20. Variation of SN Using Photo and OFT.



Prediction of Ryznar Stability Index for Treated Water of WTPs Located on Al-Karakh Side of Baghdad City using Artificial Neural Network (ANN) Technique

Asst. Prof. Dr. Awatif Soaded
Alsaqqar
Department of Civil Engineering
College of Engineering
University of Baghdad
Email: d.alsaqqar@yahoo.com

Asst. Prof. Dr. Basim Hussein
Khudair
Department of Civil Engineering
College of Engineering
University of Baghdad
Email: basim22003@yahoo.com

Lect. Dr. Sura Kareem Ali
Department of Civil Engineering
College of Engineering
University of Baghdad
Email: srak39@yahoo.com

ABSTRACT

In this research an Artificial Neural Network (ANN) technique was applied for the prediction of Ryznar Index (RI) of the flowing water from WTPs in Al-Karakh side (left side) in Baghdad city for year 2013. Three models (ANN1, ANN2 and ANN3) have been developed and tested using data from Baghdad Mayoralty (Amanat Baghdad) including drinking water quality for the period 2004 to 2013. The results indicate that it is quite possible to use an artificial neural networks in predicting the stability index (RI) with a good degree of accuracy. Where ANN 2 model could be used to predict RI for the effluents from Al-Karakh, Al-Qadisiya and Al-Karama WTPs as the highest correlation coefficient were obtained 92.4, 82.9 and 79.1% respectively. For Al-Dora WTP, ANN 3 model could be used as R was 92.8%.

Key words: artificial neural network; Reynar index; water stability; water treatment plants; correlation coefficient.

التنبؤ بمؤشر الاستقرار (RI) للمياه المعالجة من محطات تصفية الماء على جانب الكرخ من مدينة بغداد باستخدام تقنية الشبكات العصبية الاصطناعية (ANN)

م.د. سري كريم علي
قسم الهندسة المدنية
كلية الهندسة/جامعة بغداد

أ.م.د. باسم حسين خضير
قسم الهندسة المدنية
كلية الهندسة/جامعة بغداد

أ.م.د. عواطف سوّدد عبدالحميد
قسم الهندسة المدنية
كلية الهندسة/جامعة بغداد

الخلاصة

في هذا البحث تم تطبيق تقنية الشبكات العصبية الاصطناعية (ANN) للتنبؤ بمؤشر الاستقرار (RI) من المياه المتدفقة من محطات تصفية الماء في الجانب الكرخ (الجانب الأيسر) في مدينة بغداد للعام 2013. قد طورت وفحصت ثلاثة نماذج (ANN1, ANN2, and ANN3) باستخدام البيانات من أمانة بغداد بما في ذلك نوعية مياه الشرب للفترة من 2004 إلى 2013. وتشير النتائج إلى أنه من الممكن جدا استخدام الشبكات العصبية الاصطناعية في التنبؤ بمؤشر الاستقرار القياسي (RI) مع درجة جيدة من الدقة. حيث يمكن استخدام النموذج (ANN2) للتنبؤ (RI) لمياه المنتجة من محطات التصفية الكرخ، القادسية والكرامة بأعلى معامل الارتباط الذي تم الحصول عليه 92.4 ، 82.9 و 79.1% على التوالي. بينما يمكن استخدام النموذج (ANN3) لمحطة تصفية الدورة حيث كان معامل الارتباط 92.8%.

الكلمات الرئيسية: الشبكات العصبية الاصطناعية، مؤشر الاستقرار، استقرارية الماء، محطات تصفية الماء، معامل الارتباط.



1. INTRODUCTION

Water quality measurements include a variety of physical, chemical and biological parameters. Basic problem in the case water quality monitoring is the complexity associated with the analyzing the large number of variables. Different multivariate statistical techniques, such as cluster analysis, principal component analysis and factor analysis are used for the interpretation of complex data, **Vesna et al., 2010**. Water quality modeling using mathematical simulation techniques in fact classical process based modeling approach could provide good prediction for different water quality parameters. However these models rely on lengthy data and require a large number of input data which may be not available or unknown. Artificial Intelligence techniques (Artificial Neural Network, ANN) have proven their ability and applicability for simulating and modeling various physical phenomena in the water engineering field. In addition this technique (ANN) captures the embedded spatial and unsteady behavior in the investigated problem using its architecture and nonlinearity nature compared with other modeling techniques, **Najah et al. 2009**. Recently applications of ANNs in water engineering, ecological science and environmental engineering, have been reported and used intensively.

In **2005 Diamantopoulou et al.**, used ANN to drive and develop models to predict the monthly of same water parameters at the Axioupolis station of Axios River, Greece. These parameters included, DO, conductivity, NO_3 , Na, Ca and Mg. The monthly values of these parameters and six other water parameters with the discharge at this station for the period 1980 to 1994 were selected for this analysis. A feed forward and supervised ANN was achieved with kalman's learning rule to modify the ANN weights. The results indicated that the ANN models can be used for the prediction of these parameters and allowed the filling of missing values of time series of water quality parameters which are very serious problem in most of the Greek monitoring stations.

Aoyama et al., 2007, developed a model for purification mechanisms in Tamagawa River, Tokyo, Japan. The model was proposed to express changes in BOD, COD, Total Nitrogen and Total Phosphorus concentrations as the combination of inflows, streams and weirs for data in 2002. The ANN model used in this study constructed of functions based on observations and then used the derivatives to evaluate the cause and effect of pollution in the river. The model suggested that the cause of pollution in streams from inflows of sewage, the Tamagawa River has purification functions for COD and Total Phosphorus, but little ability for Total Nitrogen.

Mozejko and Gniot, 2008, applied ANNs for timeseries modeling of Total Phosphorus (P) concentrations in the Odra River Szczecin, Poland. Different types of ANN models were employed in this study, where the optimal model which gave the minimum error and best correlation between the predicated and observed data was the Generalized Regression Neural Network (GRNN) with two hiddenlayers. Data of the year's 1991 to2004 were used for the development of the model. The model performed satisfactory over the range of the data used for calibration with mean absolute error (MAE) of 0.032 mg P/dm^3 and correlation coefficient (R) 0.931. As for the prediction of P concentration in year 2005 the model gave MAE of 0.024 and R 0.865.

Predication of fecal coliform concentration in the Achencovil River, India using an ANN model was developed by **Swapna and Vijayan in 2009**. Water quality parameters used in this study were, DO, pH, temperature and turbidity in the river for the period of 1996 to 2000. The best ANN model achieved the highest correlation coefficient (R^2) was 0.911 using eight neurons in



the hidden layer. Using the same input parameters, a statistical model was developed using SPSS which gave R^2 0.874. Hence it can be inferred that the ANN model slightly outperforms the statistical model and thus can be used for predicating coliform concentrations with better accuracy.

In 2010, Vesna et al., developed a feed forward neural network (FNN) model to predict DO concentration in the Gruza reservoir, Serbia. Monthly sampling of water quality was carried out during the period of 2000 to 2003 from three sites in the reservoir. Water parameters included pH, NO_3 , NO_2 , NH_4 , Cl, Fe, Mn, P, temperature and conductivity. From the sensitivity analysis, the most effective input parameters were pH and temperature. The Levenberg Marquardt algorithm was used to train the FNN model. The results obtained that the best FNN model was having 15 hidden neurons with the highest correlation coefficient (R^2) of 0.974 for training and 0.8738 for testing. The respective values of mean absolute error (MAE) and mean square error (MSE) for the three sets were 0.4693 and 0.667 for training, 1.179 and 2.7585 for testing as for training + testing the model determined 0.5797 and 0.9923 respectively.

2. WATER TREATMENT PLANTS UNDER STUDY

The sampling sites were chosen to be the effluents from the water treatment plants on the Tigris River in Baghdad City. In Baghdad City there are eight water treatment plants located on the banks of the Tigris River along a distance of 50–60 km. These plants are Al-Karakh, Al-Karama, Al-Qadisiya and Al-Dora in Al-Karakh side (left) of the city. Where on Al-Rasafa side (right) are East Tigris, Al-Wathba, Al-Wahda and Al-Rashed WTPs. The water quality of the treated water from these plants was taken as the necessary water parameters for the determination of the water stability index (Ryznar) in this study. The different water parameters required for these calculations were provided from Baghdad Mayoralty (Amanat Baghdad) for the period from January 2004 to December 2013 for the recorded of these WTPs, which included: pH value, Alkalinity, Total Dissolved Solids, Calcium concentration and Temperature.

3. WATER STABILITY

Corrosive water can dissolve minerals and other types can deposit minerals known as scaling water, this behavior of water is known as stability. Corrosive or scaling water can be harmful to the distribution systems as it can dissolve minerals that detriment water quality or dissolve harmful metals such as lead and copper. Scaling water deposits a film of minerals that may reduce the carrying capacity of the pipes (but it may be a protective layer to prevent pipe corrosion). Also, excessive scaling may damage water heaters (boilers) and increase the friction coefficient in the pipes. Therefore the most desirable water is of stability in the range of slight scaling, Qasim et al., 2000. In general there are several ways to calculate the water stability such as Langelier and Ryznar index.

4. COMMON METHODS USED TO MEASURE WATER STABILITY

The US Environmental Protection Agency (USEPA) has recommended the use of Langelier (LSI) and Ryznar (RSI) Stability Indices to monitor the corrosion potential of water, Degremont, 1991, Kawamura, 2000. Qasim, et al., 2000 and MWH, 2005. In this study, Ryznar index is used. This index is a quantitative index of the amount of calcium carbonate scale



that would be formed and to predict the corrosiveness of waters that are not scale forming. The equation for the determination of RI is:

$$RI = 2pH_{\text{saturation}} - pH_{\text{actual}} \quad (1)$$

Where:

pH_{actual} = measured pH of water.

$$pH_{\text{saturation}} = (pk^2 - pk^s) + pCa^{+2} + pAlk + S \quad (2)$$

$(pk^2 - pk^s)$ = dissociation constant based on temperature and total dissolved solids or ionic strength.

pk^2 = acidity constant for the dissociation of bicarbonate.

pk^s = mixed solubility constant for $CaCO_3$ $pCa^{+2} = -\log$ (calcium ion in moles / liter).

$pAlk$ = $-\log$ (total alkalinity in equivalent of $CaCO_3$ / liter).

$$S = \text{salinity correction term} = 2.5 \mu^{1/2} / (1 + 5.3 \mu^{1/2} + 5.5 \mu) \quad (3)$$

Where μ = ionic strength.

For total dissolved solids content less than 500 mg/L, the ionic strength may be estimated by $2.5 \times 10^{-5} \times TDS$. An alternate approximation of ionic strength can be made using the total hardness and total alkalinity, **Millete et al., 1980**. **Table 1** lists the scale formation or corrosive tendencies of waters with various Ryznar index values, **Qasim et al., 2000**.

5. ARTIFICIAL NEURAL NETWORK (ANN)

Forecasting models can be divided into statistical and physically based approaches. Statistical approaches determine relationships between historical data sets, whereas physical based approaches models the underlying process directly. Multilayer Perception (MLP) networks are one type of Artificial Neural Networks (ANN) suited for forecasting applications and are closely related to statistical models, (the modeling philosophy for ANN is similar to that used in traditional statistical approaches), **Najah et al., 2009**.

ANN models are specified by network topology, node characteristics and training or learning rules. It is an interconnection set of weights that contains the knowledge generated by the model, **Hafizan et al., 2004**. Different types of ANNs exist; the most common types are the feed forward network and backward network multilayer perceptron. In these networks, the artificial neurons or processing units are arranged in a layered configuration as:

Input layer - connecting the input information to the network.

Hidden layer (one or more) – acting as the intermediate computational layer.

Output layer – producing the desired output.

Units in the input layer introduce normalized or filtered values of each input into the network. Units in the hidden and output layers are connected to all of the units in the preceding layer.



Each connection carries a weighting factor. The weighted sum of all inputs to a processing unit is calculated and compared to a threshold value. An activation signal then is passed through a mathematical transfer function to create an output signal that is sent to processing units in the next layer. Training an ANN is a mathematical exercise that optimizes all of the network weights and threshold values, using some fraction of the available data. ANN learns as long as the input data set contains a wide range of patterns that the network can predict. The final model is likely to find those patterns and successfully use them in its prediction, **Stewart, 2002**.

Several neural network softwares are available; Neuframe 4 has been used in this study. Three ANN models were constructed for the prediction of the Ryznar index (RI) for the four water treatment plants on the Al-Karakh Side (Al-Karakh, Al-Karama, Al-Qadisiya And Al-Dora WTPs) for the year 2013 which was considered the target year. The first step for the determination of the ANN model is the selection of the data to be the input variables. The inputs chosen for each model are listed in **Table 2**. The effect of the different combinations of these parameters has a great influence on the model performance.

The data have to be divided into three sets, training, testing and validation. This step is achieved by trial and error to select the best division with respect to the lowest testing error followed by training error and high correlation coefficient of the validation set. The general strategy adopted for finding the optimal network architecture and internal parameters that control the training process is by trial and error using the default parameters of the software. In this step, first the nodes of the hidden layer are increased until no significant improvement is gained in the model performance. Then the model is tested by changing the default parameters of the software, the momentum term which is 0.8 and the learning rate 0.2. Finally the transfer functions of the input and hidden layers are tested where the default functions of the software are, linear in the input layer and sigmoid in the hidden layer. The default alternatives of the software are to test the following functions: linear, sigmoid and hyperbolic tangent (tanh). The effect of the different combinations of these parameters will be discussed in the following section.

6. RESULTS AND DISCUSSION

1-Ryznar Stability Index (RI) was calculated using Eq.(1) for the data supplied from Baghdad Mayoralty (Amanat Baghdad) for the period from January 2004 to December 2013 for the eight WTPs in Baghdad City, which included: pH value, Alkalinity, Total Dissolved Solids, Calcium concentration and Temperature. The treated water is within the drinking water standards but the Ryznar Index of this water shows that it is corrosive to very corrosive water (RI more than 6.8).

2-ANN models that were the result of applying Neuframe 4 software and the effect of the different combinations of the input parameters are summarized in **Table 3** which shows the best model performance according to the lowest testing error and the highest correlation coefficient (R^2). All models have three layers (input layer with 5 inputs, one hidden layer with one node and one output layer). Almost all models worked best with the default parameters of the software, momentum rate 0.8 and learning rate 0.2. Finally the transfer functions of the input, hidden and output layers where also the default functions of the software which is, linear in the input layer and sigmoid in the hidden and output layers.

Model ANN 3 gave the highest R^2 (97.4%) but not the less testing error (4.0274%) where model ANN 1 for Al-Karakh WTP had the less testing model (3.7049%) and R^2 (94.3%). These three



models were tested to predict RI in the year 2013 for the four WTPs on Al-Karakh side of Baghdad city. **Table 4** shows correlation coefficient ($R^2\%$) in each plant between the predicated and observed RI values using the suggested models in **Table 3**. From this table it is clear that RI could be predicted by ANN 2 model in Al-Karakh, Al-Karama and Al-Qadisiya WTPs as the highest correlation coefficient were obtained 92.4, 82.9 and 79.1% respectively. For Al-Dora WTP ANN3 model could be used as R^2 was 92.8%. **Fig. 1 to 4** show the variation of RI in year 2013 for each plant according to the best model represented in **Table 4**.

REFERENCES

- Aoyama Tomoo, Junko Kambe, Aiko Yamauchi and Umpei Nagashima, 2007, *Construction of a Model for Water Purification Mechanisms in a River by Using a Neural Network Approach*, J. Comput. Chem. JPN., Vol. 6, No.2, PP. 135-144.
- Degremont, 1991, *Water Treatment Handbook*, 6th edition, Lavoisier Publishing, France.
- Diamantopoulou, M. J., V. Z. Antonopoulos and D. M. Papamichail, 2005, *The Use of a Neural Network Technique for the Prediction of Water Quality Parameters of Axios River in Northern Greece*, EWRA European Water 11/12, 55-62.
- Hafizan Juahir, Sharifuddin M. Zain, Mohd Ekhwan, Mazlin Mokhtar and Hasfalina Man, 2004, *Application of Artificial Neural Network Models for Predicting Water Quality Index*, Journal Kejuruteraan Awam Vol. 16, No. 2, PP. 42-55.
- Kawamura, S., 2000, *Integrated Design and Operation of Water Treatment Facilities*, 2nd edition, John Wiley & Sons, Inc. New York.
- MWH, 2005, *Water Treatment Principles and Design*, 2nd edition, John Wiley & Sons, Inc. Hoboken N.J.
- Mozejko J. and R. Gniot, 2008, *Application of Neural Networks for the Prediction of Total Phosphorus Concentration in Surface Waters*, Polish J. of Environ. Stud. Vol. 17, No. 3, PP. 363-368.
- Millette, J. R., Arthur F. Hammonds, Michael F. Pansing, Edward C. Hansen, and Patrick J. Clark, 1980, *Aggressive Water: Assessing the Extent of the Problem*, AWWA, Vol. 72, No. 5, PP. 262-266.
- Najah Ali, Ahmed Elshafie, Othman A. Karim and Othman Jaffer, 2009, *Prediction of Jobor River Water Quality Parameters Using Artificial Neural Network*, European Journal of Scientific Research, Vol. 28, No.3, PP. 422-435.
-



- Qasim S. R., E. M. Motley and G. Zhu, 2000, *Water Works Engineering Planning, Design and Operation*, Prentice Hall PTR. USA.
- Stewart A. Rounds, 2002, *Development of a Neural Network Model for Dissolved Oxygen in the Tualatin River, Oregon*, Proceedings of the 2nd Federal Interagency Hydrologic Modeling Conference, Las Vegas, Nevada July 29- August 1.
- Swapna Varma and N. Vijayan, 2009, *Prediction of Fecal Coliform Concentration in Surface Water Using Artificial Neural Network*, 10th National Conference on Technology Trends (NCTT09) 6-7 Nov.
- Vesna Rankovic, Jasna Radulovic, Ivana Radojevic, Aleksandar Ostojic and Ljiljana Comic, 2010, *Neural Network Modeling of Dissolved Oxygen in the Gruza Reservoir, Serbia*, J. Ecological Modelling, 221, PP. 1239-1244, Elsevier.

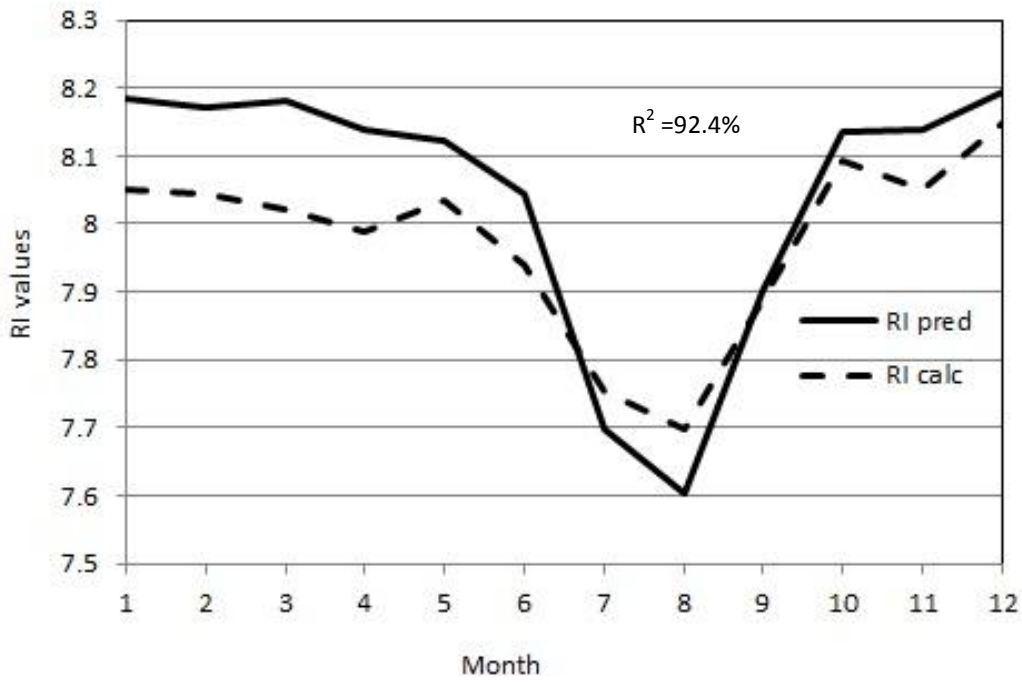


Figure 1. Calculated and predicted RI for Al-Karakh WTP during 2013 by ANN2.

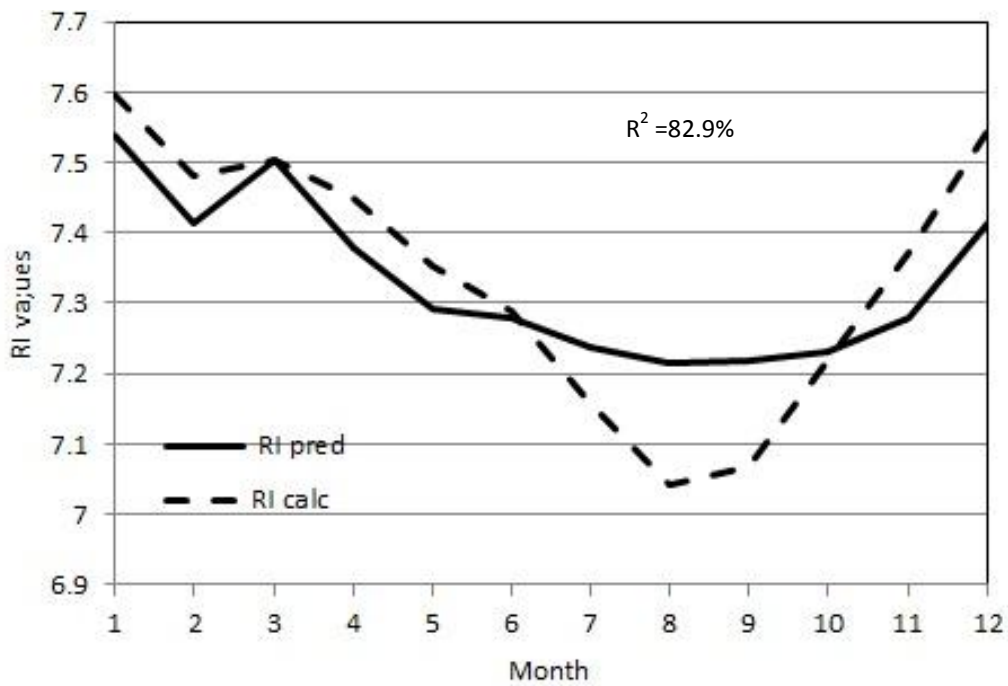


Figure 2. Calculated and predicted RI for Al-Karama WTP during 2013 by ANN2.

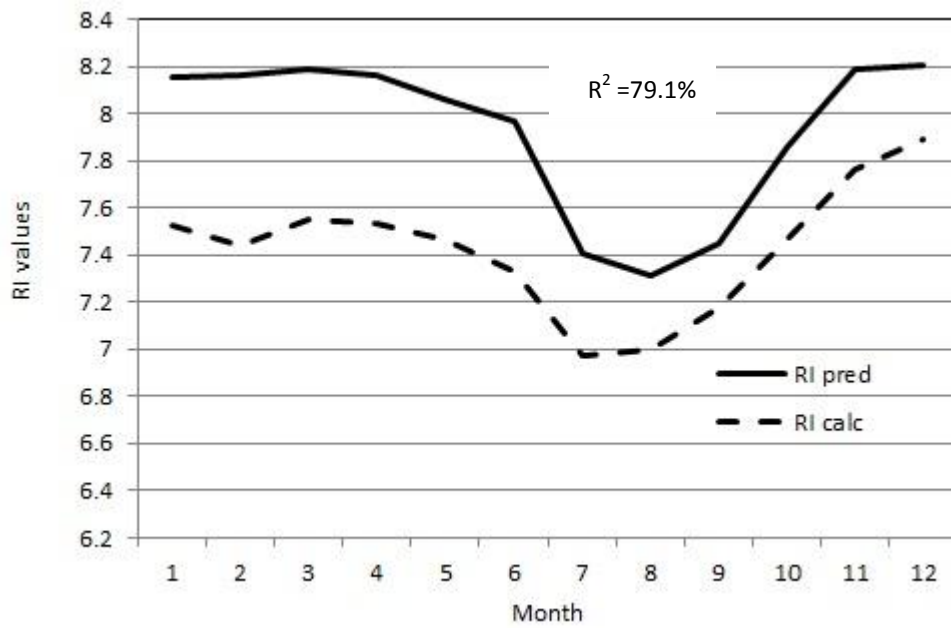


Figure 3. Calculated and predicted RI for Al-Qadisiya WTP during 2013 by ANN2.

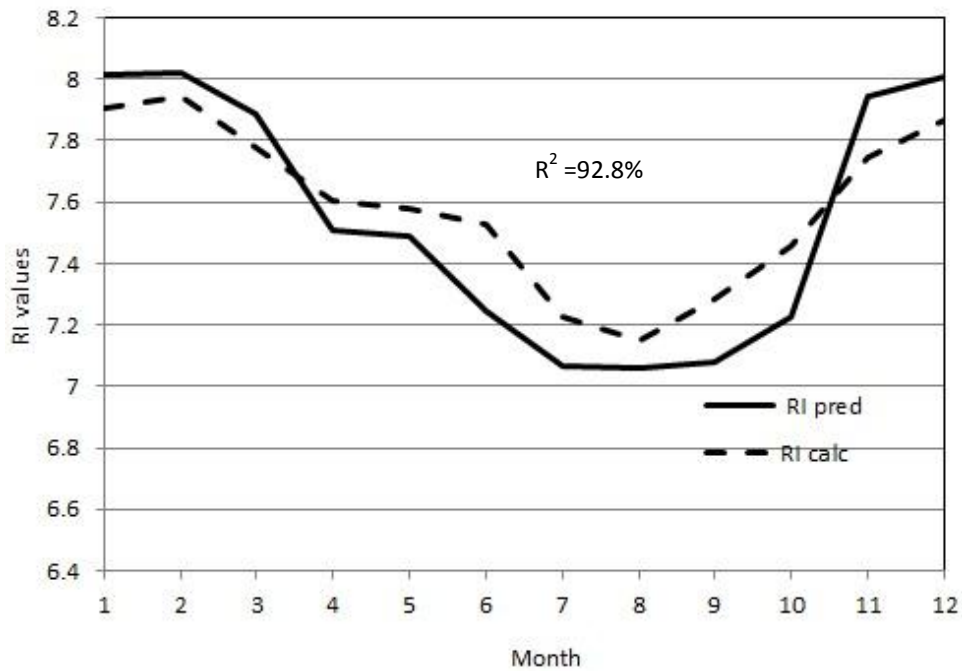


Figure 4. Calculated and predicted RI for Al-Dora WTP during 2013 by ANN3.

Table 1. Scale and corrosion tendencies of water with various Ryznar index (RI) values (Qasim et al., 2000).

RI Range	Indication
Less than 5.5	Heavy scale formation
5.5 to 6.2	Some scale will form
6.2 to 6.8	Non-scaling or corrosive
6.8 to 8.5	Corrosive water
More than 8.5	Very corrosive water

Table 2. Data used in ANN models.

Model	Input	Output
ANN 1	Water quality from each plant for 2004 to 2012	RI for each plant in year 2013
ANN 2	Water quality from the 8 plants in Baghdad for 2004 only	RI for each plant in year 2013
ANN 3	Water quality from 4 plants on Al-Karakh side from 2004 to 2012	RI for each plant in year 2013

Table 3. ANN Models, optimization and stopping criteria.

ANN model		Momentum rate	Learning rate	Testing error (%)	Training error (%)	Correlation coefficient (R ² %)
ANN 1	Al-Karakh WTP	0.8	0.2	3.7049	4.9451	94.3
	Al-Karama WTP	0.75	0.2	4.0542	5.1127	94.9
	Al-Qadisiya WTP	0.78	0.2	6.4884	4.9715	90.9
	Al-Dora WTP	0.8	0.2	6.1195	4.9809	90.2
ANN 2		0.79	0.18	4.9415	4.9286	96.5
ANN 3		0.8	0.2	4.0274	5.3908	97.4

Table 4. Correlation coefficient (R²%) in each plant.

ANN Model	WTP			
	Al-Karakh	Al-Karama	Al-Qadisiya	Al-Dora
ANN 1	79.6	72.8	77.2	90.4
ANN 2	92.4	82.9	79.1	83.3
ANN 3	87.2	56.8	61	92.8

Field Observation of Soil Displacements Resulting Due Unsupported Excavation and Its Effects on Proposed Adjacent Piles

Dr. Ala Nasir Al-Jorany

Professor

College of Engineering - University of Baghdad

alaljorany@yahoo.com

Ghusoon Sadik Al-Qaisee

Asst. Lecture

Institute of Baghdad Technology

eng_g76@yahoo.com

ABSTRACT

Soil movement resulting due unsupported excavation nearby axially loaded piles imposes significant structural troubles on geotechnical engineers especially for piles that are not designed to account for loss of lateral confinement. In this study the field excavation works of 7.0 m deep open tunnel was continuously followed up by the authors. The work is related to the project of developing the Army canal in the east of Baghdad city in Iraq. A number of selected points around the field excavation are installed on the ground surface at different horizontal distance. The elevation and coordinates of points are recorded during **23 days** with excavation progress period. The field excavation process was numerically simulated by using the finite element package **PLAXIS 3D** foundation. The obtained analysis results regarding the displacements of the selected points are compared with the field observation for verification purpose. Moreover, finite element analysis of axially loaded piles that are presumed to be existed at the locations of the observation points is carried out to study the effect of excavation on full scale piles behaviors. The field observation monitored an upward movement and positive lateral ground movement for shallow excavation depth. Later on and as the excavation process went deeper, a downward movement and negative lateral ground movement are noticed. The analyses results are in general well agreed with the monitored values of soil displacements at the selected points. It is found also that there are obvious effects of the nearby excavation on the presumed piles in terms of displacements and bending moments.

Key words: excavation, axially loaded pile, deflection, bending moment

الملاحظات الموقعية عن الازاحات في التربة الناتجة عن الحفريات غير المسندة وتأثيرها على ركيزة مجاورة افتراضية

غصون صادق القيسي

مدرس مساعد

معهد تكنولوجيا/بغداد – الجامعة التقنية الوسطى

د. علاء ناصر الجوراني

أستاذ

كلية الهندسة- جامعة بغداد

الخلاصة

ان الازاحة الجانبية للتربة الناشئة عن الحفريات المجاورة غير المسندة ذات تأثير على ركيزة مجاورة راسية محملة ، مولدة مشاكل انشائية كبيرة في مجال الهندسة الجيوتكنيكية وخاصة في حالة الركائز غير المصممة لمقاومة تأثير الازاحة الافقية للتربة . تم متابعة اعمال الحفريات الموقعية بعمق 7.0 م اثناء تنفيذ اعمال الحفريات للنفق المقترح انشاؤه في مشروع تطوير قناة الجيش شرق مدينة بغداد في العراق. تم تثبيت عدد من النقاط المراقبة المختارة على سطح الارض حول الحفريات الموقعية للنفق بمسافات أفقية مختلفة ، سجلت المناسيب والاحداثيات للنقاط خلال 23 يوم بشكل مستمر أثناء عمليات الحفر ، سير عمليات الحفر تم تمثيله باستخدام نظرية العناصر المحددة باستخدام برنامج البلاكسس (PLAXIS) . تم مقارنة نتائج التحليل التي تم الحصول عليها فيما يتعلق بالازاحات للنقاط المحددة مع المراقبة الميدانية لغرض التحقق بالاضافة الى ذلك

أجري التحليل لركائز مقترحة مفردة محملة رأسياً تم وضعها في نفس موقع نقاط المراقبة لدراسة تأثير الحفريات على سلوكية الركائز الفعلية . المراقبة الموقعية رصدت على ان الحركة الصعودية والحركة الجانبية الايجابية (عكس اتجاه الحفر) تحدث في حالة الحفريات الضحلة العمق ، ومن جهة اخرى سجلت الحركة الهبوطية والحركة الجانبية السلبية (بأتجاه الحفر) للحفريات العميقة ، بشكل عام فان المراقبة الموقعية لحركة التربة الجانبية للنقاط المختارة متوافقة مع الجانب العددي. ايضا هناك تأثير واضح للحفريات المجاورة على الركائز الافتراضية من حيث الاراحات وعزوم الانحناء .

الكلمات الرئيسية : الحفريات ، ركيزة عمودية محملة رأسياً ، الهبوط ، عزوم الانحناء

1. INTRODUCTION

Constructing the foundation of a new structure close to existing adjacent ones is a common geotechnical problem that is often encountered in practice. Such a problem becomes more complicated when the new structure requires a deep unsupported excavation such as constructing open tunnels or deep rafts for high rise buildings. Such type of excavation may cause severe damages to the adjacent structures resulting due loss of lateral confinement of the foundation soil. The design of these excavations should include an estimation of the ground movement as well as stability check of the adjacent buildings. For example, a deep foundation pit nearby a subway in Taipei was excavated, which caused the line tunnel damages and great economic losses, **Zhang, and Mo, 2014**. **Fig.1** presents case study of collapsed 13-floor building in Shanghai, China, **Ahmed, 2014** that was due to adjacent deep excavation. **Fig.2** shows lateral deformation of sheet pile nearby excavation in **Baghdad, 2015**.

The maintaining structural integrity of the pile foundations require the information of these additional loads, deflections is of great importance. It is also important to study the behavior of the structures during and after failure in order to expand knowledge of engineers after the serviceability limits of the structures, **Poulos, 1997**.

Buildings adjacent to excavation may exhibit several phenomena, **Korff, and Mair, 2013**:

- Pile capacity is reduced as smaller stress levels.
- Soil settlement below the base of pile.
- The variation of skin friction (negative or positive) due to relative movements of the soil and the pile shaft.
- Rearrangement of load between the piles.
- Lateral pile deformations.

Ong, et al., 2004, examined the case study for a building erected on soil strata including soft clay subsequent by stiffer soils. Unsupported 5-m deep slope excavation is executed beside a capped 4-pile group of 0.90m diameter bored piles during the excavation of basement. The piles were provided with strain gauges and inclinometer. Unfortunately, during the course of excavation, the slope excavation failed due to heavy rainfall. **Fig.3** shows the difference of pile deflection, lateral soil movements and maximum bending moment on the pile throughout the excavation. When the lateral movements increased, it causes increasing of induced bending moment and the pile deflection and the amount of pile deflections was significantly lesser than the consistent soil movements at the same depth. The measured bending moment override the ultimate bending moment. Severely damaged of the adjacent piles were observed due to that extreme soil movements as a result from excavation and were replaced by another group. Assessment of the influence of excavation on nearby piles is necessary but full scale tests were

considered time consuming, and needed additional cost to perform, therefore, centrifuge modeling technique was adopted to simulate the problem.

Poulos, 2007, examined the excavation for new pile cap nearby existing piles in soft to medium clay with 3.0 m and 10m depth and width of pile cap, respectively. No lateral support was available for the excavation. The examination showed the maximum bending moment was significant for the piles adjacent to the excavation. The nearby pile attempted to move upwards slightly as a result of the excavation as there was no surface pressure, while it settled when there was surface pressure. Thus, it would be observed that the bending moment and shear in the pile were developed due to lateral movement.

The case study for commercial project was carried out on the island of **Java, Indonesia**; it included the erection of three buildings: an organization building, a hotel, and a shopping mall. The investigation details showed the soil strata were soft to very soft silt underneath by firmer silt. The driven cast-in-situ piles of 0.5 m and 20 m diameter and depth respectively. The ninety piles are casted for the organization building. An excavation was progressed nearby to the shopping center where the unbraced excavation closest to the pile group with excavation depth of 4m. Horizontal movement of the soft silty soil in the direction of the excavation was observed, and it was difficult to finish the excavation. Stabilization of the excavation was attempted by steel I-beams, while it was not feasible. Also it was specified that some of the steel I-beams lied closely to the excavation were shafted more than 1m in the direction of the excavation, thereafter the building began to incline slightly. The ultimate pile capacity was significantly exceeded the design capacity due to uncontrolled excavation , **Poulos, 2007**. Displacement of the corner piles produces a transfer of the building load to the close columns of the building and causes additional bending moment in the beam and slab. Thus, cracking of the beams and slab happened, leading to additional redistribution of building loads to closely columns and slabs, and then additional cracking. The rigidity of the structure causes the inclination of building and then an increase of bending moment is caused by the eccentricity of the building load, and the tilting is worsened. Thus, the initial weakness of the piles as a result of the soil movements that caused a gradual failure of the foundation and structure throughout duration of 2 - 3 months approximately is evaluated.

Fig.4a shows the picture of cracked pile group for case study in West Malaysia throughout the construction of pile cap. Bending moment was developed in piles and led to crack and destroy of piles. **PLAXIS 3D FOUNDATION** with Hardening-Soil model was adopted to simulate the behavior of these piles throughout the excavation as shown in **Fig. 4b, Kok, et al., 2009**.

In this study, an attempt is made to investigate and evaluate some of the above mentioned side effects that result due to unsupported excavation.

2. FIELD WORK

The field work during the execution of excavation works for proposed tunnel is 7.0 m deep in the project of developing the army canal. The site location is close to east of Zayona district in the east of Baghdad city in Iraq. The project of Zayona tunnel is located between the army canal at one side and parking at Omar bin Al-Katab street in other side as presented in **Fig.5**. The tunnel occupies an approximate area about (45X28) m².

Five observations points are located at two sides close to tunnel boundaries at horizontal distance that ranges between 1.25-3.25 m from tunnel excavation edges as present in **Fig.6**.

Fig.7. shows plates of in situ points before excavation. Many difficulties are encountered after the installation and throughout the excavation due to the site activities; vehicles and worker movements, in spite of the area of points are surrounded with caution tape. The point coordinates and elevations are measured using total station before and throughout the excavation. **Table 1** shows the point horizontal distance from face of excavation and coordinates before excavation. The excavation works started in **26 June 2013** and continued for 23 days to reach the final excavation depth of 7.0 m below the natural ground level. Point's coordinates are monitored throughout the excavation period. **Fig.8** presents plates of tunnel project after excavation.

3. RESULTS OF FIELD WORK

Fig.9 displays the variation of point's displacements with time until reaching the 7.0 m depth of excavation. All points are exposed to vertical upward (positive) displacement with increasing depth of excavation until reaching depth 4.0 m (at the ten the day) after that downward vertical (negative) displacements are detected. In general the vertical displacement of points whether it is positive or negative increased with decreasing the horizontal distance between points and excavation face.

Figs.10 and 11 indicate the variation of points displacement **x** and **y** with excavation time, all points vary with excavation progress. In the beginning of excavation to excavation depth 4.0 m (at the ten the day), the positive variation is observed of points displacement whether at **x** or **y**. After that depth, negative variation of point displacement is noticed (towards the excavation).

4. NUMERICAL MODELING

4.1. Numerical Modeling of Field Work

In first part of numerical analysis, a series of **3D** finite element analyses are performed using **PLAXIS 3D** foundation program to model the ground movement at location of observation points nearby the excavation. Single pile is then assumed to be installed at same location of observation points. The pile deflection and bending moment profile are examined for each pile with excavation depth. The soil profile in the project site is consisting of approximately 20 m of Silty clay low plasticity. The Silty clay layer is modeled with hardening soil model and soil properties are listed in **Table 2** depending on soil tests and investigation report of the project. The numbers of excavation stages are five stages at 1, 2, 3, 5 and 7 m respectively. **Fig.12** displays the top view of outer boundaries of tunnel and the observation points.

4.2. Results of Numerical Modeling of Field Work

Fig.13 presents the distribution of vertical ground movement for each excavation depth. The upward vertical ground surface movement (positive) is observed for all observation points; generally, the positive vertical movement of observation points increase with increasing depth of excavation until 5.0 m deep and then decrease. The upward (positive) vertical movement is range from 15 to 60 mm in central area of tunnel pit while it is range from 3 to 15 mm at the location of observation points.

Fig.14 presents the distribution of lateral ground movement for each excavation depth. Firstly, the lateral grounds surface movements reverse to excavation direction (positive) are detected when the excavation depth is less than or equal 3.0m deep and that lateral grounds surface movements are increased with increasing excavation depth until reach excavation depth is less than or equal 3.0m deep. After that depth of excavation , the lateral grounds surface movements

reverse to the excavation (positive) are reduced and the negative lateral ground movements (towards the excavation) developed below the level of ground surface.

The comparisons are made between the field measurements and numerical analysis regarding the vertical ground movement of observation points that are shown in **Fig. 15**. Good agreements are noticed in distributions and magnitudes for depth about 4-5 m (less than the 10 days); meanwhile less agreement is observed when the depth of excavation exceeded 5 m (more than the 10 days).

4.3 Numerical Modeling of Large Scale Model Pile Performance

The response of proposed full scale axially single pile was studied due to nearby excavation of tunnel. Single pile is installed separately at each location of observation points of length and diameter 13m and 0.28 m respectively of L/d_{eq} ratios equal 46. The axial working load is evaluated about 250 KN.

Fig. 16 and 17 present the variation of pile deflection and bending moment along pile length for five excavation depths 1, 2, 3, 5 and 7 m and with 1.25m, 2.25m and 3.25 m horizontal distance from face of excavation. It can be observed that for depth of excavation less than or equal 3.0 m the pile deflection and bending moment are slightly affected compared to that occur of the deeper excavation. When the excavation depth is equal or more than 5.0 m ($L/2$), the pile deflection is almost changed to be towards the excavation (negative). The pile deflection and bending moment values decreases with increasing the horizontal distance of excavation for all depth of excavation as the comparisons present in **Fig. 18 and 19** with respect to each depth of excavation and different horizontal distance of excavation. The maximum deflection is located at pile head that reached about 8% and 10% of pile diameter for horizontal distance of excavation 3.25m and 1.25m, respectively. The minimum deflection is located at pile tip about 1/3 maximum deflection at pile head. The pile bending moments exhibits double curvature response when the excavation depth is more than 5.0 m ($L/2$) for all examined horizontal distance of excavation 1.25, 2.25 and 3.25 m.

5. CONCLUSIONS

1. Insignificant effect of excavation on pile head deflection and bending moment as the excavation depth less than half pile length.
2. Noticeable effect of excavation as the excavation depth is equal or more than 5.0 m ($L/2$), the pile deflection is almost changed to be towards the excavation (negative).
3. The pile deflection and bending moment values decreases with increasing the horizontal distance of excavation for all depth of excavation.
4. The pile bending moments are exhibited double curvature response when the excavation depth is more than half pile length ($L/2$) for all examined horizontal distance of excavation.

**REFERENCES**

- Ahmed S.A., 2014, *State-of-the-Art Report: Deformations Associated with Deep Excavation and Their Effects on Nearby Structures*, Ain Shams University, Faculty of Engineering, Structural Engineering Dept. Geotechnical Engineering Group DOI: 10.13140/RG.2.1.3966.9284.
- Kok, S. T., Haut, B.K., Noorzai, j. and Jaafar, M.S., 2009, *Modeling of Passive Piles*,. EJGE, Vo. 16 ,Bund P.
- Korff, M. and Mair, R.J. , 2013, *Response of Piled Buildings to Deep Excavations in Soft Soils*, Proceedings of the 18th International Conference on Soil Mechanics and Geotechnical Engineering, Paris 2013, 2035-2039.
- Ong, D.E.L. Leung, C.F. and Chow, Y.K., 2004, *Pile Behavior Behind a Failed Excavation*, International Conference on Structural and Foundation Failures, August 2-4, 2004, Singapore.
- Poulos, H. G. and Chen, L. T., 1997, *Pile Response Due to Excavation-Induced Lateral Soil Movement*, ASCE, Journal of Geotechnical and Geoenvironmental Engineering, Vol.123 No.2, pp.94-99.
- Poulos, H. G., 2007, *The Influence of Construction “Side Effects” On Existing Pile Foundations*, Lane Cove West, NSW, Australia, and Emeritus.
- Poulos, H. G., 2007, *Ground Movement- A Hidden Source of Loading on Deep Foundations*, DFI Journal Vol. No.1, 37:54.
- *Plaxis 3D foundation*; Material models manual V1.6 (2006).
- Zhang, A and Mo, H., (2014) , *Analytical Solution for Pile Response Due to Excavation-induced Lateral Soil Movement*, Journal of Information & Computational Science, 1111–1120.



Figure 1. Failure of a building in China in 2009 that was initiated by a nearby deep excavation, Ahmed, 2014.



Figure 2. Lateral movement of sheet pile due to nearby deep excavation, Baghdad ,2015.

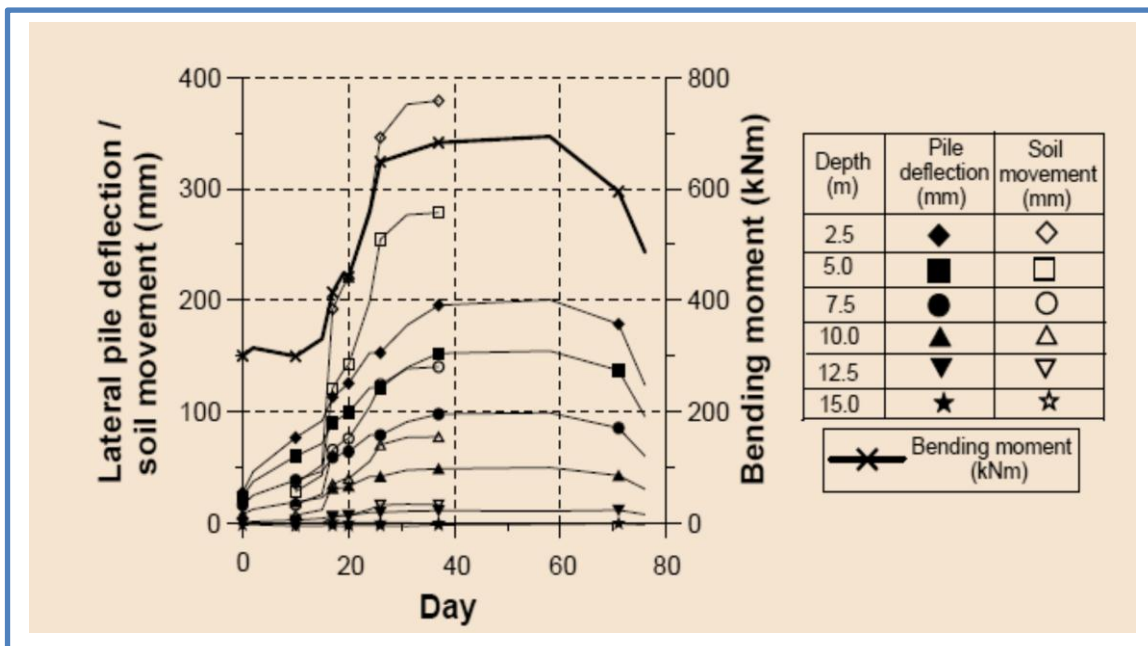


Figure 3. The induced bending moment of pile with depth for sandy soil , Chow et al., 2004.

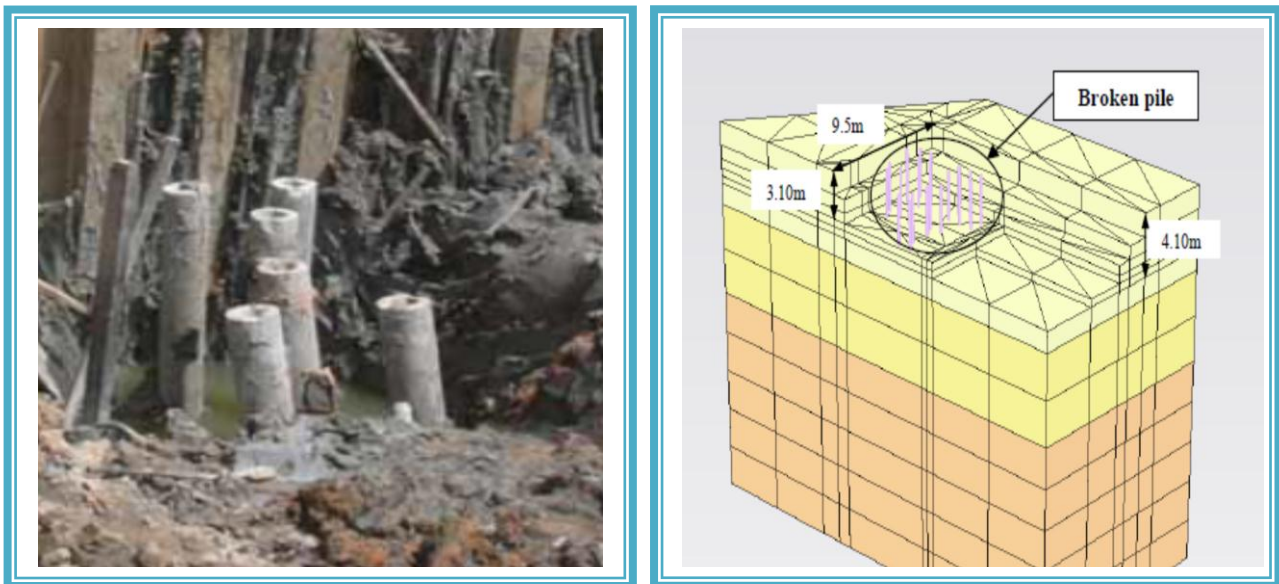


Figure 4. (a) Picture showing a 3-pile group of broken piles: (b) Excavation profile for final phase of staged construction ,Kok et al., 2009.

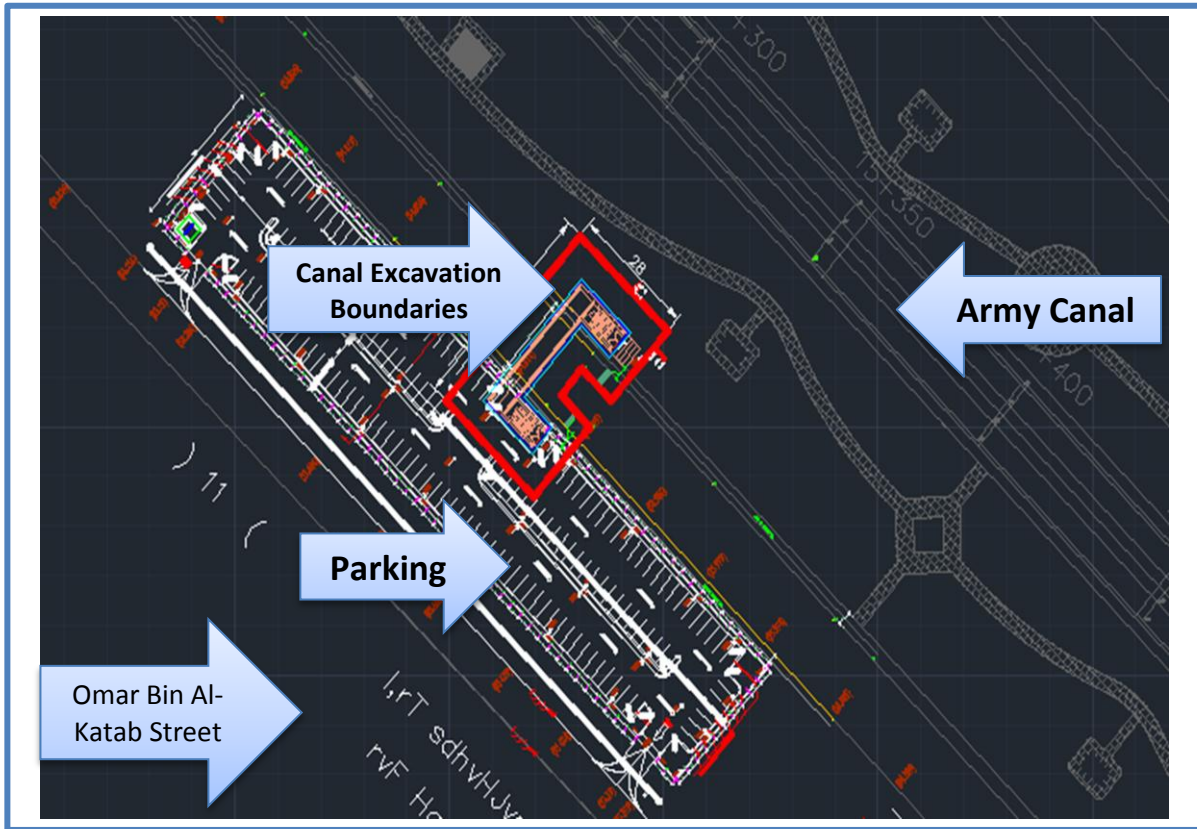


Figure 5. The project of Zayona tunnel at army canal and surrounding activities .



Figure 6. The project of Zayona tunnel at army canal and observation points.



Figure 7. Photos of points installation before excavation of Zayona tunnel at army canal.



Figure 8. Photos of excavation work of Zayona tunnel at army canal project.

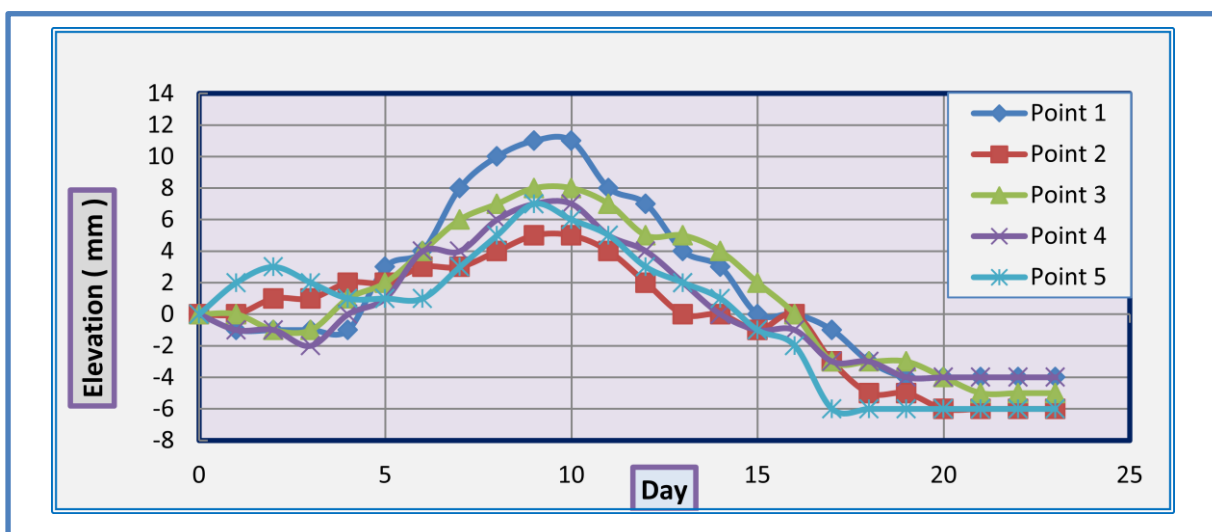


Figure 9. Vertical displacement of observation points.

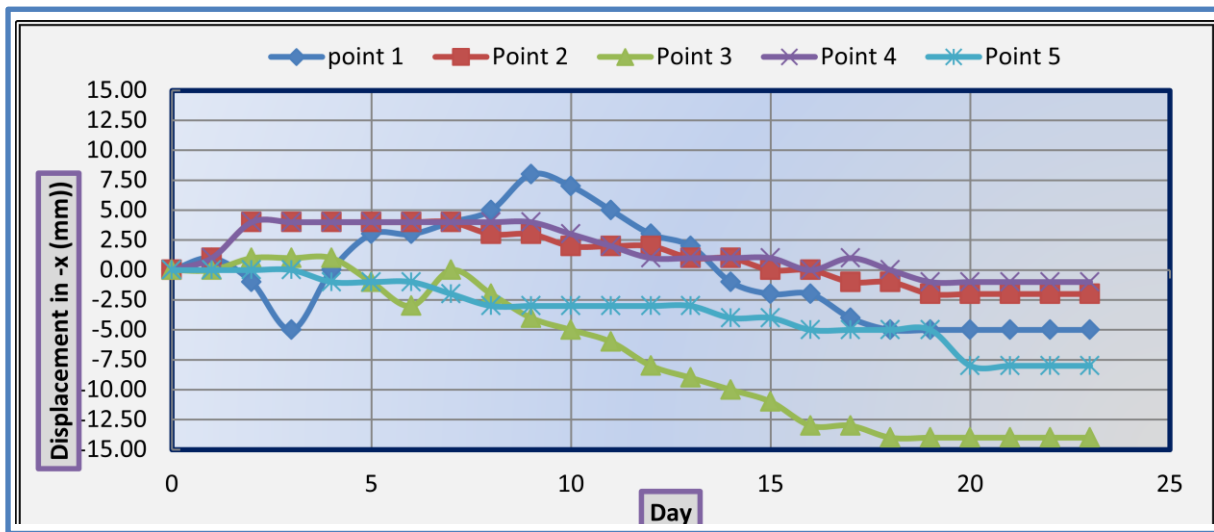


Figure 10. X- coordinates variation of observation points.

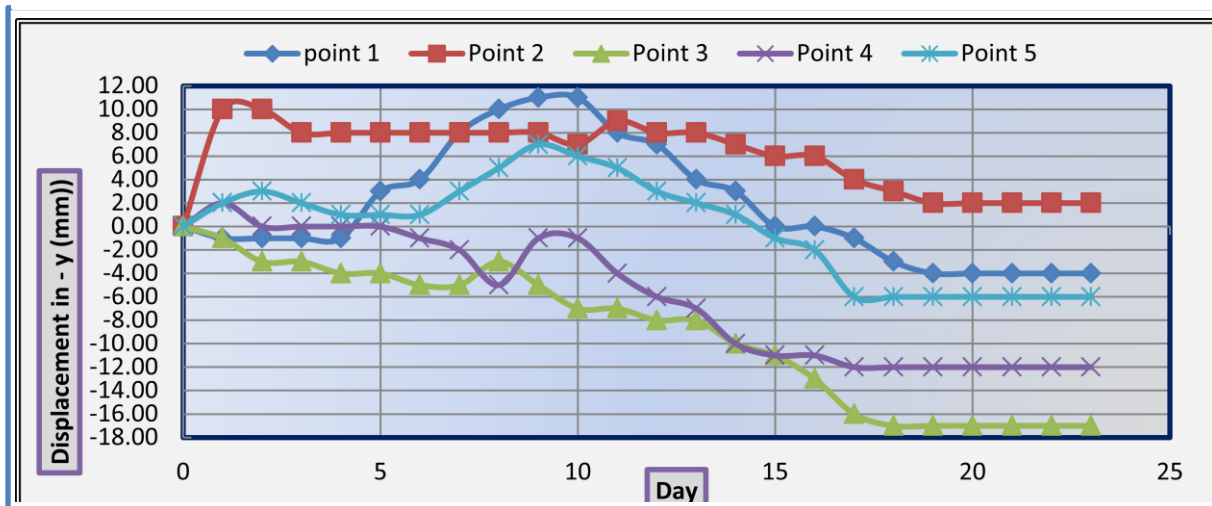


Figure 11. Y- coordinates variation of observation points.

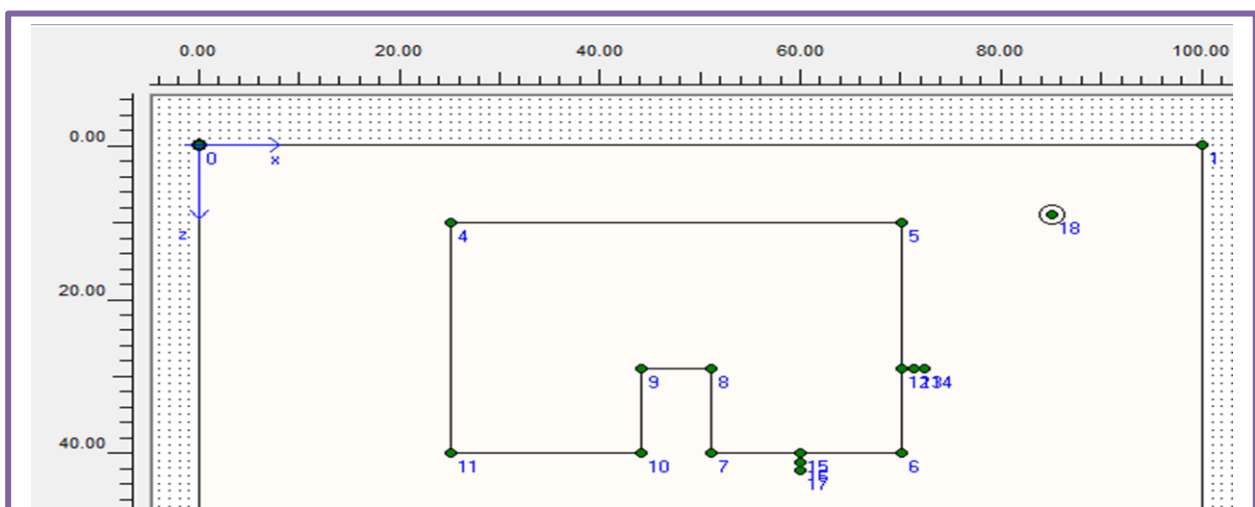


Figure 12. Top view of tunnel boundaries and on of observation points.

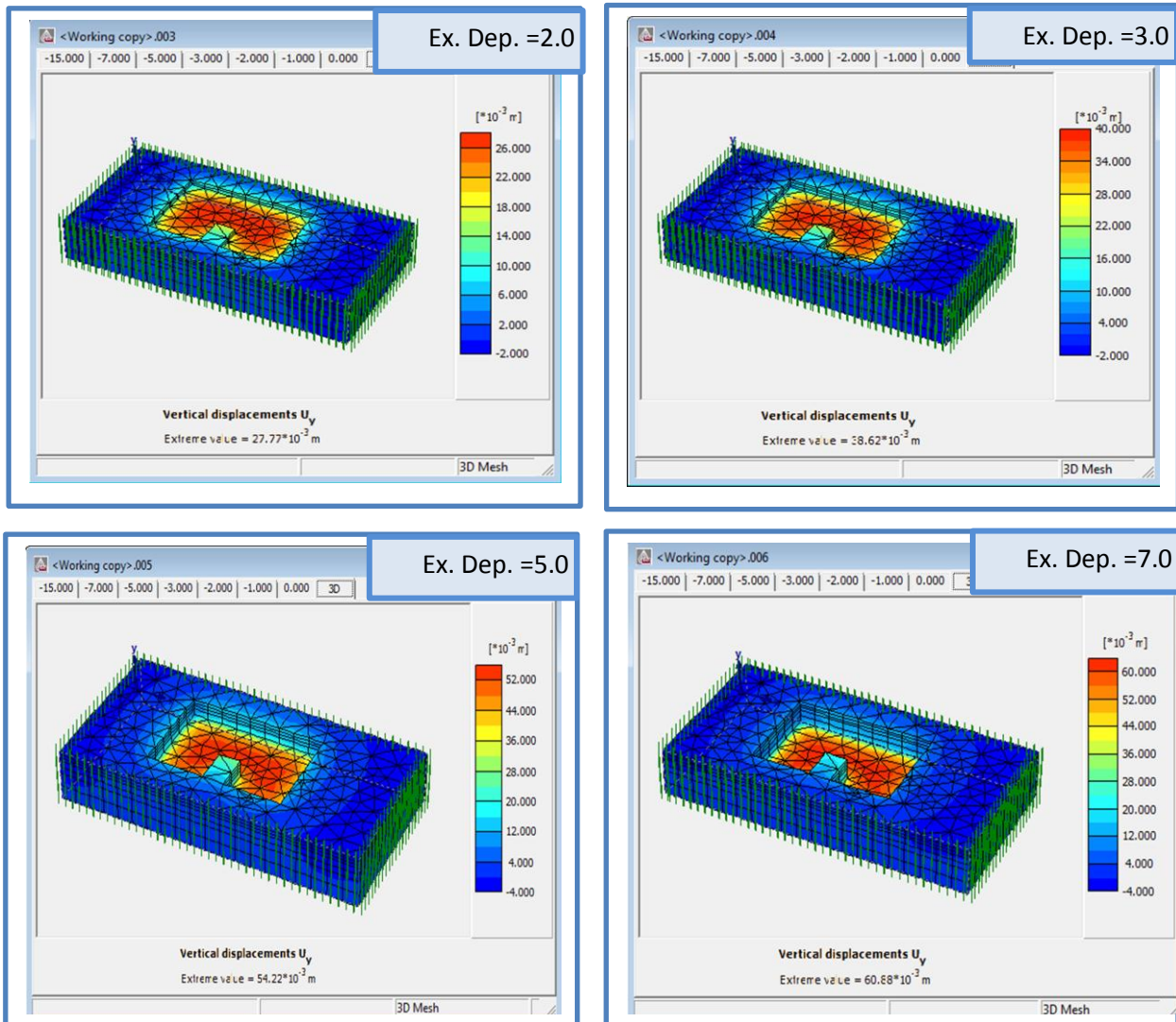


Figure 13. Vertical ground movement distribution with excavation depth.

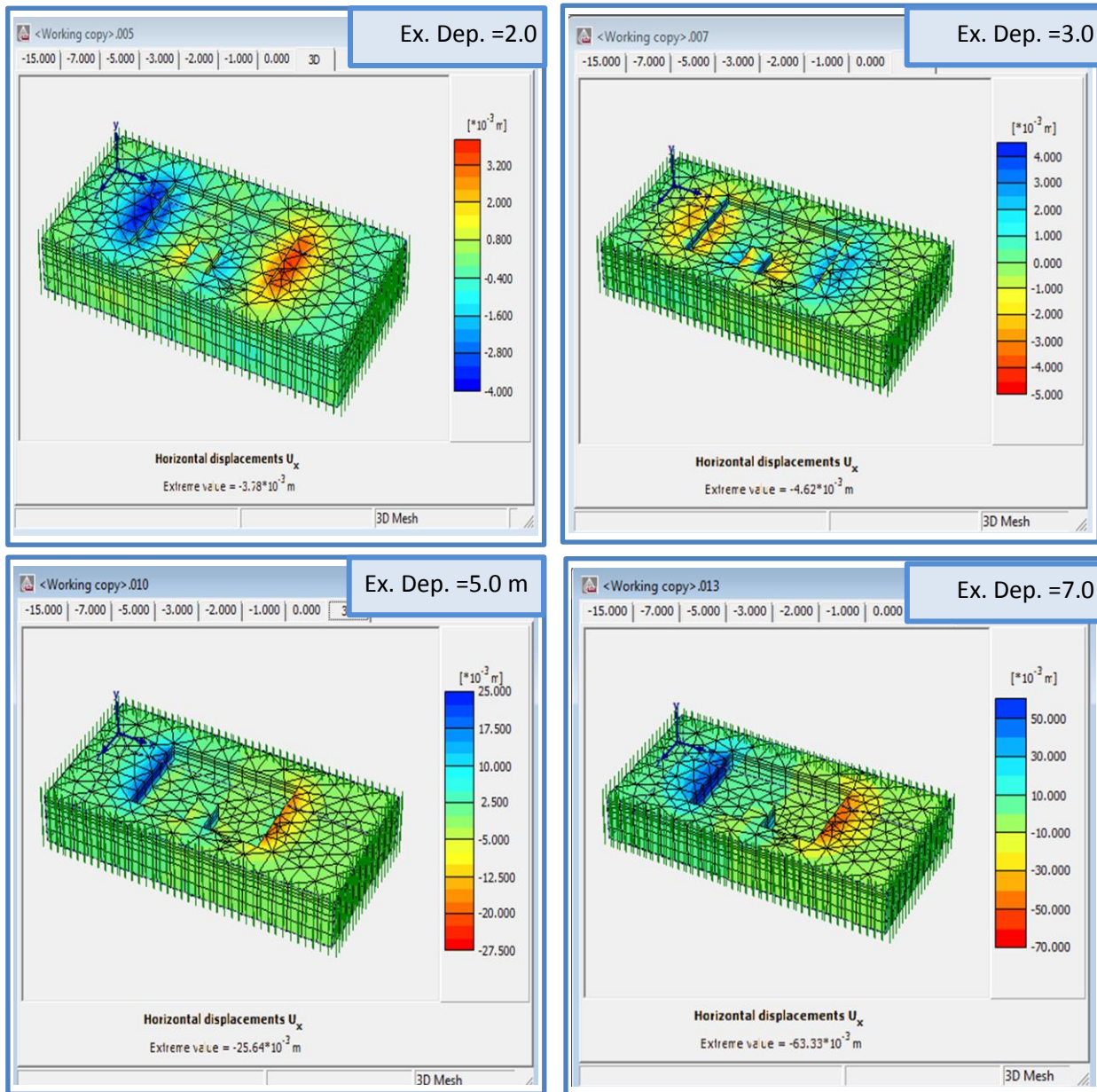


Figure 14. Lateral ground movement distribution with excavation depth

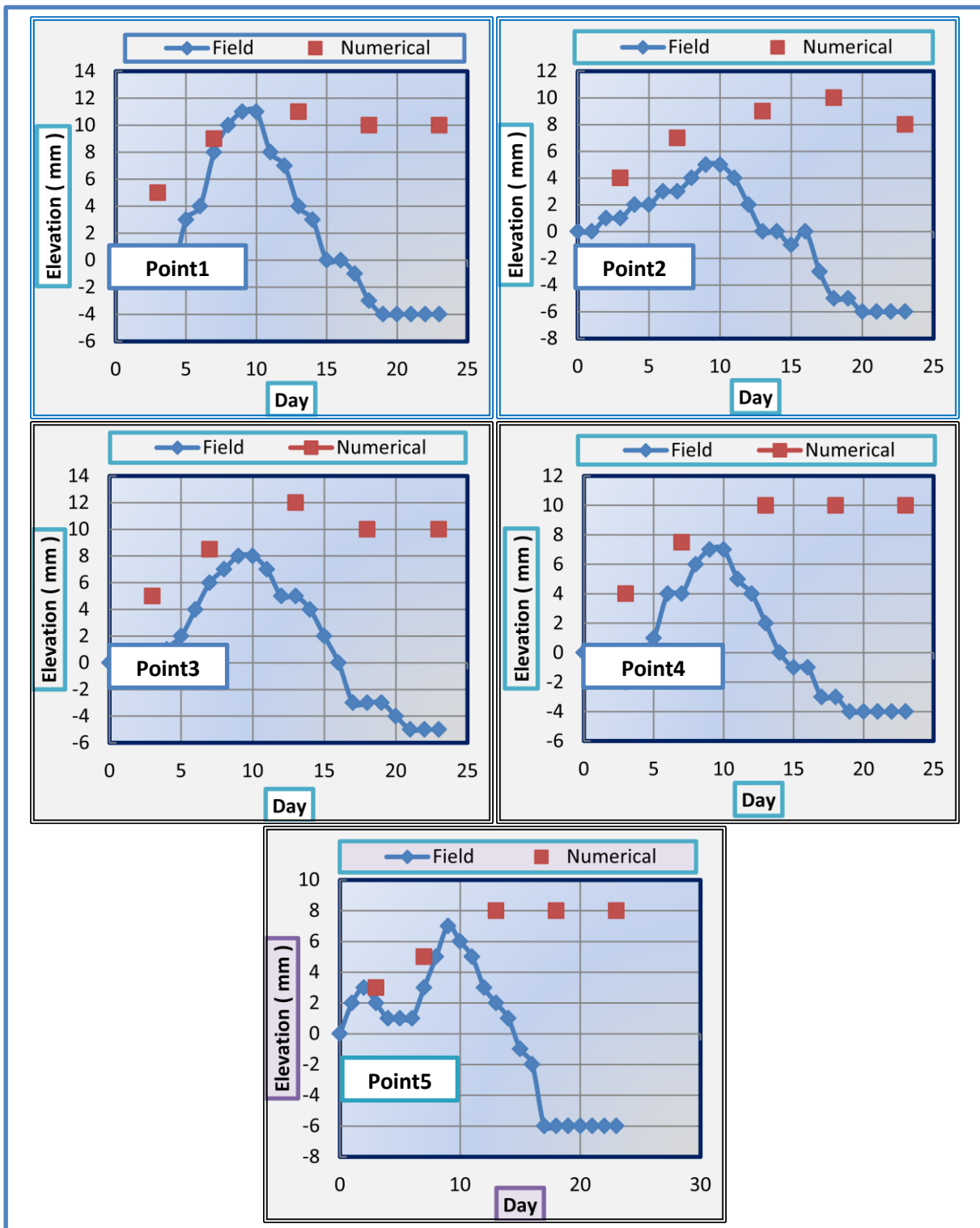


Figure 15. The comparisons of the field and numerical vertical ground movement of observation points.

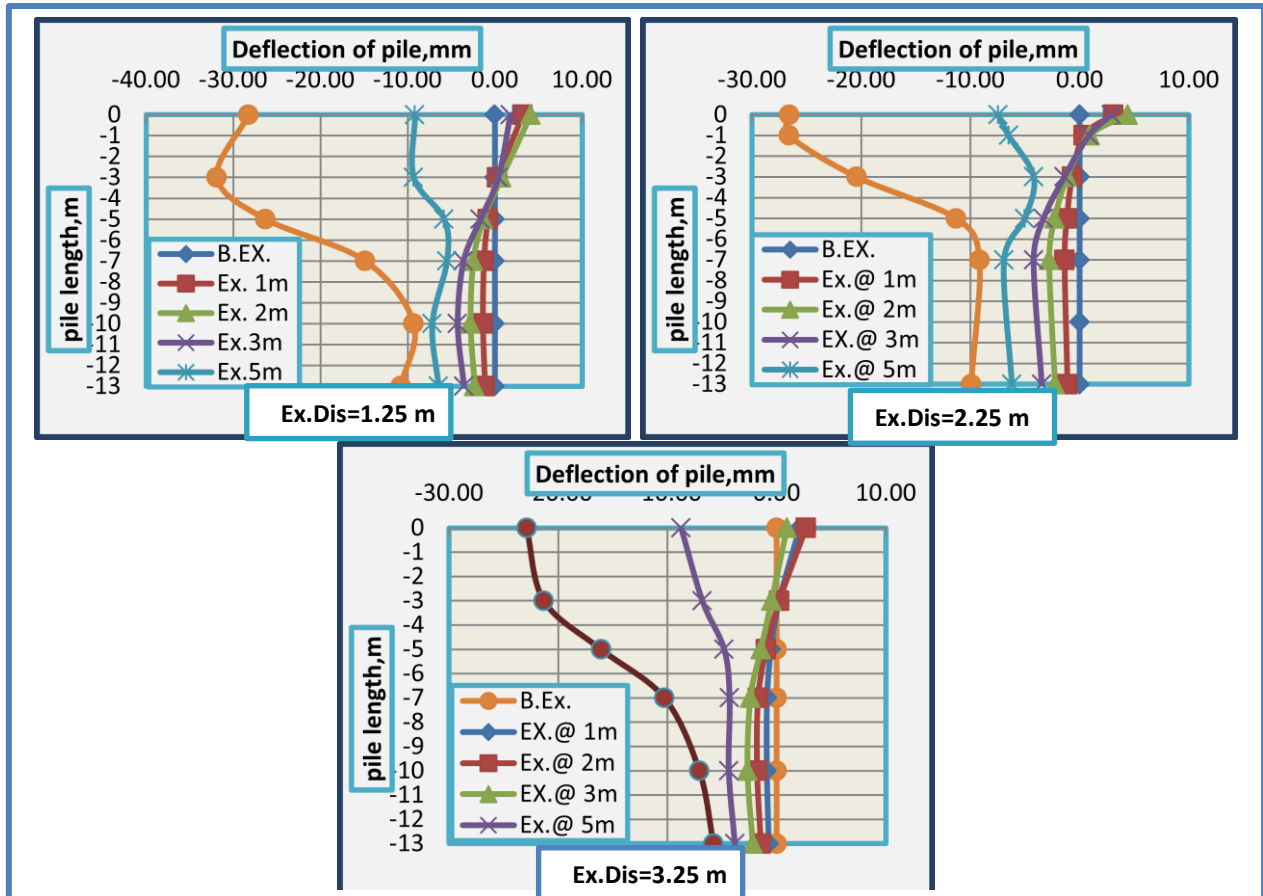


Figure 16. The variation of pile deflection with excavation depth and for each horizontal distance of excavation.

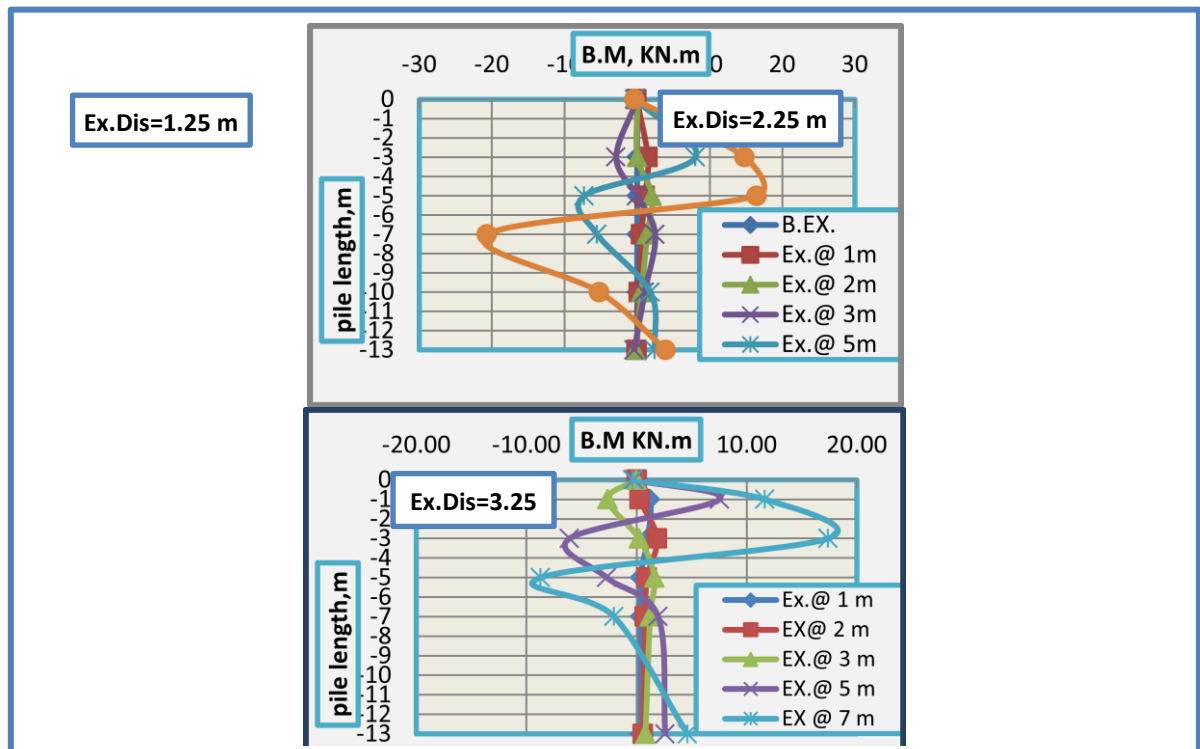


Figure17. The variation of pile bending moment variation with depth and for each horizontal distance of excavation.

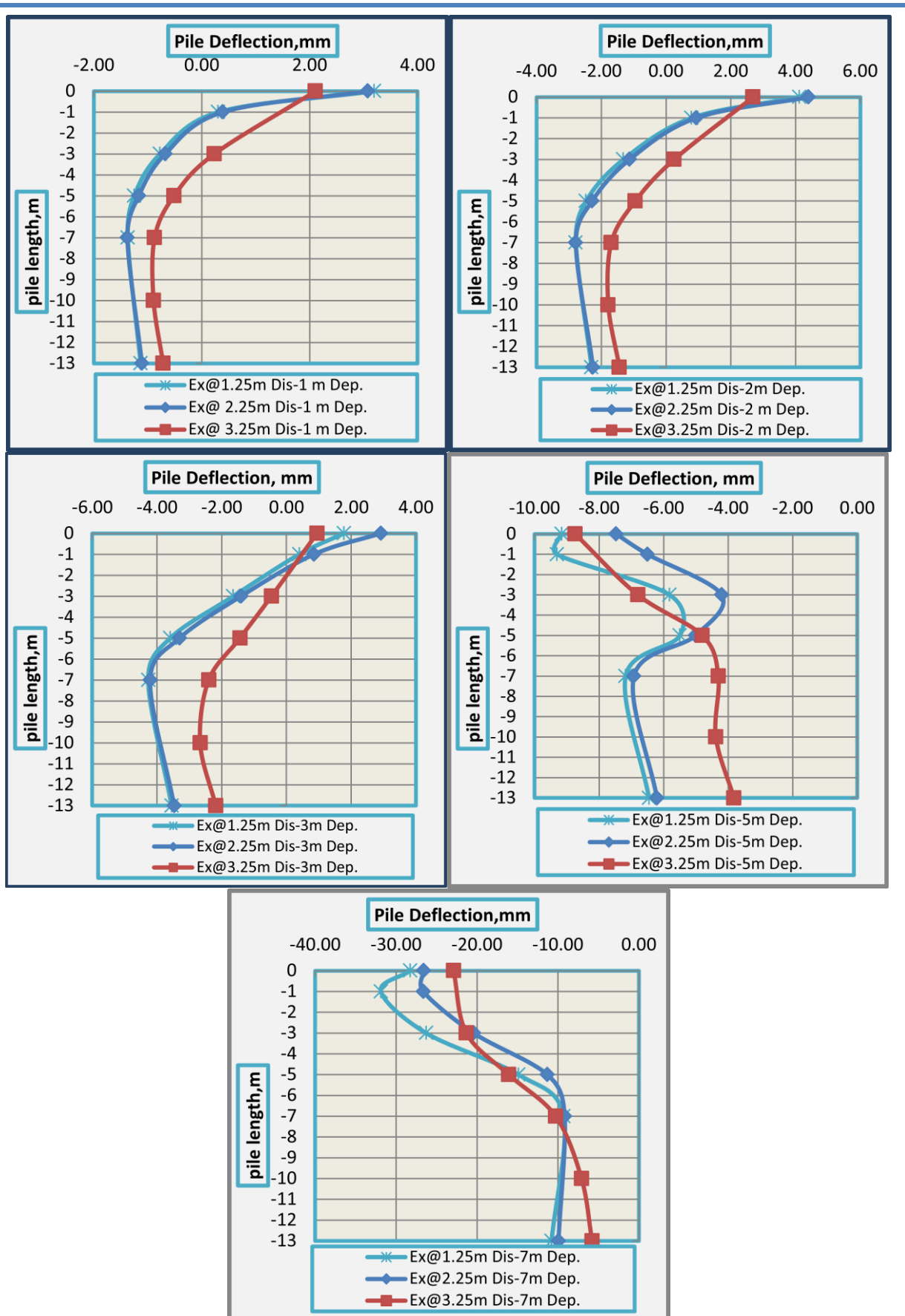


Figure 18. Comparisons of piles deflection with excavation depth and horizontal distance of excavation.

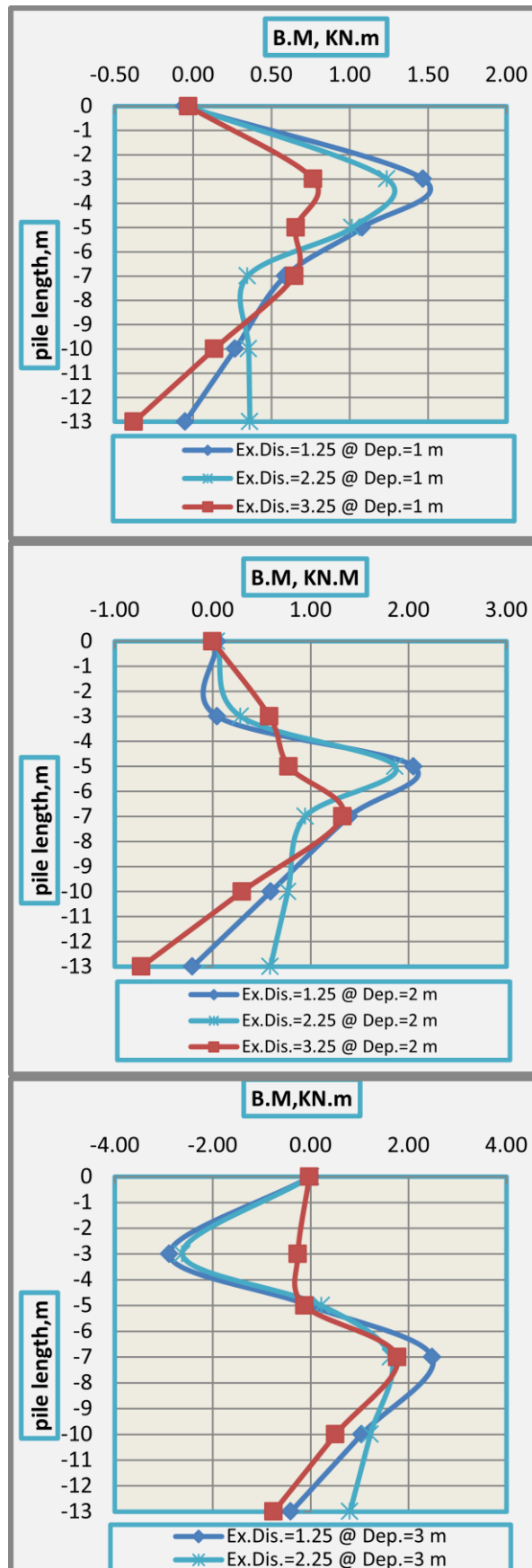


Figure 19. Comparisons of piles bending moment with excavation depth and horizontal distance of excavation.

**Table 1.** Location and global coordinates before excavation of observation points.

Point	Perpendicular distance from excavation face, m	x	y	Z
1	1.25	450493.517	3688077.891	33.363
2	2.25	450494.225	3688078.589	33.339
3	1.25	450498.727	3688065.220	33.500
4	2.25	450499.461	3688064.558	33.504
5	3.25	450500.164	3688063.851	33.508

Table 2. Material properties of in situ soil.

Parameter	Name	Value	Unit
Material model	Model	Hardening soil model	-
Type of material behavior	Type	Drained	-
Unit weight of soil	γ_{unsat}	18.0	KN/m ³
Young's Modules	E_{50}^{ref}	6500	KN/m ²
	$E_{\text{oed}}^{\text{ref}}$	6500	KN/m ²
	$E_{\text{ur}}^{\text{ref}}$	15000	KN/m ²
Poisson's ratio	ν	0.30	-
Cohesion	C_{ref}	75.0	KN/m ²
Friction angle	ϕ	15.0	°

Experimental Behavior of Laced Reinforced Concrete One Way Slab under Static Load

Abaas Abdulmajeed Allawi

Assistant. Professor

College Engineering - University of Baghdad

E-mail: abbasallawi2004@yahoo.com

Hussain Askar Jabir

Assistant Lecture

College Engineering - University of Wassit

E-mail: askar_hussain@yahoo.com

ABSTRACT

Test results of eight reinforced concrete one way slab with lacing reinforcement are reported. The tests were designed to study the effect of the lacing reinforcement on the flexural behavior of one way slabs. The test parameters were the lacing steel ratio, flexural steel ratio and span to the effective depth ratio. One specimen had no lacing reinforcement and the remaining seven had various percentages of lacing and flexural steel ratios. All specimens were cast with normal density concrete of approximately 30 MPa compressive strength. The specimens were tested under two equal line loads applied statically at a thirds part (four point bending test) up to failure. Three percentage of lacing and flexural steel ratios were used: (0.0025, 0.0045 and 0.0065). Three values of span to effective depth ratio by (11, 13, and 16) were considered, the specimens showed an enhanced in ultimate load capacity ranged between (56.52% and 103.57%) as a result of increasing the lacing steel ratio to (0.0065) and decreasing the span to effective depth ratio by (31.25%) respectively with respect to the control specimen. Additionally the using of lacing steel reinforcement leads to significant improvements in ductility by about (91.34%) with increasing the lacing steel ratio to (0.0025) with respect to the specimen without lacing reinforcement.

Key words: one way slab, laced reinforced concrete, ductility, crack, static loading.

تصرف البلاطات الاحادية الاتجاه والحاوية على حديد متعرج تحت تأثير الاحمال الساكنة

حسين عسكر جابر
مدرس مساعد
كلية الهندسة-جامعة واسط

عباس عبد المجيد علاوي
أستاذ مساعد
كلية الهندسة-جامعة بغداد

الخلاصة

في هذا البحث تم مناقشة النتائج العملية لثمانية بلاطات خرسانية احادية الاتجاه مسلحة وحاوية على تسليح متعرج. ان الغرض من هذا البحث هو دراسته تأثير استخدام التسليح المتعرج على سلوك البلاطات الاحادية الاتجاه. وكانت المتغيرات نسبة حديد التسليح المتعرج و هي (0, 0.0025, 0.0045, 0.0065)، نسبة الحديد الرئيسي و هي (0.0025, 0.0045, 0.0065) ونسبة الطول الصافي الى العمق الفعال للبلاطة و هي (11, 13, 16). احد العينات لا تحتوي على حديد متعرج اما العينات المتبقية فكانت تحتوي على نسب مختلفة من حديد التسليح المتعرج والرئيسي. بينت النتائج العملية بان التحمل الكلي للبلاطات تحسن بمقدار (56,52%) نتيجة لاستخدام الحديد المتعرج بنسبة (0.0065) و بمقدار (103,57%) كنتيجة لتقليل نسبة الطول الصافي الى العمق الفعال بمقدار (31,25%) للبلاطات الحاوية على حديد متعرج بنسب متساوية. من ناحية اخرى فأن استخدام الحديد المتعرج حسن وبشكل ملحوظ معامل المطيلية للبلاطات حيث كانت نسبة الزيادة حوالي (91,34%) للبلاطة ذات نسبة تسليح متعرج (0.0025) مقارنة مع البلاطة بدون حديد تسليح متعرج.

الكلمات الرئيسية: البلاطة الاحادية الاتجاه، خرسانة الحديد المتعرج، المطيلية، التشقق، التحميل الساكن.

1. INTRODUCTION

Conventional reinforced concrete (RC) is known to have limited ductility and concrete confinement capabilities. The structural properties of RC can be improved by modifying the concrete matrix and by suitably detailing the reinforcements. A laced element is reinforced symmetrically, i.e., the compression reinforcement is the same as the tension reinforcement, The straight flexural reinforcing bars on each face of the element and the intervening concrete are tied together by the truss action of continuous bent diagonal bars as shown in **Fig. 1**. The dashed lacing bar indicates the configuration of the lacing bar associated with the next principal steel bar. In other words, the positions of the lacing bars alternated to encompass all temperature steel bars. LRC enhances the ductility and provides better concrete confinement, **UFC 3-340-02, 2008**.

The primary purpose of shear reinforcement is not to resist shear forces, but rather to improve performance in the large-deflection region by tying the two principal reinforcement mats together. In the design of conventional structures, the primary purpose of shear reinforcement is to prevent the formation and propagation of diagonal tension cracks, **Stanley C. Woodson, 1992**.

The lacing bar permits the element to attain large deflections and fully develop the reinforcement through its strain hardening region. The maximum deflection of a laced element corresponds to 12 degrees support rotation; the maximum deflection of an element with single leg stirrups is limited to 6 degrees support rotation under flexural action or 12 degrees under tension membrane action, thus the shear reinforcement is significantly effect in enhancing the ductility of flexural element, **UFC 3-340-02, 2008**.

Extensive experimental investigations were carried out by **Parameswaran et al., 1986**, showed that the end support rotations are varied between 6° to 8° . The results of the investigations suggested that a plastic hinge rotation of 4° at end supports and 8° at all other plastic hinge locations in continuous construction. The continuous lacings are normally inclined at 45° and 60° to horizontal. The significance of shear resistance in enhancing the ductility of a flexure element can be observed. A sudden shear failure is obvious in the event of inadequate capacity. A test programme to understand the behavior of laced reinforced concrete structural elements under blast loading was undertaken by **Keshava Rao et al., 1992**, to see whether the ductility realized in monotonic tests could be achieved under blast loading, whether an increase of 25% in strength as recommended can be used in design.

Anandavlli N. et al., 2012, A new approach for finite element modeling of RC/LRC structural elements that are primarily under flexure is proposed. The current approach considers RC/LRC as a homogenous material whose stress-strain characteristics are derived based on the moment curvature relationship of the structural component. The proposed model is extended for the application to the LRC slab, where the slab is simply supported on all four sides and subjected to uniform pressure loading.

Madheswaran C.K. et al., 2015, Describes the ductility behavior of Laced Reinforced Geopolymer concrete beam (LRGPC), for the beams with shear span-to-depth ratio is less than 2.5, for these beams the ductile failure of Reinforced Concrete (RC) with conventional stirrups is not possible. Therefor they improved ductile failure of these members by proper detailing of reinforcement with inclined bars in the case of normal concrete mix. Monotonic load testing on two specimens with 45° lacing are conducted.

2. RESEARCH SIGNIFICANCE

Knowledge of the effectiveness of the lacing reinforcement on the behavior of the one way slab. A better understanding of the contributions of the shear reinforcement will allow the designer to compare the benefits of using (or not using) shear reinforcement. The static behavior of laced reinforced concrete one way slab under four point loads was studied experimentally. The tests focused on the influences of lacing steel ratio, flexural steel ratio and clear span to effective depth ratio of slab.

3. TEST SPECIMENS

The slabs were designed to reflect the interaction of the lacing reinforcement with the other primary parameters. All slabs were designed to be simply supported conditions, the dimensions, and steel reinforcement ratios were selected according to **ACI 318M-2014** code, and to satisfy and meeting with **UFC 3-340-02, 2008**, requirements for the laced reinforced concrete structures. Details of the test specimens, both with and without laced reinforced steel are discussed hereafter. The dimensions of the tested slabs are (2000mm × 700mm) and different thickness of (H=135mm, 160mm and 185mm). One of these slabs were without lacing reinforcement (Reference specimen), and seven specimens were have the lacing reinforcement with various tension steel ratio ($\rho_t=0.0025, 0.0045, \text{ and } 0.0065$) lacing steel ratio ($\rho_s=0.0025, 0.0045, \text{ and } 0.0065$), and clear span to effective depth ratio ($L/d=11, 13, 16$), as shown in **Fig. 2**. A total of eight specimens (**SS45/0, SS45/25, SS45/45, SS45/65, SS25/45, SS65/45, SM45/25** and **SL45/25**) were tested. The specimen designation can be explained as follows. The first symbol indicates the type of load (S=static load) the second symbol indicates the thickness of slab (S=small thickness=135mm, M=medium thickness=160mm, and L=large thickness=185mm), the third symbol before slash indicates the flexural steel ratio (25=0.0025, 45=0.0045, and 65=0.0065), and the last symbol denotes to the lacing steel ratio (0=no lacing reinforcement, 25=0.0025, 45=0.0045, and 65=0.0065). The entire characteristics and details of the tested specimens are listed in **Table 1**, and **Table 2** shows the details of each group.

The properties of the steel used in the reinforcing mats of the slabs are listed in **Table 3**. The specimens were constructed using a normal density concrete with a compressive strength of approximately 30 MPa. A mechanical mixer was used to produce the concrete using normal portland cement, fine aggregate, and crushed coarse aggregate of 19 mm maximum nominal size. The mixing processes were performed according to the procedure of **ASTM C192-2002**. **Table 4** lists the final strengths based on the average values from the tests performed on at least three 150 x 300mm cylinders for each test specimen. The tensile strength of the concrete was determined by performing the split cylinder tests.

4. INSTRUMENTATION

The instrumentation of the slab specimens was designed to register the maximum quantity and most reliable data of local strains, deflections and crack widths, to achieve the behavior of the laced reinforced concrete one way slab. Uniaxial electrical resistance (foil) strain gage was the adopted method to measure the strain in both concrete and steel. Two different sizes of pre-wired strain gages of (120 Ω) resistance, made in Japan for TML, were used in the test, All the used types of strain gages were normally installed by the recommended adhesive (CN-E and CN-Y) before which the contact surface was suitably prepared. In order to measure the vertical

deflection of the tested slabs LVDT (Linear variable differential transformer) was adopted tool to measure the deflection at mid span and at the two thirds part of the tested slab, were attached to lower steel beams of the testing machine under the tension face of the specimens.

5. TEST PROCEDURE

All specimens were tested using the hydraulic testing frame. The specimens were a simply supported condition where supported on the shorter opposite sides as shown in **Fig. 3** the specimens placed inside the testing frame so that supports lines, points load, LVDT were fixed in their correct locations, as shown in **Fig. 4**. Four point bending test were carried out by load increment of (3.5 kN) applied statically by using a hydraulic jack of (500 kN) capacity.

At each loading stage, the test measurements included the magnitude of the applied load, deflection of the slab at three locations, cracks width, strain in steel reinforcements (flexural and lacing), and strain in compressive face of slab were recorded also. At the end of each test, the cracks propagated were marked and the crack pattern and mode of failure for each specimen were carefully examined.

6. TEST RESULTS AND DISCUSSION

6.1 General Behavior and Crack Patterns

The first crack (flexural) occurred at the tension face for the middle third of slab, and then growths slowly across the width of the slab (i.e. parallel to the supports). Development and formed of flexural cracks occurred parallel to that crack and slowly propagated throughout the thickness of the slab, on increasing the application of static load. **Fig. 5-a to 5-h** shows the crack pattern of the tested specimens. It is clear from these figures that the generated of flexural cracks are approximately parallel and did not show any cracking on either side of the specimen near the support regions. Generally it is notice that the cracks develops and growths throughout the slab thickness on increasing the applied load are parallel and vertically up to failure for the specimen without lacing reinforcement. While the cracks are curved and connected together through the slab thickness for the specimens with lacing reinforcement, and this overlap increase as the lacing steel ratio increased, as illustrated in **Fig. 6-a and 6-b** respectively. Finally, the modes of failure for specimens were occurs by excessive yielding of tension steel reinforcement and followed by concrete crushing at the top surface of the slab at failure.

6.2 Cracking and Failure Loads

The experimental results for cracking and ultimate loads of all specimens are given in **Table 5**. The test results show that, the initial crack, there was compatibility between all the tested specimens. The first cracks (flexural) occurred at a load range of about (18.6% to 22.58%) of the ultimate load capacity of these specimens. Also, it is clear that from the experimental test results, the ultimate load capacity enhanced by about (56.52%) for the specimen with the highest lacing steel ratio with respect to the specimen **SS45/0**. And the ultimate load was decreased by about (3.13%) for the specimens with highest flexural steel ratio with respect to the specimens **SS45/25**. As a result of increasing the stiffness and the moment of inertia of the specimen due to increase the slab thickness, the load capacity were improved by about (103.57%) for the specimen **SL45/25** that have the largest thickness compared with the specimen **SS45/25**.

6.3 Load-Deflection Response

The behavior of the specimens is compared to the behavior of control specimen for each group at two load stages: a service load stage and the failure load stage. The serviceability limit is about (70-75%) of the peak load **Tan and Zhao, 2004**. In the presented discussion of deflections, the service loads are considered to 70% of the peak load of control specimens. The failure loads of the control specimens are equal to the recorded load, in **Table 5**.

Generally when a specimen is subjected to a gradually load increase, the deflection increases linearly with the load in an elastic manner. After the cracks start developing, deflection of the slab increases at a faster rate. After cracks have developed in the slab, the load-deflection curve is approximately linear up to the yielding of flexural reinforcement after which the deflection continues to increase without an appreciable increment in load.

Fig. 7 illustrated that the effect of increasing the lacing steel ratio and compared with the control specimen without lacing reinforcement. The experimental test results show that, the influence of the lacing ratio on the recorded deflections at service stage is relatively small, where the deflection reduced by about (4.15%, 12.89% and 19.82%) for the specimens **SS45/25**, **SS45/45** and **SS45/65** at service load with the respect to the control specimen **SS45/0**. At failure, these percentages increases to (10.64%, 45.54% and 55.94%) compared with the control specimen.

From **Fig. 8** it can be observed that, there is a maximum decrease in the recorded deflection at service load was (23.53%) for the specimen with the highest flexural steel ratio. At failure load, there is no significant decrease in the recorded deflection just by a bout (2.11%) for the specimen **SS45/45** compared with the specimen **SS25/45**. As expected, the deflection will be decrease as the slab thickness increase, where it is reduced by about (68.72%) for the specimen **SL45/25** at the service load, and by about (86.20%) at the failure load of the control specimen, as shown in **Fig. 9**. All percentages of central deflection of tested specimens at service and ultimate loads are listed in **Table 6**.

6.4 Load-Strain Relations

The load-strain relations of steel reinforcements and the compression concrete surface were measured to get a better understanding for the response and behavior of the laced reinforced concrete one way slab. Generally, it is so clear that the effect of lacing reinforcement to restrain the flexural reinforcement through its plastic region for all specimens with lacing reinforcement compare with the specimen without lacing reinforcement **SS45/0**. It is notice that from **Fig. 10-a to 10-c** the flexural steel reinforcement are yielded and the maximum compressive strain at the top of concrete surface is (2245) microstrain, while the lacing reinforcement within the elastic limit, at service load stage. At ultimate load, the concrete is crushed and the lacing reinforcements are yielded. **Fig. 11-a to 11-c** showing that the flexural steel reinforcement are yielded, the concrete uncrushed with recorded microstrain by a bout (2558.4), and the lacing reinforcement within the elastic limit, at the service load of the specimens. At failure, the concrete reached to crushing with the range of microstrain by about (4873 - 5637), and the lacing reinforcement were yielded. As expected, as the slab thickness increase the strain will be decrease compared with the specimen with the smallest thickness, this is illustrated in **Fig. 12-a to 12-c** where the maximum compressive microstrains in concrete reached to (1913), and the lacing reinforcement still within the elastic limit, at the service load of the specimens, whereas the flexural steel reinforcement are yielded. Thereafter, the concrete excess the crushing strain and the lacing reinforcement are yielded at the failure load of the specimens.

6.5 Ductility Factor

The ductility factor defined as the ratio of deflection at failure (ultimate deflection) to the deflection at steel yielding for the tested specimens. Thus, it is notice that from **Fig. 13** the ductility factor for all specimens with lacing reinforcement was found to be the higher compared with the specimen without lacing reinforcement, and it is recorded the maximum enhancement in ductility factor by about (91.34%) for the specimen with the lower lacing steel ratio.

As demonstrated in **Fig. 14** the ductility factor decreased by about (29.42%) for the specimen with the highest flexural steel ratio with respect to the specimen **SS25/45**, this is due to increasing the stiffness of the slab as the flexural steel ratio increased.

Fig. 15 show the clear dropping in the ductility factor of the tested slabs as the slab thickness increase, where the ductility factor decrease by about (29.95% and 34.94%) respectively for the specimens **SM45/25** and **SL45/25** with respect to the specimen **SS45/25**, this is due to increasing the flexural stiffness of the slabs. The ductility factor is calculated and tabulated, as shown in **Table 7**.

7. CONCLUSIONS

A series of experimental tests were performed on eight one-way simply-supported slabs reinforced with alternative lacing bars. As predicted that all specimens were failed in flexural mode by yielding of tension steel reinforcement, the first flexural crack always initiated at the bottom face of the slabs at the middle third of slab (constant moment) and propagated across the width and depth of the slab in the direction Parallel to the supports axis, and it was observed that the cracks were curved and connected together for the specimens with lacing reinforcement, and also notice that for all slabs with lacing steel reinforcement the crack width smaller than what observed in the control slab (specimen without lacing reinforcement) during the same loading stage.

Increasing the lacing steel reinforcement causes an increasing in the cracking load by (20%) and improving the ultimate load capacity by about (56.52%) with respect to the control specimen, and there is no significantly affected on enhanced the ultimate load capacity of the specimens when increasing the flexural steel reinforcement, whereas the ultimate load capacity increased by about (103.57%) as a result of decreasing the (L/d) ratio by (31.25%) with respect to the control specimen. While the deflection at the service load was decreased by about (19.82%) for the slab with the highest lacing steel ratio, and reduced by about (23.53%) and (68.72%) for the specimens with the highest flexural steel ratio and with the smallest (L/d) ratio respectively.

The load strain response for the flexural steel reinforcement of all the specimens with lacing reinforcement was similar, and it is so clear that the effect of lacing reinforcement to re-strain it through the plastic region, while the concrete strain at the extreme compressive fiber behaved non-linearly with load until failure of the specimen.

The ductility factor of all the laced slabs were observed more than that the slab without lacing reinforcement, where it is enhanced by about (91.34%) for the specimen with the lower lacing ratio, however the ductility factor decrease with increasing the lacing steel ratio. Also, the ductility factor of the slabs increased with decrease the flexural steel ratio, and with increasing the (L/d) ratio.

**REFERENCES**

- ❖ ACI Committee 318, 2014, *Building Code Requirements for Structural Concrete ACI 318M-14 and commentary*, American Concrete Institute, Farmington Hills, 503pp.
- ❖ Anandavalli, N., Lakshmanan, N., G.M. Samuel Knight, 2012, *Simplified Approach for Finite Element Analysis of Laced Reinforced Concrete Beams*, ACI Structural Journal, Vol. 109, No.1, pp. 91-100, February.
- ❖ ASTM Designation C192/C192M-02, 2002, *Making and Curing Concrete Test Specimens in Laboratory*, Annual Book of ASTM Standards, American Society for Testing and Materials, Philadelphia, Pennsylvania, Vol. 4, 02.
- ❖ Keshava Rao, M.N., Lakshmanan, N., Srinivasulu, P. and Dharaneepathy, M. V., 1992, *Application of Laced Reinforced Concrete Construction Techniques to Blast Resistant Structures - Phase II*, Report No. S-015, CSIR-SERC.
- ❖ Madheswaran C.K., Gnanasundar G. and Gopalakrishnan N., 2015, *Performance of Laced Reinforced Geopolymer Concrete (LRGPC) Beams under Monotonic Loading*, Advances in Structural Engineering, mechanics, Vol. 1, pp 355-367.
- ❖ Parameswaran, V.S., Lakshmanan, N., Srinivasulu, P, Krishnamoorthy, T.S., Balasubramanian, K., Thandavamoorthy, T.S. and Arumugam, M., 1986, *Application of Laced Reinforced Concrete Construction Techniques to Blast Resistant Structures*, Report No. RCC-SR-86-1, CSIR-SERC.
- ❖ Stanley C. Woodson, 1992, *Lacing Versus Stirrups an Experimental Study of Shear Reinforcement in Blast Resistant Structures*, U.S. Army Engineer Waterways Experiment Station, 3909 Halls Ferry Road, Vicksburg, March.
- ❖ Tan, K. G. And Zhao, H. , 2004, *Strengthening of Openings in One-Way Reinforced-Concrete Slabs Using Carbon Fiber-Reinforced Polymer Systems*, Journal of Composites for construction ,ASCE, Vol. 8, No. 5, pp. 393-402.
- ❖ Unified Facilities Criteria UFC 3-340-02, 2008, *Structures to Resist the Effects of Accidental Explosions*, Department of Army, Navy and the Air Force, U.S.A., Washington, 05 December.

Table 1. Characteristics of the tested slabs.

No.	Specimen designation	Slab thickness (mm)	$\frac{L}{d}$ ratio	Tension steel ratio (ρ_t)	Lacing steel ratio (ρ_s)	Lacing angle (θ)	Lacing steel details
1	SS45/0	135	16	0.0045	0	-	Without lacing
2	SS45/25	135	16	0.0045	0.0025	45°	$\emptyset 6$ mm at 100 mm c/c
3	SS45/45	135	16	0.0045	0.0045	45°	$\emptyset 6$ mm at 60 mm c/c
4	SS45/65	135	16	0.0045	0.0065	45°	$\emptyset 8$ mm at 70 mm c/c
5	SS25/45	135	16	0.0025	0.0045	45°	$\emptyset 6$ mm at 60 mm c/c
6	SS65/45	135	16	0.0065	0.0045	45°	$\emptyset 6$ mm at 60 mm c/c
7	SM45/25	160	13	0.0045	0.0025	45°	$\emptyset 6$ mm at 80 mm c/c
8	SL45/25	185	11	0.0045	0.0025	45°	$\emptyset 6$ mm at 70 mm c/c

Table 2. Details of slabs groups.

Group	Description	Specimens
I	$\frac{L}{d} = 16$ $\rho_t = 0.0045$ ρ_s Variable (Lacing)	1. SS45/0 ($\rho_s=0$) 2. SS45/25 ($\rho_s=0.0025$) 3. SS45/45 ($\rho_s=0.0045$) 4. SS45/65 ($\rho_s=0.0065$)
II	$\frac{L}{d} = 16$ $\rho_s = 0.0045$ ρ_t Variable	1. SS25/45 ($\rho_t=0.0025$) 2. SS45/45 ($\rho_t=0.0045$) 3. SS65/45 ($\rho_t=0.0065$)
III	$\rho_t = 0.0045,$ $\rho_s = 0.0025$ $\frac{L}{d} = \text{Variable}$	1. SS45/25 ($d=112.5\text{mm}, L/d=16$) 2. SM45/25 ($d=137.5\text{mm}, L/d=13$) 3. SL45/25 ($d=162.5\text{mm}, L/d=11$)

Table 3. Properties of steel reinforcement.

Nominal diameter (mm)	Measured diameter (mm)	Yield stress f_y MPa	Ultimate strength f_u MPa
6	5.83	724.4	777.4
8	7.87	626.24	775.34

Table 4. Mechanical properties of concrete.

Specimen ID	Compressive strength at time of specimen testing (MPa)		Modulus of rupture f_r at time of specimen testing (MPa)	Splitting tensile strength f_t at time of specimen testing (MPa)	Modulus of elasticity at time of specimen testing (GPa)
	f_{cu}	f_c			
SS45/0	42.92	35.28	3.87	3.57	24.43
SS45/25	43.96	34.85	3.82	3.29	22.32
SS45/45	43.35	33.92	3.7	3.42	22.79
SS45/65	45.22	34.36	3.91	3.15	27.35
SS25/45	45.19	35.31	3.41	3.2	24.18
SS65/45	47.07	36.27	3.63	3.35	24.72
SM45/25	44.89	37.12	3.51	3.6	24.71
SL45/25	46.87	35.81	3.9	3.25	25.67

Table 5. Cracking and ultimate loads of the tested slabs.

Specimens		Crack load (Pcr) (kN)	Ultimate load (Pu) (kN)	% Pcr/Pu	% Increase in first cracking load with respect to control	% Increase in ultimate load with respect to control
Group I	SS45/0	18.15	83.49	21.74	Ref.	Ref.
	SS45/25	21.78	101.64	21.43	20	21.74
	SS45/45	21.78	116.16	18.75	20	39.13
	SS45/65	21.78	130.68	16.67	20	56.52
Group II	SS25/45	18.15	116.16	15.63	Control	Control
	SS45/45	21.78	116.16	18.75	20	0.00
	SS65/45	25.41	112.53	22.58	40	-3.13
Group III	SS45/25	21.78	101.64	21.43	Control	Control
	SM45/25	29.04	156.09	18.6	33.33	53.57
	SL45/25	43.56	206.91	21.05	100	103.57

Table 6. Central deflections of the tested slabs at service and ultimate loads.

Specimens		Deflection at service load of control specimen (mm)	% Decrease in deflection at service load	Deflection at ultimate load of control specimen (mm)	% Decrease in deflection at ultimate load
Group I	SS45/0	14.23	Ref.	40.40	Ref.
	SS45/25	13.64	4.15	36.10	10.64
	SS45/45	12.40	12.86	22.00	45.54
	SS45/65	11.41	19.82	17.80	55.94
Group II	SS25/45	22.10	Control	64.22	Control
	SS45/45	20.80	5.88	62.86	2.11
	SS65/45	16.90	23.53	*	*
Group III	SS45/25	23.40	Control	77.4	Control
	SM45/25	9.82	58.03	15.54	79.92
	SL45/25	7.32	68.72	10.68	86.20

*Ultimate load of control specimen is beyond the failure load of specimen SS65/45.

Table 7. Ductility factor of the tested slabs.

Specimens		Ultimate load (kN)	Yield deflection (mm)	Ultimate deflection (mm)	Ductility factor
Group I	SS45/0	83.49	12.05	40.40	3.35
	SS45/25	101.64	12.08	77.40	6.41
	SS45/45	116.16	12.26	62.85	5.13
	SS45/65	130.68	13.53	61.54	4.55
Group II	SS25/45	116.16	11.25	64.22	5.71
	SS45/45	116.16	12.26	62.85	5.13
	SS65/45	112.53	12.37	49.86	4.03
Group III	SS45/25	101.64	12.08	77.40	6.41
	SM45/25	156.09	13.14	59.09	4.49
	SL45/25	206.91	13.64	56.99	4.17

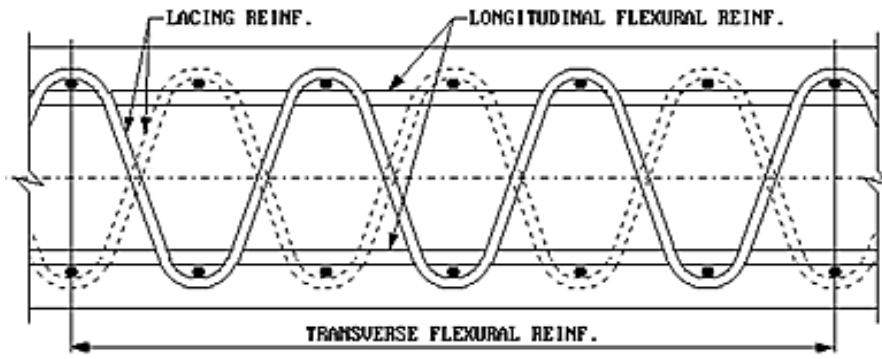
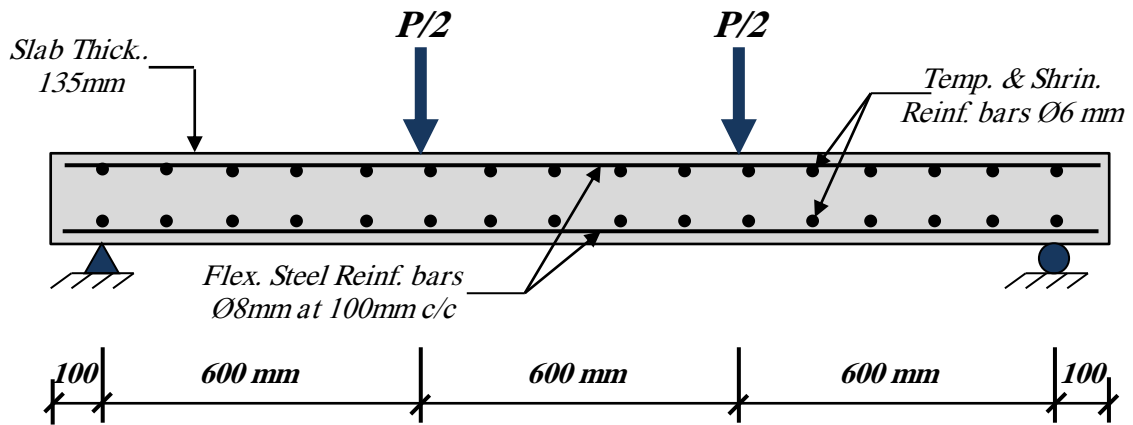
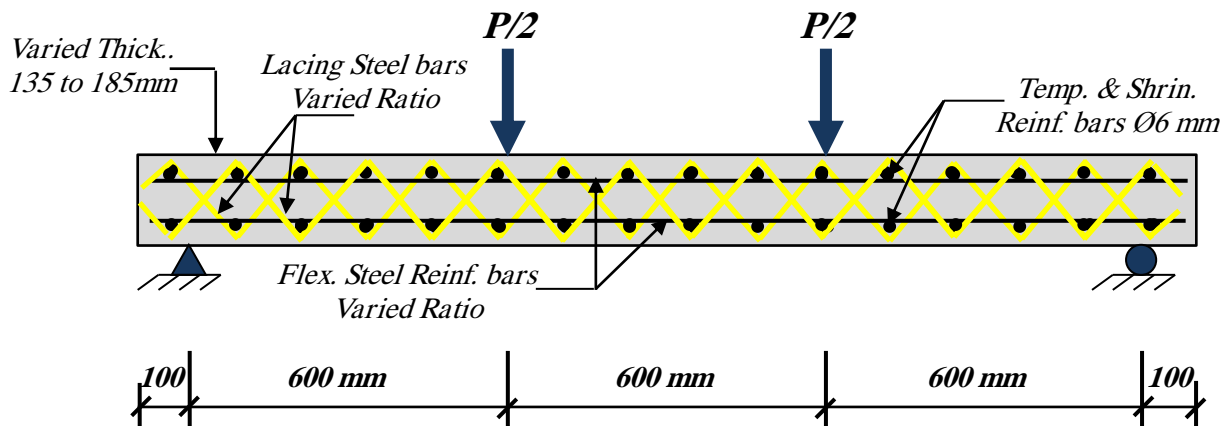


Figure 1. Typical laced reinforced concrete structural element.



a. Longitudinal section in slab without lacing reinforcement.



b. Longitudinal section in slab with lacing reinforcement.

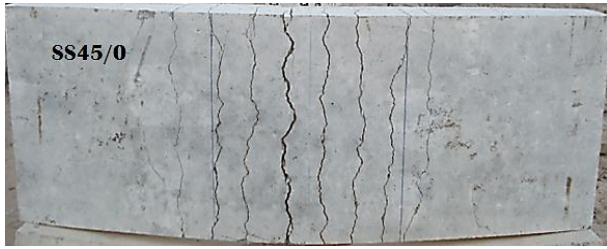
Figure 2. Details and dimensions of the test slab specimens.



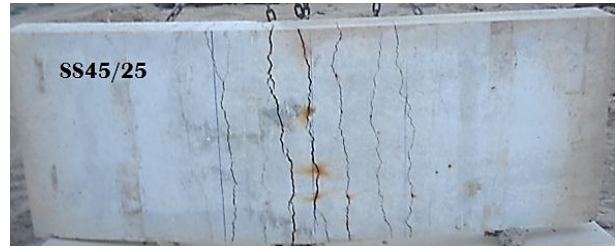
Figure 3. Photograph of specimen setup.



Figure 4. Photograph of instruments setup.



a. specimen SS45/0



b. specimen SS45/25



c. specimen SS45/45



d. specimen SS45/65



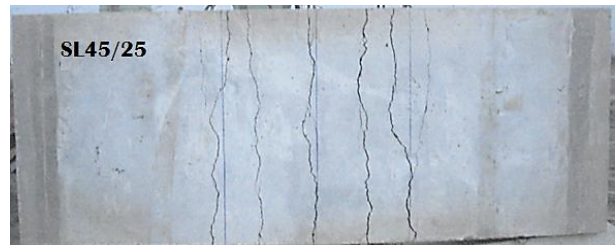
e. specimen SS25/45



f. specimen SS65/45



g. specimen SM45/25

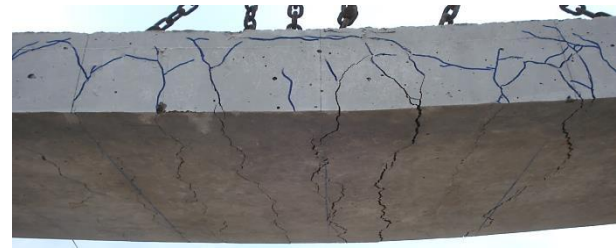


h. specimen SL45/25

Figure 5. Cracks pattern for the tension face of specimens tested after failure.



a. specimen without lacing reinforcement.



b. specimen with lacing reinforcement.

Figure 6. Typical cracks pattern for the side face of specimens tested after failure.

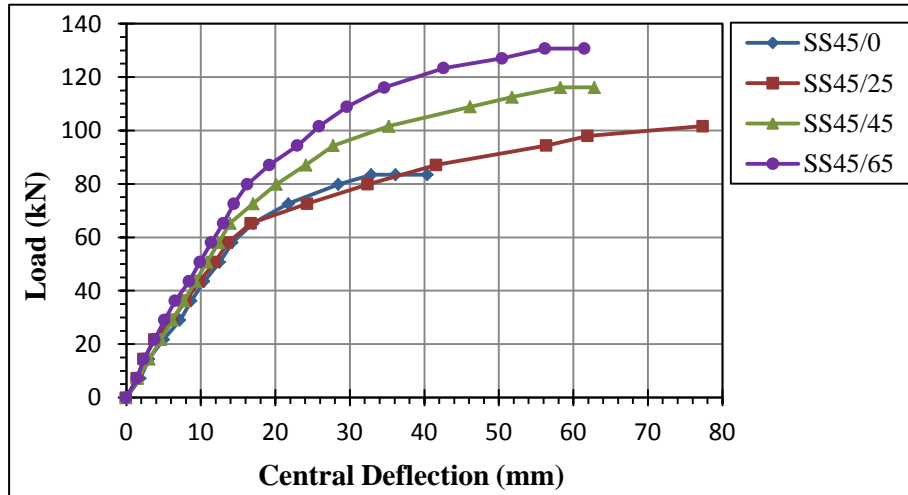


Figure 7. Influence of the lacing steel ratio on load-central deflection behavior for group (I).

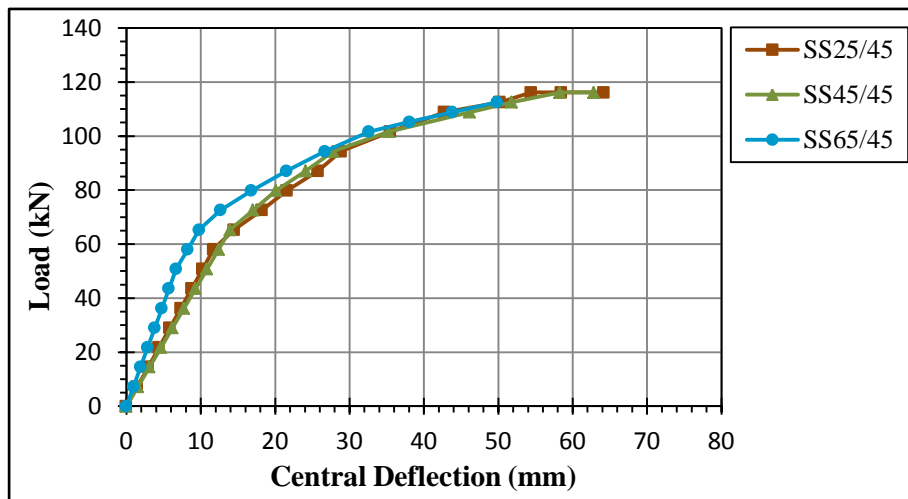


Figure 8. Influence of the flexural steel ratio on load-central deflection behavior for group (II).

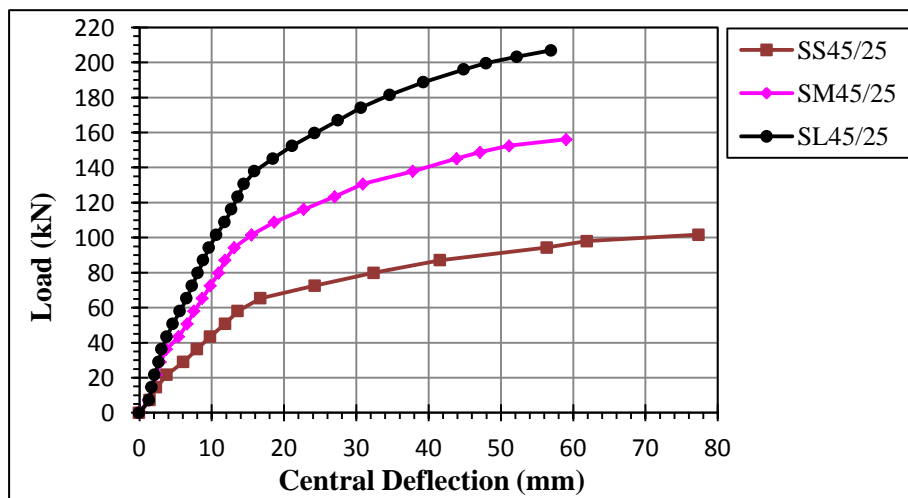
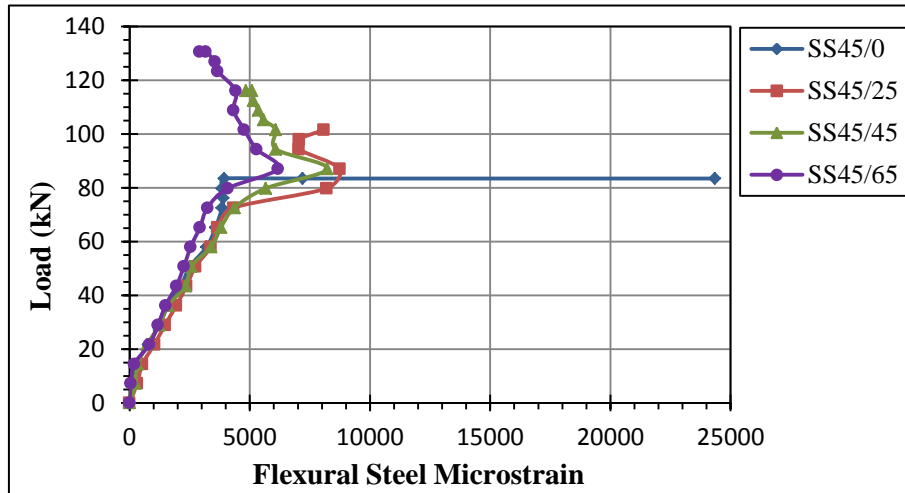
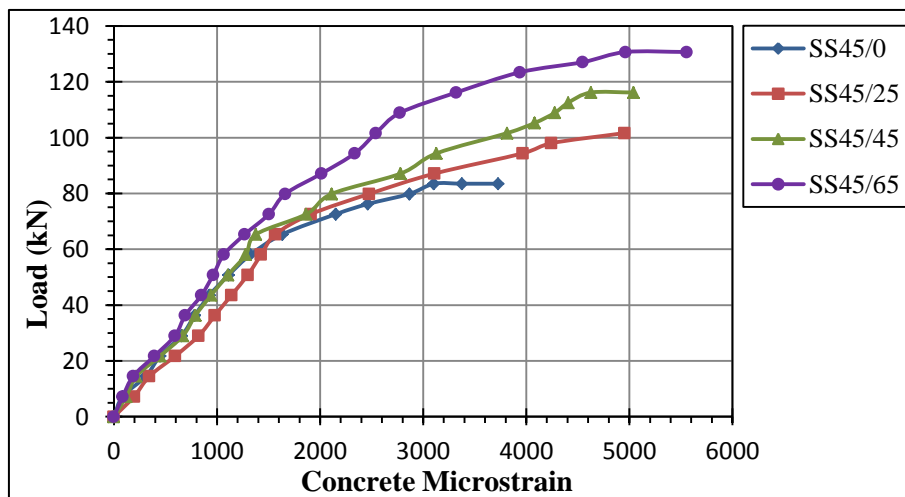


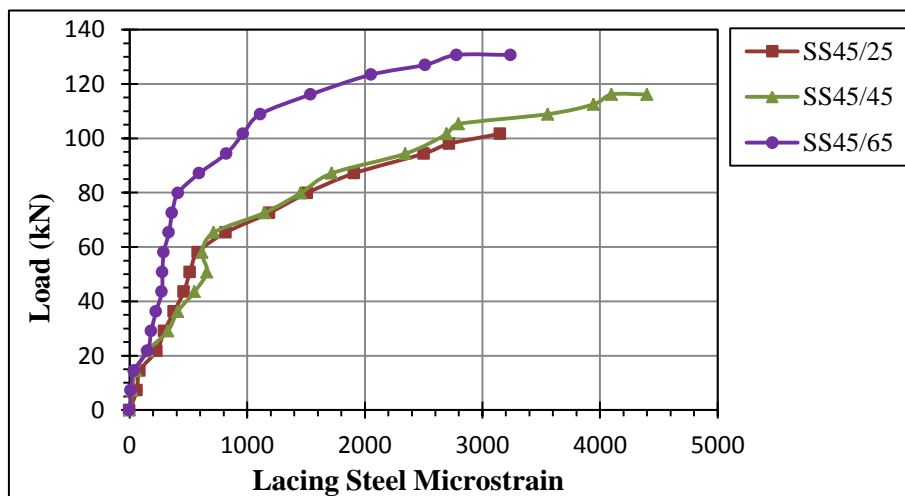
Figure 9. Influence of the L/d ratio on load-central deflection behavior for group (III).



a. Load–strain curves at the flexural steel reinforcement.

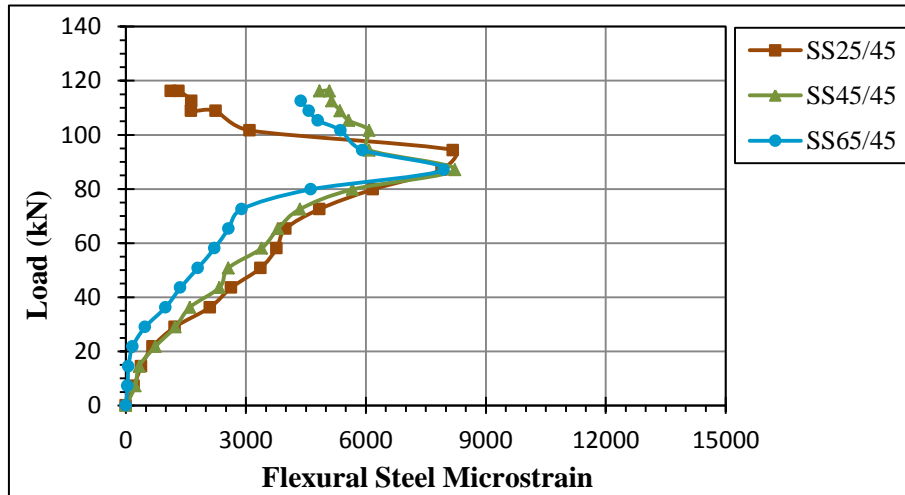


b. Load–strain curves at the top surface of concrete.

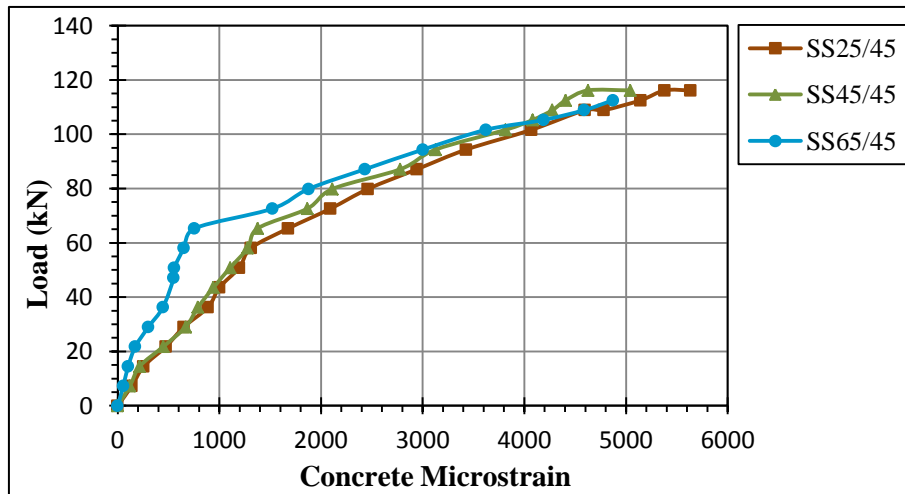


c. Load–strain curves at the lacing steel reinforcement.

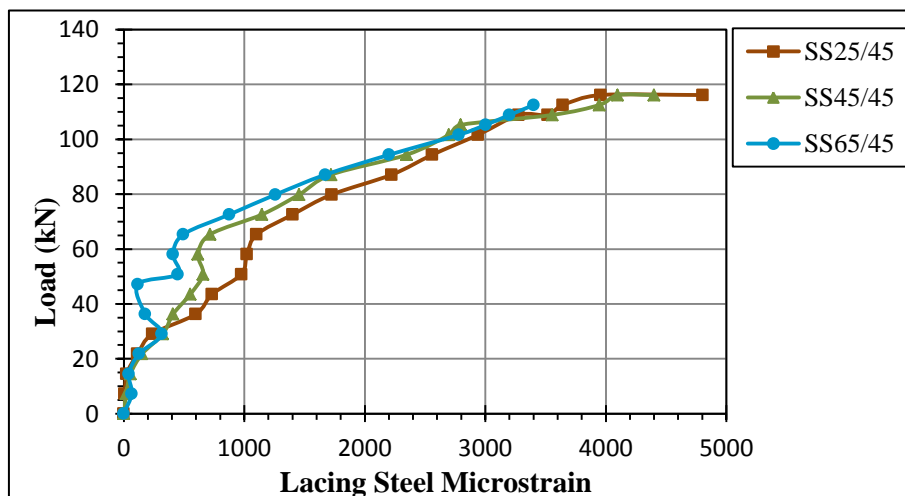
Figure 10. Influence of the lacing steel ratio on load–strain curves at mid-span for group (I).



a. Load–strain curves at the flexural steel reinforcement.

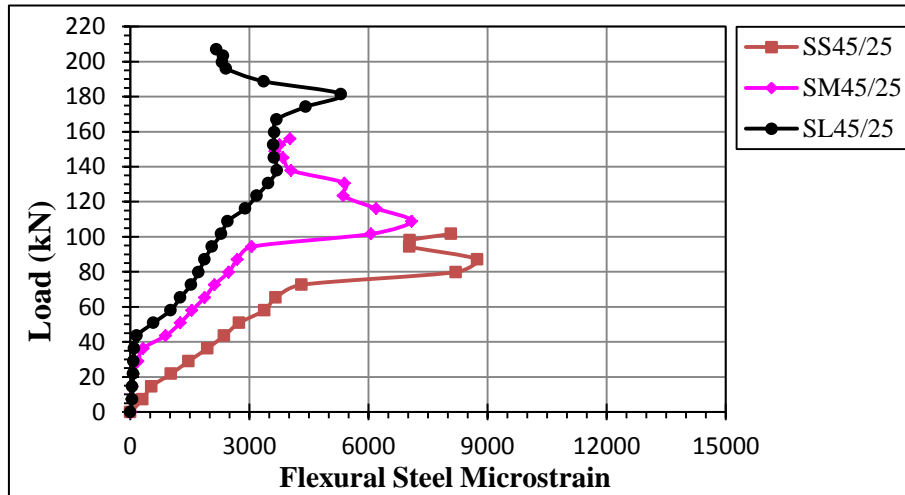


b. Load–strain curves at the top surface of concrete.

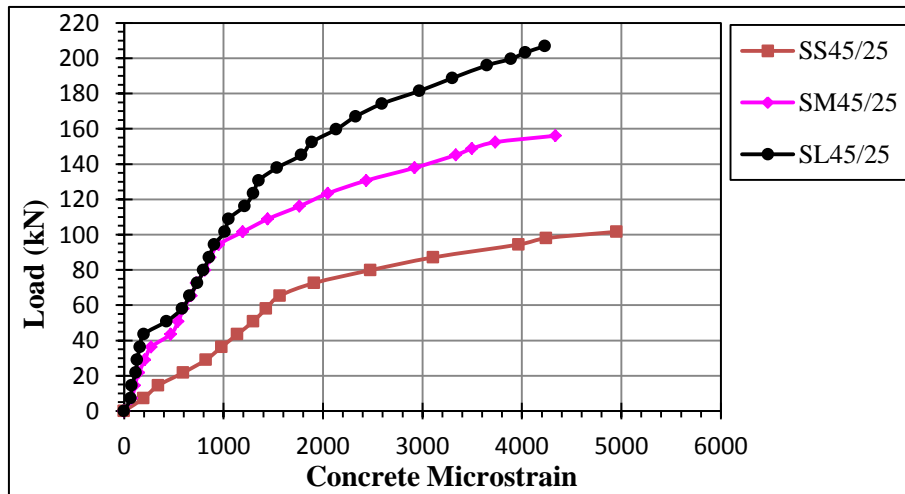


c. Load–strain curves at the lacing steel reinforcement.

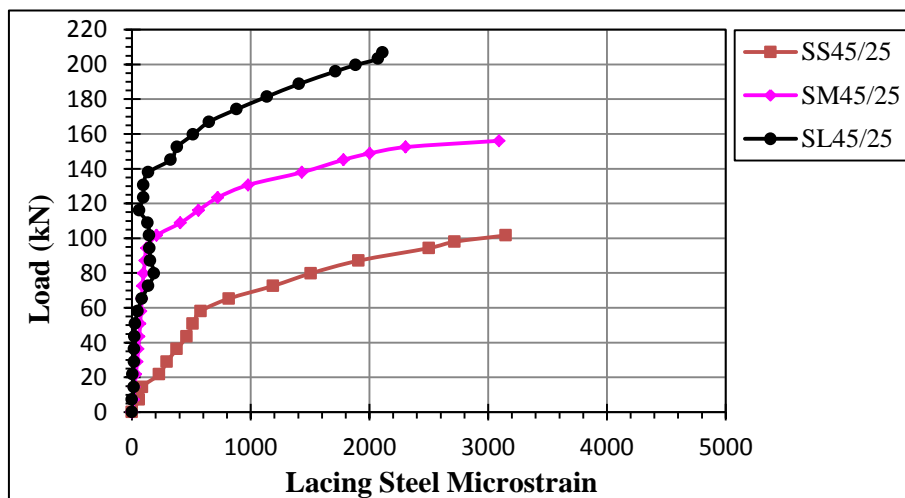
Figure 11. Influence of the flexural steel ratio on load–strain curves at mid-span for group (II).



a. Load–strain curves at the flexural steel reinforcement.



b. Load–strain curves at the top surface of concrete.



c. Load–strain curves at the lacing steel reinforcement.

Figure 12. Influence of the L/d ratio on load–strain curves at mid-span for group (III).

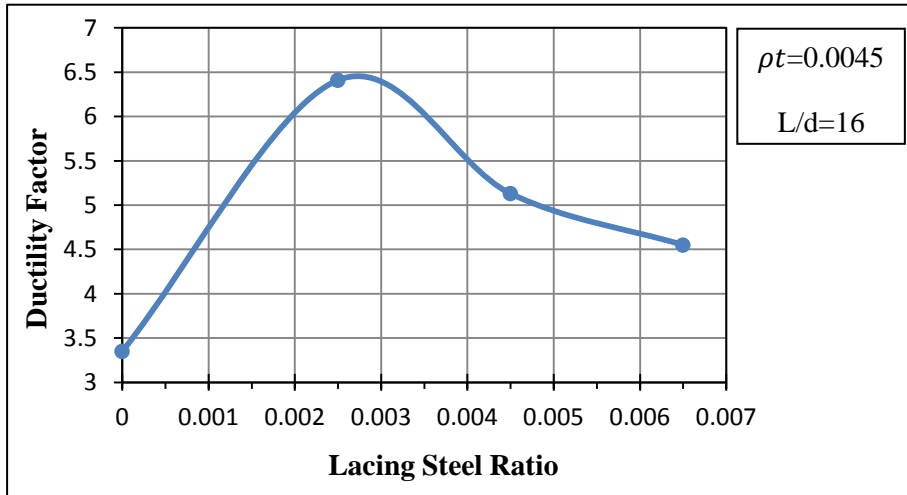


Figure 13. Ductility factor versus lacing steel ratio.

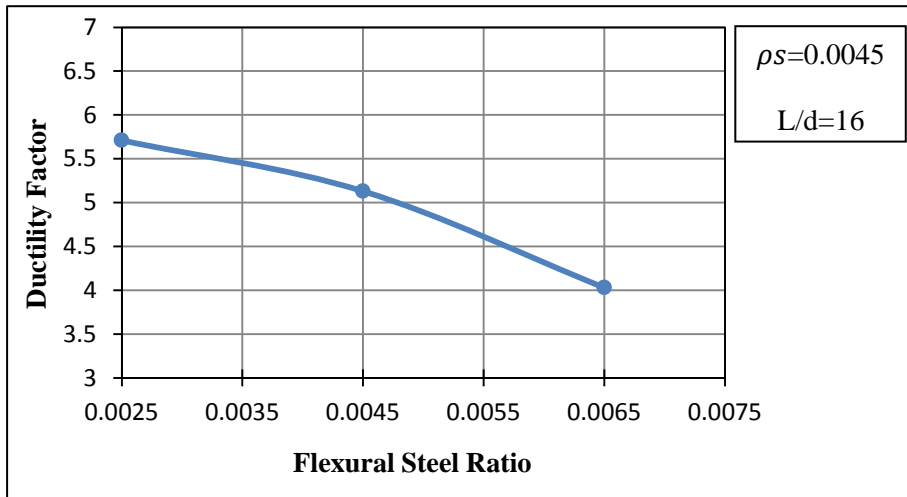


Figure 14. Ductility factor versus flexural steel ratio.

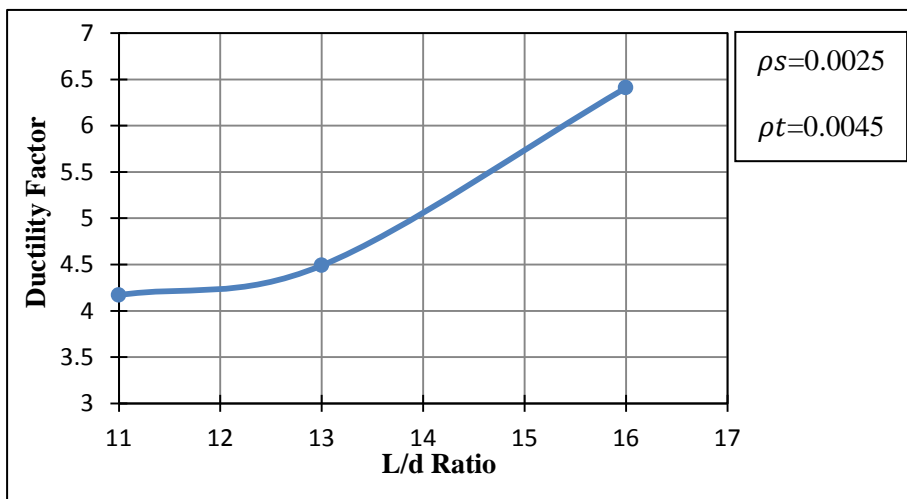


Figure 15. Ductility factor versus L/d ratio.



Three-Dimensional Finite Element Simulation of the Buried Pipe Problem in Geogrid Reinforced Soil

Hala Hamed. Mohammed Al-Kalali

Graduate student

College Engineering - University of Baghdad

Email: enghalahm@yahoo.com

Bushra Suhail. Zbar

Assistant Professor

College of Engineering – University of Baghdad

Email: albusoda@yahoo.com

Mohammed Yousif. Fattah

Professor

Building and Construction Department

University of Technology

Email: myf_1968@yahoo.com

ABSTRACT

Buried pipeline systems are commonly used to transport water, sewage, natural oil/gas and other materials. The benefit of using geogrid reinforcement is to increase the bearing capacity of the soil and decrease the load transfer to the underground structures.

This paper deals with simulation of the buried pipe problem numerically by finite elements method using the latest version of PLAXIS-3D software. **Rajkumar and Iamaruthi's study, 2008** has been selected to be reanalyzed as 3D problem because it contain all the properties needed by the program such as the modulus of elasticity, Poisson's ratio and angle of internal friction. It was found that the results of vertical crown deflection for the model without geogrid obtained from PLAXIS-3D are higher than those obtained by two-dimensional plane strain by about 21.4% while this percent becomes 12.1 for the model with geogrid, but in general, both have the same trend. The two dimensional finite elements analysis predictions of pipe-soil system behavior indicate an almost linear variation of pipe deflection with applied pressure while 3-D analysis exhibited non-linear behavior especially at higher loads.

Key words: buried flexible pipe, finite elements, static loads, soil reinforcement.

تمثيل ثلاثي الابعاد لمسألة الانابيب المدفونة في تربة مسلحة بشبكة بطريقة العناصر المحددة

هالة حامد محمد الكلالي

باحثة

كلية الهندسة-جامعة بغداد

د. محمد يوسف فتاح

استاذ

هندسة البناء والإنشاءات / الجامعة التكنولوجية

د. بشرى سهيل زبار

استاذ مساعد

كلية الهندسة-جامعة بغداد

الخلاصة

تستخدم شبكات الأنابيب المدفونة عادة لنقل المياه والصرف الصحي والنفط الطبيعي / الغاز وغيرها من المواد. من فوائد استخدام شبكة تسليح في التربة زيادة قدرة تحملها وتقليل نقل الحمل الواصل إلى المنشآت المشيدة تحت الأرض. يتناول هذا البحث محاكاة مسألة الأنابيب المدفونة عددياً باستخدام طريقة العناصر المحددة باستخدام أحدث نسخة من برنامج (2013) PLAXIS-3D وتم

أخذ دراسة سابقة ل (راجكومار والمبورثي، 2008) أعيد تحليل المسألة كمسألة ثلاثية الأبعاد وتم اختيار هذه الدراسة لأنها تحتوي على جميع الخصائص التي يحتاجها البرنامج مثل معامل المرونة، ونسبة بواسون، زاوية الاحتكاك الداخلي. وقد وجد أن نتائج الانفعال الرأسي لقمة الأنبوب لنموذج من دون شبكة جيولوجية تم الحصول عليها من PLAXIS-3D هي أعلى من تلك التي حصل عليها راجكومار عندما حلل المسألة كثنائية الأبعاد بنحو 21.4، في حين تصبح هذه النسبة 12.1 للنموذج مع شبكة تسليح، ولكن بصورة عامه لديهما نفس الاتجاه. بصورة عامة النتائج قي تحليل المسألة كثنائية الأبعاد يظهر تصرف خطي بينما في المسألة الثلاثية يظهر تصرف لاخطي خصوصا بالأحمال الكبيرة.

كلمات مفتاحية: الانانبيب المرنة المدفونه، العناصر المحددة، الاحمال الساكنة، تسليح التربة

1. INTRODUCTION

Many engineering problems that not always could solve through analytical calculations can now be solved with numerical analyses using the finite element method (FEM). The finite element method, known for nearly 50 years, has been effectively implemented in various computer software packages aiding the designing and analysis of engineering structures, such packages are ABAQUS, ANSYS, PLAXIS, **Kliszczewicz, 2013**.

A numerical model of the soil-pipe system is necessary to analyze or predict the detailed behavior of buried pipelines. Analytical theories of soil-structure interaction such as Burns-Richard method provides mathematical model that is used to design or analyze buried pipelines. These theories do not account for the actual interaction between the pipe and the surrounding soil during construction, service, and ultimate conditions, due to the nonlinearities, no homogeneity and other complexities. Numerical modeling is the best approach to adequately model the pipe-soil system. The finite element method is the most common numerical technique that can be used to analyze and design buried pipelines, **Bashir, 2000**.

The problem is usually analyzed as a two-dimensional problem, even though the system is clearly three-dimensional. For long culverts, treating the problem as a plane-strain two-dimensional problem is generally not a serious limitation, but in some cases the three-dimensional effects cannot be neglected. There are three-dimensional finite element analysis programs available, but generally they do not have the proper constitutive relationship for modeling soil and do not provide interface elements that allow slip between the soil and the pipe. In these cases, it may be necessary to compare two- and three-dimensional solutions for conditions that can be modeled and then to extrapolate to the real case.

Bildik et al., 2012, studied the behavior of buried pipe numerically by finite elements method. Their results showed that, the pipe behavior influenced by the intensity of the surcharge load. The pipe displacements increased linearly with increase in surcharge load. Also their results showed that the pipe displacement decreased with increase of embedment ratio. This behavior can be explained using stress- displacement behavior. The vertical stresses decrease with increase on embedment ratio. The variation of vertical stress with embedment ratio from the PLAXIS analyses showed generally similar behavior with Boussinesq theory. The pipe behavior was strongly influenced by the relative density of sand. The displacement of the pipe decreased with the increase in relative density of sand. The results showed that, pipe displacement decreased with increase on rigidity of pipe and the concrete pipe displacements were less than PE pipes.



Kliszczewicz, 2013, presented 3D numerical analysis of interaction of a pipeline structure with stratified subsoil loaded across a certain area. The analysis enabled to evaluate the effort state of the pipe and the changes taking place in the soil mass. The impact of the load was particularly evident in the sub-surface soil layers immediately within the load working area. A distribution zone of the stresses excited by a load working within the entire soil mass, especially in the direct surrounding of the pipelines, can also be identified. Considering the stratification of the subsoil with a layer of low-bearing ground with varied thickness and the fact of varied material parameters in the zones of virgin soil, bedding and backfill in the excavation, one can observe clear disturbances in the distribution of stresses in the direct surrounding of the pipe (excavation) and in the further zones of the soil. As the load is situated specifically as shifted in relation to the pipe axis, the deformation and effort state of the pipe side surface is non-uniform. This signifies irregular distribution of generalized internal forces in such structure. Such results of the activity of surface loads onto the pipe structure situated in stratified subsoil are identifiable only by building numerical pipe- soil system models and by analyzing their behavior when simulating the activity of loads..

The objective of the present study is to investigate the dimensional effects of numerical simulation of the buried pipe problem. The problem is conventionally analyzed as two-dimensional plane strain, but in present paper it is reanalyzed as three dimensional problems. Geogrid reinforcement layer is placed above the pipe to reduce load transfer.

2. PLAXIS-3D NONLINEAR SOLUTION STRATEGY

PLAXIS-3D employs a solution strategy known as the direct iterative method, or more simply called trial and error. This method has proven to be robust and readily accommodates the wide variety of nonlinear models such as tensile cracking and elastic-plastic behavior of pipe models, hyperbolic constitutive laws for soil models, frictional sliding and separation for interface models, and geometric nonlinearity for large deformation analysis ,**Plaxis Manual, 2013**. When two consecutive iterations produce the same stiffness matrices for all elements within small error limits, then the solution has converged and we proceed to the next load step. Once a converged solution increment has been found, all the mechanical responses were updated based on the last iteration solution, **Plaxis Manual, 2013**.

3. MATERIAL PROPERTIES

Rajkumar and Ilamparuthi ,2008, described numerically and experimentally the interaction between the soil and flexible PVC pipes buried in sand bed and subjected to surface pressures. The tests were conducted with and without Netlon Geogrid reinforcement. They studied the behavior of the soil-pipe interaction by using of the 2D Finite element analysis software PLAXIS. Moreover, in the presence and absence of geogrid reinforcement, they measured the variation of the vertical crown deflection due to the applied surface pressure, with a noticeable difference between the numerical and experimental results for both cases.

Table 1 shows the values of material properties that were used by, **Rajkumar and Ilamparuthi, 2008**. PLAXIS-2D software was used by, **Rajkumar and Ilamparuthi, 2008** to model the behavior of PVC pipes buried in dense sand under surface loads. The results were compared with those measured experimentally and expected numerically by ,**Rajkumar and Ilamparuthi, 2008**.

4. BOUNDARY CONDITIONS AND MODELING

The finite element analysis was performed to model the response of the buried flexible plastic pipes in different backfills, embedded at different levels and compare the behavior with the experimentally obtained results.

The dimensions of the soil model adopted by, **Rajkumar and Ilamparuthi, 2008** were (1200 mm × 600 mm). The pipe model system was considered a plane strain condition with 15-node elements. Mohr-Columbe plasticity model was specified to solid element which symbolizes soil around the pipe. The pipe used in the analysis had a diameter of 200 mm and wall thickness of 0.5 mm. To exactly simulate the experimental model the right hand boundary was selected at 1.5D away from the trench center with a restricted horizontal displacement and free vertical displacement. The bottom boundary was located at 1.2 m below the surface with a restricted vertical displacement and free horizontal displacement. Six circular segment elements were used to represent the pipe. Fifteen noded plane strain triangular elements were used by, **Rajkumar and Ilamparuthi, 2008** to model the backfill. The numerically simulated model is as shown in **Fig. 1**.

The study consists of two stages, the first one deals with the vertical crown deflection on the pipe under 50, 100, 150 kPa surface loads with 400 mm backfill cover without geogrid reinforcement as shown in **Fig. 1**. To reduce the effect of surface load on the pipe and increase the performance of it, the geogrid are used in the second stage as shown in **Fig. 2**. **Table 1** summarizes the material properties of sand, pipe and geogrid. **Fig. 3** shows the problem in Plaxis-3D.

5. RESULTS AND DISCUSSION

In the presentation of results, standard terms have been used throughout presentation of the results. These terms are defined below:

The definition of the Vertical Diametric Strain (VDS) of a pipe is shown in **Fig. 4** and relates to the change of the internal vertical diameter of a pipe compared to its external diameter. The Horizontal Diametric Strain (HOS) conversely relates to the change of the internal horizontal diameter of the pipe compared to its external diameter. A positive VDS or HOS denotes a decrease in pipe diameter and both are expressed as a percentage.

In order to inquest the Plaxis-3D software, the model has been prepared and run by using the same data and boundary conditions under the same load stages. Then the results of crown strain and diametrical strain with applied surface load for both loose and dense sand are compared with those obtained by, **Rajkumar and Ilamparuthi, 2008** as shown in **Figs. 5 to 8**.

It can be seen from **Fig. 5** that the results of vertical crown deflection for the model without geogrid obtained from PLAXIS-3D are higher than those obtained by two-dimensional plane strain, **Rajkumar and Ilamparuthi, 2008** by about 21.4% while this percent becomes 12.1 for the model with geogrid, but in general, both have the same trend. The difference increases as the applied surface load increases.

The match with the experimental data was reasonably good owing to inadequacies of the 2D predictions involving the assumption of a rigid side boundary. The walls of the laboratory test box may not have been perfectly rigid and this factor could have influenced the finite element analysis

predictions. The correspondence of the finite elements analysis output with the horizontal pipe strain was less satisfactory. It is also apparent that the two dimensional finite elements analysis predictions of pipe-soil system behavior indicate an almost linear displacement of pipe deflection with applied pressure while 3-D analysis exhibited non-linear behavior especially at higher loads.

In **Figs. 5** and **6**, the applied pressure and the corresponding crown deflection of the pipe are compared for 400 mm of backfill cover with and without geogrid reinforcement in dense and loose conditions of sand, respectively.

Geogrid functions in two ways: reinforcement and separation which are the techniques of improving poor soil with geo-grid, to increase the stiffness and load carrying capacity of the soil through frictional interaction between the soil and geo-grid material.

A geogrid reinforced soil is stronger and stiffer and gives more strength than the equivalent soil without geo-grid reinforcement. Geo-grids provide improved aggregate interlock in stabilizing road infrastructure through soil restraint reinforcement applications. Geogrid reinforcement provided between the soil layers carries the shear stress induced by vehicular loads.

Geogrid mesh provides better interlocking with the soil particles thus ensuring adequate anchorage during loading. The improvement in the load carrying capacity could be attributed to improved load dispersion through reinforced soil. This in turn, results in lesser intensity of stresses getting transfer to underlying soil, thus leading to lesser distress in the pipe.

Figs. 7 and **8** show the results of diametric and crown strain of the pipe both vertically and horizontally plotted against the surface pressure under backfill cover of 400 mm versus the applied surface load which was obtained from **Plaxis 3D, 2013** program by entering the data of **Table 1**. The results of, **Rajkumar and Ilamparuthi, 2008** are drawn on the same figure to facilitate the comparison process. The upper half of the diagram consists of negative diametric strains or compression of the pipe at the crown. The lower half consists of positive or extensions of the pipe at the level of the spring line. The Fig. shows that 3-D analysis reveals higher strains than 2-D.

The pipe response to the applied pressure is almost linear both in 2-D and 3-D analysis which results in an elliptical deformed shape of the pipe. The pipe deformations were quite localized. The greatest reduction in diameter vertically occurred under the centre of the loading plate. The pipe crown deflected most directly beneath the centre of the loading plate. The invert of the pipe suffered little movement but tended to rise slightly well away from the loaded area. It can be seen in **Figs. 7** and **8** which represent the pipe strain with applied pressure that the vertical diametric strain is usually significantly higher than the horizontal strain. This is true in 2-D and 3-D analyses.

The deformation response of the pipe soil system to the external loading was nonlinear. The pipes were usually observed to regain their shapes after they were recovered from the buried pipe installation.

It is noticed from **Fig. 8** that there is clear convergence in results. The small difference between the two results is because the problem is solved by **Rajkumar and Ilamparuthi, 2008** as plane strain while the current analysis considers the problem as three dimensional problems. It is acceptable difference.

These results are expected and compatible with those obtained by ,**Hosseini and Moghddas Tafreshi, 2002** who studied the laboratory tests of small diameter pipes buried in reinforced sand and found that the deflection behavior and failure mechanism of the system highly depend on soil density. The results are also compatible with the findings of, **Arockiasamy et al., 2006** who studied the soil pipe interaction, and interpreted that whatever the soil is well compacted it absorbs the bulk of the load transferred to the pipe and thus reduce the strain of the pipe's wall. However, in relatively loose soils, due to weak contacts and poor interlocking of the grains and special arrangement of the soil fabric, regardless of the embedment depth, even under low loads, the failure of the system usually occurred in low applied load due to local buckling or large deflection of the pipe together with excessive settlement of the loading plate.

Figs. 9 to 17 present visualization of the output map results generated in PLAXIS 3D software.

A uniformly distributed load of the surcharge causes soil mass deformation shown with a deformed net of the pipe soil system model **Fig. 9** presents the deformed mesh. **Fig. 10** presents the total volumetric strain ϵ_v , while **Fig. 11** shows the total displacement $|u|$ (which represents absolute total displacement). **Fig. 12** presents the total horizontal displacement u_x , the resultant displacements are displayed in characteristic sections of the model, i.e. in planes perpendicular and parallel to the pipe axis. It is pointed out by analyzing the maps that the impact of the surcharge load is most important directly in the place of its application, covering a significant area of the soil mass and reaching the pipeline placement zone.

Fig. 14 presents total mean stress p , **Fig. 15** shows the deviator stress q which indicates that the most stressed zone extends to a depth of about (1.0-1.5) the footing width (loaded area).

Fig. 16 presents Cartesian total stress σ_{zz} , it can be shown that the influence zone by the surface load extent to reach the pipe while **Fig. 17** shows the plastic points around the pipe. The impact of the load is particularly evident in the sub-surface soil layers immediately within the load working area. A distribution zone of the stresses excited by a load working within the entire soil mass, especially in the direct surrounding of the pipelines, can also be identified.

The maximum vertical displacement of nodes on the soil mass model reaches 0.02 m. The maximum vertical displacement of the pipe model nodes are 0.003 m and occur in the central part of the surface model.

6. CONCLUSIONS

1. The results of vertical crown deflection for the model without geogrid obtained from PLAXIS-3D are higher than those obtained by two-dimensional plane strain by about 21.4% while this percent becomes 12.1 for the model with geogrid, but in general, both have the same trend.
2. The two dimensional finite elements analysis predictions of pipe-soil system behavior indicate an almost linear displacement of pipe deflection with applied pressure while 3-D analysis exhibited non-linear behavior especially at higher loads.
3. The pipe response (strain) to the applied pressure is almost linear both in 2-D and 3-D analysis which results in an elliptical deformed shape of the pipe. The pipe deformations were quite localized. The greatest reduction in diameter vertically occurred under the centre of the loading plate.



4. The reliability of the outcomes obtained is linked to the correct construction of the model including correct model dimensions, discretization density, selection of appropriate material parameters and an adequate constitutive model of soil and of the modeled structure. Numerical analyses can be regarded as an attractive tool for examining limit states of the bearing capacity and serviceability of buried piping

REFERENCES

- Arockiasamy, M., Chaallal, O., Limpeteeparakarn, T., 2006, *Full-Scale Field Tests on Flexible Pipes Under Live Load Application*, Journal of Performance of Constructed Facilities", ASCE, Vol. 20, No. 1, pp. 21-27.
- Bashir R., 2000, *Analysis and Design of Buried Pipelines*, M.Sc. Thesis, King Fahd University of Petroleum and Minerals, Dhahran, Saudi Arabia.
- Bildik, S., Laman, M. and Suleiman, M.T., 2012, *Parametric Studies of Buried Pipes Using Finite Element Analysis*, 3rd International Conference on New Developments in Soil Mechanics and Geotechnical Engineering, Near East University, Nicosia, North Cyprus.
- Byrne J. H., 1987, *Analysis of a Corrugated Steel Box-Type Culvert*, M.Sc. Thesis, Ohio University.
- Gerscovich, D.M.S., Sieira A.C.C.F., 2008, Fereira A.M., *Numerical Simulation of the Mechanical Behavior of Buried Pipes in Trench*, The 12th International Conference of International Association for Computer Methods and Advances in Geomechanics (IACMAG), India, Goa, 2008.
- Goltabar, A. M, Shekarachi M., 2010, *Investigation of Traffic Load on the Buried Pipeline by Using Real Scale Experiment and Plaxis-3D Software*, Research Journal of Applied Sciences, Engineering and Technology 2(2), pp.107-113.
- Hosseini, M. M., S.M. and Moghddas Tafreshi, S. N., 2002, *Soil-Structure Interaction of Embedded Pipes Under Cyclic Loading Conditions*, International Journal of Engineering, Vol. 15, No. 2, July 2002, pp. 117-124.
- Janson, L. E., 1996, *Plastic Pipes for Water Supply and Sewage Disposal*, Published by Borealis.
- Madryas, C., Kolonko A., Wysocki L., 2002, *Constructions of Sewage Pipes*, Publishing House of Wroclaw University, Wroclaw.
- Moghaddas Tafreshi, S. N., and Khalaj, O, 2008, *Laboratory Tests of Small-Diameter HDPE Pipes Buried in Reinforced Sand under Repeated-Load*, Geotextiles and Geomembranes, 26, pp. 145–163.
- Plaxis 3D Manual, Geotechnical Finite Element Software, Delft University of Technology & PLAXIS bv, The Netherlands.
- Rajkumar, R. and Ilamparuthi, K., 2008, *Experimental Study on the Behavior of Buried Flexible Plastic Pipe*, Electronic Journal of Geotechnical Engineering EJGE, Vol. 13, pp. 1-10.
- Zienkiewicz O. C., 1977, *The Finite Element Method*, McGraw Hill Book Company.

NOMENCLATURE

D_0 = original external diameter (mm).

V.D.S= vertical diametric strain.



δ = change in internal diameter (mm).

σ_{zz} = vertical stress.

ϵ_v = volumetric strain.

$|u|$ = absolute total displacement.

u_x = the total horizontal displacement.

Table 1. Material properties of the soil-pipe system, **Rajkumar and Ilamparuthi, 2008.**

Properties	Loose sand	Dense sand	PVC pipe	Netlon geogrid
Dry unit weight (kN/m ³)	15	17	–	–
Modulus of elasticity E (kN/m ²)	9000	19000	0.933*10 ⁶	–
Poisson ratio ν	0.3	0.3	0.31	–
Friction angle ϕ	32	42	–	–
Dilation angle ψ	2	12	–	–
Axial stiffness (kN/m)	–	–	–	60

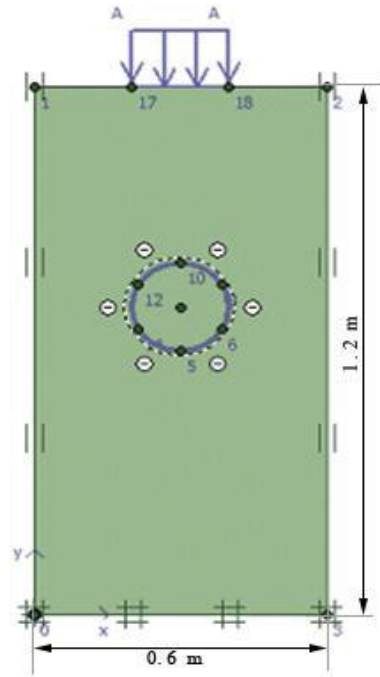


Figure 1. Two-dimensional geometric model of soil-pipe without reinforcement, after Rajkumar, et al., 2008.

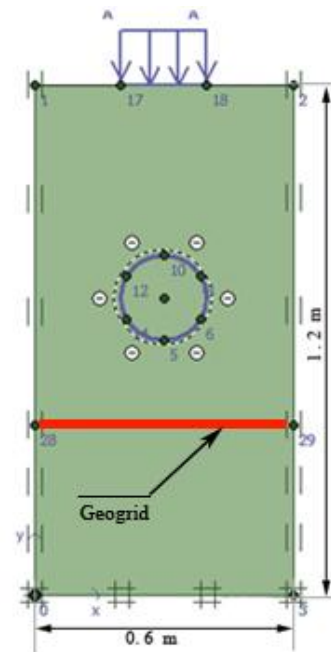
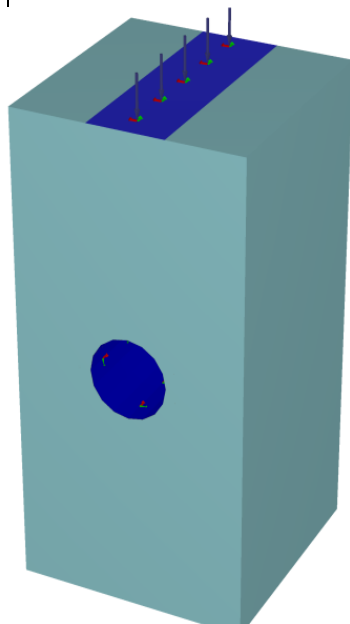
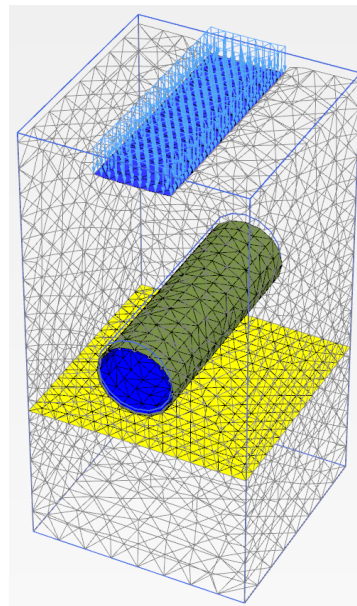


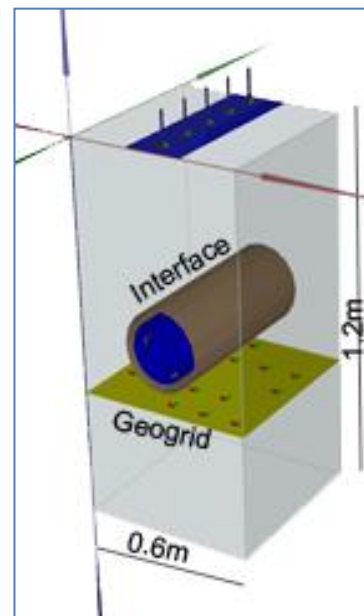
Figure 2. Geometry model of soil pipe with geogrid reinforcement, after Rajkumar, et al., 2008.



(a) general view



(b) mesh view



(c) structure & interface view

Figure 3. Geometrical model of 3D soil pipe, ,

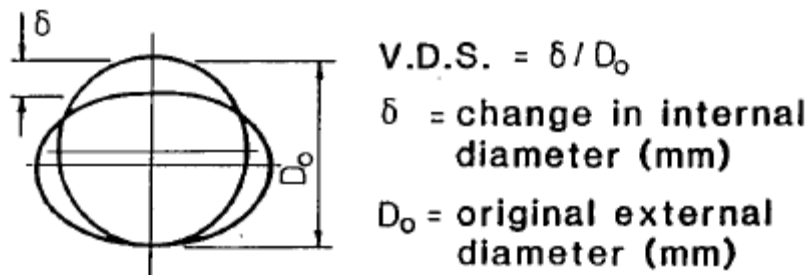


Figure 4. Definition of vertical diametric strain.

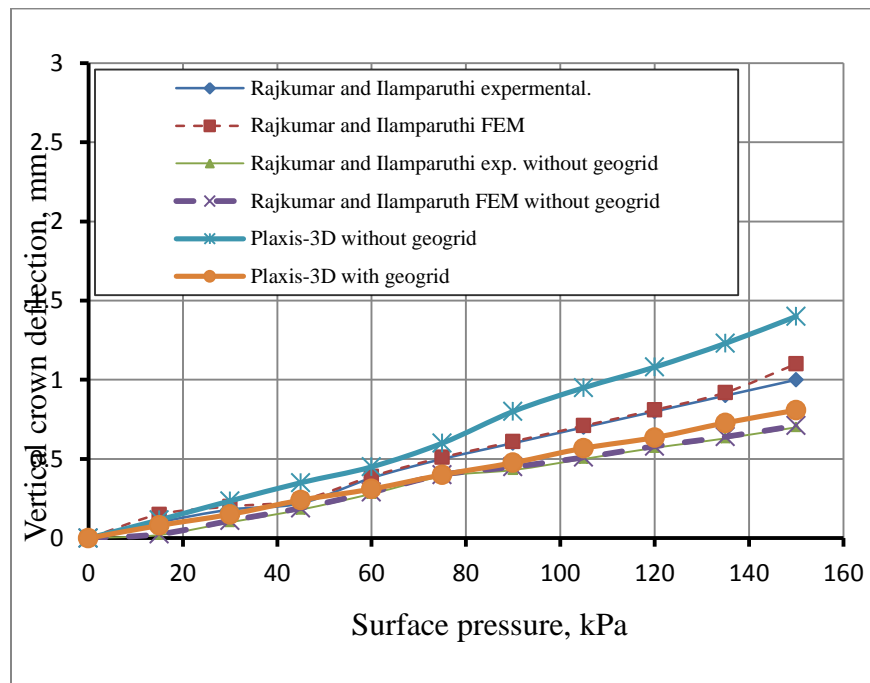


Figure 5. Comparison of the vertical crown deflection of the pipe obtained from PLAXIS-3D with experimental and numerical results of **Rajkumar and Ilamparuthi, 2008** with and without geogrid reinforcement in dense sand.

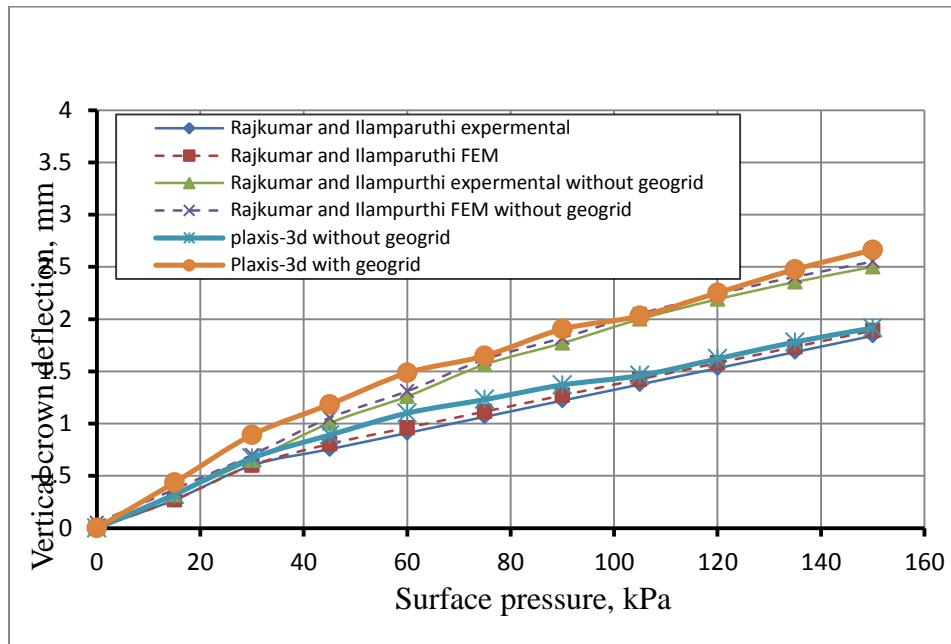


Figure 6. Comparison of vertical crown deflection of the pipe obtained from PLAXIS =3D with experimental and numerical results of **Rajkumar and Ilamparuthi, 2008** with and without geogrid reinforcement in loose sand.

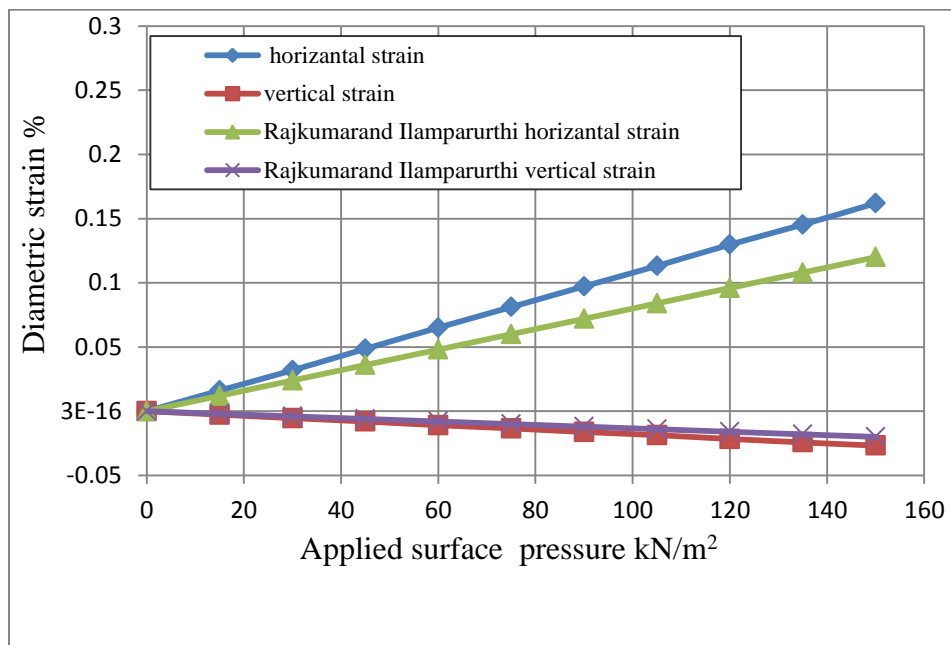


Figure7. Comparison of dimetric strain of the pipe obtained from PLAXIS-3D with the results of **Rajkumar and Ilamparuthi, 2008** in loose sand.

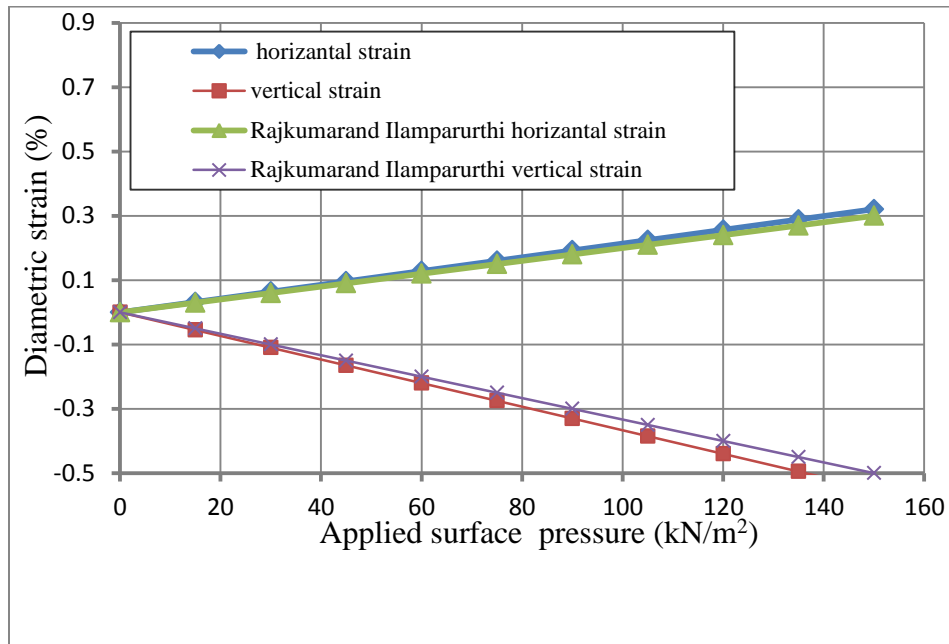


Figure 8. Comparison of crown strain of the pipe obtained from PLAXIS-3D with the results of **Rajkumar and Ilamparurthi, 2008** in dense sand.

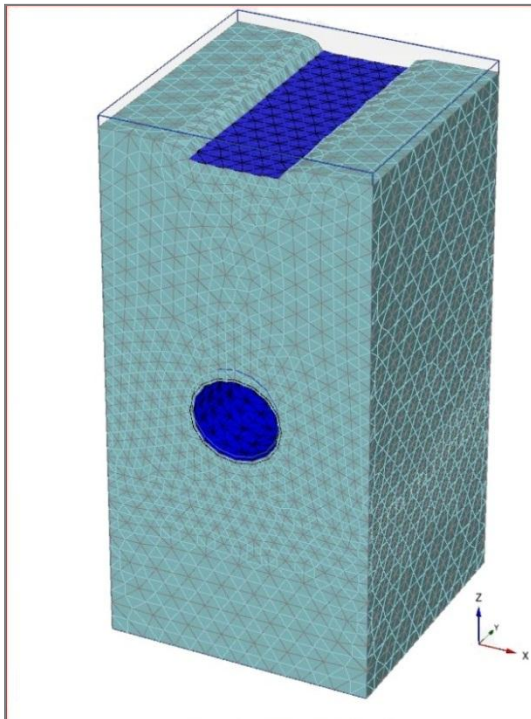


Figure 9. Results of Plaxis 3D representing the deformed mesh.

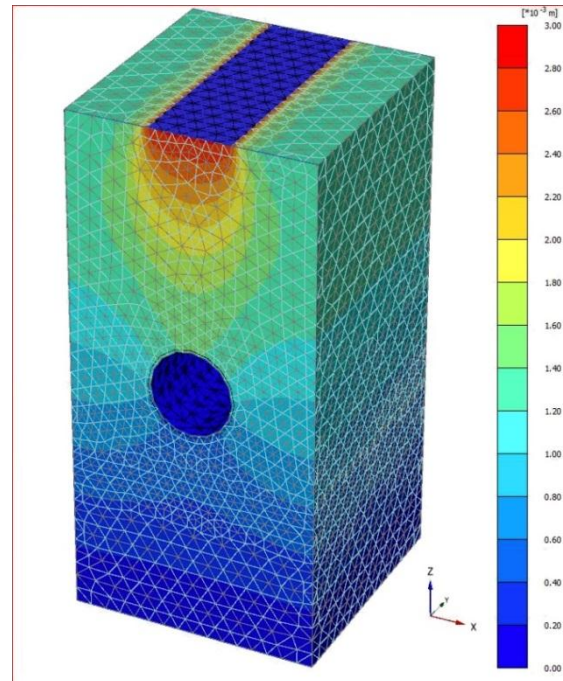


Figure 10. Results of Plaxis 3D representing total volumetric strain ϵ_v .

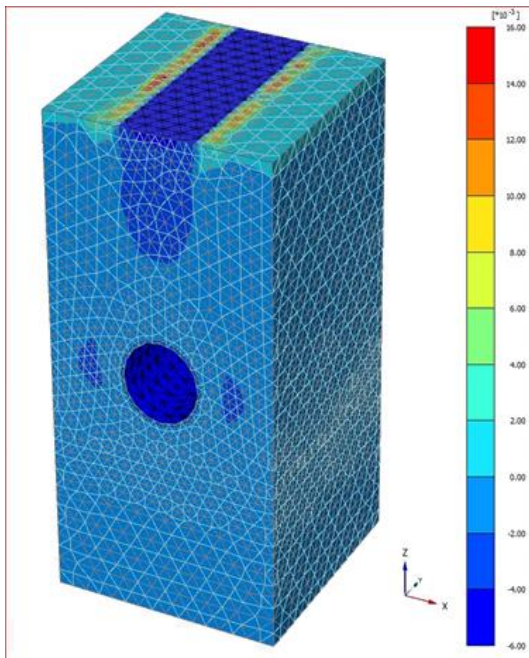


Figure 11. Results of Plaxis 3D representing the total absolute displacement (m).

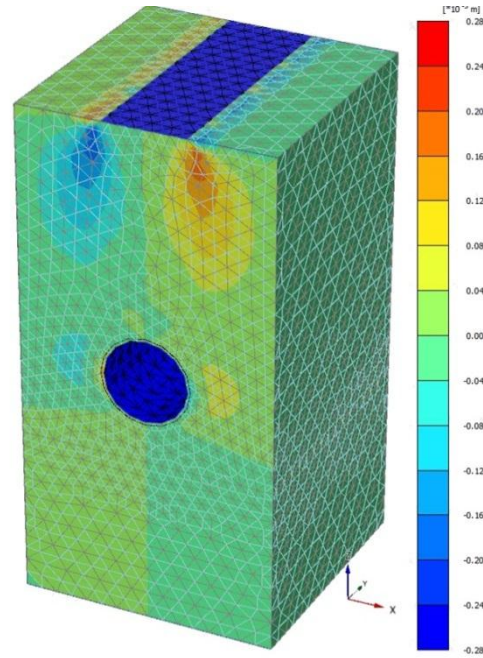


Figure 12. Results of Plaxis 3D representing the total horizontal displacement u_x

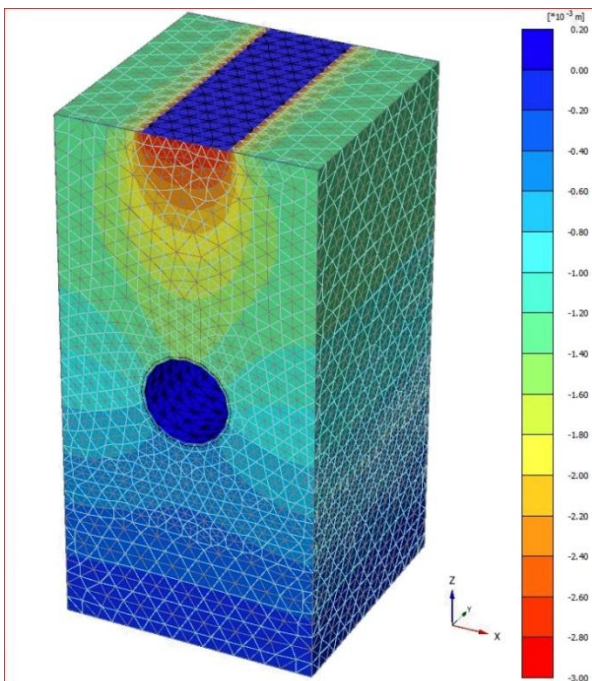


Figure 13. Results of Plaxis 3D representing the total vertical displacement, u_z .

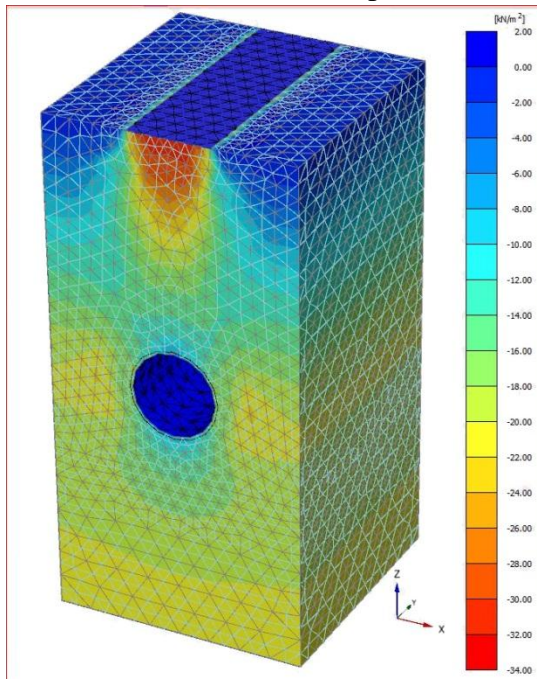


Figure 14. Results of Plaxis 3D representing the total mean stress p (kN/m^2).

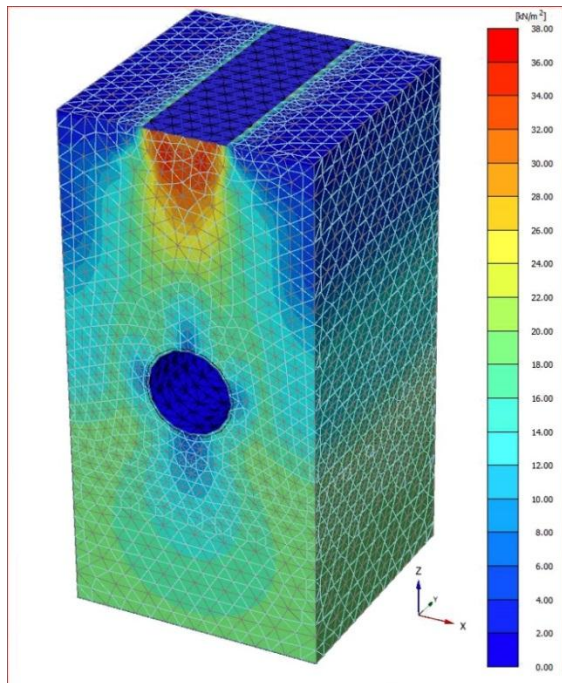


Figure 15. Results of Plaxis 3D representing the deviatoric stress q (kN/m^2).

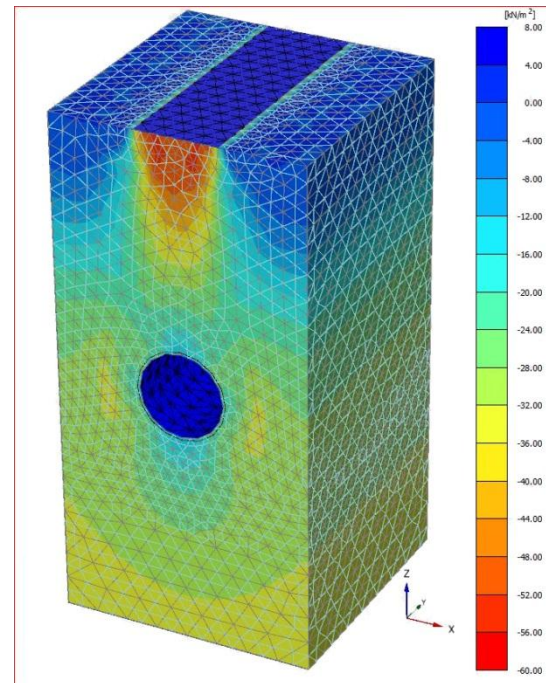


Figure 16. Results of Plaxis 3D representing the total vertical stress σ_{zz} (kN/m^2).

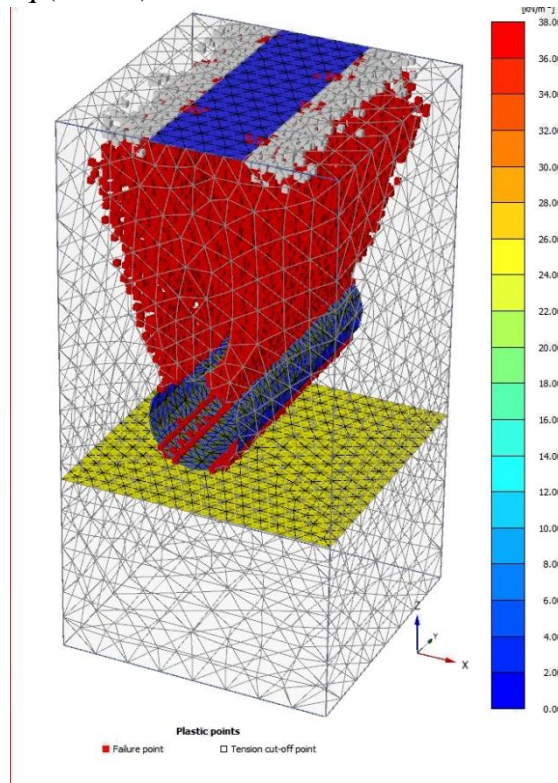


Figure 17. Result of Plaxis 3D represent plastic point.

Production of Methyl Ester (Biodiesel) from Used Cooking Oils via Trans-esterification process

Asst. Prof. Sameer Mohammed Salman
Department of Energy Engineering
College of Engineering
University of Baghdad
Emil:Dr.Samir88@yahoo.com
.com

Asst. Prof. Malik Mustafa Mohammed
Department of Biochemical Engineering
College of Al kwarizmi Engineering
University of Baghda
Emil:dr_malik1957@yahoo.com

Student. Fatima Lateef Mohammed
Department of Energy Engineering
College of Engineering
University of Baghdad
Emil:fatimalateef974@yahoo.com

ABSTRACT

Used cooking oil was undergoing trans-esterification reaction to produce biodiesel fuel. Method of production consisted of pretreatment steps, trans-esterification, separation, washing and drying. Trans-esterification of treated oils was studied at different operation conditions, the methanol to oil mole ratio were 6:1, 8:1, 10:1, and 12:1, at different temperature 30, 40, 50, and 60 °C, reaction time 40, 60, 80, and 120 minutes, amount of catalyst 0.5, 1, 1.5, and 2 wt.% based on oil and mixing speed 400 rpm. The maximum yield of biodiesel was 91.68 wt.% for treated oils obtained by trans-esterification reaction with 10:1 methanol to oil mole ratio, 60 °C reaction temperature, 80 minute reaction time and 0.5 wt.% of NaOH catalyst. The physical properties such as specific gravity, kinematic viscosity, acid number, flash point, pour point, and water content, were measured and compared them with American Standard Test Methods (ASTM D6751). The results of these properties for biodiesel product at (6:1, 8:1, 10:1, and 12:1 of methanol to oil mole ratio) were within the range of American Standard Test Methods (ASTM D6751).

Keywords:Biodiesel, trans-esterification, used cooking oils

انتاج الميثيل استر (الديزل الحيوي) من زيوت الطهي المستخدمة بواسطة عملية الاسترة التبادلية

طالبة. فاطمة لطيف محمد
قسم هندسة الطاقة
كلية الهندسة/جامعة بغداد

أ.م. مالك مصطفى محمد
قسم الهندسة الكيميائية الاحيائية
كلية الهندسة الخوارزمي/جامعة بغداد

أ.م. سمير محمد سلمان
قسم هندسة الطاقة
كلية الهندسة/جامعة بغداد

الخلاصة

خضع زيت الطهي المستخدم لتفاعل الاسترة التبادلية لانتاج وقود الديزل الحيوي. طريقة الانتاج تضمنت المعالجة، الاسترة التبادلية، الفصل، الغسل والتجفيف. درست الاسترة التبادلية للزيوت المعالجة في ظروف تشغيل مختلفة، النسبة المولية للميثانول الي الزيت كانت 6:1، 8:1، 10:1، و 12:1 عند درجات حرارة مختلفة 30، 40، 50 و 60م°، زمن التفاعل 40، 60، 80 و 120دقيقة، كمية العامل المساعد 0,5، 1، 1,5 و 2% نسبة وزنية وسرعة الخلط 400 دورة بالدقيقة. اعلى انتاج من وقود الديزل الحيوي كان 91,68 نسبة وزنية من الزيوت المعالجة التي تم الحصول عليها عن طريق تفاعل الاسترة التبادلية مع 10:1 نسبة مولية للميثانول الي الزيت، 60م° درجة حرارة التفاعل، 80 دقيقة زمن التفاعل، 0,5 % نسبة وزنية من هيدروكسيد الصوديوم العامل المساعد. الخواص الفيزيائية مثل الكثافة النوعية، اللزوجة، عدد الحمضية، نقطة الوميض، نقطة الانسكاب و المحتوى المائي، قيست ثم قورنت مع طريقة الاختبار الامريكية القياسية ASTM D6751. نتاج هذه الخصائص لمنتج وقود الديزل الحيوي عند (6:1، 8:1، 10:1 و 12:1 من الميثانول الي الزيت كنسبة مولية) كانت ضمن مدى معايير ASTM D6751 .

الكلمات الرئيسية: وقود الديزل الحيوي، الاسترة التبادلية، زيوت الطهي المستخدمة

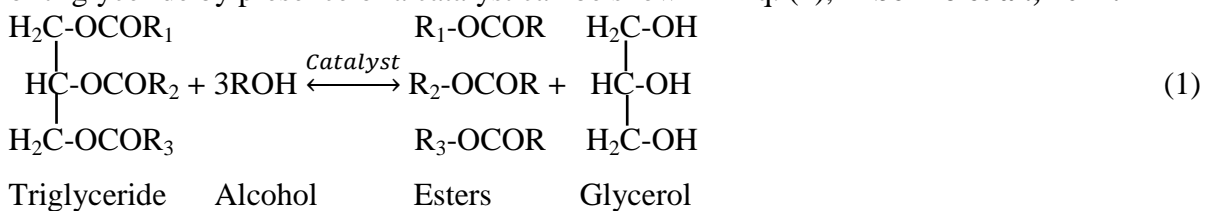
1. INTRODUCTION

Biodiesel is a mono alkyl ester of long chain fatty acids biodegradable, nontoxic fuel oil that is essentially free from sulfur and aromatics, producing lower exhaust emissions than conventional diesel fuels derived from renewable lipid such as vegetable oils and animal fats, **Hassan et al., 2013**. In view of the crises of petroleum fuel depletion and the rise in price of petroleum fuel. Therefore, there are a strong need to reduce the world's dependence on fossil fuels and replace it with other more sustainable energy sources such as geothermal energy, solar energy, tidal energy, wind energy, and biofuel, **Nakpong and Wootthikanokkhan, 2010 and Ayodeji et al., 2014**. Biodiesel is renewable and contributes less to global warming than petroleum fuel due to its closed carbon cycle. The primary feedstock can grow season after season and most of carbon in the fuel was originally removed from the air by the plant. **Fig. 1**, shows the biodiesel carbon cycle, **Prah, 2010**. Biodiesel also contains little or no sulphur and it has a higher flash point. The higher flash point of biodiesel allows safe handling and storage, **Kumar et al., 2010**. Biodiesel is safe can be used in diesel engines with few or no modifications needed, faster biodegradation. Biodiesel has greater lubricity than conventional diesel, which results in longer engine component life. All these advantages will make biodiesel as a friendly fuel for environment, **Jaichandar and Annamalai, 2011**.

This work, intend to produce methyl ester (biodiesel) from used cooking oils. Used cooking oils are a promising alternative to vegetable oil for biodiesel production because it is cheaper than pure vegetable oil. Selecting used cooking oil can lead to reduce the water pollution from pouring the used cooking oils into river, also the restaurants can no longer reused of used cooking oils which may causes the cancer from dioxin, because during frying many harmful compounds are formed, **Fan et al., 2009**. The concentration of free fatty acid in used cooking oil, indicating whether esterification must be performed or not, in this work the concentration of free fatty acid less than 3%, therefore the acid-catalyzed esterification was not necessary, **Ribeiro et al., 2011**. This research focused on biodiesel production from used cooking oils via alkali-catalyst trans-esterification. Various parameters were used to produce biodiesel such as alcohol (methanol) to oil mole ratio, reaction temperature, reaction time, and amount of catalyst (sodium hydroxide).

2. TRANS-ESTERIFICATION REACTION

Trans-esterification is the method in which the vegetable oils or animal fats are reacted with alcohol in the presence of a suitable catalyst to form esters and glycerol, trans-esterification reaction of triglyceride by presence of a catalyst can be shown in Eq. (1), **Riberiro et al., 2011**.



Trans-esterification has the sole aim of lowering the viscosity of the oil, **Jaichandar and Annamalai, 2011**.

3. EXPERIMENTAL WORK

3.1 Material

The materials used in this study are summarized in **Table 1**.

3.2 Equipment

The equipment used in this study to produce biodiesel from used cooking oil is summarized in **Table 2**.

3.3 Estimation of Free Fatty Acid (FFA)

The free fatty acid in the used cooking oil was analyzed using titration method. 10 g of filtered oil mixed with 40 ml of iso-propyl alcohol and 2-3 drops of phenolphthalein, **Gadwal and naik., 2014**. The mixture put on conical flask and then titrated with 0.1N of sodium hydroxide solution (4 gram of sodium hydroxide in 1 liter of water) with constant shaking until a pink color persists for 30 second. The percentage of free fatty acid was calculated using Eq. (2), **Gadwal and naik., 2014**.

$$FFA\% = \frac{28.2 * 0.1 * \text{titer value}}{\text{weight of used cooking oil (g)}} \quad (2)$$

3.4 Apparatus

A three neck flask was placed on a hotplate stirrer, an overhead stirrer was fixed on center neck of three neck flask, a reflux condenser and thermometer in other two neck as shown in **Fig. 2**. A condenser was used to condense any escaped vapors, and a thermometer is used to monitor the temperature of the reaction.

3.5 Biodiesel Production

1. The first step of biodiesel production is pretreatment of used cooking oil, used cooking oils contain considerable amount of solid particles, and water. To get rid of water, the used cooking oils heated on hotplate stirred at 120 ° C for 2 hours. Solid particles are can very easily be removed using Buchner funnel and filtering flask. Used cooking oils poured through a filter paper (Ø 125 mm) in a Buchner funnel. The solid particles are trapped by filter paper and oil is drowning through the funnel into filtering flask below by a vacuum pump.
2. Mixing of alcohol and catalyst, the volume of alcohol (methanol) was measured and poured into conical flask. The catalyst (sodium hydroxide) in pellet form was weight and mixed with alcohol to produce alkoxide solution (sodium alcoxide). The mixture was then heated to desirable temperature and shaking until all the catalyst dissolved. The flask was covered with watch glass during shaking to reduce the loss of alcohol by evaporate easily.
3. The trans-esterification reaction is carried out at constant agitation at 400 rpm. The operation parameters were the mole ratio of methanol to oil 6:1, 8:1, 10:1, and 12:1, reaction temperature were 30, 40, 50, and 60 ° C, the amount of sodium hydroxide were 0.5, 1, 1.5, and 2 wt.% based on oil, and at different reaction time 40, 60, 80, and 120 minutes. The pretreated oil of 100 ml was measured and poured into the three-neck flask and heated until reached to the reaction temperature. The alcohol and catalyst mixture is transferred into three-neck flask containing heated oil and the agitation started. The reaction considered starting at this moment.
4. After trans-esterification reaction is completed, the mixture was placed in a separating funnel. Then allowed to settle down overnight to ensure complete separation the reaction mixture into two layers, the upper layer is biodiesel (yellow) and lower layer is glycerol (red to orange) and may contains unreacted oil, methanol and catalyst. The lower layer was drained off from the mixture. The upper layer was drained for next steps.
5. After trans-esterification the upper ester layer (biodiesel) was separated from the bottom glycerol phase. The biodiesel layer may contain sodium hydroxide (NaOH), methanol and traces of

glycerol. The biodiesel was washed with warm distilled water (40-60) ° C and the volume of distilled water added was approximately 20% of biodiesel volume, **Ahmed et al., 2009**. Washing is carried out by spraying warm water into the top of the separating funnel, stirred gently for few minutes to prevent the soap formation. After that the washed biodiesel allowed to settle in the separating funnel. The washing process was repeated for several times (3-6) times, until pH of washed water became equal to the 7 by using Universal indicator paper.

6. After washing step was completed, the biodiesel may contain some traces of water and methanol. Biodiesel was placed in oven at 110 ° C for 1 hour to remove the remaining methanol and traces of water, **Gadwal and Naik, 2014**. And then the final product of biodiesel stored for further use.

3.6 Properties Measurement of the Biodiesel

Specific gravity, kinematic viscosity, acid number, flash point, pour point, and water content properties of used cooking oil and biodiesel were determined by using various methods according to American Standard Test Methods (ASTM D6751).

3.6.1 Specific gravity (Sp.gr) (15 ° C)

Density is the weight of a unit volume of fluid while the specific gravity is the ratio of the weight of the same volume of the oil to the weight of the same volume of water, **Balat and Balat, 2008**. This property is usually measured at 15 ° C , **Mata et al., 2010**.

Specific gravity measurements were carried out using a pycnometer in accordance with ASTM D-941 standards. The specific gravity was calculated using Eq. (3).

$$Sp. gr = \frac{W_3 - W_1}{W_2 - W_1} \quad (3)$$

Where

W1= weight of empty pycnometer

W2= weight of pycnometer with water

W3= weight of pycnometer filled oil.

3.6.2 Kinematic viscosity

Kinematic viscosity is a measure of the resistive flow of a fluid under gravity, **Samuel et al., 2013**. Kinematic viscosity was measured for used cooking oil and biodiesel at 40 ° C, by measuring the time for a volume liquid to flow under gravity through U-Tube Viscometer in accordance with ASTM D-445.

3.6.3 Acid number

Acid Number is defined as the quantity of base, expressed in milligram of potassium hydroxide, that is required to neutralize all acidic (free fatty acid) constituents present in one gram of oil, **Fan et al., 2009**. It is determined for used cooking oil and biodiesel according to the ASTM D-664.

3.6.4 Flash point

The flash point of a fuel is the minimum temperature at which the fuel will ignite (flash) on application of an ignition source. Minimum flash point temperature is required for proper safety and handling of diesel fuel, **Samuel et al., 2013**. Flash point was determined by Pensky-Martens Closed Cup test until accordance with ASTM D-93.

3.6.5 Pour point

Pour point refers to the temperature at which the oil in solid form starts to pour, **Yap et al., 2011**. Pour point is useful in estimating the relative amount of wax in oil, **Balat and Balat, 2008**. It is determined in accordance with ASTM D- 97.

3.6.6 Water content

Water content for used cooking oil and biodiesel product was determined in accordance with ASTM D-2709.

4. RESULT AND DISSCUSIONS

4.1 Determination of Fatty Acid Composition

The fatty acid composition of used cooking oil was determined using gas chromatography (UNITED TECHNOLOGIES PACKARD) using a column SE-30, and flame ionization detector (FID). The initial column temperature 100°C , and then increased to 300°C at $10^{\circ}\text{C}/\text{minute}$. Injector temperature was 300°C and detector temperature was 325°C . The flow rates of gases helium He (carrier gas), the flow rate of carrier gas was 30 ml/minute this process was carried out in Ibn Sina Center. The fatty acid composition of used cooking oil determined using gas chromatography with flame ionization detector is shown in **table 3**, shows that the major fatty acid is stearic acid with mass concentration of 49.3065%.

4.2 Effect of Reaction Temperature on the Biodiesel Yield

Reaction temperatures were that used in this work from 30 to 60°C , the highest reaction temperature 60°C was selected because it is near the boiling point of methanol (64°C) with reaction time 40, 60, 80, 120 minutes. All experiences carried out at 40 minute of reaction time for different temperature to choose the best reaction temperature for different mole ratio.

Fig. 3, shows the biodiesel yield with reaction temperature and mole ratio of the transesterification reaction at 40 minute. The lower yield of biodiesel was 70.81 wt.% at the reaction temperature 30°C with 12:1 methanol to oil mole ratio. The best yield percentage was 90.185 wt% obtained using 60°C reaction temperature with 10:1 methanol to oil mole ratio. As shown in **Fig. 3**, the biodiesel yield increased with reaction temperature.

Higher reaction temperature increases the reaction rate and shortened the reaction time due to the reduction in viscosity of oils, increasing the temperature causes an increase in molecule activity. This means that more molecule have more energy; thus, the possibility of molecule to collision increased. Then consequently, higher conversion values that lead to increase in yield of product material are obtained. However, the increase reaction temperature beyond the optimal level (60°C) leads to decrease of biodiesel yield, because higher reaction temperature accelerates the saponification of triglycerides and causes methanol to vaporize resulting in decreased yield. And the transesterification reaction temperature should be below the boiling point of alcohol (methanol) to prevent the alcohol evaporation, if the temperature of reaction is high, methanol lend to evaporate faster and finally the reaction loses one of the important ingredients.

4.3 Effect of Reaction Time on the Biodiesel Yield

Fig.4 shows the biodiesel yield with reaction time and mole ratio. After choosing the best temperature for each mole ratio, the experiments were carried out at different times with the best temperature. The lower yield of biodiesel was 70.95 wt% at reaction time 120 minutes with 12:1 methanol to oil mole ratio. The best yield percentage was 91.68 wt.% obtained after 80 minutes reaction time with 10:1 methanol to oil mole ratio.

Biodiesel yield increased clearly from 40 to 80 minute. However, the reaction time was increased beyond 80 minute, the biodiesel yield was decreased. This behavior was clear at minute 120. Effect longer reaction time gives higher yield than using shorter time. So, 80 minute of reaction time gave a good result than other reaction times used here, in other words, the biodiesel yield increases with increasing the reaction time. However, based on the results, it shows that the biodiesel yields were lower when reaction time of 120 minute was used. This undesirable result may be due to the higher soap formation when longer reaction time was used. Thus, the rate of soap formation was also increased.

4.4 Effect of Catalyst Concentration on the Biodiesel Yield

The yield of biodiesel is also affected by the concentration of catalyst. The type and amount of catalyst required in the trans-esterification process usually depend on the level of free fatty acid and water content on oil, which is used to produce biodiesel, **Kumar et al., 2010**. Used cooking oil, which has been used in the present work, has low level of free fatty acid and water, alkali catalyst trans-esterification is suitable to be used, **Kumar et al., 2010**. Sodium hydroxide was used as alkali catalyst, because it is cheaper and is widely used, **Ma and Hanna, 1999**.

Fig. 5 shows the biodiesel yield with concentration of NaOH catalyst at different methanol to oil mole ratio. Four different catalyst percentages, 0.5, 1, 1.5, and 2 wt.% of sodium hydroxide, were selected for trans-esterification reaction. These percentages were weight fraction based on oil. The results show that the biodiesel yield decreases with increasing amount of catalyst from 0.5 to 2 wt.%. The best yield of biodiesel was achieved at 0.5 wt.% of NaOH catalyst at different methanol to oil mole ratio. The lower yield of biodiesel was 32.21% with 2 wt.% of NaOH catalyst, at 6:1 methanol to oil mole ratio and 60 °C. The best conditions of reaction temperature 60 °C, reaction time 80 minute, and methanol to oil mole ratio 10:1, the experimental carried out for 0.3 and 0.7 wt.%, when the catalyst was 0.3 wt.%, the yield of biodiesel was 89.09%, while at 0.7 wt.%, the yield of biodiesel was 86.7%. Increasing the catalyst concentration from 0.3 to 0.5 wt.% the biodiesel yield increased. Increasing the catalyst concentration from 0.7 to 2 wt.% the biodiesel yield decreased. Restricted according to the reaction level of NaOH in methanol if it above or not. The results showed that the best suited catalyst concentration giving the best yields and viscosities of the ester is 0.5 wt.% for higher values the yields were lower. Catalyst concentration is closely related to the free acidity of the oil. When there is free fatty acid content, the addition of more sodium hydroxide, compensates this acidity and avoids catalyst deactivation. The addition of an excessive amount of catalyst, however, giving rise to the formation of an emulsion, which increase the viscosity and leads to the formation of gels that because NaOH became above saturation in sodium methoxide solution. These hinder the glycerol separation and, hence, reduce the apparent ester yield. Increases in catalyst concentration will not increase the conversion and will lead to extra costs because it is necessary to remove it from the reaction medium at the end.

4.5 Effect of Methanol to Oil Mole Ratio on Biodiesel Yield

The mole ratio of alcohol to oil is most important factors that influence the conversion of oils to its ester. Theoretically, three moles of alcohol are required for each mole of triglyceride to produce three moles of biodiesel and one mole of glycerol. But since trans-esterification is a reversible reaction, excess amount of alcohol are used to ensure that oils will be completely converted to ester, **Anitha and Dawn, 2010**. In reality the mole ratio should be higher than the theoretical ratio to drive the reaction to completion.

Methanol was used as alcohol in this work, because of its low cost. Adding the methanol has an ability to react with triglycerides quickly and sodium hydroxide is easily dissolved in it, **Ahmed et al., 2009**.

Alcohol to oil mole ratio always has positive effect on biodiesel yield. Experiments were conducted with methanol to oil mole ratio of 6:1, 8:1, 10:1, and 12:1 using a constant mixing speed of 400 rpm. **Fig. 6** shows the increasing of biodiesel yield with temperature. The biodiesel yield increased as the mole ratio increased, with best results 90.182 wt.% being for a mole ratio 10:1 at 60 °C. nevertheless, a later increase of mole ratio to 12:1 did not result in an increase in the yield, at higher reactant ratio a large amount of alcohol is present in the trans esterified products, requires large amount of energy to distill the products, since a lower value is obtained 88.36 wt.%

Fig. 7 shows the evolution of biodiesel with catalyst concentration. The biodiesel yield increased as the methanol to oil mole ratio increased. As can be observed, with 6:1 methanol to oil mole ratio, the biodiesel yield was 85.58 wt.% at 0.5 wt.% of NaOH. While, the best results 91.684 wt.% being for a mole ratio 10:1. As shown in **Fig. 7**, increasing catalyst concentration from 0.5 to 2 wt.%, cause decreasing in biodiesel yield, but at a high methanol to oil mole ratio the decreases is lower. As can be observed the yield of biodiesel when the catalyst concentration increased from 0.5 to 2 wt.% with 6:1, the result decreased from 85.58 to 32.21 wt.%, while the biodiesel yield with 12:1 mole ratio decreased from 88.36 to 64.62 wt.% when NaOH concentration increased from 0.5 to 2 wt.%.

The higher alcohol to oil mole ratio interferes with the separation of glycerol because there is an increase of solubility of alcohol in glycerol. In addition, an excess of alcohol was able increase the conversion of di-monoglycerides, but there is possibility of recombination of esters and glycerol to form monoglycerides because of their high ratio and increasing during the course of the reaction, in other words the reactions conducted with low mole ratio. At the beginning ester yield increases with increase in mole ratio of methanol to oil but the incremental gain in ester yield decreases with increase in the mole ratio.

4.6 Selection of Best Operation Conditions and Effect of Mole Ratio on Physical Properties

The best operation conditions of the trans-esterification process to produce biodiesel from used cooking oil, which gives the higher yield of biodiesel were, 10:1 methanol to oil mole ratio, 60 °C reaction temperature, 80 minute reaction time and 0.5 wt.% of NaOH catalyst at constant stirring speed 400 rpm. The higher yield was achieved at these condition was 91.68 wt.%.

The used cooking oil and biodiesel were tested to determine the physical properties according to ASTM. **Table 4** shows the test result for used cooking oil and biodiesel product at 6:1, 8:1, 10:1, and 12:1 methanol to oil mole ratio. These physical properties depend on the practical parameters which used to produce biodiesel.

As shown in **Table 4** the kinematic viscosity of used cooking oil was 50.099 cSt. Kinematic viscosity is a very important property of a diesel fuel because it affects the engine fuel injection system predominantly at low temperature, **Balat and Balat, 2008**. The high viscosity may lead to poor atomization of the fuel, incomplete combustion, choking of the injectors, ring carbonization and accumulation of the fuel in the lubricating oils, one of the best way to avoid those problems and reduce the viscosity is trans-esterification process. After trans-esterification process the kinematic viscosity of biodiesel from 6:1, 8:1, 10:1, and 12:1 methanol to oil mole ratio were, 6.098, 6.098, 5.6, and 5.28 respectively. Hence, an increase in the methanol to oil mole ratio reduced the kinematic viscosity as shown in **Fig.8**. These results show that the value of kinematic viscosity of biodiesel were at the same range of ASTM standard (1.9 to 6) cSt, but these value are higher than value of diesel (2.6 cSt). So it is preferable to get biodiesel of low viscosity that can not cause any problems in fuel injection.

Specific gravity is another important property of the fuels that affects the fuel injection system. The specific gravity is measured at 15 °C for used cooking oil and biodiesel product at different methanol to oil mole ratio. The specific gravity of used cooking oil was 0.9276, and for biodiesel were, 0.887, 0.8776, 0.873, and 0.861 at 6:1, 8:1, 10:1, and 12:1 respectively of methanol to oil mole

ratio. It is note the value of specific gravity decreased after trans-esterification reaction, and it is decreased with increasing methanol to oil mole ratio as shown in **Fig.9**. The values of specific gravity were within the range of ASTM standard (0.86 to 0.9), which is higher than that of the petroleum diesel (0.85). So that the biodiesel produced has a good specific gravity.

The flash point for used cooking oil was 180°C , while the flash point of biodiesel which produced at 6:1, 8:1, 10:1, and 12:1 methanol to oil mole ratio were 150, 166, 100, and 80°C respectively, shown in **Fig.10**. Biodiesel have higher flash point than the petroleum diesel meaning that they are less flammable hence they are safer to handle and storage, though the flash point of biodiesel is high, still some storage precautions are needed to be taken. The flash point for each 6:1, 8:1, and 10:1 mole ratio are higher than diesel flash point, while the flash point of biodiesel at 12:1 mole ratio it's within the value of flash point of diesel as (50 to 80°C), **Ahmed et al., 2009**.

Pour point refers to the temperature at which the oil in the solid form starts to pour or melt. In cases where the temperatures fall below the pour point, the entire fuel system including all fuel lines and fuel tank will need to be heated. Pour point for used cooking oil was -8°C , while the pour point for biodiesel which produce at different methanol to oil mole ratio were, -6, -5, -8, and -10 at 6:1, 8:1, 10:1, and 12:1 respectively. The pour point of biodiesel is higher than pour point of petroleum diesel fuel. **Fig.11** shows the value of pour point at different methanol to oil mole ratio. These results of pour point of biodiesel were found to be agreement with ASTM biodiesel standard (-15 to 10°C).

The water content in used cooking oil was 0.095% by volume. The presence of water in biodiesel can cause corrosion of metallic engine parts or produce soaps when it reacts with triglycerides. Water may also induce the formation of microorganisms, due to these negative effects. The ASTM standard limit for water content was 0.05% by volume of biodiesel, **Fan et al., 2009**. In this experimental, it was found that there was no water content in biodiesel produced from used cooking oil at different methanol to oil mole ratio.

Acid number is used as a guide in the quality control as well as monitoring oil degradation during storage. Acid number for used cooking oil was measured and it was found 1.04 mg KOH/g of oil. The ASTM standard for acid number for biodiesel is 0.8 mg KOH/g of oil. The acid number of biodiesel in this work as shown in **Fig.12** at 6:1, 8:1, 10:1, and 12:1 methanol to oil mole ratio were, 0.53, 0.5, 0.43, and 0.39 respectively, these results are positive character of biodiesel.

5. CONCLUSION

The biodiesel production from used cooking oil was affected by, methanol to oil mole ratio, temperature of reaction, reaction time and catalyst concentration, the following conclusions were obtained

1. At the gas chromatography analysis found the major fatty acid composition is Stearic acid with mass concentration of 49.3065%.
2. Biodiesel yield was increasing with temperature of reaction within the range of (30 - 60°C).
3. Biodiesel yield was slightly affected by reaction time, it was increased when the reaction time increases from 40 to 80 minutes then the yield decreases beyond 80 minute of reaction time.
4. Increasing the methanol to oil mole ratio causes the yield to increase up to methanol to oil ratio of 10:1, then it will decrease beyond 10:1.
5. There was a negative effect of increasing sodium hydroxide concentration on the biodiesel yield.
6. The maximum yield of biodiesel produced by trans-esterification was 91.68 wt.% at the conditions methanol to oil mole ratio 10:1, reaction temperature 60°C , 80 minute of reaction time and 0.5 wt.% based on oil of sodium hydroxide concentration.
7. The characterization results of biodiesel produced such as specific gravity, kinematic viscosity, acid number, flash point, pour point and water content at 10:1 methanol to oil mole ratio were 0.873, 5.6, 0.43mg KOH/g of oil, 100°C , -8°C and 0 respectively, they were within the range of ASTM D6751.

**REFERENCES**

- Ahmed, M., Rashid, S., Khan, M.A., Zafar, M., Sultana, S., Gulzar, S., 2009, *Optimization of Base Catalyzed Transesterification of Peanut Oil Biodiesel*, African Journal of Biotechnology, Vol.8, No.3, pp.441-446.
- Anitha, A., and Dawn, S. S., 2010, *Performance Characteristics of Biodiesel Production from Waste Groundnut Oil Using Supported Heteropolyacids*, International Journal of Chemical Engineering and Applications, Vol.1, No.3.
- Ayodeji, A., Wonderatt, Idongesit, S., 2014, *INVESTIGATION ON BIODIESEL PRODUCTION USING TWO BASE CATALYSTS*, Impact Journals, Vol.2, pp.99-104.
- Balat, M., and Balat, H., 2008, *A Critical Review of Bio-Diesel as a Vehicular Fuel*, Energy Conversion and Management, Vol.49, pp. 2727-2741.
- Fan, X., Burton, R., Austic, G., 2009, *Preparation and Characterization of Biodiesel from Recycled Canola Oil*, The Open Fuels & Energy Science Journal, Vol.2, pp.113-118.
- Gadwal, R., and Naik, G. R., 2014, *Hibiscus Species Seed Oils as Potential Feedstock for Biodiesel Production, its Performance in Compression Ignition Engine Along with its Blends*, Journal of Chemical and Pharmaceutical Research, Vol.6, No.10, pp. 212-223.
- Hassan, F. M., Alibory, I. F., Kassim, T. I., 2013, *An Attempt to Stimulate Lipids for Biodiesel Production from Locally Isolated Microalgae in Iraq*, Baghdad Science Journal, Vol.10, No.1.
- Jaichandar, S., and Annamalai, K., 2011, *The Status of Biodiesel as an Alternative Fuel for Diesel Engine- An Overview*, Journal of Sustainable Energy & Environment, Vol.2, pp. 71-75.
- Kumar, G., Kumar, D., Singh, S., Kothari, S., Bhatt, S., Singh, C. P., 2010, *Continuous Low Cost Transesterification Process for the Production of Coconut Biodiesel*, Energies, Vol.3, pp. 43-56.
- Ma, F., and Hanna, M. A., 1999, *Biodiesel Production: a Review*, Bioresource Technology, Vol.70, pp. 1-15.
- Mata, T. M., Cardoso, N., Ornelas, M., Neves, S. and Caetano, N. S., 2010, *Sustainable Production of Biodiesel from Tallow, Lard and Poultry Fat and its Quality Evaluation*, CHEMICAL ENGINEERING TRANSACTIONS, Vol.19.
- Nakpong, P., and Wootthikanokkhan, S., 2010, *Mixtures of Vegetable Oil and Used Frying Oils as Feedstock for Biodiesel Production in THAILAND*, Suranaree J.Sci. Technol., Vol.17, No.2, pp. 193-202.
- Prah, E., 2010, *Biodiesel Analytical Development and Characterisation*, Thesis (Chemical Engineering) In the Department of Process Engineering, Stellenbosch University.
- Riberiro, A., Castro, F., Carvalho, J., 2011, *Influence of Free Fatty Acid Content in Biodiesel Production on Non-Edible Oils*, Wastes: Solutions, Treatments and Opportunities, 1st International Conference.

- Samuel, O. D., Waheed, M. A., Bolaji, B. O., Dario, O. U., 2013, *Production of Biodiesel from Nigerian Restaurant Waste Cooking Oil using Blender*, INTERNATIONAL JOURNAL OF RENEWABLE ENERGY RESEARCH, Vol.3, No.4.

- Yap, Y. H. T., Abdullah, N. F., Basri, M., 2011, *Biodiesel Production via Transesterification of Palm Oil Using NaOH/Al₂O₃ Catalysts*, Sains Malaysiana, Vol.40, No.6, pp. 587-594.

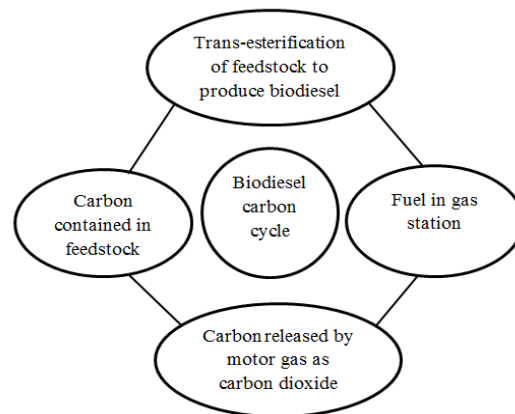


Figure 1. Biodiesel carbon cycle.



Figure 2. Equipment of trans-esterification Reaction.

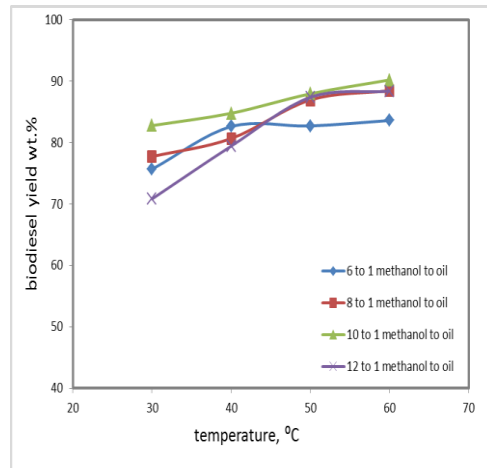


Figure 3. Effect of temperature on the biodiesel yield.

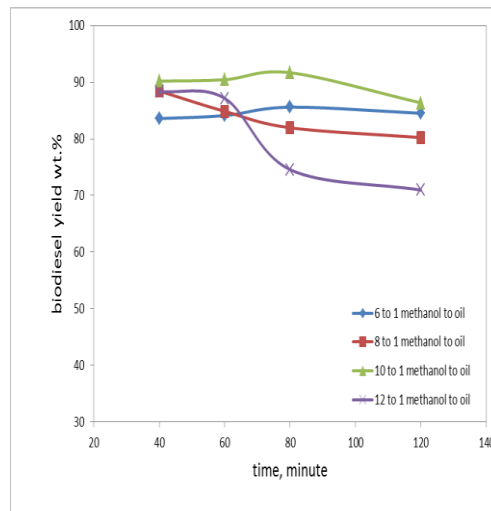


Figure 4. Effect of time on the biodiesel yield.

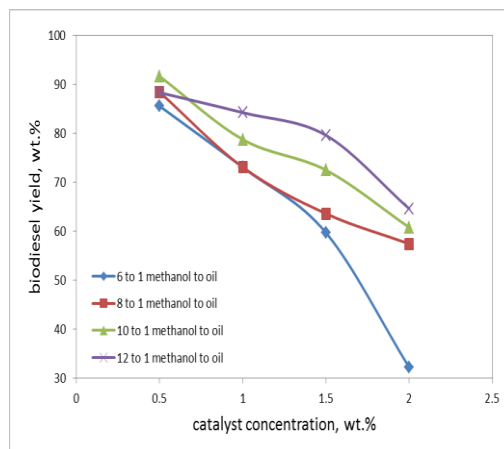


Figure 5. Effect of catalyst concentration on biodiesel yield.

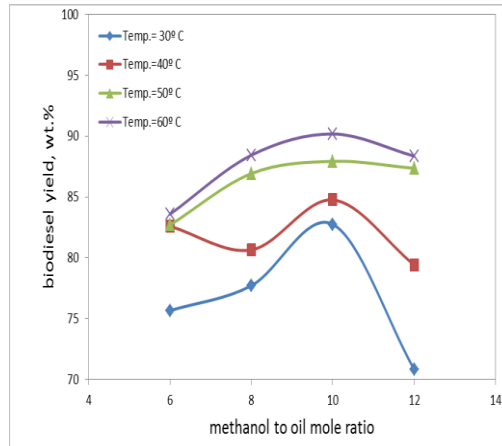


Figure 6. Effect of methanol to oil mole on biodiesel yield at different temperature.

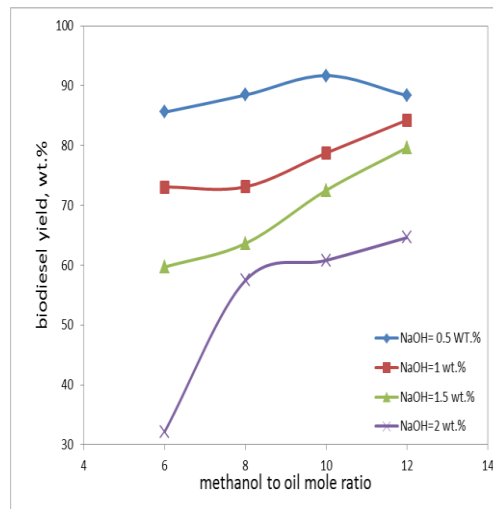


Figure 7. Effect of methanol to oil mole ratio biodiesel yield at different catalyst concentration.

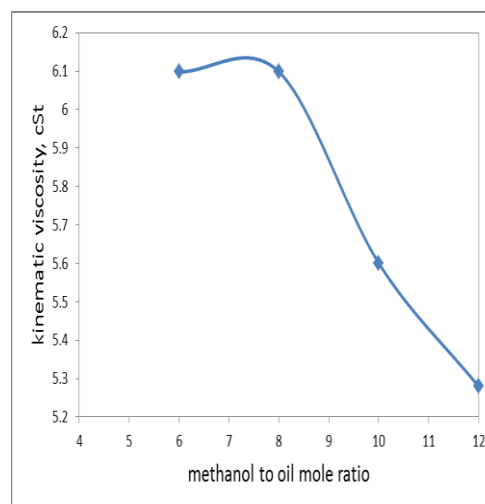


Figure 8. Kinematic viscosity of biodiesel at different methanol to oil mole ratio.

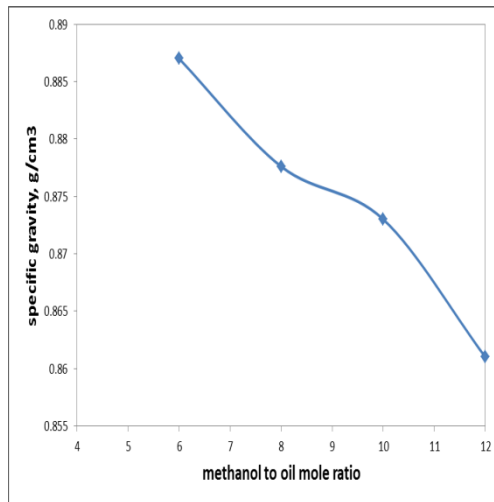


Figure 9. Specific gravity of biodiesel at different methanol to oil mole ratio.

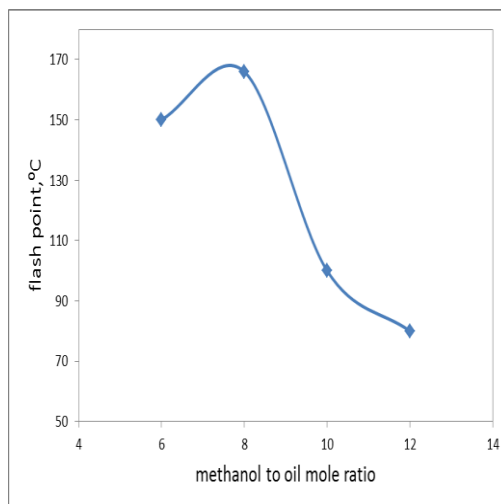


Figure 10. Flash point of biodiesel at different methanol to oil mole ratio.

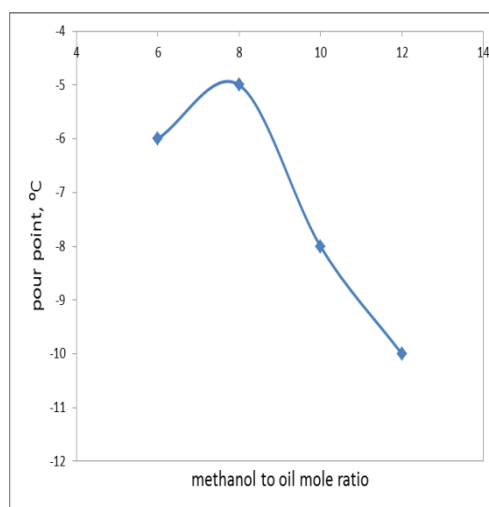


Figure 11. Pour point of biodiesel at different methanol to oil mole ratio.

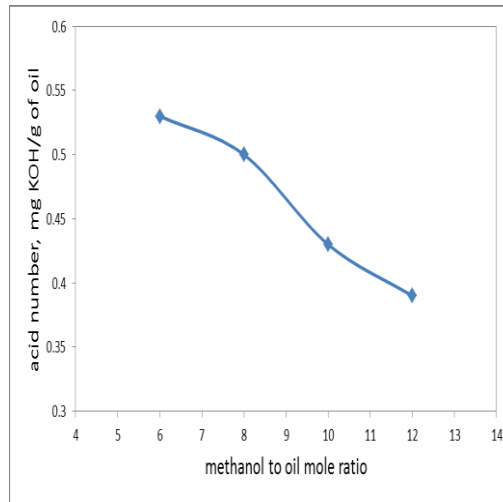


Figure 12. Acid value of biodiesel at different methanol to oil mole ratio.

Table 1. The materials used and their sources.

No	Materials	Sources
1	Used cooking oil	kitchen
2	Methanol (CH ₃ OH)	LOBAL Chemie (local market)
3	Sodium hydroxide pellets (NaOH)	LOBAL Chemie (local market)
4	Iso-propyl alcohol ((CH ₃) ₂ CHOH)	THOMAS BAKER
5	Phenolphthalein C ₂₀ H ₁₄ O ₄	THOMAS BAKER

Table 2. The Apparatus used and their sources or origin.

No	Name of equipment	Sources/ origin
1	Hotplate stirrer	DAIHAN LABTECH CO., LTD/ Lab Tech
2	Buchner funnel and filter flask	Germany
3	Reflux condenser	Germany
4	Mercury thermometer	Germany
5	Three-neck flask	Germany
6	Digital overhead stirrer	PHOENIX instrument RSO 20D
7	Electronic balance	KEREN (max 320g)
8	Separation funnel	ISOLAB/ Germany

Table 3. Fatty acid composition of used cooking oil.

Common Name	C: D	Retention Time, minute	Mass concentration %
Palmitic acid	C _{16:0}	13.103	6.1262
Stearic acid	C _{18:0}	15.287	49.3065
Oleic acid	C _{18:1}	16.655	1.1993
Linoleic acid	C _{18:2}	14.24	0.0228

M.Wav

881.454g/mol

C= Carbon atoms, D= Double bond

M.Wav= Average Molecule Weight.

Table 4. Shows the physical property of the used cooking oil and biodiesel.

Physical property	Used				
	cooking oil	6:1	8:1	10:1	12:1
Specific gravity (g/cm ³)	0.9276	0.887	0.877	0.873	0.861
Kinematic viscosity ,cSt	50.099	6.098	6.098	5.6	5.28
Flash point , °C	180	150	166	100	80
Pour point, °C	-8	-6	-5	-8	-10
Water content, Vol%	0.095%	0	0	0	0
Acid number, mg KOH/g of oil	1.04	0.53	0.5	0.43	0.39

Encoding of QC-LDPC Codes of Rank Deficient Parity Matrix

Mohammed Kasim Mohammed Al-Haddad

Lecturer

College of Engineering - University of Baghdad

Email: mkmih12@gmail.com

ABSTRACT

The encoding of long low density parity check (LDPC) codes presents a challenge compared to its decoding. The Quasi Cyclic (QC) LDPC codes offer the advantage for reducing the complexity for both encoding and decoding due to its QC structure. Most QC-LDPC codes have rank deficient parity matrix and this introduces extra complexity over the codes with full rank parity matrix. In this paper an encoding scheme of QC-LDPC codes is presented that is suitable for codes with full rank parity matrix and rank deficient parity matrix. The extra effort required by the codes with rank deficient parity matrix over the codes of full rank parity matrix is investigated.

Key words: Low density Parity Check (LDPC) Codes, Quasi-Cyclic (QC), Circulant Matrix.

ترميز QC-LDPC ذات مصفوفة التطابق ناقصة الرتبة

محمد قاسم محمد الحداد

مدرس

كلية الهندسة - جامعة بغداد

قسم الهندسة الالكترونية

الخلاصة

ان عملية ترميز فحص التطابق ذو الكثافة الواطئة (LDPC) في حال الرموز الطويلة تمثل تحدي مقارنةً بعملية فك الترميز. بينما ترميز الـ LDPC الشبه دائري (QC) له محاسن لتقليل حجم التعقيد الذي تتطلبه كلتا عمائتي الترميز وفك الترميز بسبب بنية الـ QC. معظم حالات ترميز الـ QC-LDPC يكون لها مصفوفة التطابق ذات رتبة ناقصة وهذا يؤدي الى زيادة في التعقيد مقارنةً بحالات الترميز التي يكون لها مصفوفة تطابق كاملة الرتبة. في هذا البحث يجري استعراض طريقة لترميز QC-LDPC ملائمة لكلا حالتين مصفوفة التطابق الكاملة الرتبة والناقصة الرتبة. وقد جرى حساب الجهد الاضافي الذي تتطلبه حالات مصفوفة التطابق ذات الرتبة الناقصة على الجهد الذي تتطلبه حالات مصفوفة التطابق ذات الرتبة الكاملة.

1. INTRODUCTION:

Low Density Parity Check (LDPC) codes are subclass of linear block codes, it was first discovered by **Gallager** in 1962, but due to the available technology at that time and the codes computational demand the LDPC codes remained outside the fields of practice and research until it was rediscovered by **McKay, 1999**. The advantage of the LDPC codes over the algebraic codes comes from the fact that their decoding complexity is linear with code length which makes it practical to design long codes that approach Shannon channel capacity limit. The main disadvantage of the LDPC codes is that their encoding complexity is very high. The only competitor of LDPC codes is the turbo codes which are also Shannon limit approaching codes with slightly lower performance than LDPC codes but with better encoding complexity. The research in construction and encoding of LDPC codes is still an open field.

An LDPC code is defined by the $m \times n$ parity check matrix \mathbf{H} that should be a sparse matrix from which Tanner graph is constructed. Tanner graph consists of two groups of nodes, the first is the variable nodes (or bit nodes) representing each bit in the code and the check nodes (or constraint nodes) representing the parity-check equations with connections, called edges, between the variable nodes and the check nodes each connection (or edge) represents a 1 in the \mathbf{H} matrix. So, if there is a 1 in the i^{th} row and the j^{th} column of \mathbf{H} then the i^{th} check node would be connected to the j^{th} variable node as shown in **Fig. 1**. A cycle in a Tanner graph is defined as the number of edges counted starting from a certain node and ending in the same node, the minimum size cycle is called the girth which is an important parameter of the code because the larger the girth the better error correcting capability of the code. A code with no cycles is said to have infinite girth, and the minimum possible value of the girth is 4, **Moreira, and Farrell, 2006**. Codes with girth equal to 4 show degraded performance, so, the cycles of size 4 should be removed from the \mathbf{H} matrix in the construction of an LDPC code. These size-4 cycles can be easily located in the \mathbf{H} matrix if there are 4 1's forming a rectangle.

LDPC codes fall into two main categories, regular and irregular codes. If the rows and columns of \mathbf{H} have a constant weight (number of bits), then the code is regular, if not, it is irregular code. Irregular codes have the advantage of larger girth and hence better bit error correction capability but their lack of structure makes the encoder and decoder implementation more complex. In regular code, the coding rate can be given in terms of the column weight w_c and row weight w_r

$$R \geq 1 - \frac{m}{n} = 1 - \frac{w_c}{w_r} \quad (1)$$

Here the equality holds if \mathbf{H} is a full rank matrix. More will be said about rank of parity matrix later.

2. CONSTRUCTIONS OF LDPC CODES:

The construction of LDPC codes is basically the construction of its parity matrix \mathbf{H} . There is no specific way for constructing LDPC code; instead there are constraints or guidelines. The first constraint is that the \mathbf{H} matrix should be sparse, this is important for the decoding complexity reduction. The second is that there should be no two rows (or two columns) that have two 1's in the same positions; this is called the row-column (RC) constraint which makes the LDPC code free of cycles of size 4. Basically there are two main categories of approaches used in construction LDPC codes; the first is the random-like LDPC codes such as **Gallager, 1962** codes and **McKay, 1999**

codes, progressive-edge-growth (PEG) codes, approximate cycle extrinsic message degree (ACE) codes. The second category is the structured quasi cyclic LDPC codes like protograph codes and codes based on the finite fields and finite geometry mathematics. In general the LDPC code that possesses a structure is preferred over the nonstructured codes because of the reduced complexity in encoding and decoding. The QC-LDPC codes are elegantly structured codes and can be encoded efficiently using shift registers. **Song et al., 2009** presented a unified approach for constructing QC-LDPC codes based on finite fields the construction is based on primitive elements, additive subgroups, and cyclic subgroups of finite fields. **Tao et al., 2011** presented a search algorithm to first construct a QC-LDPC codes of column-row weight (k,k) and girth g and then a random LDPC codes was derived with column-row weight $(2,k)$ and girth $2g$ a girth of up to 36 was achieved. **Park et al.**, presented a search method based on graph theoretic approach to detect subgraphs that cause short cycles in order to be avoided in the construction of the LDPC code, the design achieved codes of girth greater than 14. **Huang and Lee, 2013** constructed a block circulant RS based LDPC codes which have the advantage over the random RS based LDPC codes in terms of decoding complexity. **Wang et al., 2013** constructed a high girth hierarchical quasi-cyclic (HQC) LDPC codes in the form of a hierarchy of block circulant submatrices instead of the common block circulant based QC-LDPC codes. Since we are interested in the encoding of QC-cyclic LDPC codes an examples of constructing such codes will be provided later.

3. DECODING OF LDPC CODES:

Unlike algebraic codes like Reed-Solomon (RS) codes, LDPC codes can be decoded with complexity linearly proportional to code length and this is a very important feature of LDPC codes making it possible to implement long codes that can approach Shannon capacity limit. The decoding of LDPC codes is based on message-passing iterative algorithms, where messages are passed along the edges of the Tanner graph of the code between the variable nodes and the check nodes. The process is iterated until all parity check equations are satisfied or until a predetermined number of iterations is reached. In case of hard decision decoding the algorithm is called bit flipping where each bit of the code is recalculated using the remaining bits using all the parity check equations and based on the majority logic of the outcomes of the parity check equations, that bit may be flipped or kept as it is. In case of soft decision the information passed along the edges of the Tanner graph represents the probability (or likelihood) that each parity check equation is satisfied according to the possible of the code bit 0 or 1. This algorithm is called belief propagation and has many variations like the sum product algorithm. Although the message passing algorithms are in fact suboptimal algorithms but their impressive performance in error correction gives them significant advantage over algebraic codes.

4. ENCODING OF LDPC CODES:

Although the decoding of long LDPC codes is manageable in term of complexity, the encoding in general presents a challenge. In coding theory, a linear code such as the LDPC codes, the length of the code is $n=k+m$ bits where k is the number of message bits and m is the parity bits, there is an $m \times n$ parity-check matrix H and a $k \times n$ generator matrix G such that $GH^T = \mathbf{0}$, where $\mathbf{0}$ is $k \times m$ zero matrix. If G is in systematic form then $G = [I_k \ P^T]$ where I_k is $k \times k$ identity matrix and P^T is the transpose of the $k \times m$ P matrix. The G matrix can be obtained by transforming the H matrix to the form $H = [P \ I_m]$, where I_m is $m \times m$ identity matrix and $GH^T = \mathbf{0}$ is satisfied. Now, if H is the parity

matrix of an LDPC code then it is a sparse matrix (low density) and by applying the elementary row operation to \mathbf{H} in order to get $\mathbf{H}=[\mathbf{P} \mathbf{I}_m]$, the result is that \mathbf{H} or particularly \mathbf{P} is no longer a sparse matrix and that produce a dense \mathbf{G} matrix **Moreira, and Farrell, 2006**. Therefore, if traditional brute force implementation of the encoding as $\mathbf{v}=\mathbf{u}\mathbf{G}$, where \mathbf{v} is the code vector and \mathbf{u} is the message vector, and if we assume that on average that the \mathbf{P} matrix has equal number of 1's and 0's, then the number of XOR gates needed for the encoding and the amount of storage required for storage of the \mathbf{P} matrix will be proportional to $k \times m$ or $(n-m) \times (n-k)$ that is almost proportional to n^2 and for very long codes this is a very big number that is impractical to implement. The alternative approach is that instead of encoding using the generator matrix \mathbf{G} , the parity check matrix \mathbf{H} is used for encoding, where the parity check equations are solved for the parity bits.

$$\mathbf{v}\mathbf{H}^T=\mathbf{0} \quad (2)$$

The first novel approach for solving the parity equations is by **Richardson and Urbanke** in 2001 where the \mathbf{H} matrix is decomposed using column permutation such that

$$\mathbf{H} = \begin{bmatrix} \mathbf{A} & \mathbf{B} & \mathbf{T} \\ \mathbf{C} & \mathbf{D} & \mathbf{E} \end{bmatrix} \quad (3)$$

Where \mathbf{T} is the largest lower triangular matrix that can be obtained using column permutations with dimensions $(m-g) \times (m-g)$ and \mathbf{E} is a $g \times (m-g)$ matrix. The form of the \mathbf{H} matrix is called Approximate Lower Triangle (ALT). The algorithm is based on making the value of g (called the gap) as small as possible and this can make the complexity proportional to $n+g^2$. Although Richardson's algorithm works just fine for small values of g , the problem is that not every \mathbf{H} matrix of LDPC codes can be decomposed into the form for Eq. (3) with small value of g by simple column permutations especially the quasi cyclic codes. In the case of QC-LDPC codes, the encoding can be performed using shift registers. **Li et al., 2006** presented an elegant approach for encoding QC-LDPC codes by first constructing the generator matrix in systematic form with block circulant structure. The block circulant structure of the generator matrix makes it possible to use shift registers that are loaded with the first row of the generator matrix and by circularly shifting its contents the remaining rows of the circulant block is generated. This saves the amount of the required storage and the number of XOR gates. Li presented two methods for constructing the generator matrix, the first is for a full rank parity matrix where the generator matrix is a block circulant matrix, the complexity in terms of storage, logic gates and number of clocks is provided. The second method is for a rank deficient parity matrix where the generator matrix is not fully block circulant and the complexity is increased but no metric for complexity for this case was provided. **Xia et al., 2008** proposed a method of construction of the \mathbf{H} matrix using permutation matrices in a way to further reduce the computations required by Richardson's method. **Freundlich et al. 2008** worked on constructing LDPC codes having ALT with $g=\sqrt{n}$ in order to make encoding complexity proportional to n . **Huang et al. 2014** used Galois Fourier Transform for encoding QC-LDPC codes. **Lu and Moura, 2010** presented the label and decide algorithm suitable for linearly encoding LDPC codes that have tree or pseudo-tree structures.

5. ENCODING OF QC-LDPC CODES

Given that the parity matrix \mathbf{H} is a block circulant matrix, which is given in the form

$$\mathbf{H} = \begin{bmatrix} \mathbf{A}_{11} & \mathbf{A}_{12} & \cdots & \mathbf{A}_{1b} \\ \mathbf{A}_{21} & \mathbf{A}_{22} & \cdots & \mathbf{A}_{2b} \\ \vdots & \vdots & \ddots & \vdots \\ \mathbf{A}_{a1} & \mathbf{A}_{a2} & \mathbf{A}_{a3} & \mathbf{A}_{ab} \end{bmatrix} = [\mathbf{H}_1 \quad \mathbf{H}_2] \quad (4)$$

Where \mathbf{H} is $a \times b$ array of sparse $q \times q$ circulant matrices $\mathbf{A}_{r,s}$ where $1 \leq r \leq a$ and $1 \leq s \leq b$ making \mathbf{H} a sparse QC parity matrix of dimension $aq \times bq$. The \mathbf{H} matrix is better partitioned as two parts $\mathbf{H} = [\mathbf{H}_1 \quad \mathbf{H}_2]$, the first part \mathbf{H}_1 is $(b-a) \times a$ array of circulants and the second part is $a \times a$ array of circulants and by applying the appropriate matrix operations, the \mathbf{H}_2 part is converted to the identity matrix and the \mathbf{H} matrix is transformed as $\mathbf{H} = [\mathbf{H}_1 \quad \mathbf{H}_2] \rightarrow [\mathbf{P} \quad \mathbf{I}_m]$ as discussed earlier.

Since the circulant matrix is the building block of the QC-LDPC parity matrix, it is worthwhile at this point to discuss its main properties, **Lu and Moura, 2010**. First the matrix multiplication is commutative, if \mathbf{A} and \mathbf{B} are circulants then $\mathbf{AB} = \mathbf{BA}$. Second the circulant matrix is characterized by its first row which is called the generator row, the subsequent rows are simply the circular shift of this generator row. If the generator row consists of one nonzero element, then each row and column will have only one nonzero element and circulant will be a permutation matrix and it is called circulant permutation matrix CPM. If the generator row is represented as a polynomial of x where the powers of x are the position and the coefficients are the elements of the generator row, then there will be a one-to-one mapping between circulants and binary polynomials, and the matrix addition and multiplication is replaced by polynomial addition and multiplication modulo $x^q + 1$. This is called isomorphism where mathematically it is represented by, **Joyner, et al. 2004**

$$\phi(\mathbf{A}) + \phi(\mathbf{B}) = \phi(\mathbf{A} + \mathbf{B}) \quad (5a)$$

$$\phi(\mathbf{A}) \times \phi(\mathbf{B}) = \phi(\mathbf{A} \times \mathbf{B}) \quad (5b)$$

Where $\phi(\cdot)$ is any one-to-one onto mapping. The polynomial ring is referred to as $GF_2[x]/[1+x^q]$, where GF_2 represent the binary field $\{0,1\}$. In a ring not every element has an inverse, therefore if α and β are elements of a ring and $\alpha\beta=0$, it is possible to have $\alpha \neq 0$ and $\beta \neq 0$, in this case α and β are called zero-divisors and zero-divisors do not have multiplicative inverse. In our case of binary polynomials $GF_2[x]/[1+x^q]$ there are some examples of zero-divisor polynomials like **Lu and Moura, 2010**

$$\gamma(x)(1 + x + x^2 + \dots + x^{q-1}) = 0 \quad (6)$$

Where $\gamma(1)=0$ which means that $\gamma(x)$ has even number of terms, here both polynomials multiply to zero meaning that both polynomials are zero-divisors and hence have no inverses and the corresponding circulants will be rank deficient. Another example is

$$(1 + x^p + x^{2p} + \dots + x^{q-p}) \tag{7}$$

Where p is a divisor of q , here shifting by p positions will generate the same polynomial and the corresponding circulant will have repeated rows and hence will be rank deficient. The fact that rings having elements with no multiplicative inverse makes the equation

$$\alpha x = \beta \tag{8}$$

Does not always have a solution where α and β are elements of a ring. Interestingly Eq. (8) can have a solution even though the element α does not have a multiplicative inverse but for a certain condition. To see this, consider the ring of integers modulo- n (mathematically referred to as Z/Z_n) where n is any integer. Equation (8) can now be written as **Joyner, et al. 2004**

$$\alpha x = \beta \text{ mod } n$$

$$\alpha x - \beta = qn$$

$$\alpha x - qn = \beta$$

The above equation can have a solution if $\text{gcd}(\alpha, n)$ divides β **Meyer, 2000**, where $\text{gcd}(\alpha, n)$ is the greatest common divisor of α and n . Note, as a special case, if n is a prime then the ring becomes a field and every element has a multiplicative inverse and Eq. (8) always have a solution, on the other hand $\text{gcd}(\alpha, n)=1$ which always divides β . Although this result is shown to apply to ring of integers, it also applies to ring of polynomials and hence circulants and the condition of Eq. (8) to have a solution modifies to $\text{gcd}(\alpha(x), x^f+1)$ divides $\beta(x)$ where $\alpha(x)$ and $\beta(x)$ are the generator polynomials of the circulants α and β . From the above it can be seen that Eq. (8) can have a solution even if the circulant α is not a full rank matrix, but still there is no guarantee that Eq. (8) always has a solution. In general it is desirable to transform the H matrix into the form given by Eq. (9) using elementary row operations.

$$H = [P \quad I_{aq}] = \begin{bmatrix} P_{1,1} & P_{1,2} & \dots & P_{1,(b-a)} & I_q & \mathbf{0} & \dots & \mathbf{0} \\ P_{2,1} & P_{2,2} & \dots & P_{2,(b-a)} & \mathbf{0} & I_q & \dots & \mathbf{0} \\ \vdots & \vdots & \ddots & \vdots & \vdots & \vdots & \ddots & \vdots \\ P_{a,1} & P_{a,2} & \dots & P_{a,(b-a)} & \mathbf{0} & \mathbf{0} & \dots & I_q \end{bmatrix} \tag{9}$$

Where $P_{r,s}$ are $q \times q$ block circulant matrices, $1 \leq r \leq a$, $1 \leq s \leq b-a$, I_q is an $q \times q$ identity matrix and $\mathbf{0}$ is the all zero matrix, P is an $a \times (b-a)$ array of circulant. It can be seen from the transformed form of H in Eq. (9) that the H matrix is a full rank matrix, i.e., $\text{rank}=aq$. The form of Eq. (9) can only be obtained if the original parity matrix H in Eq. (4) is a full rank matrix **Li et al., 2006**, and this is true

if the partition matrix H_2 is invertible and hence $P=H_1H_2^{-1}$. In terms of polynomials if $h_2(x)$ is the matrix of polynomial corresponding to the partition of circulants H_2 , then H_2 is invertible if and only if $\det[h_2(x)]$ is not a zero-divisor, **Lu and Moura, 2010**. An example of such matrix is shown in **Fig. 2** where the 1's are shown as black dots.

The QC-LDPC code can be encoded using Linear Feedback Shift Registers (LFSR) and simple logic circuits. Since for the case of a full rank QC parity check matrix H , the P matrix is also QC and this makes it possible to store only the generator row of each $P_{r,s}$ circulant in a shift register (SR) and generating the remaining rows by cyclically shifting the SR contents. Therefore the H matrix in Eq. (9) can be reduced to an $a \times (b-a)$ array of $1 \times q$ vectors by taking the generator rows $p_{r,s}$ of the circulants $P_{r,s}$ and the result is an $r \times (b-a)q$ parity generator matrix PG as below

$$PG = \begin{bmatrix} P_{1,2} & P_{1,2} & \cdots & P_{1,(b-a)} \\ P_{2,1} & P_{2,2} & \cdots & P_{2,(b-a)} \\ \vdots & \vdots & \ddots & \vdots \\ P_{a,1} & P_{a,2} & \cdots & P_{a,(b-a)} \end{bmatrix} \tag{10}$$

The remaining rows of the circulants $P_{r,s}$ can be expressed as the cyclic shift of $p_{r,s}$ denoted as $p_{r,s}^{(t)}$ where t is the shift, $0 \leq t \leq q$, and $p_{r,s}^{(0)} = p_{r,s}^{(q)} = p_{r,s}$.

By representing the codeword in systematic form as $c=[u \ v]$ where u is the message bits vector of length $q(b-a)$ bits and v is the parity bits vector of length aq bits, the problem of encoding reduces to evaluating the v vector. Since each codeword c satisfies the parity equations given by the H matrix, then $cH^T=[u \ v] [P \ I_m]^T=0$, so $v=uP^T$. Using the form of the H matrix in Eq. (9), the parity bits v_i , $1 \leq i \leq m=aq$ can be expressed in terms of the message bits u_j , $1 \leq j \leq k=n-m=(b-a)q$ as

$$v_i = \sum_{j=1}^{(b-a)q} u_j p_{i,j} \quad 1 \leq i \leq aq \tag{11}$$

Where v_i is the i^{th} parity bit of the vector v and $p_{i,j}$ is the matrix element in the i^{th} row and j^{th} column of the matrix P . The direct realization of Eq. (11) is referred to as brute force realization, it is inefficient in terms of cost and it is general to any structure of the parity matrix H . An efficient realization of Eq. (11) would obviously require the utilization of the QC structure of the parity matrix P . This suggests dividing both the message vector u and the parity vector v into blocks of size q resulting in $(b-a)$ q -size message blocks u_s , $1 \leq s \leq b-a$, $u=[u_1 \ u_2 \ \dots \ u_{b-a}]$ and a q -size parity blocks v_r , $1 \leq r \leq a$, $v=[v_1 \ v_2 \ \dots \ v_a]$. According to this, Eq. (11) can be rewritten as

$$v_i = \sum_{s=1}^{b-a} u_s [p_{r,s}^{(t)}]^T = \sum_{s=1}^{b-a} w_{r,s,t} \tag{12}$$

$$i = (r-1)q + t + 1$$

Where $1 \leq r \leq a$, $0 \leq t \leq q-1$, and the notation $[\]^T$ is used for transpose. From Eq. (12), the r^{th} block of the parity vector \mathbf{v}_r is obtained by fixing r and incrementing the shift index t from 0 to $q-1$. Note that the product inside the summation is a row-vector product and can be expressed as

$$w_{r,s,t} = \mathbf{u}_s [\mathbf{p}_{r,s}^{(t)}]^T = \sum_{\ell=1}^q u_s^\ell p_{r,s}^{(t),\ell} \tag{13}$$

Where u_s^ℓ is the ℓ^{th} element of the block vector \mathbf{u}_s , $1 \leq \ell \leq q$, and $p_{r,s}^{(t),\ell}$ is the ℓ^{th} element of the generator row $\mathbf{p}_{r,s}$ after shifting t positions. The quantity $w_{r,s,t}$ represents the partial sums generated by Eq. (13) which will be summed by Eq. (12) to produce the respective parity bit. The circuit implementation of Eq. (13) is shown in **Fig. 3** and it is the building block of the encoder, it consists of a shift register and modulo-2 adder (XOR), so it is referred to as shift register-adder (SRA) and it is one of the encoder implantation adopted by Li **Li, et al., 2006**. The overall encoder implementation is shown in **Fig. 4**, the number of the SRA's in the encoder will equal to $b-a$ blocks, each block will be parallel loaded a times with the generator rows of the r^{th} row of the \mathbf{PG} matrix and shifted $q-1$ times. The contents are multiplied by the message vector \mathbf{u} and the results are added modulo- 2 (XOR) to generate parity bit p_i with every clock cycle, which will be a total of $m=aq$ which is the number of the parity bits. In case of rank deficient \mathbf{H} matrix there will be more SRA's as will be shown later.

6. PARITY MATRIX WITH RANK DEFICIENCY

Transforming a QC sparse rank-deficient parity matrix as in **Fig. 5** into the form of Eq. (9) results in a random \mathbf{P} matrix and not a block circulant as in **Fig. 6**. In this case, there will be no way of efficient implementation of the encoding of the corresponding LDPC code. The main aim of this paper is to present an algorithm that transforms the \mathbf{H} matrix into a form that is as close as possible to the form of Eq. (9) while maintaining the QC structure. This will make it possible to make the encoding using the circuit of **Fig. 4** with some modifications. Specifically speaking, a rank deficient \mathbf{H} matrix cannot be diagonalized while keeping the QC structure and since the latter is more important, the goal will be to make \mathbf{H}_2 matrix a sparse lower triangular matrix, so the parity bits can be evaluated in back substitution manner. The core of the approach of this paper is to work the Gauss-Jordan elimination on circulant blocks rather than on individual bits. This is to guarantee that the \mathbf{H} matrix remains in the QC format because the result of addition and multiplication of circulants is also a circulant this is obvious from the circulant-polynomial isomorphism. Since in this case the \mathbf{H} matrix is rank deficient, it is expected that there is a number of redundant parity equation and a number of redundant (free) parity bits. The application of Gaussian elimination algorithm on bit level will make the matrix in reduced echelon form **Meyer, 2000** where some of the diagonal elements are zeros and some rows will be an all zero row. The column positions of the zero diagonal elements correspond to the free parity bits or simply free bits and basically can be used as message bits. The all zero rows represent the redundant parity equation.

The application of Gauss-Jordan algorithm on circulant block level to \mathbf{H} matrix in order to diagonalize the \mathbf{H}_2 matrix, two objectives are needed to be accomplished

1- Set every block $A_{r,s}$ above and below the block diagonal of \mathbf{H}_2 (i.e. $s \neq r+b-a$) to all zero matrix. This is equivalent to solving the matrix equation

$$\mathbf{AX} = \mathbf{B} \tag{14}$$

for the \mathbf{X} matrix where \mathbf{A} is a diagonal block of \mathbf{H}_2 ($\mathbf{A}_{r,r+b-a}$) and \mathbf{B} is nondiagonal block that is in the same column i.e $\mathbf{B}=\mathbf{A}_{k,r+b-a}$, $k \neq r$. So, by applying the elementary row operation

$$\mathbf{H}_{k,:} = \mathbf{H}_{k,:} + \mathbf{H}_{r,:} \mathbf{X} \quad (15)$$

The $\mathbf{A}_{k,r+b-a}$ block will be eliminated. Here the notation $\mathbf{H}_{k,:}$ means the k^{th} row of the matrix \mathbf{H} .

2- Set every block on the diagonal ($\mathbf{A}_{r,r+b-a}$) to the identity matrix \mathbf{I}_q . This is equivalent to solving the equation

$$\mathbf{A} \mathbf{X} = \mathbf{I}_q \quad (16)$$

For the \mathbf{X} matrix where \mathbf{A} is a diagonal block $\mathbf{A}_{r,r+b-a}$. By applying the elementary row operation

$$\mathbf{H}_{r,:} = \mathbf{H}_{r,:} \mathbf{X} \quad (17)$$

The $\mathbf{A}_{r,r+b-a}$ block is converted to the identity matrix. Because the elementary row operations involved in the steps above are applied on the block circulant level, the blocks $\mathbf{A}_{r,s}$ remain circulants and hence maintain the QC structure of the \mathbf{H} matrix. If the solutions, \mathbf{X} , of Eqs. (14) and (16) exist for each step, the \mathbf{H} matrix will be converted to the form of Eq. (9) and the circuit of **Fig. 4** can be used for the encoding. Solving Eqs. (14) and Eq. (16) is performed by augmenting the matrix \mathbf{A} and the first column of matrix \mathbf{B} and \mathbf{I}_q respectively and performing Gauss-Jordan elimination. After diagonalizing matrix \mathbf{A} , the last column of the augmented matrix will be the first column of matrix \mathbf{X} and the remaining columns of matrix \mathbf{X} is generated by circular shifts of the first column. This is explained in Eq. (18) below

$$[\mathbf{A} \mid \mathbf{B}_{:,1}] \rightarrow [\mathbf{I}_q \mid \mathbf{X}_{:,1}] \quad (18a)$$

$$[\mathbf{A} \mid \mathbf{I}_{q,1}] \rightarrow [\mathbf{I}_q \mid \mathbf{X}_{:,1}] \quad (18b)$$

Unfortunately, for a rank-deficient \mathbf{H} matrix, the solution of Eqs. (14) and (16) does not exist for all the steps and hence the \mathbf{H} matrix cannot be reduced to the form of Eq. (9). In order to evaluate the parity bits in a cost efficient manner, the \mathbf{H} parity matrix will be transformed as below

$$\mathbf{H} = [\mathbf{H}_1 \quad \mathbf{H}_2] \rightarrow [\mathbf{P} \quad \mathbf{T}] \quad (19)$$

Where \mathbf{P} is the dense parity matrix in a block circulant form and \mathbf{T} is a sparse lower block triangular matrix also in block circulant form. The parity bits are evaluated in terms of the message bits and the previously evaluated parity bits unlike the work presented by **Li et al., 2006** where the parity pits are evaluated in terms of the message bits only.

In order to evaluate the parity bits, the location of the free parity bits must be determined in advance and this is achieved by applying Gauss-Jordan elimination to the \mathbf{H} matrix on the bit level and the free parity bits are identified where there is a zero pivot. The column indices of the matrix \mathbf{T} where

the free bits appear are stored in the set FP. The location and number of the free parity bits are used to define two vectors, \mathbf{fn} and \mathbf{fl} . The vector $\mathbf{fn}=[fn_1, fn_2, \dots, fn_a]$ is $1 \times a$ vector where a is the number of block columns of the \mathbf{T} matrix, the components of \mathbf{fn} are the number of free bits in each block column of the \mathbf{H}_2 matrix. The vector $\mathbf{fl}=[fl_1, fl_2, \dots, fl_{qa}]$ is $1 \times aq$ vector and it is a q fold extension of the \mathbf{fn} vector, i.e. each component of the \mathbf{fn} vector is repeated q times in the \mathbf{fl} vector. To explain this, consider the example where \mathbf{H} is an array of 3×6 circulants each circulant is a 10×10 matrix. This makes the \mathbf{H}_2 matrix to have 3 block columns and 30 bit columns, so the \mathbf{fn} and \mathbf{fl} vectors will have 3 and 30 components respectively. Assuming that two free bits appeared in the 1st and 11th columns of the \mathbf{H}_2 matrix, then $FP=\{1,11\}$, and since $q=10$, this means that the 1st and 2nd block columns of \mathbf{H}_2 each has one free bit and the 3rd does not have any, so $\mathbf{fn}=[1 \ 1 \ 0]$. The first 20 components of \mathbf{fl} , fl_1-fl_{20} , will be all 1's and the last 10 components, $fl_{21}-fl_{30}$ will be all 0's. It has been mentioned earlier that the Gauss-Jordan elimination is implemented starting from last column instead of the first and this makes the free parity bits to appear in the beginning of each block column. These definitions help in relating the parity bit index to the respective row index of the \mathbf{H} matrix which is actually the equation used to evaluate the parity bit. This is because of the presence of the free bits; the evaluated parity bit will no longer have the same index which is represented as i in Eq (11). So, Eq. (11) will be modified to

$$v_i = y_i + z_i = \sum_{j=1}^{(b-a)r} u_j p_{i,j} + \sum_{k=1}^{i-1} v_k t_{i,k} \quad 1 \leq i \leq aq \quad i \notin FP \tag{20}$$

Where

$$i' = i - fl_i \tag{21}$$

Eq. (21) gives a correction factor for relating the evaluated parity bit and the evaluating parity equation, so the example above will have the parity bits evaluated as follows: the parity bits 1 and 11 are not evaluated as they are free, parity bits 2-10 and 12-20 will use equations 1-9 and 11-19 respectively ($i=i'-1$), equations 10 and 20 are redundant and parity bits 21-30 will use equations 21-30 ($i=i'$). The temporary variables y_i and z_i correspond to the first and second summation of Eq. (20) respectively and they will help in the encoder description later. The bits components v_k in the second summation are not all parity bits, some of them are the free bits that can either be extra message bits or simply set to zero according to the designer's preference, they are given the same parity bits notation only as a matter of convenience. Because the matrix \mathbf{T} is a sparse matrix as will be seen in the results section, the summation over k actually does not involve many computations as it might seem, since only few entries $t_{i,j}$ are nonzero.

The algorithm of converting the \mathbf{H} matrix in the form of Eq. (19) is presented by the steps below.

1- Locating the free bits: As explained earlier, the free bits are used as extra message bits, in this case the coding rate will be

$$R = \frac{k}{n} = \frac{(b-a)q + n_{fp}}{bq} = 1 - \frac{a}{b} + \frac{n_{fp}}{bq} \tag{22}$$

Where n_{fp} is the total number of the free parity bits. Gauss-Jordan algorithm is applied to the \mathbf{H} matrix on the bit level to diagonalize \mathbf{H}_2 and after identifying the free bits; FP , \mathbf{fn} and \mathbf{fl} are determined as described earlier. The diagonalization of \mathbf{H}_2 may not be so straightforward, because $\text{rank}(\mathbf{H}_2)$ should be equal to $\text{rank}(\mathbf{H})$, if it is not, then column permutations is performed on the block level to preserve the QC structure of the \mathbf{H} matrix. In order to have $\text{rank}(\mathbf{H}_2)=\text{rank}(\mathbf{H})$, any all zero row in \mathbf{H}_2 there should be a corresponding all zero row in \mathbf{H}_1 .

2- Pivoting: For the s^{th} column, $b-a+1 \leq s \leq b$, find the block circulant $A_{k,s}$, $1 \leq k \leq a$, whose rank is maximum and move it to diagonal position by making block row interchange between the k^{th} block row and the r^{th} block row where $r=s-(b-a)$.

3- Solve Eq. (14) using Gauss-Jordan elimination: Because of the pivoting performed in the previous step, the possibility for having a solution for Eq. (14) is maximized since in this case the circulant \mathbf{A} will have the maximum possible number of linearly independent rows and hence minimum number of linearly dependent rows that will be reduced to all zeros rows when transforming the augmented matrix $[\mathbf{A}|\mathbf{B}_{:,1}]$ to the reduced echelon form, and it is known that the system $[\mathbf{A}|\mathbf{B}_{:,1}]$ is consistent if a row of the form, **Meyer, 2000.**

$$[0 \ 0 \ 0, \dots, 0 \ | \ x], \ x \neq 0 \tag{23}$$

Never appears. If Eq. (14) fails to have a solution for at least one block $A_{r,s}$, the s^{th} column of the is permuted with a block column in the left side of \mathbf{H} . This column permutation is repeated so that Eq. (14) should have a solution for all circulants above the diagonal position in order to have all blocks circulant above the diagonal are eliminated by the next step, this is necessary to transform \mathbf{H}_2 to the lower block triangular matrix \mathbf{T} . The column permutation of this step must be performed in accordance with the column permutations in the first step such that if step 1 and step 3 require column permutation at block columns s_1 and s_2 respectively with $s_1 > s_2$, the column permutation at s_1 is performed. The column permutation is performed with a left side (lower index) column; the algorithm is stopped and started all over.

5- Elimination of blocks above and below the diagonal: For every column in \mathbf{H}_2 , this process is performed $a-1$ times using Eq. (15). This step is very much related to the previous step because it depends on the solution of Eq. (14).

6- Transform the diagonal blocks to identity matrix: This is performed by Solving Eq. (16) using Gauss-Jordan elimination. This step is very much like step 3 but with different purpose, here it is required to find the matrix \mathbf{X} that is the inverse of the diagonal matrix ($A_{r,r+b-a}$) and by multiplying the rows by the inverses of the diagonal blocks (with the elimination step) the \mathbf{H}_2 matrix is converted to a diagonal matrix, but that does not happen if \mathbf{H} is rank deficient and in this case some of the diagonal blocks will be rank deficient. If a diagonal block is rank deficient, it does not mean that it should be left as it is because it is no longer sparse due to the row operations of step 4. Since we know that there are free bits located in the \mathbf{H}_2 matrix and these free bits are located by the first step, then the entries of the row generator of the diagonal block corresponding to these free bits need to be set to 1's in order to be taken into account in the evaluation of the parity bit that comes next to these free bits. The polynomial of the generator row of the diagonal of \mathbf{T} should be

$$t_{r,r} = \sum_{i=0}^{n_{fr}} x^i \tag{24}$$

Note that if the r^{th} column of the H_2 (or T) matrix does not have free bits then $n_{f_r}=0$ and hence the polynomial in Eq. (24) reduces to the polynomial of the identity matrix which is 1. The augmented column of Eq. (16b) is modified accordingly; this will make Eq. (16) to have a solution.

Due to the rank deficiency of the H matrix and the presence of the rank deficient circulants in the block diagonal positions, it is expected that not all nondiagonal block circulants are eliminated even after exhausting all possible column permutations in step 3, but it is still possible that the H_2 matrix can be transformed into the T matrix. Now by looking at Fig. 7 where the H matrix for two typical different cases is shown, important common features can be observed upon which the circuit implementation shown in Fig. 8 is made as described below.

- 1- The P matrix is a dense block circulant matrix and it corresponds to the temporary variable y_i shown in Eq. (20). The implementation of this part is similar to the implementation of the full rank case shown in Fig. 4.
- 2- In the T matrix, the diagonal blocks corresponding to the columns where there are free bits, there is no identity matrix, instead there are multiple parallel bit level diagonals which are consequence of Eq. (24). The number of these diagonal blocks is denoted by d . For this part, the corresponding temporary variable z_i given by Eq. (20) can be expressed as.

$$z_i = \sum_{k=i-fn_r}^{i-1} v_{(r-1)q+k} \tag{25}$$

Where $i=(r-1)q+t, fn_r+1 \leq t \leq q-1, 1 \leq r \leq d$. Equation (25) is a reduced form of the second summation in Eq. (20) where the positions of 1's only are taken into account. An important case is that when there is only one free bit per block column, in such case $d=n_{fp}, fn_r=1$ and Eq. (25) reduces to

$$z_i = v_{(r-1)q+i-1} \tag{26}$$

The implementation of this part is made by first parallel loading the free bits corresponding to r^{th} block column of T into the first SR and after evaluating the current parity bit $v_i=y_i+z_i$ using the left summator, it will be serially shifted into the SR for the evaluation of the subsequent parity bit and so on until the SR is full. This is repeated d times and the parity bits are linearly shifted continuously into the subsequent SR's until all the d SR's are full, the parity bits will appear in reverse order in the SR's as shown in Fig. 8.

- 3- There are nonzero block circulants below the d rank deficient diagonal blocks mentioned above. These circulants that are not eliminated can be either dense as in Fig. 7a or sparse as in Fig. 6b. These nonzero block circulants appeared in one row for all the LDPC codes tested by this algorithm. To evaluate the parity bits in the next block column ($r=d+1$), the previously evaluated parity bits will be required which are now all stored in the SR's from the previous step. Noting that the subsequent column has no free bits and the diagonal block is identity matrix, the evaluation of the temporary variable z_i is made by adding the previously evaluated parity bits that correspond to the nonzero pits in these nonzero circulants of T that are not eliminated

$$v_i = y_i + z_i = y_i + \sum_{\substack{k=1 \\ i,k=1}}^{dq} v_k \quad dq+1 \leq i \leq (d+1)q \quad i \notin FP \quad (27)$$

These nonzero positions can be picked up by hardwiring and directly added by XOR gates without using AND gates, these hardwiring are shown as random taps in **Fig. (8)** taken from the SR's to the right summator. The block circulant structure of T is employed such that the contents of the SR's are now circularly shifted in order to generate the subsequent rows of the respective circulants of T . A 2-to-1 multiplexers are used in the input of the SR's in order to control the choice of linear shifting and the circular shifting and also to control the evaluation of v_i according to Eq. (25,26) or Eq. (27), all multiplexers have a common control signal x . The complexity of this part is not much affected by the nonzero circulants being sparse or dense as long as they appear in one row since hardwiring is used. If more than one row appears with non zero circulants in the T matrix, AND gates will be needed as used in the SRA described earlier. The cases that were considered in this work have all resulted in a single nonzero block row in the T matrix, which suggest the using of hardwiring and no AND gates are needed for the implementation of the z_i part.

4- The next diagonal blocks where $d+2 \leq r \leq a$ are identity matrices and all circulants to the left are zero circulants, therefore $z_i=0$ and hence $v_i=y_i$ and no further process is needed.

7. RESULTS

Before discussing results, the construction of a QC-LDPC code is presented. In general the construction of QC-LDPC codes is based on finite fields or finite geometry. The codes used in this work are based on finite field and the construction is explained as follows, **Ryan and Lin, 2009**: Let $GF(p)$ be a finite field of p elements where p is a prime number or a power of a prime. Let α be a primitive element of the field such that every nonzero element can be represented as α^i where $0 \leq i < q=p-1$ with the special case of $0 = \alpha^{-\infty}$ by convention. Define the $1 \times q$ vector

$$\delta(\alpha^i) = [\delta_0 \ \delta_1 \ \dots \ \delta_{q-1}] \quad (28)$$

where $\delta_i=1$ and the remaining $q-1$ components are all zeros, this is called the location vector of the element α^i and $\delta(0)$ is the all zero $1 \times q$ vector. Generate a $q \times q$ A matrix whose rows are the location vectors of the elements α^j $0 \leq j < q$. Note that the first row of A is the location vector of α^0 and the subsequent rows are each the right cyclic shift of the row above by one position. Now A is a circulant permutation matrix (CPM) assigned for each element of $GF(p)$ and it is called the dispersion matrix of the element α^i . It is clear that for any two different elements of $GF(p)$ their dispersion matrices are different CPM's over $GF(2)$. Now construct the circulant matrix

$$W = \begin{bmatrix} w_0 \\ w \\ \vdots \\ w_{q-1} \end{bmatrix} = \begin{bmatrix} 0 & \alpha - 1 & \alpha^2 - 1 & \cdots & \alpha^{q-1} - 1 \\ \alpha^{q-1} - 1 & 0 & \alpha - 1 & \cdots & \alpha^{q-2} - 1 \\ \alpha^{q-2} - 1 & \alpha^{q-1} - 1 & 0 & \cdots & \alpha^{q-3} - 1 \\ \vdots & \vdots & \vdots & \ddots & \vdots \\ \alpha - 1 & \alpha^2 - 1 & \alpha^3 - 1 & \cdots & 0 \end{bmatrix} \quad (29)$$

Where the generator row $w_0 = \alpha^i - 1, 0 \leq i \leq q-1$, next replace each element of W by its respective dispersion CPM to obtain the array of CPM's

$$H_{qc,disp} = \begin{bmatrix} 0 & A_1 & A_2 & \cdots & A_{q-1} \\ A_{q-1} & 0 & A_1 & \cdots & A_{q-2} \\ A_{q-2} & A_{q-1} & 0 & \cdots & A_{q-3} \\ \vdots & \vdots & \vdots & \ddots & \vdots \\ A_1 & A_2 & A_3 & \cdots & 0 \end{bmatrix} \quad (30)$$

Where the CPM A_i is the dispersion matrix of the element $\alpha^i - 1, 0 \leq i \leq q-1$. $H_{qc,disp}$ is a $q \times q$ array of CPM's each of size $q \times q$ and the diagonal blocks are $q \times q$ matrices. The QC-LDPC code parity matrix H is taken as an $a \times b$ subarray from the $H_{qc,disp}$ matrix where $1 \leq a < b \leq q$, if this subarray is chosen such that it lies either above or below the main diagonal of $H_{qc,disp}$, then it contain no zero submatrix and hence will have a constant row and column weights and therefore will make a regular QC-LDPC code. The constructed QC-LDPC code satisfies the RC-constraint mentioned earlier and hence has a girth of at least 6, **Ryan and Lin, 2009**. The choice of the parameters a and b controls the choice of the code size ($n=bq$) and the code rate which is at least $(b-a)/b$. In this work the H matrix is chosen as the subarray from the bottom left corner of $H_{qc,disp}$, this will impose the condition $a+b \leq q$ in order to have a regular code, otherwise the code is irregular. The values of p are all chosen as prime numbers. **Table 1** below shows the chosen code parameters along with the amount of component needed by the circuit of **Fig. 8** in terms of number of FF's and XOR gates. It has been noticed that for all codes used in the result analysis that after the block diagonalization, the free bits are distributed such that there is one free bit in each block column, this means that $d=n_{fp}$. Different codes parameters are used for the analysis, the codes length ranges from $n=48$ to $n=5000$ with coding rate of $R=0.5$ to $R=0.72$. It has been assumed that the P matrix has an equal number of zeros and 1's and it will be taken as a benchmark for measuring the extra hardware required by the T matrix which is due to the rank deficiency of the matrix H . As discussed before there will be extra FF's and XOR gates needed to work on the part of the T matrix where there are some block circulants that are not eliminated. **Table 1** shows both the numbers of these FF's and XOR gates and there percentage relative to the number of FF's and XOR's needed by the P part. This is due to the fact that the effort required to implement the P matrix part is the same whether the H matrix is full rank or rank deficient. The number of FF and XOR gates needed by the P matrix according to the circuit implementation of **Fig. 4** is k and $k/2$ respectively because all the information bits are needed to be stored and the number of XOR gates equals the number of 1's (which are assume to equal the number of 0's) in the generator rows $p_{r,s}$. The number of FF's and XOR gates required by the T

matrix are shown under the column title FF and XOR respectively and their percentages are shown under the column titles δ_F and δ_X .

Table 1. The number of FF's and XOR gates needed to implement the T matrix part for QC-LDPC codes with different parameters.

Code Parameters						Results Parameters					Code Parameters						Results Parameters				
p	a	b	n	k	R	d	FF	XOR	δ_F	δ_X	p	a	b	n	k	R	d	FF	XOR	δ_F	δ_X
13	4	8	96	48	0.50	3	36	3	75.0	12.5	19	6	13	234	126	0.54	4	72	4	57.1	7.4
13	4	9	108	60	0.56	2	24	2	40.0	8.3	19	6	14	252	144	0.57	3	54	29	37.5	53.7
13	4	10	120	72	0.60	1	12	9	16.7	37.5	31	7	14	420	210	0.50	6	180	6	85.7	5.7
13	5	10	120	60	0.50	1	12	5	20.0	16.7	31	7	15	450	240	0.53	6	180	6	75.0	5.7
17	5	10	160	80	0.50	4	64	4	80.0	10.0	31	7	16	480	270	0.56	6	180	6	66.7	5.7
17	5	11	176	96	0.55	4	64	4	66.7	10.0	31	8	16	480	240	0.50	7	210	7	87.5	5.8
17	5	12	192	112	0.58	3	48	3	42.9	7.5	31	8	17	510	270	0.53	7	210	7	77.8	5.8
17	5	13	208	128	0.62	2	32	14	25.0	35.0	31	8	18	540	300	0.56	7	210	7	70.0	5.8
17	5	14	224	144	0.64	1	16	9	11.1	22.5	31	8	19	570	330	0.58	7	210	7	63.6	5.8
17	6	12	192	96	0.50	3	48	17	50.0	35.4	31	8	20	600	360	0.60	7	210	7	58.3	5.8
17	6	13	208	112	0.54	2	32	16	28.6	33.3	31	8	22	660	420	0.64	7	210	7	50.0	5.8
17	6	14	224	128	0.57	1	16	7	12.5	14.6	31	8	24	720	480	0.67	5	150	71	31.3	59.2
17	7	14	224	112	0.50	1	16	9	14.3	16.1	31	8	28	840	600	0.71	1	30	13	5.0	10.8
19	4	8	144	72	0.50	3	54	3	75.0	8.3	53	10	20	1040	520	0.50	9	468	9	90.0	3.5
19	4	9	162	90	0.56	3	54	3	60.0	8.3	53	15	50	2600	1820	0.70	1	52	21	2.9	5.4
19	5	10	180	90	0.50	4	72	4	80.0	8.9	53	15	30	1560	780	0.50	14	728	14	93.3	3.6
19	5	11	198	108	0.55	4	72	4	66.7	8.9	53	20	40	2080	1040	0.50	11	572	281	55.0	54.0
19	5	12	216	126	0.58	4	72	4	57.1	8.9	73	20	40	2880	1440	0.50	19	1368	19	95.0	2.6
19	5	13	234	144	0.62	4	72	4	50.0	8.9	73	25	50	3600	1800	0.50	21	1512	725	84.0	80.6
19	6	12	216	108	0.50	5	90	5	83.3	9.3	101	25	50	5000	2500	0.50	24	2400	24	96.0	1.9

It can be seen that the number of FF is directly proportional to the value of d and actually it equals dq , (see **Fig. 8**). The number of XOR gates is not exactly proportional to d because as has been mentioned earlier that the block circulant that has not been eliminated in the T matrix can be either dense or sparse and that affect the number of the XOR gates. A frequency analysis of the value δ_X shows that about 65% of the codes have the value of δ_X below 10%. This means that many codes have their T matrix with sparse nonzero block circulant which significantly reduces the number of XOR gates.

8. CONCLUSION

An encoding scheme of QC-LDPC codes that have rank deficient H matrix is presented. The low density block circulant H matrix is diagonalized on the block level so each parity bit is evaluated in terms of the message bits, free parity bits and the previously evaluated parity bits. In this way the parity bits can be evaluated serially. Extra logic is needed for the rank deficient case over the full rank case which is investigated and the results shows that QC-LDPC codes of certain parameters can have a very small amount of the extra logic compared to the overall required logic.



REFERENCES

- ▶ Andrews, K., Dolinar, S., and Thorpe, J., *Encoders for Block-Circulant LDPC codes*, IEEE International Symposium on Information Theory, 2005. ISIT, Australia, 2005.
- ▶ Freundlich, S, Burshtein, D., and Litsyn, S., *Approximately Lower Triangular Ensembles of LDPC Codes with Linear Encoding Complexity*, IEEE Transactions on Information Theory, Vol. 53, No. 4, April 2007.
- ▶ Gallager, R. G., *Low Density Parity-Check Codes*, IRE Trans. Information Theory, vol. 8, No. 1, pp. 21-28, January 1962.
- ▶ Huang, Q., Tang, L., He, S., Xiong, Z., and Wang, Z., *Low-Complexity Encoding of Quasi-Cyclic Codes Based on Galois Fourier Transform*, IEEE Transactions on Communications, Vol. 62, No. 6, June 2014.
- ▶ Hwang, S., and Lee, H., *Block-Circulant RS-LDPC Code: Code Construction and Efficient Decoder Design*, IEEE Transactions On Very Large Scale Integration (VLSI) Systems, Vol. 21, No. 7, July 2013.
- ▶ Joyner, D., Kreminski, R. and Turisco, J., *Applied Abstract Algebra*, Johns Hopkins Press, 2004.
- ▶ Li, Z., Chen, L., Zeng, L., Lin, S., and Fong, W. H., *Efficient Encoding of Quasi-Cyclic Low-Density Parity-Check Codes*, IEEE Trans. Communications, Vol. 54, No. 1, 2006.
- ▶ Lu, J. and Moura, J. M. F., *Linear Time Encoding of LDPC Codes*, IEEE Transactions on Information Theory, Vol. 56, No. 1, January 2010.
- ▶ MacKay, D., *Good Error Correcting Codes Based on Very Sparse Matrices*, IEEE Trans. Information Theory, Vol. 45, no. 3, pp. 399-431, March 1999.
- ▶ Meyer, C. D., *Matrix Analysis and Applied Linear Algebra*, SIAM, 2000.
- ▶ Moreira, J. C, and Farrell, P. G., *Essentials of Error-Control Coding*, John Wiley, 2006.
- ▶ Park, H., Hong, S., No, J. S. and Shin, D. J., *Protograph Design With Multiple Edges for Regular QC LDPC Codes Having Large Girth*, IEEE International Symposium on Information Theory Proceedings, St. Petersburg, 2011.
- ▶ Richardson, T. J. and Urbanke, R., *Efficient Encoding Of Low-Density Parity-Check Codes*, IEEE Trans. Information Theory, vol. 47, no. 2, pp. 638-656, February 2001.
- ▶ Ryan, W. E. and Lin, S., *Channel Codes Classical and Modern*, Cambridge University Press, 2009.
- ▶ Tao, X., , Zheng, L., Liu, W., and Liu, D., *Recursive Design of High Girth (2,k) LDPC Codes from (k,k) LDPC Codes*, IEEE Communications Letters, Vol. 15, No. 1, January 2011
- ▶ Song, S., Zhou, B., Lin, S., and Abdel-Ghaffar, K. *A Unified Approach to the Construction of Binary and Nonbinary Quasi-Cyclic LDPC Codes Based on Finite Fields*, IEEE Transactions on Communications, Vol. 57, No. 1, January 2009.
- ▶ Wang, Y., Draper S. C., and Yedidia, J. S, *Hierarchical and High-Girth QC LDPC Codes*, IEEE Transactions On Information Theory, Vol. 59, No. 7, July 2013.
- ▶ Xia, D, He, H., Xu, Y. and Cai, Y., *A Novel Construction Scheme with Linear Encoding Complexity for LDPC Codes*, IEEE 4th International Conference on Wireless Communications, Networking and Mobile Computing, 2008, China.

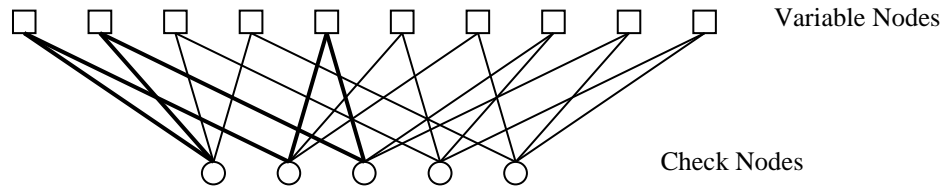


Figure 1. Tanner graph of girth equals to 6.

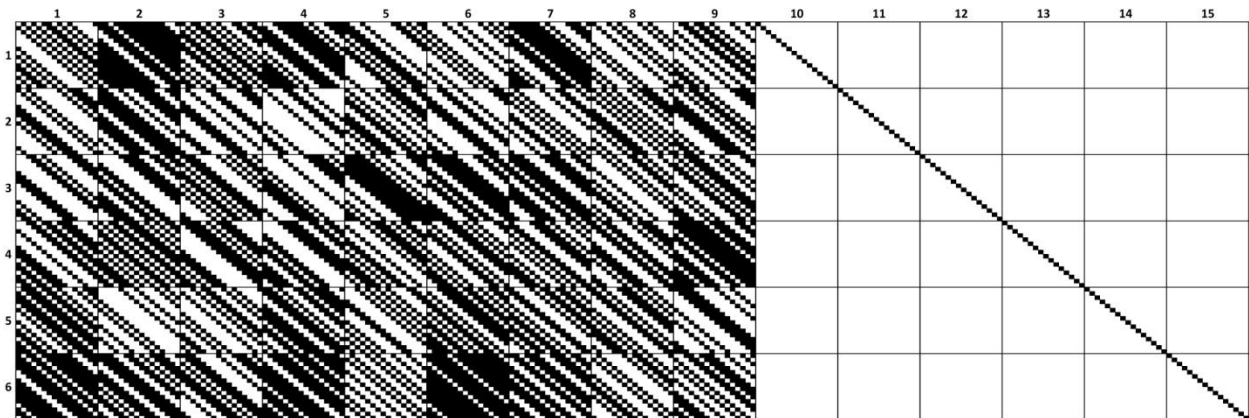


Figure 2. The diagonalization of a full rank QC parity matrix.

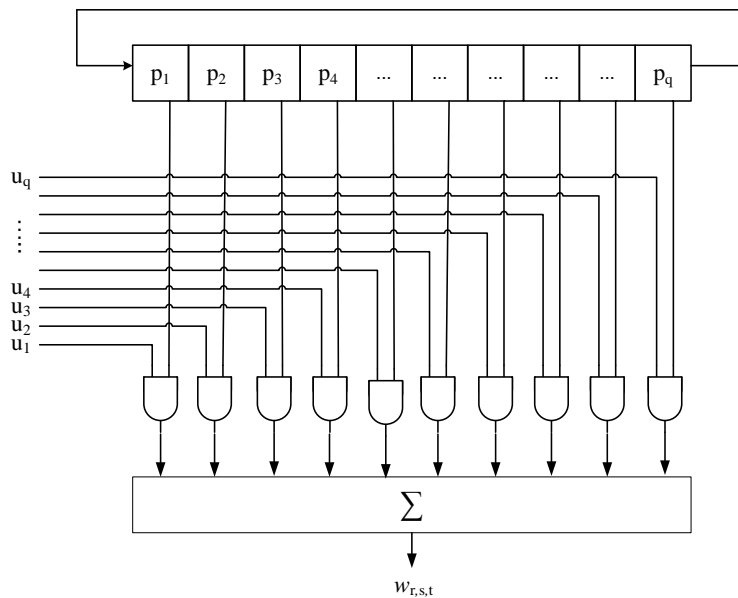


Figure 3. An SRA block of a QC-LDPC encoder.

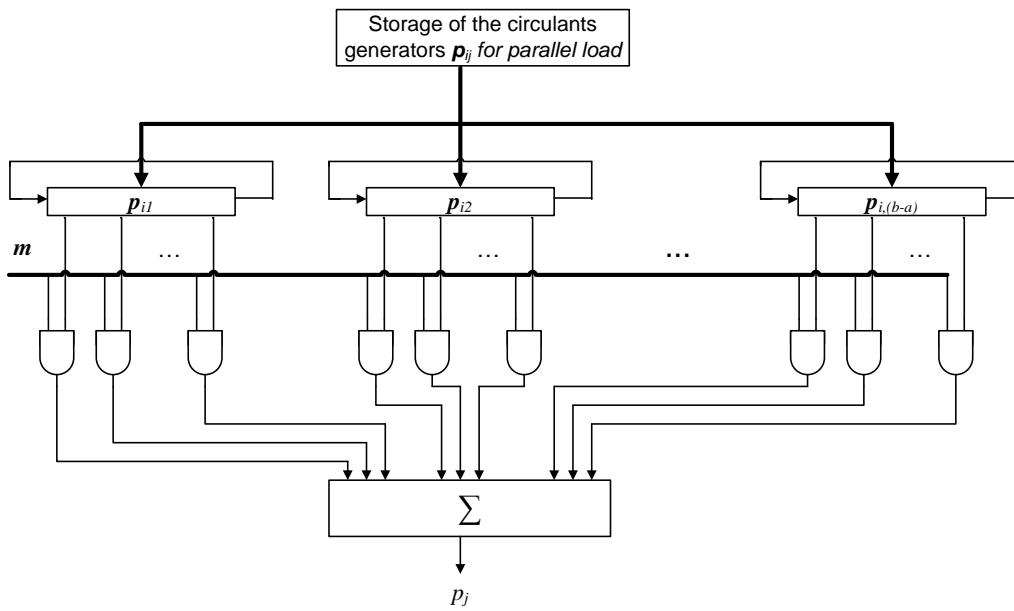


Figure 4. Encoder circuit of QC LDPC code with full rank parity matrix.

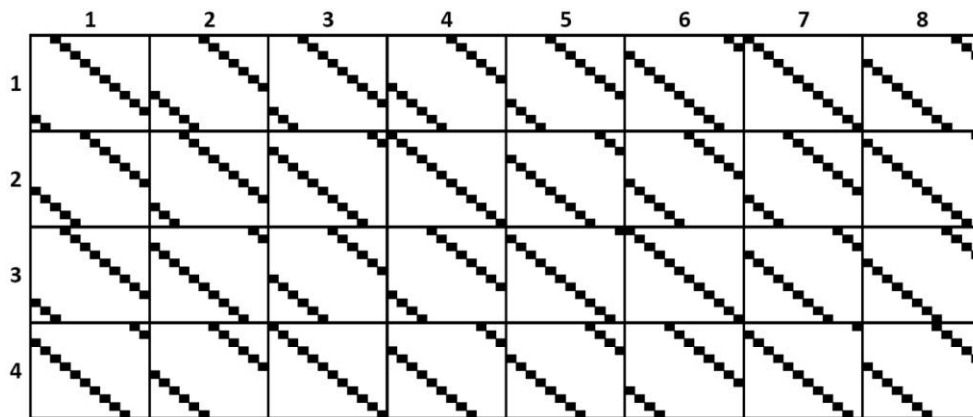


Figure 5. A QC parity matrix with rank deficiency.

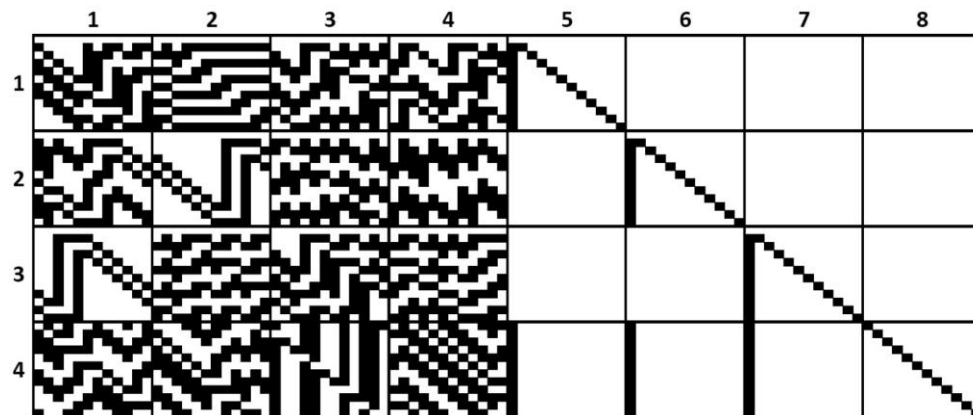
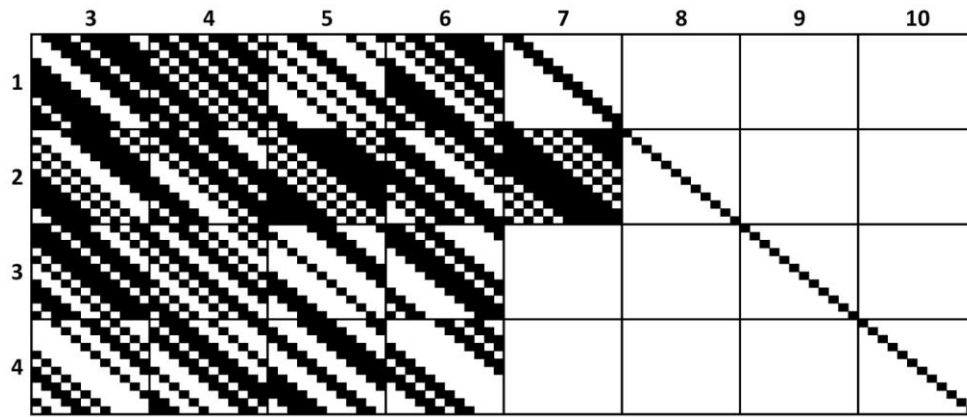
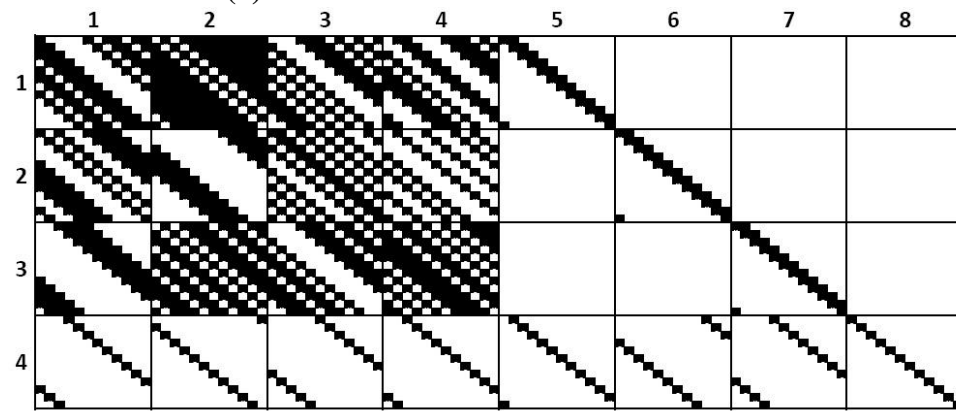


Figure 6. Bit level diagonalization of a rank deficient H matrix of Fig. 2.



(a) T matrix with nonzero dense circulant



(b) T matrix with nonzero sparse circulants

Figure 7. Block level diagonalization of a rank deficient H matrix.

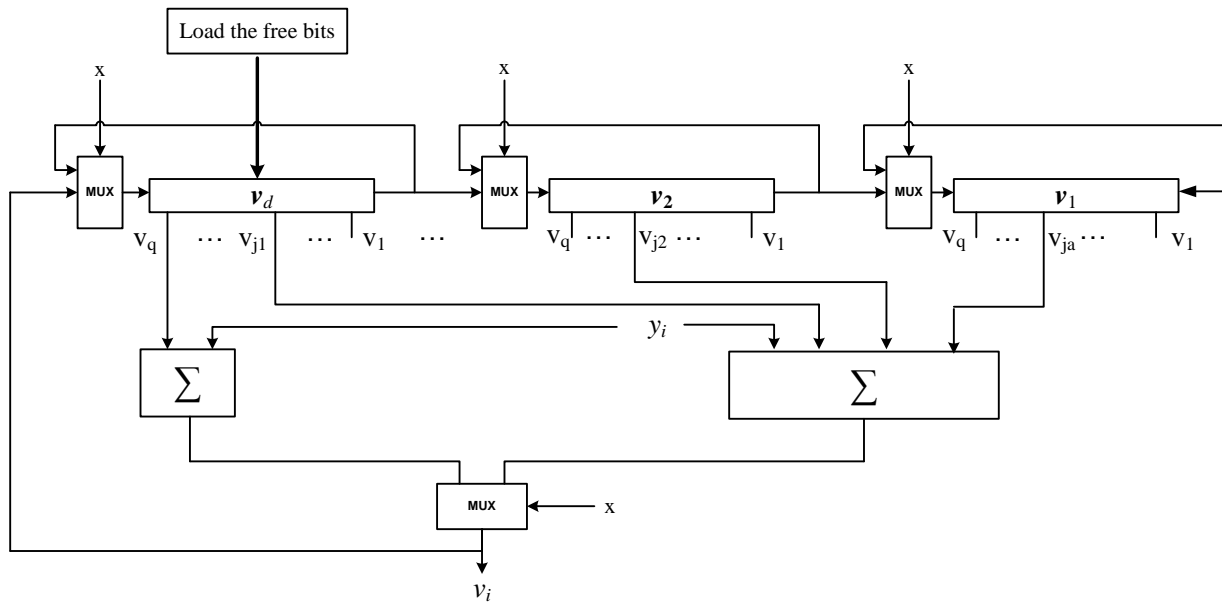


Figure 8. The encoder circuit of QC LDPC code with rank deficient parity matrix.

Numerical Investigation Using Harmonic and Transient Analysis To Rotor Dynamics

Prof. Adnan Naji Jameel Al Tamimi
Department of Mechanical Engineering
College of Engineering
University of Baghdad
Email: adnanaji2004@yahoo.com

Ph.D. Student. Jassim Farij Thiheel Al Draji
Department of Mechanical Engineering
College of Engineering
University of Baghdad
Email: jassim_aldrajy@yahoo.com

ABSTRACT

The rotor dynamics generally deals with vibration of rotating structures. For designing rotors of a high speeds, basically its important to take into account the rotor dynamics characteristics. The modeling features for rotor and bearings support flexibility are described in this paper, by taking these characteristics of rotor dynamics features into standard Finite Element Approach (FEA) model. Transient and harmonic analysis procedures have been found by ANSYS, the idea has been presented to deal with critical speed calculation. This papers shows how elements BEAM188 and COMBI214 are used to represent the shaft and bearings, the dynamic stiffness and damping coefficients of journal bearings as a matrices have been found with the variation of rotation speed of the rotor which are vary with eccentricity of journal with bearings and this eccentricity is a function of Sommerfeld number, the first critical speed analysis has been done from Campbell diagram, the critical speed it is the speed at which resonance case happen, the unbalance response analysis has been done with changing the unbalance mass then finding the maximum response of the rotor for each unbalance mass case, by Campbell diagram plot recognizing the stability of the system and find the line of un stability, above and down this line the system is stable and if speed lies on this line the system is unstable, the main reason of analysis of rotor dynamics is to help Engineers to characterize the lateral dynamics characteristics of a given design with Campbell diagram plot, can find the critical speed, the unbalance response and the system stability .

Key words: rotor dynamics, critical speed, unbalance response, stability

دراسة عددية للتحليل الحركي المتناسق والوقتي للمحور الدوار

طالب دكتوراه. جاسم فرج ثجيل الدراجي
قسم الهندسة الميكانيكية
كلية الهندسة / جامعة بغداد

استاذ. عدنان ناجي جميل التميمي
قسم الهندسة الميكانيكية
كلية الهندسة / جامعة بغداد

الخلاصة

ان حركة المحاور الدوارة بصورة عامة تتعامل مع اهتزازات الهياكل ، لغرض تصميم المحاور ذات السرعة العالية من المهم ان تأخذ بالحسبان الخصائص الحركية للمحور الدوار. ان مميزات تمثيل المحور مع المحامل ضمن المرونة قد درست في هذا البحث، وبأخذ هذه الخصائص عن طريق التحليل بواسطة الشريحة المحددة وقد وجدت طريقة للتحليل المتناسق والوقتي بواسطة ال ANSYS ، ان الفكرة الاساسية هي كيفية التعامل مع حسابات السرعة الحرجة وتم التبيان عن كيفية استخدام الشريحة نوع BEAM188 ونوع COMBI214 لتمثيل المحور الدوار والمحامل الهيدروليكية، ان النابضية والتخميد المتولدتان في المحامل نتيجة الحركة الدورانية كقيم مصفوفات تم ايجادها مع تغيير بالسرعة الدورانية والتي بدورها تتغير مع اللامركزية بين المحور والمحامل الذي يعمل معها وان هذه اللامركزية هي بالاساس دالة لرقم Sommerfeld، تم ايجاد السرعة الحرجة الاولى من مخطط Campbell وهي السرعة التي تحدث عندها حالة ال Resonance وكذلك تم ايجاد الاستجابة للمحور مع التغيير في كتلة عدم التوازن وايجاد اعلى استجابة لكل حالة من كتلة عدم التوازن وكذلك من خلال رسم مخطط Campbell تم تحديد منطقة الاستقرار حيث ان المناطق اسفل واعلى الخط الافقي الاول هي مناطق استقرار حركي اما اذا وقعت على الخط فان النظام غير مستقر، ان السبب الرئيسي للتحليل

الحركي للمحور الدوار هو لمساعدة المهندسين لمعرفة خصائص الحركة العمودية على مركز محور الدوران وبوجود مخطط Campbell ممكن ان نعرف السرعة الحرجة، استجابة النظام بوجود كتلة عدم التوازن واستقرارية النظام الحركي.
الكلمات الرئيسية: حركة المحور، السرعة الحرجة، استجابة عدم الاتزان، الاستقرارية.

1. INTRODUCTION

Because the rotors are wide used in industry like steam turbines, gas turbines, fans and stator of electric motors. The growth in power and more difficult design of turbomachines accompanied by higher requirements to their reliability. To increase the life of rotors is also one of the main targets to get better quality, modern computational method is used to determine strength and reliability characteristics. Generally the rotor dynamics is a main branch of engineering to studies the lateral and torsional vibrations of rotors with objective of expecting the rotor vibrations and containing the vibration level with acceptable limitations, the main components of a rotor dynamic system are the shaft of rotor with disk, the bearings and the seals, the shaft with the disk is the rotating part of the system **Nagaraju and Srinivas, 2014**.

Basically there are three types of vibrations associated with the motion of the rotor, axial, torsional and lateral vibrations. The axial vibration is the dynamics of the rotor in the axial direction while torsional vibration is the dynamics of the shaft in the rotational direction, basically this is very little influenced by the bearings that support the rotor and that is not a major problem, lateral vibration, the primary concern is the vibration of the rotor in lateral directions, **Abdul Ghaffar, at al., 2010**.

The bearings could be regarded as important parts in finding the lateral vibrations of the rotor, we will investigate the basic concepts of lateral dynamics of the rotor, with ever increase in demand for large size and speed in modern machines, rotor dynamics becomes more important in the mechanical engineering design. It is famous that torsional vibration in rotating machines, reciprocating machines installation and geared system, whirling of rotating shaft, the effect of flexible bearing, instability because of asymmetric cross-section shafts, hydrodynamics bearings, hysteresis, balancing of rotor can be understood only on the basis of rotor dynamics studies. Rotor dynamics is an important branch of the discipline of dynamics that pertains to the behavior of a huge assortment of rotary machines, **Maurice, 2010**. The aim of a standard rotor dynamics analysis and design checking is to help to characterize the transverse dynamic design characteristics but analysis of some rotary equipment may need analysis specific to the unit, a general method has used for performing the standard lateral analysis of vibration by using FEA with selected BEAM188 element for shaft and COMBI214 element for bearings in the ANSYS software.

2. FUNDAMENTAL EQUATIONS

2.1 Fluid Film Bearings

There are many parameters and physics phenomena that control the rotors apart from stationary structures but the main differences is the fluid film supports if we want to

understand the rotor dynamics as in **Fig.1**, In the past they were believe that the lubricant in the cavity of the bearing will decrease the friction and minimize the losses, and then they discovered that the fluid film doing many things more than the losses of the friction. If looking at **Fig.2**, the bearing center C and the journal center \tilde{C} will form an attitude of the bearing and makes the angle α with the vertical load (W), the clearance h will varying between two values.

From the bearing geometry and speed, eccentricity, pressure and attitude angle Sommerfeld derived such parameter to give an indication about the bearing eccentricity as, **Michael, et al.,2012**.

$$S = \frac{\mu DLN}{W} * \left(\frac{r}{h}\right)^2 \quad (1)$$

The radial and tangential forces F_r, F_t is

$$F_r = -\frac{D\Omega\mu L^3\epsilon^2}{2h^2(1-\epsilon^2)^2} \text{ and } F_t = -\frac{\pi D\Omega\mu L^3\epsilon}{8h^2(1-\epsilon^2)^{3/2}} \quad (2)$$

The force F_t opposes the sliding motion so that the power dissipation $F_t * \Omega D/2$, the resultant force on the bearing must be opposite to the load applied to the rotor.

$$F = \sqrt{F_r^2 + F_t^2} = \frac{\pi D\Omega\mu L^3\epsilon}{8h^2(1-\epsilon^2)^2} \left(\left(\frac{16}{\pi^2} - 1\right)\epsilon^2 + 1\right)^{1/2} \quad (3)$$

If the load on bearing is known then the modified Sommerfeld number is given by **Yukio and Toshio, 2012**.

$$S_s = \frac{D\Omega\mu L^3}{8fh^2} \quad (4)$$

These forces F_r and F_t are applied on both bearing bush and the journal, the tangential force F_t opposes the sliding motion so that the power dissipation is $F_t \Omega D/2$.The resultant force on the rotor (through the bush) must be equal and opposite to the load applied on the rotor, from Eq. (2), the magnitude of the resultant force as in Eq. (3), a vertical resultant force is common, where the load is due to the rotor weight; in this case, the position the journal takes in the bearing ensures that the load is indeed vertical. If the magnitude of this load is known, then the bearing eccentricity may be obtained by rearranging Eq. (3) to give Eq. (5), where S_s from Eq. (4) is called modified Sommerfeld number or Ocvirk number and is known for a particular speed, load, and oil viscosity, **Michael, et al.,2012**.

$$\epsilon^8 - 4\epsilon^6 + (6 - S_s^2(16 - \pi^2))\epsilon^4 - (4 + \pi^2 S_s^2)\epsilon^2 + 1 = 0 \quad (5)$$

The values of eccentricity ratio ϵ is equal $\frac{\bar{c}-c}{h}$ always taken between 0-1 so the value of ϵ has been found by iteration method from 0 to 6000 RPM by computer program of MATLAB.

When a linear bearing model is used in machine, the displacement should be checked to be small because a linear analysis does not include any constraints on the displacement, we considered only short bearing so the matrices is 2×2 for stiffness and damping matrices could be found as , **Michael, et al.,2012**.

$$K = \frac{F}{h} \begin{bmatrix} a_{xx} & a_{xy} \\ a_{yx} & a_{yy} \end{bmatrix} = \begin{bmatrix} K_{xx} & K_{xy} \\ K_{yx} & K_{yy} \end{bmatrix} \tag{6}$$

$$c = F/(h \times \Omega) \begin{bmatrix} b_{xx} & b_{xy} \\ b_{yx} & b_{yy} \end{bmatrix} = \begin{bmatrix} c_{xx} & c_{xy} \\ c_{yx} & c_{yy} \end{bmatrix} \tag{7}$$

Where $ho = \frac{1}{(\pi^2(1-\epsilon^2)+16\epsilon^2)^{3/2}}$ (8)

$$a_{xx} = ho \times 4(\pi^2(2 - \epsilon^2) + 16\epsilon^2) \tag{9}$$

$$a_{xy} = ho \times \frac{\pi((\pi^2(1-\epsilon^2)^2)-16\epsilon^4)}{\epsilon\sqrt{1-\epsilon^2}} \tag{10}$$

$$a_{yx} = -ho \times \frac{\pi(\pi^2(1-\epsilon^2)(1+2\epsilon^2)+32\epsilon^2(1+\epsilon^2))}{\epsilon\sqrt{1-\epsilon^2}} \tag{11}$$

$$a_{yy} = ho \times 4(\pi^2(1 + 2\epsilon^2) + \frac{32\epsilon^2(1+\epsilon^2)}{(1-\epsilon^2)}) \tag{12}$$

$$b_{xx} = ho \times \frac{2\pi\sqrt{1-\epsilon^2}(\pi^2(1+2\epsilon^2)-16\epsilon^2)}{\epsilon} \tag{13}$$

$$b_{xy} = b_{yx} = -ho \times 8(\pi^2(1 + 2\epsilon^2) - 16\epsilon^2) \tag{14}$$

$$b_{yy} = ho \times \frac{2\pi((\pi^2(1-\epsilon^2)^2)+48\epsilon^2)}{\epsilon\sqrt{1-\epsilon^2}} \tag{15}$$

The stiffness matrix is not symmetric, therefore, hydrodynamic bearings is anisotropic supports in to the machine. The MATLAB computer program has been designed to study the relations between eccentricity and modified Sommerfeld number, then getting the relation between modified Sommerfeld number and stiffness and Sommerfeld with damping. We take in to account the effect of dynamic forces acting on the bearings, generally the force-displacement relation is nonlinear but, its provided that amplitude of resultant is small, so can assume a linear force-displacement relation. We consider short bearing ($L/D < 1$), where the matrix are 2×2 , the stiffness and damping matrices may be written in closed form in term of eccentricity and load as shown in Eqs.(6) and (7). The representation of spring and damper of COMBI214 is 2-dimensions element with longitudinal tension and compression capability as shown in **Fig.3**.

2.2 Dynamic Equations

The concept of rotor dynamics has demonstrated by using the rotor which has disk lies at an equal distance from bearings, the bearings that taken with the rotor is short journal bearing $L < D$ and $A \neq B$ as shown in **Fig. 1**

The rotor consists of long flexible shaft with flexible journal bearing on both ends the bearings has support stiffness K_{xx}, K_{yy}, K_{xy} and K_{yx} associated with damping c_{xx}, c_{yy}, c_{xy} and c_{yx} .

in both ends in bearing 1 and bearing 2 as shown in **Fig.3**, there is a disk of mass m_d and the mass of shaft is m_s , the equivalent mass of the rotor is, **Michael, et al.,2012**.

$$m = m_d + \frac{17}{35} m_s \quad (16)$$

The center of gravity of disk is offset from the shaft geometry center by an eccentricity e , the motion of disk center is described by two translational displacements (x_r, y_r) .

The main form of equation of motion for all vibration problems is given by **Xu, et al, 2004**.

$$[m]\{\ddot{y}_r\} + ([c] + [cg])\{\dot{y}_j\} + ([K] + [H])\{y_j\} = \{f\} \quad (17)$$

Where

$[m]$ = symmetric mass matrix, $[c]$ = symmetric damping matrix, $[K]$ = symmetric stiffness matrix, $\{f\}$ = external force vector, $\{y\}$ = generalized coordinate vector.

The Eq. (17) is for motion a symmetric rotor and rotates at constant speed Ω about its spin axis but it is accompanied by skew symmetric gyroscopic matrix $[Cg]$ and skew symmetric circulatory matrix $[H]$. Both of $[Cg]$ and $[H]$ matrices are affected by rotational speed Ω . When the speed Ω is zero, the $[Cg]$ and $[H]$ in Eq. (17) vanished represents an ordinary stand still structure, the $[Cg]$ matrix has inertia terms and derived from kinetic energy because of the gyroscopic moments acting on the rotary parts of the machine, if this equation is described in rotary reference body this gyroscopic matrix $[Cg]$ Also has the terms which associated with Coriolis acceleration. The circulatory matrix $[H]$ is come mainly from internal damping of rotating elements, **Nagaraju and Srinivas, 2014**.

From Newton's second law of motion in x and y directions to get the equations of motion including the stiffness and damping of bearings

$$\sum F_x = m\ddot{x} \quad (18)$$

$$\sum F_y = m\ddot{y} \quad (19)$$

$$(K_x + K_{xx1} + K_{xx2})X_j + (K_{yx1} + K_{yx2})y_j + (c_{xx1} + c_{xx2})\dot{X}_j + (c_{xy1} + c_{xy2})\dot{y}_j - K_{xr} = m \frac{d^2}{dt^2} (X_j + e \cos(\Omega t + \Phi e)) \quad (20)$$

$$(K_{xy1} + K_{xy2})X_j + (K_{yy1} + K_{yy2} + K)y_j + (c_{xy1} + c_{xy2})\dot{X}_j + (c_{yy1} + c_{yy2})\dot{y}_j - K_{yr} = m \frac{d^2}{dt^2} (y_j + e \sin(\Omega t + \Phi e)) \quad (21)$$

Where Φe is the phase angle of mass unbalance, the above equations of motion gives indications about the motions in x and y directions are both decoupled in case of static and dynamic for this model therefore they can be solved separately to find response amplitude in x and y directions at any time.

2.3 Modeling and Design Data Input

The modeling features for rotor and bearing support flexibility are described in this papers and show how element BEAM188, COMBI214 are used to model the shaft with bearings and MASS21 for disk to model the masses. The stiffness and damping of both bearings with cross coupling directions and stiffness with damping of the shaft has been taken into account in this analysis including their variations with the changing of rotational spin speed to get accurate results. Beam element (BEAM188) is good for analyzing slender to moderately stubby or thick beam structures, it is a linear (2 –nodes) as shown in **Fig.4**, beam188 element has six or seven degrees of freedom at each node, with the number of degrees of freedom depending on the KEYOPT(1) value, when KEYOPT(1) = 0 at each node, these include translations in the x, y and z directions and rotations about x, y and z axes, when KEYOPT(1) = 1, a seven degree of freedom (warping magnitude) is also considered, this element is well suited for linear large relation and/or large strain nonlinear applications, MASS21 element for lumped mass disk is a point element having up to six degree of freedom displacement in x, y, z directions and rotation about x, y and z axes. A different mass and rotary inertia may be assigned to each coordinate direction, **Nagaraju and Srinivas, 2014**.

Tables 1 and **2** represent the values of stiffness and damping of bearings with the variations of spin speed so can represent the COMBI214 element in ANSYS for each bearing and at any speed, the results are from MATLAB program which has been designed to solve a set of equations from Eqs. (1) to (15). The values of damping coefficients decreased with rotational speed till to 2000 RPM then its change very small and its approximately considered constant values but the cross coupling values continue decreasing while the stiffness also change rapidly till to 2000, is seem stable and stiffness in cross coupling directions is not equal and varied small amounts as shown in **Figs. (5)** and **(6)**.

3. RESULTS AND DISCUSSION

Modal analysis without any rotation is performed on the rotor model. The Eigen frequency obtained for the rotor model at 0 RPM are drawn in **Fig. 7** which shows first mode shape of operation 6000 rpm by ANSYS, **Table 4** shows the dimension of the selected model ($A \neq B$). For Critical Speed and Campbell Diagram, In this analysis, the first

Eigen frequency analysis are done on the rotor model for speed range from 0 to 6000 rpm with an increment of 100 rpm using multiple load step, the fundamental Eigen frequency of the rotor model corresponding to different rotational spin speeds are plotted in Campbell diagram with limitation of the stability of the rotor as shown in **Fig.8**.

The Campbell diagram is used to find critical speed of the system by ANSYS which is 4920 RPM, often rotor critical speed against natural frequency of the system, the rotor is supported by two tilting pad short bearings, stiffness and damping coefficients of bearings are varied with spin speed and in this case the natural frequency of the system are varied, if the natural frequency equal to rotating spin speed, the speed is called critical speed, as shown in Campbell diagram the stability limit at 80.4 Hz and it called threshold limit so if the frequency less than threshold, it mean under the purple color line and the system is stable, if the frequency more than threshold, it mean up the purple color line and the system is stable too, if the frequency is 80.4 it mean, it is on the purple color line and the system is unstable.

For the harmonic analysis it has been showed that the unbalance response of the rotor at the disk location by apply the unbalance forces at the center position to get the displacement which vary sinusoidal at the same know frequency domain then the comparison has been done by changing the value of unbalance masses (0.5g, 1g, 1.5g, 2g and 2.5g) as shown in **Table 5**, to understand its effect on the rotor while its operating, it can be conclude that by increasing the unbalance masses, the displacement will also increase at the disk region and the relation between them shown in **Fig.13**, the unbalance harmonic response shown in **Figs. 9, 10, 11, 12, 13 and 14**. The maximum displacement happens at the critical speed case, the dynamic amplitude plotted against the unbalance mass as shown in **Fig.15**, the amplitude vary nonlinear till to 1g unbalance mass then it varies approximately linear after 1g to 2.5g.

For the transient analysis at start up, the response of the rotor system at the disk region to arbitrary time-varying load to find the stability of the system at different spin speeds, if the amplitude of the rotor decrease with the time, that means the system is stable otherwise the system is not stable. Also the values like rise time (t_r), overshoot (PM), settling time (t_s) has been calculated for transient start up case with changing the speed from 0 to 6000 rpm and for (0.5g, 1g, 1.5g, 2g, and 2.5g) unbalance mass as listed in **Table 6**, the transient has been compared just only as a behavior of the curves with **Ignacio, et al, 2013**, the comparison also has been done just only for understanding the behavior of curve for transient bending stress in z and y directions with **Ignacio, et al, 2013**. where blue color is bending stress in y direction and red color is bending stress in z direction, the maximum stress in y direction is $\mp 90E6 \frac{N}{m^2}$, while in z direction the maximum stress $\mp 62E6 \frac{N}{m^2}$, both of them happens at 6.55sec. the behaviors were in good agreement if compare with transient stress as in **Ignacio, et al, 2013** as shown in **Figs.16, 17, 18, 19, 20 and 21** for displacement and **Figs.22 and 23** for bending stress for a rotor has 1g unbalance mass.



4. CONCLUSION

It can be conclude that.

- 1- The Eigen frequency calculated as a first critical speed by ANSYS, to get the fundamental frequency and mode shape by using Campbell diagram which is the resonance speed, it found 4920 rpm for a given dimensions of rotor as in **Table.4**, resonance speed is more dangerous case to avoid it by making its period of time as small as possible to avoid failure.
- 2- The harmonic analysis has been taken for many unbalance masses 0.5g to 2.5g (step 0.5g) and finding the response for each case, the peak value of response happen at 80.4 Hz on frequency-response relation and also could be conclude that the unbalance response varies nonlinear with unbalance mass till to 1g then it became approximately linear variation with unbalance masses from 1g to 2.5g.
- 3- The transient response and transient bending stresses has been studied and compared as a behavior of curve, it found in good agreement, the rise time changed from 0.2% - 1% as increasing percentage from 0.5g to 2 g while its 20% increasing if change from 2g to 2.5g but the overshoot not varies so much, the settling time jumped to 8.312 sec. at 2.5g unbalance mass, the peak response of transient case also increases by increasing the unbalance mass, from the other hand the bending stress in y-direction is more than in z-direction and the maximum case of response and stresses happen at 6.55sec. the transient response and stresses has been compared as a behavior of curves with **Ignacio, et al, 2013**, it found in good agreements.

REFERENCES

- Abdul Ghaffar Abdul Rahman, Ong Zhi Chao and Zubaidah Ismail, 2010, *Effectiveness of Impact-Synchronous Time Averaging in Determination of Dynamic Characteristics of a Rotor Dynamic System*, Technical Paper, Mechanical Engineering Department, Faculty of Engineering, University of Malaya, 50603 Kuala Lumpur, Malaysia.
- Chen Y. S , Cheng Y. D , Liao J. J and Chiou C. C, 2008, *Development of A Finite Element Solution Module for the Analysis of the Dynamic Behavior and Balancing Effects of an Induction Motor System*, Technical Paper, Department of Mechanical Engineering, Yuan-Ze University, Chungli 320 Taiwan, ROC.
- Ignacio Ramirez Vargas, Luis Manuel Palacios Pineda, and Humberto Corro Hernandez, 2013, *Vibrational Response of a Rotor Supported in Hydrodynamics Short Bearings*, Memories Del Xix International Congress of Her Annual Somim, 25 Al 27 De September, 2013 PACHUCA, HIDALGO, MEXICO.

Kris Matthys, Marco Perucchi and Koenraad De Bauw, *Rotor Dynamic modeling as powerful support tool for vibration Analysis on large Turbo machinery.* ○



- Maurice L, Adams, 2001, *Rotating Machinery Vibration*, From analysis to Troubleshooting, Marcel Dekker, Inc.
- Michael, I. Friswell., John E. T. Penny, and Arthur W. Lees, 2012 , *Dynamics of Rotating Machines*, Cambridge University Press, 32 Avenue of the Americas New York NY 10013-2473 USA, First Published 2010, Reprinted 2012, pp177-183.
- Nagaraju Tena and Srinivas Kadivendi, 2014, *Rotor Dynamic Analysis of Steam Turbine Rotor Using ANSYS*. IJMERR, ISSN2278-0149, Vol.3, No1.
- Xu Yang, Zhao Lei and Yu Suyuan, 2004, *Dynamics Analysis of Very Flexible Rotor* ,Technical Paper, Institute of Nuclear Energy Technology, Tsinghua University, Beijing 100084, P.R.China.
- Yukio Ishida and Toshio Yamamoto, 2012, *Linear and Nonlinear Rotor Dynamics,(A Modern Treatment with Applications*, 2nd Enlarged and Improved Edition, Wiley-VCH Verlag, Germany, pp307-320.

NUMENCLATURE

- a_{xx} = factor of stiffness of bearing in x-direction.
- a_{xy} = factor of cross coupling stiffness of bearing in xy-direction.
- a_{yx} = factor of cross coupling stiffness of bearing in yx-direction.
- a_{yy} = factor of stiffness of bearing in y-direction.
- b_{xx} = damping parameter of bearing in x-direction.
- b_{xy} = cross coupling damping parameter in xy-direction.
- b_{yx} = cross coupling damping parameter in yx-direction.
- b_{yy} = damping parameter of bearing in y-direction.
- C = center of bearing.
- \tilde{C} = center of journal.
- c_{xx} = damping of bearing in x-direction, N.s/m
- c_{xy} = cross coupling damping of bearing in xy-direction, N.s/m
- c_{yx} = cross coupling damping of bearing in yx-direction, N.s/m
- c_{yy} = damping of bearing in y-direction, N.s/m
- D_s = shaft diameter, m
- E = Young's modulus of elasticity, $\frac{N}{m^2}$
- F = resultant force in bearing, N
- F_r = radial force in bearing, N
- F_t = tangential force in bearing, N
- H = disk thickness, m
- h = clearance between shaft and bearing, m.
- K_{xx} = stiffness of bearing in x-direction, N /m
- K_{xy} = cross coupling stiffness of bearing in xy-direction, N /m



K_{yx} = cross coupling stiffness of bearing in yx-direction, N /m

K_{yy} = stiffness of bearing in y-direction, N /m

K_{yr} = stiffness of rotor in y-direction, N /m

L = length of journal bearing, m

m = equivalent mass of rotor, Kg

m_d = mass of disk, Kg

m_s = mass of shaft, Kg

N = rotational speed, RPM

O = center of shaft before rotation.

S = Sommerfeld number.

S_s = modified Sommerfeld number.

t = time, sec.

u = generalized coordinate with lateral direction.

w = weight effect on bearing, N

x, y, z coordinates of the rotor

π = constant, 22/7

ϵ = eccentricity ratio.

Ω = excitation angular velocity, rad/sec.

θ = angle of hydrodynamic pressure, rad.

μ = viscosity of oil of bearing,

φ = pressure angle of oil film bearing, rad.

ρ = mass density of shaft material, $\frac{Kg}{m^3}$

ϑ = Poisson's Ratio.

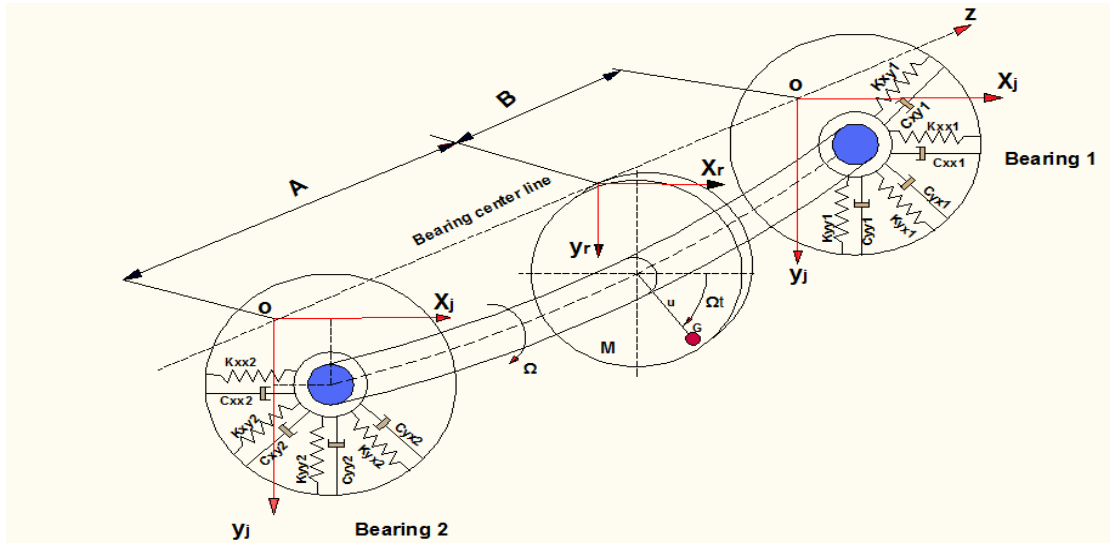


Figure 1. The bearings that taken with the rotor springs and damper representation.

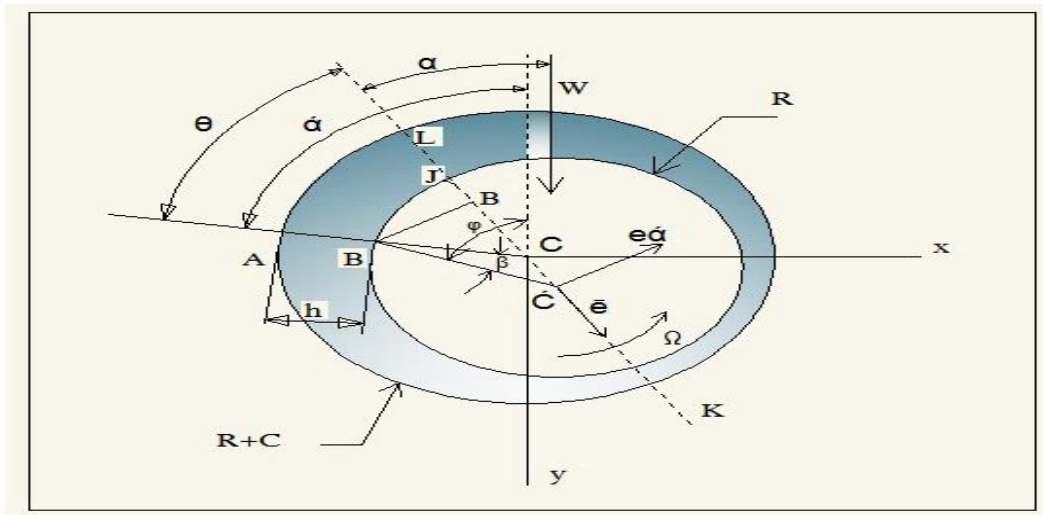


Figure 2. Fluid film bearing shows the eccentricity between shaft and bush.

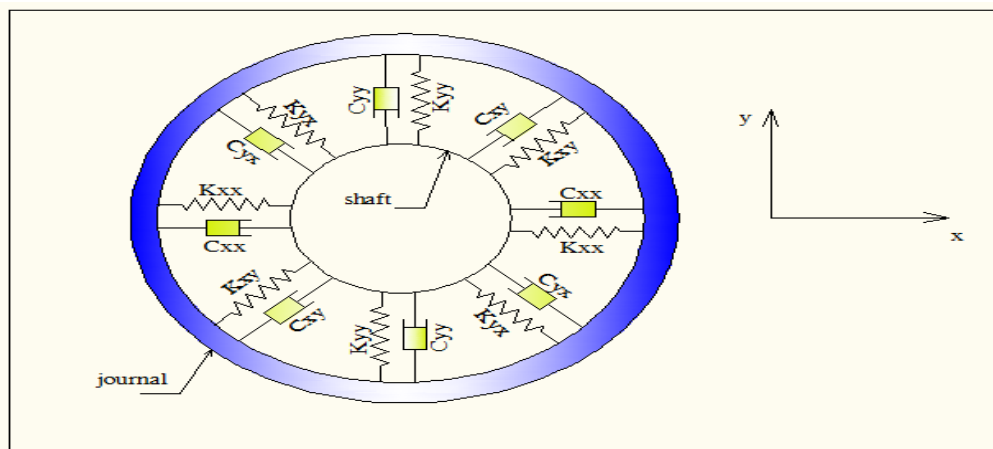


Figure 3. Springs and dampers with cross coupling of oil film journal bearing COMBI214 element geometry.

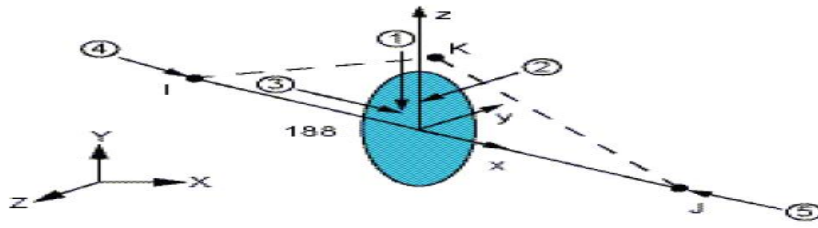


Figure 4.Element Beam188 type 6 degree of freedom system, **Kris, et a.l,**

Table 1. Properties of Bearing number 1, (Stiffness and damping).

Speed RPM	Eccentricity ratio	$K_{xx1}^* \cdot 10^3$	$K_{xy1}^* \cdot 10^3$	$K_{yx1}^* \cdot 10^3$	$K_{yy1}^* \cdot 10^3$	$c_{xx1}^* \cdot 10^3$	$c_{xy1}^* \cdot 10^3$	$c_{yx1}^* \cdot 10^3$	$c_{xx1}^* \cdot 10^3$
500	0.4419	3010	1646.8	-5273.5	3307.5	92.808	-58.21	-58.21	171.52
1000	0.2938	3199.2	3584.5	-5992.5	2345.2	78.512	-30.726	-30.726	104.39
1500	0.2158	3275.2	5448.3	-7221.7	2032.2	74.329	-20.916	-20.916	86.99
2000	0.1690	3311.0	7291.4	-8682.6	1895.6	72.552	-15.839	-15.839	79.988
2500	0.1382	3330.2	9133.1	-10272	1825.0	71.689	-12.737	-12.737	76.550
3000	0.1167	3341.4	10965	-11927	1784.4	71.157	-10.640	-10.640	74.581
3500	0.1008	3348.5	12804	-13636	1759.0	70.870	-9.1422	-9.1422	73.406
4000	0.0887	3353.2	14634	-15365	1742.2	70.641	-8.0095	-8.0095	72.593
4500	0.0791	3356.6	16475	-17128	1730.4	70.532	-7.1259	-7.1259	72.080
5000	0.0714	3359.0	18303	-18893	1721.9	70.411	-6.4174	-6.4174	71.668
5500	0.0650	3360.8	20149	-20685	1715.6	70.377	-5.8368	-5.8368	71.418
6000	0.0597	3362.2	21973	-22466	1710.7	70.288	-5.3523	-5.3523	71.165

Table 2. Properties of bearing number 2, (Stiffness and damping).

Speed RPM	Eccentricity ratio	$K_{xx2}^* \cdot 10^3$	$K_{xy2}^* \cdot 10^3$	$K_{yx2}^* \cdot 10^3$	$K_{yy2}^* \cdot 10^3$	$c_{xx2}^* \cdot 10^3$	$c_{xy2}^* \cdot 10^3$	$c_{yx2}^* \cdot 10^3$	$c_{xx2}^* \cdot 10^3$
500	0.3703	2251.4	1760.4	-3956.9	2008.4	85.47	-43.38	-43.38	132.91
1000	0.2289	2364.4	3663.7	-5025.7	1504.7	75.68	-22.658	-22.658	102.74
1500	0.1624	2401.8	5527.7	-6496.4	1361.4	73.096	-15.318	-15.318	79.99
2000	0.1249	2417.7	7385.5	-8131.4	1303.3	72.096	-11.556	-11.556	76.079
2500	0.1012	2425.7	9237.4	-9842.1	1274.7	71.588	-9.2718	-9.2718	74.169
3000	0.0849	2430.2	11094	-11601	1258.6	71.337	-7.739	-7.739	73.142
3500	0.0731	2433.0	12944	-13381	1248.7	71.156	-6.6406	-6.6406	72.488
4000	0.0641	2434.9	14806	-15189	1242.2	71.069	-5.8144	-5.8144	72.118
4500	0.0571	2436.1	16655	-16997	1237.7	71.007	-5.1708	-5.1708	71.817
5000	0.0515	2437.1	18494	-18802	1234.5	70.901	-4.6553	-4.6553	71.558
5500	0.0469	2437.7	20330	-20611	1232.1	70.811	-4.2331	-4.2331	71.355
6000	0.0430	2438.3	22193	-22450	1230.3	70.823	-3.8811	-3.8811	71.281



Table 3. Shaft material AISI4140 Properties.

Material Properties	
Young Modulus (E)	$2.05 \times 10^{11} \text{ N/m}^2$
Poisson's Ratio (ν)	0.29
Density (ρ)	7850 Kg/m^3

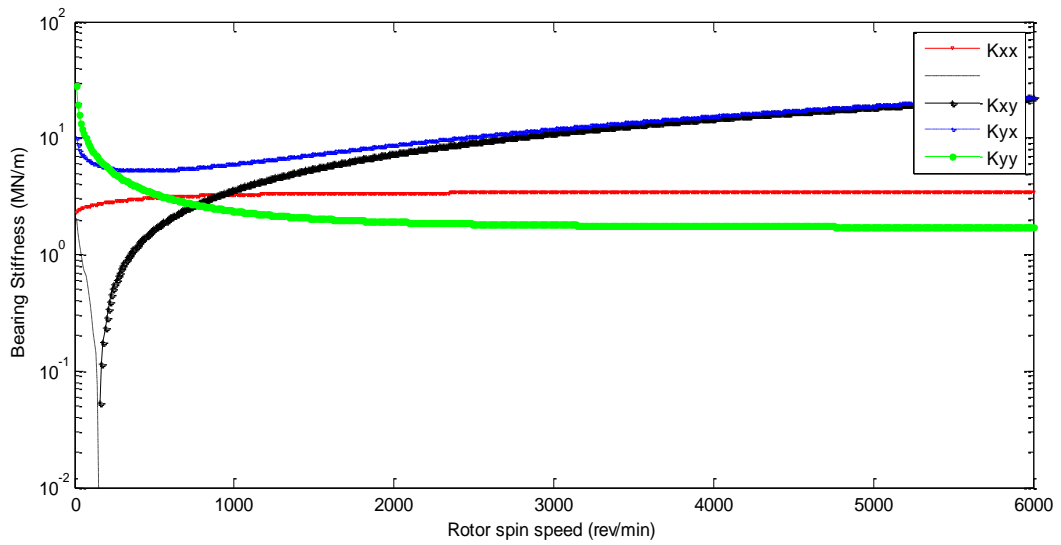


Figure 5. Stiffness of the journal bearing verses spin speed of rotor.

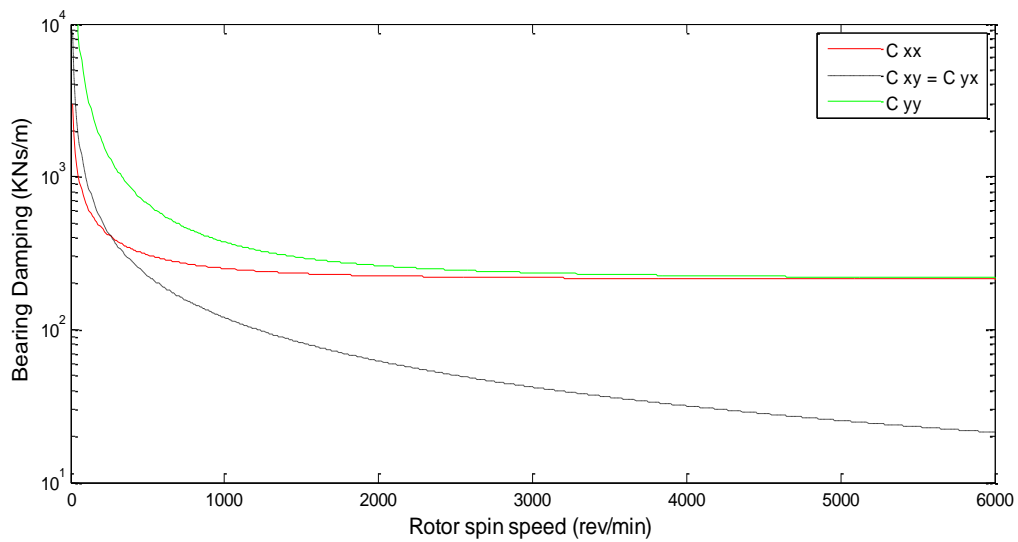


Figure 6. Rotor spin speed verses damping of fluid film bearing.

Table 4. Dimensions of Selected model For Study.

Description	Dimensions of selected model
Total shaft length (m)	0.654 m
Shaft diameter (m)	0.048 m
Disk diameter (m)	0.34 m
Distances between disk and bearings (m)	A=0.414m , B =0.24m
Disk thickness (m)	0.02m
Total rotor mass (Kg)	23.25 kg

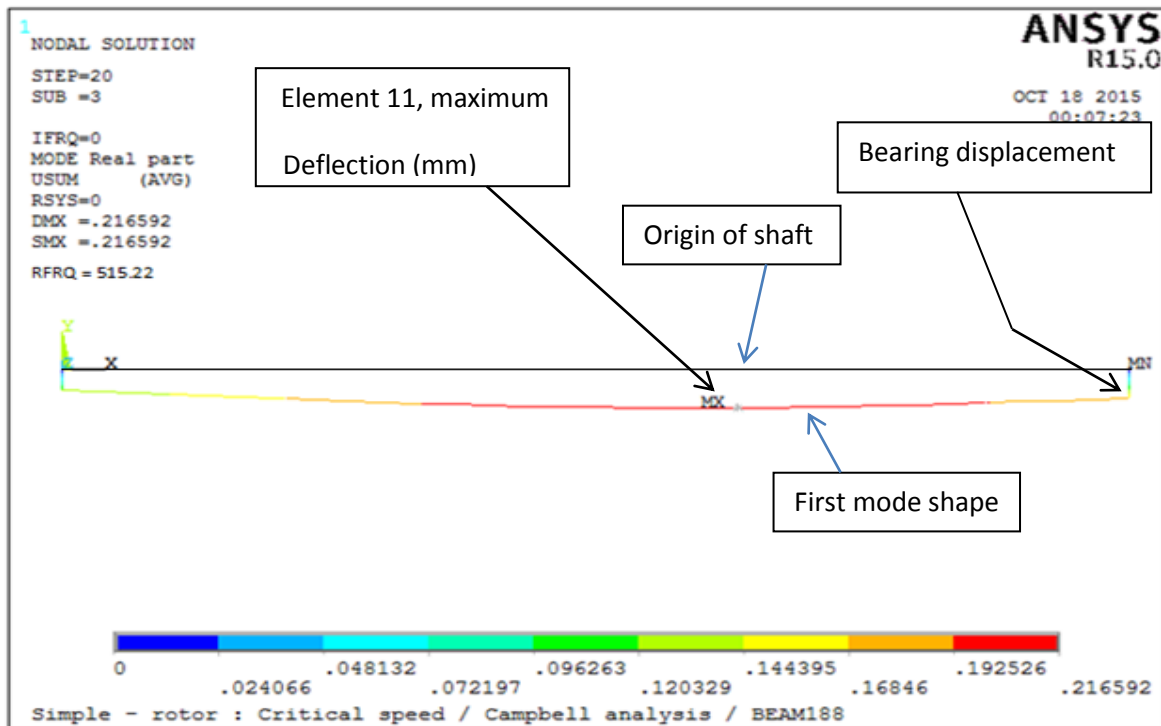


Figure 7. Mode shape of the rotor for first natural damped frequency.

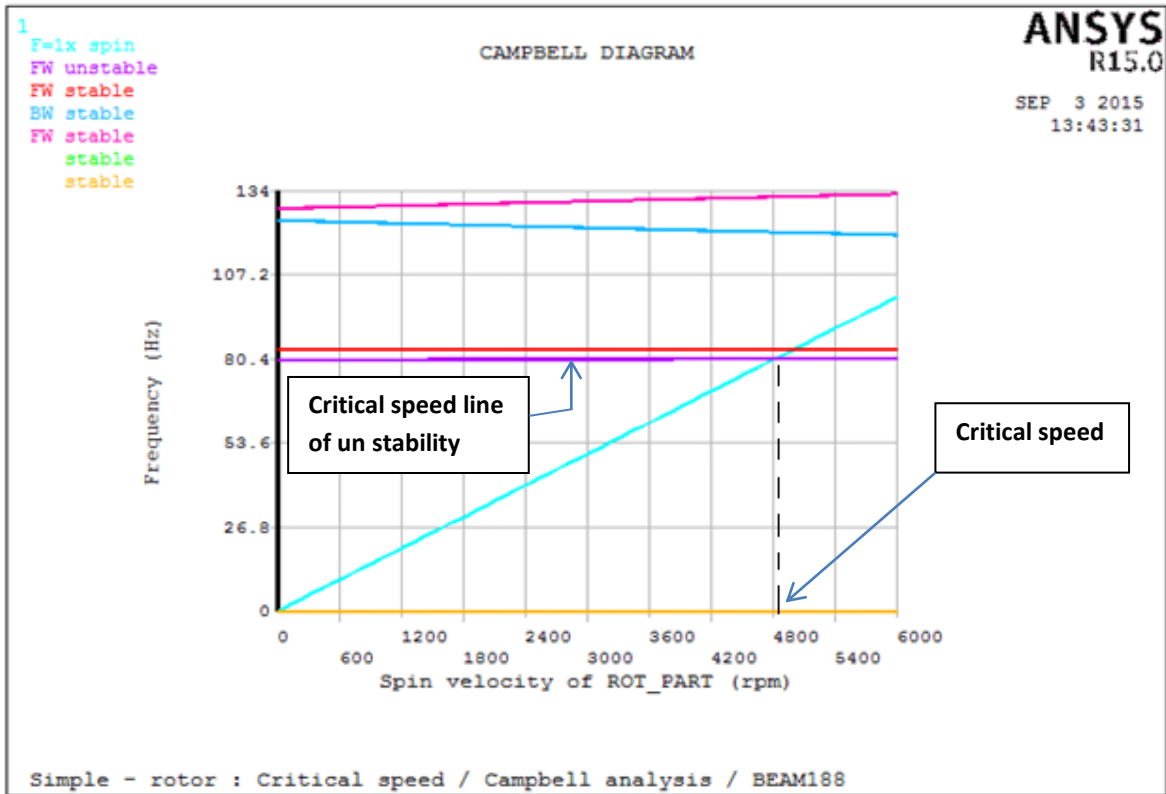


Figure 8. Campbell diagram of the rotor shows the critical speed at 4920 rpm.

Table 5. Response of the rotor in disk region of harmonic unbalance at critical speed.

Unbalance mass (g)	Response of the rotor in disk region (m) at 4920 rpm	% Percentage of changing response
0.5	0.7762E-03	0
1	0.8954E-03	13.31
1.5	0.1119E-02	19.98
2	0.1343E-02	16.67
2.5	0.1492E-02	9.986

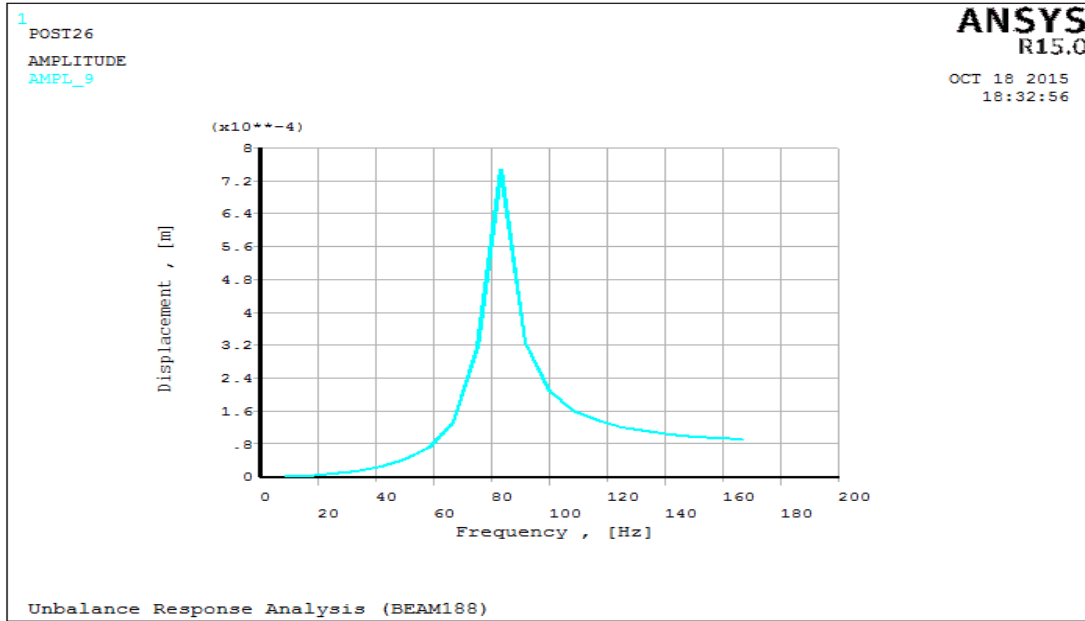


Figure 9. Response displacement for 0.5 g Harmonic unbalances mass.

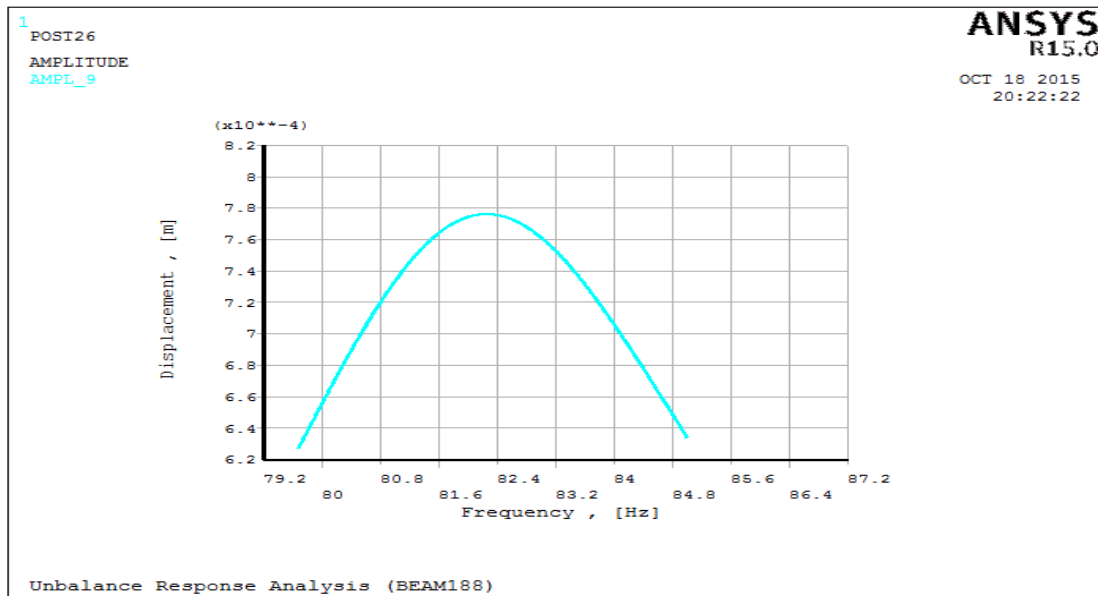


Figure 10. Response displacement for 0.5 g Harmonic unbalances mass, to show exact response value.

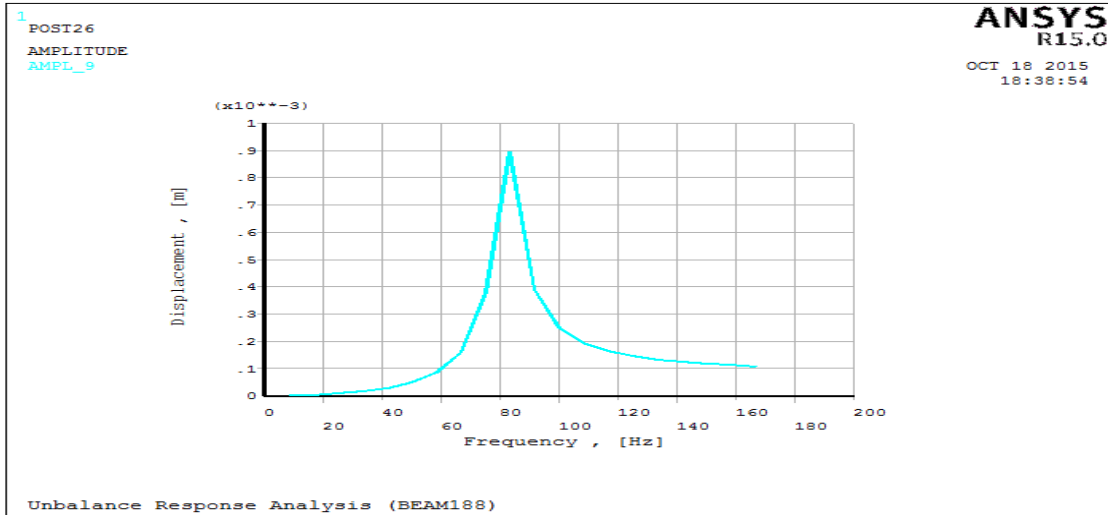


Figure 11. Response displacement for 1 g Harmonic unbalances mass.

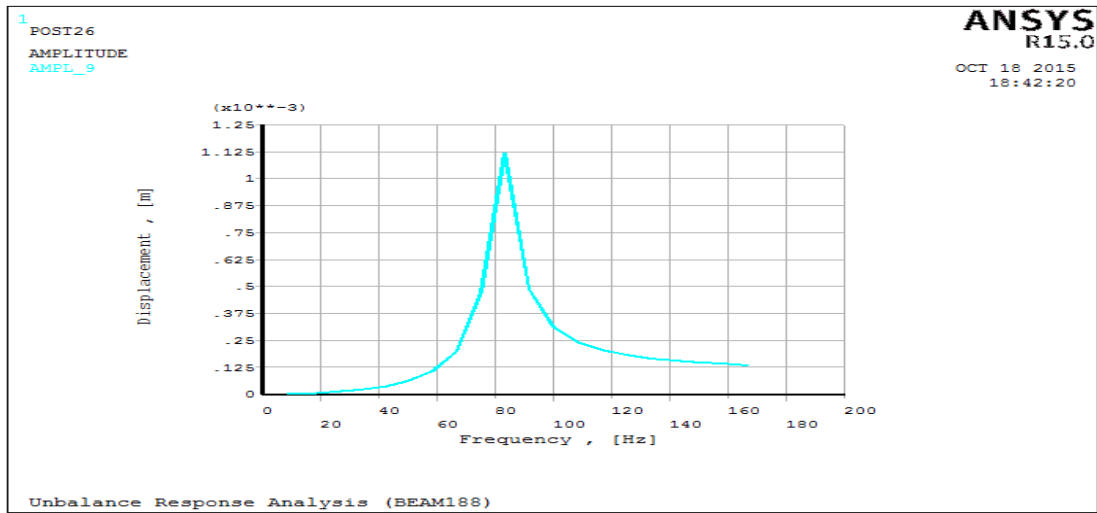


Figure 12. Response displacement for 1.5 g Harmonic unbalances mass.

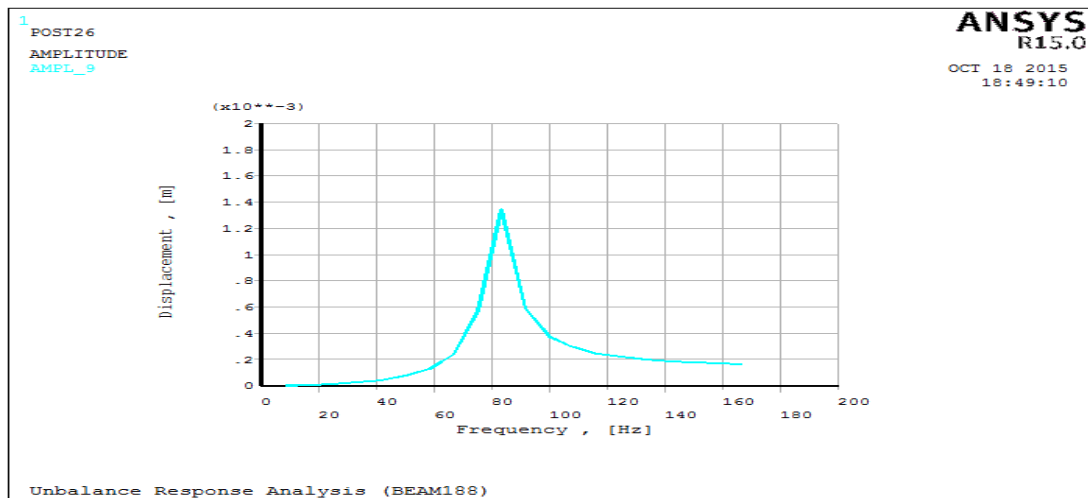


Figure 13. Response displacement for 2 g Harmonic unbalances mass.

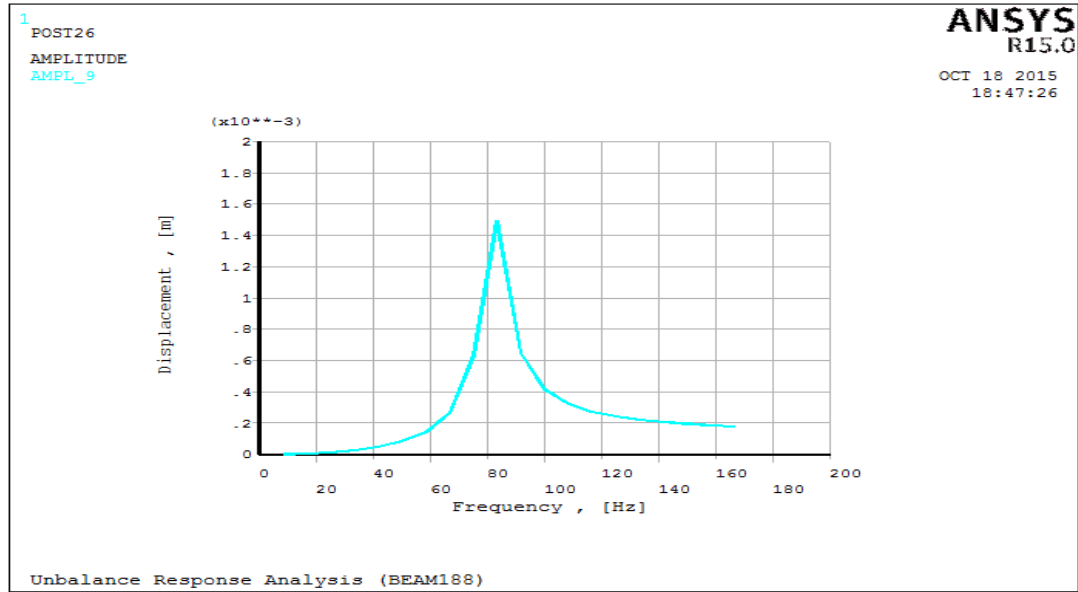


Figure 14. Response displacement for 2.5 g Harmonic unbalances mass.

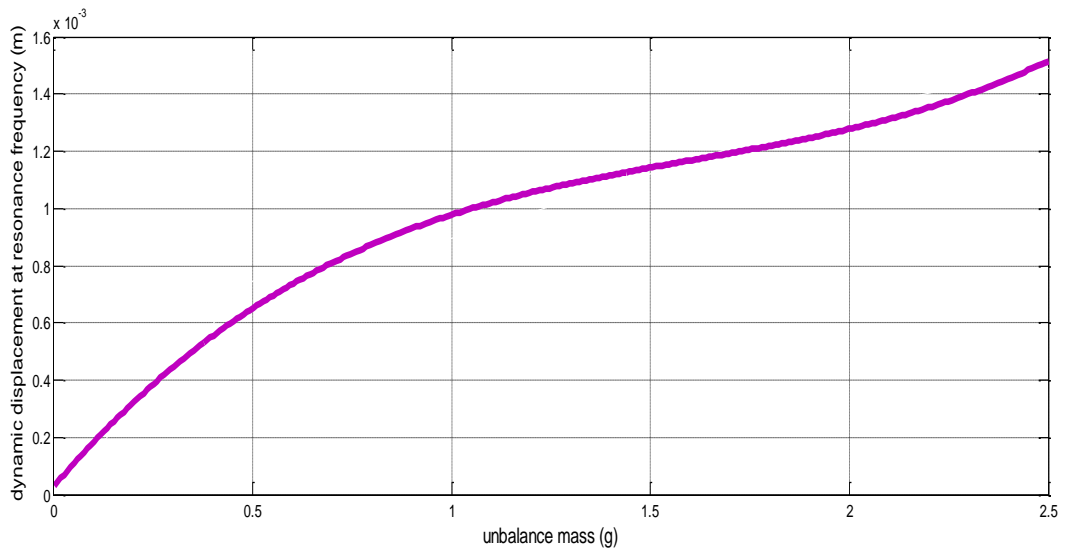


Figure 15. Response displacement versus unbalance mass at speed 4932 rpm.

Table 6. Transient response analysis at start up.

Transient analysis at start up for changes of unbalance mass					
Parameter	Time in second for 0.5g	Time in second for 1g	Time in second for 1.5g	Time in second for 2g	Time in second for 2.5g
Rise time t_r	6.172	6.187	6.253	6.285	7.9166
Settle time t_s	8.28	8.30	8.35	8.45	9.583
% overshoot MP	66.49	66.48	66.48	66.493	66.48
Maximum displacement near disk	0.7462E-03m at 6.478sec.	0.895E-03m at 6.50 sec.	0.1119E-02 m at 6.58 sec	0.1343E-02m at 6.650 sec.	0.1492E-2m at 8.312 sec.

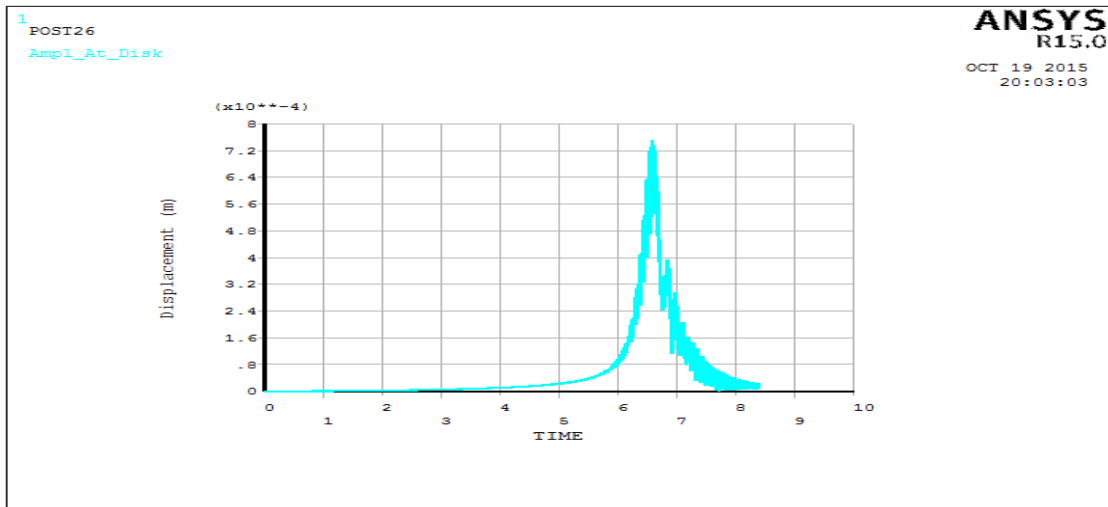


Figure 16. Transient Response Analysis Verses the Time for speed 0 to 6000 rpm with 0.5g unbalance mass.

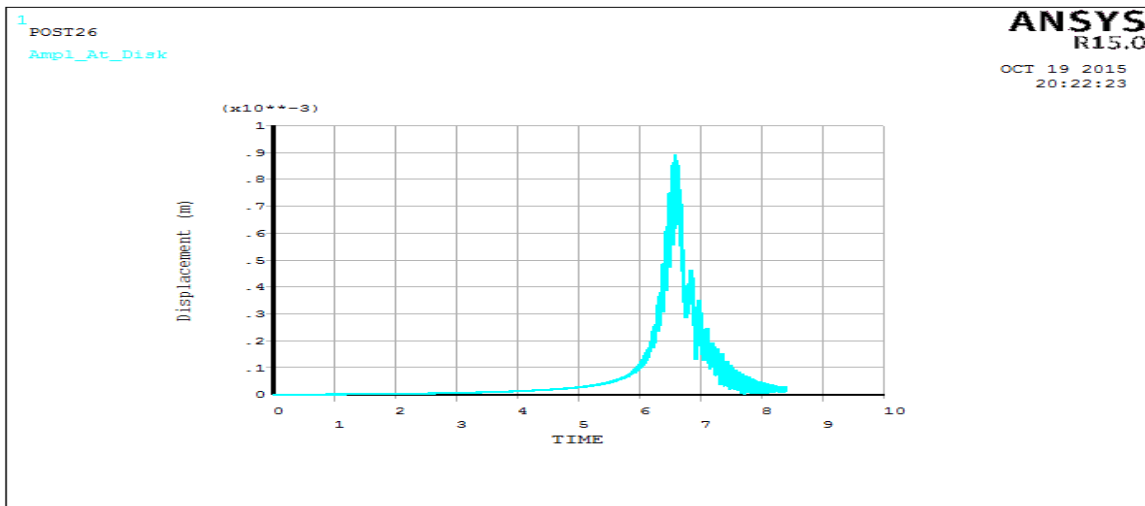


Figure 17. Transient Response Analysis Verses the Time for speed 0 to 6000 rpm with 1g unbalance mass.

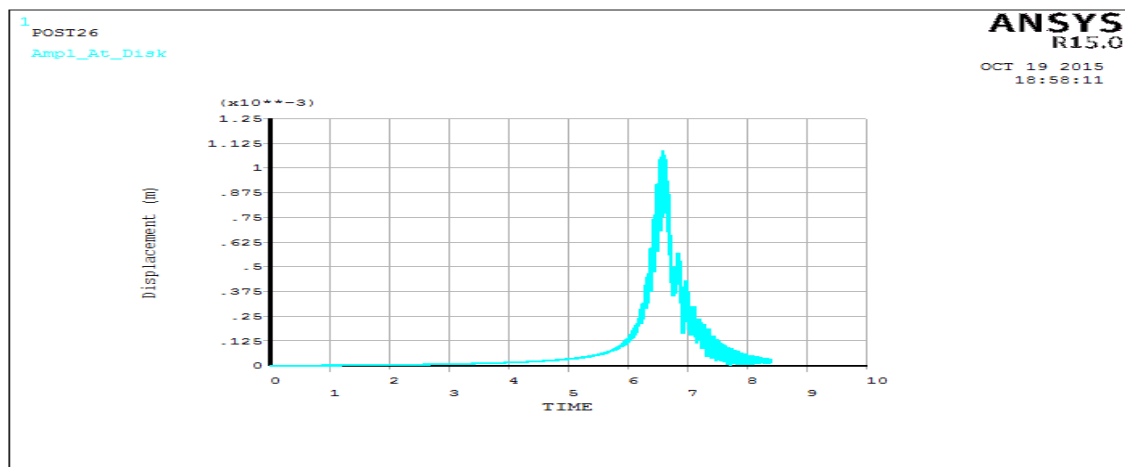


Figure 18. Transient Response Analysis Verses the Time for speed 0 to 6000 rpm with 1.5g unbalance mass.

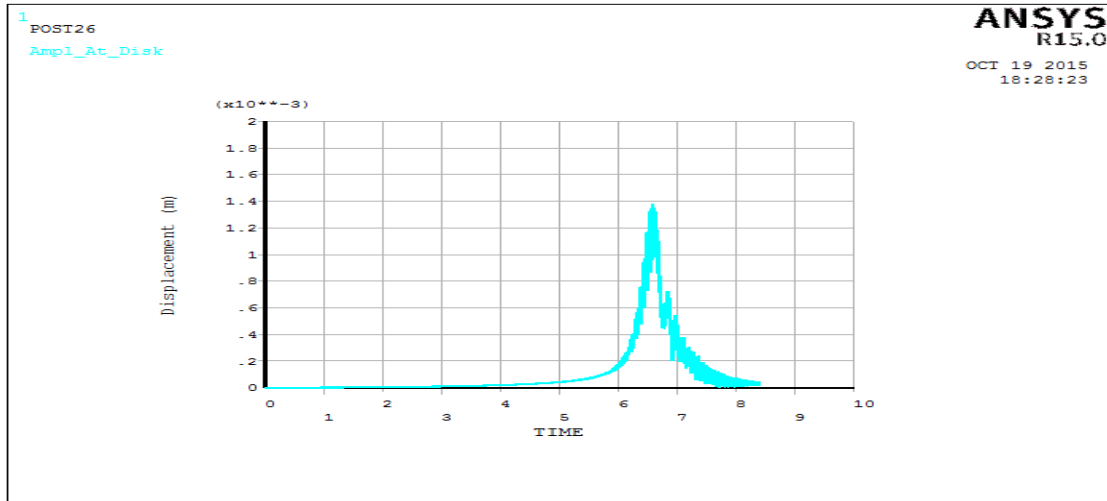


Figure 19. Transient Response Analysis Verses the Time for speed 0 to 6000 rpm with 2g unbalance mass.

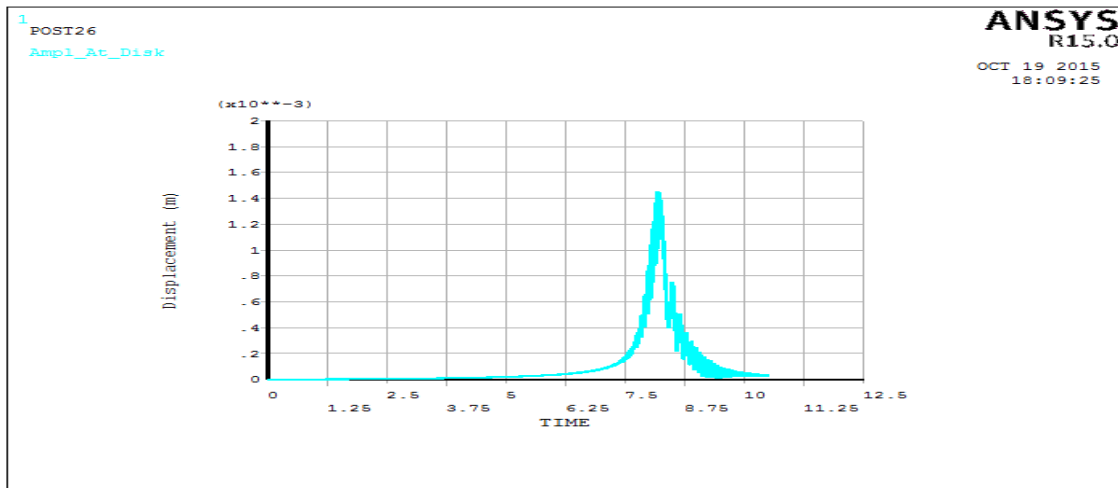


Figure 20. Transient response analysis verses the time for speed 0 to 6000 rpm with 2.5g unbalance mass.

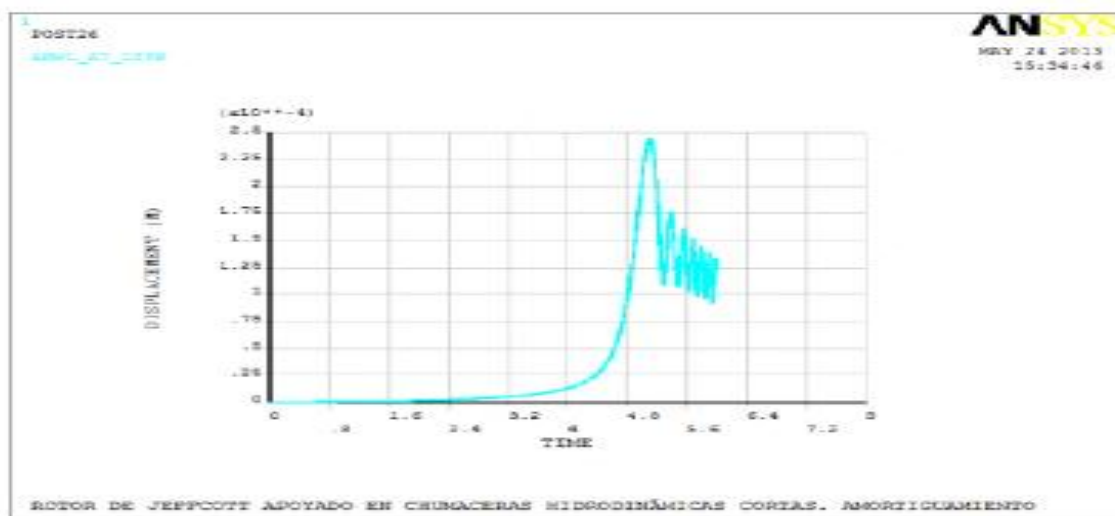


Figure 21. Transient response analysis verses the time as in, **Ignacio, et al., 2013.**

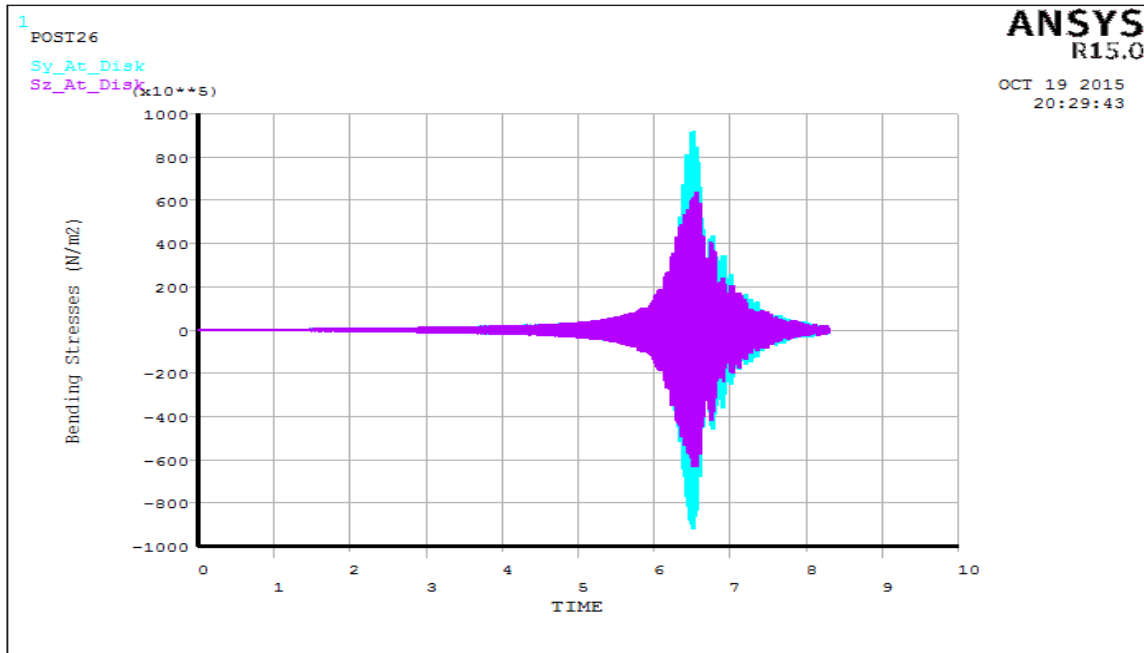


Figure 22. Bending stresses in z and y direction verses the time for transient at start up.

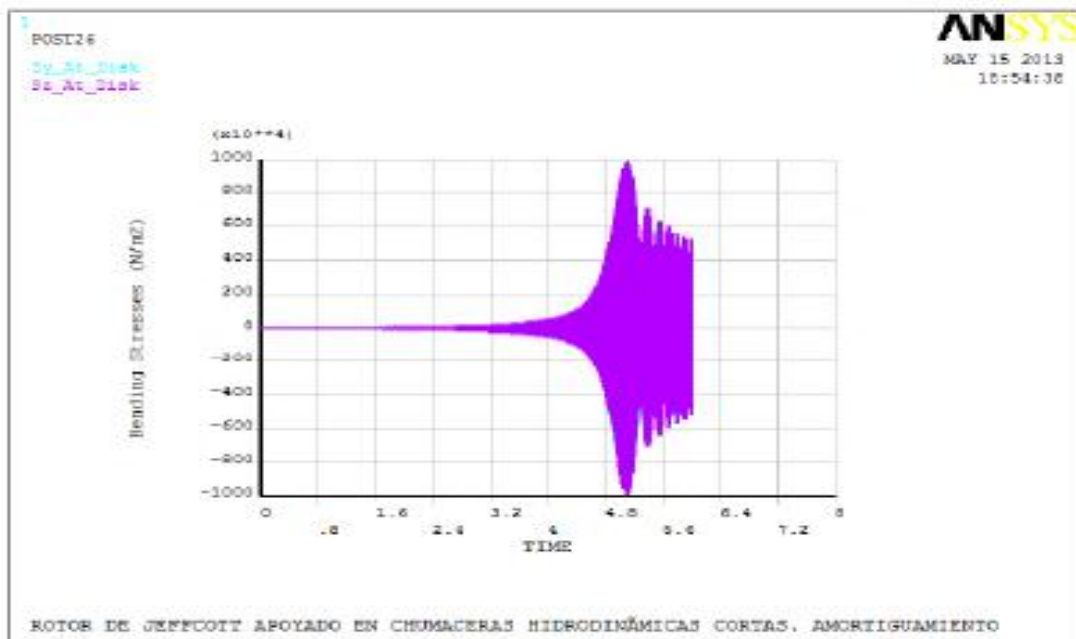


Figure 23: Bending stresses in z and y direction verses the time for transient at start up, Ignacio, et al., 2013.

Temperature Effect on Power Drop of Different Photovoltaic Modules

Emad Talib Hashim

Assistant Professor
Department of Energy Engineering
College of Engineering/ University of Baghdad
emadchem70@yahoo.com

Akram Abdulameer Abbood

M.Sc. Student
Department of Energy Engineering
College of Engineering/ University of Baghdad
akramabdulameer@gmail.com

ABSTRACT

Solar module operating temperature is the second major factor affects the performance of solar photovoltaic panels after the amount of solar radiation. This paper presents a performance comparison of mono-crystalline Silicon (mc-Si), poly-crystalline Silicon (pc-Si), amorphous Silicon (a-Si) and Cupper Indium Gallium di-selenide (CIGS) photovoltaic technologies under Climate Conditions of Baghdad city. Temperature influence on the solar modules electric output parameters was investigated experimentally and their temperature coefficients was calculated. These temperature coefficients are important for all systems design and sizing. The experimental results revealed that the pc-Si module showed a decrease in open circuit voltage by $-0.0912\text{V}/^\circ\text{C}$ while mc-Si and a-Si had nearly $-0.07\text{V}/^\circ\text{C}$ and the CIGS has $-0.0123\text{V}/^\circ\text{C}$. The results showed a slightly increase in short circuit current with temperature increasing about $0.3\text{mA}/^\circ\text{C}$, $4.4\text{mA}/^\circ\text{C}$ and $0.9\text{mA}/^\circ\text{C}$ for mc-Si, pc-Si and both a-Si and CIGS. The mc-Si had the largest drop in output power about $-0.1353\text{W}/^\circ\text{C}$ while -0.0915 , -0.0114 and $-0.0276\text{W}/^\circ\text{C}$ for pc-Si, a-Si and CIGS respectively. The amorphous silicon is the more suitable module for high operation temperature but it has the lowest conversion efficiency between the tested modules.

Key words: photovoltaic system, solar module, temperature effect, temperature coefficient

تأثير درجة الحرارة على انخفاض القدرة لأنواع مختلفة من الألواح الفوتوفولتائية

أكرم عبد الأمير عبود

طالب ماجستير

قسم هندسة الطاقة /كلية الهندسة/جامعة بغداد

عماد طالب هاشم

أستاذ مساعد

قسم هندسة الطاقة/كلية الهندسة/جامعة بغداد

الخلاصة

تمثل درجة حرارة الوح الشمسي العامل الثاني الأكثر تأثيراً في أداء المنظومات الشمسية الفوتوفولتائية بعد مقدار الاشعاع الشمسي. يقدم هذا البحث مقارنة اداء لاربعة انواع مختلفة من الألواح الفوتوفولتائية : سيليكون احادي التبلور، سيليكون متعدد التبلور، سيليكون غيرمنتظم التبلور ونحاس انديوم (غالسيوم) ثنائي السلينايد تحت الظروف المناخية لمدينة بغداد. تم التحقق عملياً من تأثير درجة الحرارة على مخرجات الألواح الشمسية وتم حساب معاملات درجة الحرارة والتي لها التأثير المباشر على تصميم وتقدير سعة المنظومات الفوتوفولتائية. بينت النتائج العملية ان لوح السيليكون متعدد التبلور أظهر هبوط في مقدار فولتية الدائرة المفتوحة بمقدار -0.0912 فولت/درجة مئوية، بينما للوحي السيليكون احادي التبلور والسيليكون غير منتظم التبلور -0.07 فولت/درجة مئوية وللوح النحاس كان مقدار الهبوط حوالي -0.0123

فولت/درجة مئوية. كما أظهرت النتائج زيادة طفيفة في تيار دائرة القصر مع زيادة درجة الحرارة بمقدار 0.3 ملي أمبير/درجة مئوية ، 4.4 ملي أمبير/درجة مئوية للوح السيليكون احادي التبلور، السيليكون متعدد التبلور على التوالي و 0.9 ملي أمبير/درجة مئوية لكل من لوحي السيليكون غير منتظم التبلور والنحاس. بالنسبة للقدرة العظمى الخارجة من اللوح الشمسي، لوح السيليكون احادي التبلور اظهر الانخفاض الاكبر من بين الألواح المدروسة بمعامل حرارة حوالي 0.1353- واط/درجة مئوية بينما كان الانخفاض 0.0915-، 0.0114- و 0.0276- واط/درجة مئوية للوح السيليكون متعدد التبلور، السيليكون غير منتظم التبلور ولوح النحاس على التوالي.

كلمات رئيسية: النظام الفوتوفولتائي، اللوح الشمسي، تأثير درجة الحرارة، عامل درجة الحرارة.

1. INTRODUCTION

Nowadays we get about 80% of the supplied energy is from depleted pollutant energy sources, e.g. fossil fuels. The environment damaged by the emissions currently generated by the use of fossil fuels such as serious environmental problems e.g., greenhouse effect, acid rain and ozone layer depletion, which are irreversible, **Dincar, 2003**. Recently, the enormous consumption of fossil fuel resulted in great interest to develop renewable energy sources such as solar energy. Photovoltaic power is a well-known technology and has lately experienced rapid growth over the last twenty years.

The solar cell is a p-n semiconductor junction exposed to sunlight, and generate electrical direct current. PVs have several advantages such as: no environmental pollution, high reliability, no noise and low maintenance cost. PV systems represents one of the most promising means of maintaining our energy intensive need. Like any other solar energy technology, PV system depends mainly on the amount of the incident solar radiation. In the other hand, the operating temperature of the PV cell has a noticeable influence on the performance of the PV system.

Solar photovoltaic cells like to be kept cool – they perform very well in strong winter sunshine. But Solar cells convert around 80% of absorbed sunlight into heat which gets trapped in the module and increases its operating temperature by as much as 20-30°C above ambient **Mattei et al., 2006**. Thus it can reach 70°C or more in hot climates, Building integrated photovoltaic (BIPV), Concentrated photovoltaic (CPV) systems. Solar power Systems designers make sure to permit an effective ventilation and cooling to remove the heat as much as possible.

The problems of PV in Iraq were various natural parameters such as solar irradiance, ambient temperature, wind speed, and relative humidity. Iraq has a dry hot climate dominated in summer from March to November. Iraq is located near the equator where day length in summer lasts for 12-14 hours with a bright sunshine of 6-8 hours and monthly mean temperature is 40-50°C. In such a climate, the working temperature of photovoltaic (PV) modules was measured as high as 75°C.

In literature, it is well documented that the electrical efficiency decrease with an increase in the working temperature of PV module. Many researchers have investigated that influence in a controlled environment using a sun simulator and/or environmental chamber. Other authors made their experiments under outdoor exposure for more realistic behavior and actual operation environment. In such experiments, all other variables for example, irradiance, wind speed, etc. are kept constant.

Many researchers have been examined the effect of temperature on different PV technologies. **Vokas et al., 2006**, showed the electrical efficiency of the PV panel reduces with temperature increases. **Makrides et al., 2009** evaluated the temperature influence of 13 PV modules of different types, which exposed to actual conditions in Stuttgart, Germany and Nicosia, Cyprus. The temperature coefficient for mono crystalline varied -0.353 to -0.456 $\%/^{\circ}\text{C}$, for multi crystalline and amorphous silicon was -0.403 to -0.502 $\%/^{\circ}\text{C}$ and -0.039 to -0.461 $\%/^{\circ}\text{C}$ respectively. **Makrides et al., 2012** analyzed the temperature effect on different PV technologies in Cyprus. The results showed that the highest average losses in annual energy yield were for mono crystalline silicon about 8% and 9% for poly crystalline silicon modules. For thin film technologies, the average losses were 5%. **Buday (2011)** studied the effect of solar radiation, module temperature and the incidence angle on PV module performance in United Solar Ovonic (USO), Michigan, USA. The PV modules were mc-Si, a-Si also CIGS. Mc-Si module had a power drop of $-0.5\%/^{\circ}\text{C}$, while $-0.24\%/^{\circ}\text{C}$ and $-0.0021\%/^{\circ}\text{C}$ for CIGS and a-Si respectively.

If the Cell temperature increased, this will increase the reverse saturation current of the PV cell which significantly decreases the open circuit voltage. Also, the band gap of the PV material decreases which leads to a small increase in photo generated current **Nelson, 2003**.

This paper presents a comparison study of experimental testing results for the performance of four different solar modules (mono-crystalline silicon, poly-crystalline silicon, amorphous silicon and copper indium gallium di-selenide) under natural sun and outdoor exposure in Baghdad for five consecutive months. The data collected were, the open circuit voltage, short circuit current and maximum power output with a wide range of ambient temperatures and keeping the incident solar radiation constant. Also, to investigate how the operating module temperature affect the performance of the used solar modules by presenting accurate temperature coefficients. The importance of these coefficients serves as a guide for the design and sizing of any PV systems in similar climates around the globe.

2. PHOTOVOLTAIC MODULE OUTPUT PARAMETERS

- The short-circuit current I_{sc} , is the current that flows through the external circuit when the electrodes of the solar cell are short circuited. The short-circuit current of a solar cell depends on the photon flux density incident on the solar cell, that is determined by the spectrum of the incident light. The I_{sc} depends on the area of the solar cell.
- The open-circuit voltage V_{oc} , is the voltage at which no current flows through the external circuit. It is the maximum voltage that a solar cell can deliver. The V_{oc} corresponds to the forward bias voltage, at which the reverse saturation current compensates the photo-current.
- The maximum power output, P_m is a key parameter since solar cells are used to produce electrical energy. When a solar cell is in an open-circuit or short-circuit state, it produces no power. At a defined point known as the maximum power point (MPP), a solar cell reaches its maximum power and thus $P = P_m$, $I = I_m$ and $V = V_m$ and this is clear in **Fig.1**. The power of a solar cell can produce at the MPP is always lower than the hypothetical value obtained by multiplying open-circuit voltage V_{oc} by short-circuit current I_{sc} . The ratio of P_m

to the product of V_{oc} and I_{sc} is a key measurement value of a solar cell, along with efficiency. This ratio is known as the Fill Factor, FF as shown in Eq.(1):

$$FF = \frac{P_m}{V_{oc} I_{sc}} \quad (1)$$

- The fill factor is a measure of the squareness of the current-voltage (I–V) curve and it is an indicator for how the total internal electrical resistances effect the output current. A squarer curve indicates a greater maximum power and ideality. The closer this number is to 1 the more square the curve is but that is in an ideal non-exist case. Commercially available solar cells' fill factor ranges from around 60% to 80%, while this factor for lab cells can go as high as about 85%.

3. EXPERIMENTAL SETUP

Performance of four different (PV) solar modules are tested for five months from 1st January to 1st June 2015 under solar radiation of 1000 W/m². The four tested solar modules were mono-crystalline silicon, poly-crystalline silicon, amorphous silicon and copper indium gallium diselenide (see **Fig.2**). The tests were done under the outdoor exposure in Baghdad city, at the energy laboratory / department of energy Engineering / Baghdad University. The electrical specifications of the modules at standard test conditions STC (solar radiation of 1000W/m², air mass AM 1.5, cell temperature 25°C) are presented in **Table 1**.

The four modules were placed on a steel holding stand which is not fixed to the ground but movable to follow the sun and keep the incident irradiance at the required value (1000 W/m²) as shown in **Fig.3**. Solar module analyzer PROVA 200A is used to test the characteristics (V_{oc} , I_{sc} , P_m , I_m and V_m), efficiency and Fill Factor of solar panel, also provides the IV and PV curves. Solar radiation was kept constant as possible, Solar Power Meter TES1333R is used to measure the total incident solar radiation (see **Fig.4**). The temperature of the modules was measured using digital thermometer (TPM-10) attached firmly to the back of the module. **Table 2** provides some of the technical specifications of the apparatus used in this study.

4. RESULTS AND DISCUSSION

The monthly average temperature of the four modules and the ambient are shown in **Fig.5** only for the time of doing the tests which was mostly between 9 AM to 1 PM for the months 1st January until 1st June, 2015. The pattern of how much the modules were heated does not change noticeably. The poly-crystalline module which has large area had nearly 20°C above the ambient temperature while the temperature of the CIGS module with much smaller area was 15°C. In June or July, it is expected that the tendency of the solar module still to heat up in the same and may be more because of the solar radiation and the shortage in wind speed. Usually in summer, in the afternoon time where the solar radiation reaches its maximum values, the recorded

ambient temperature in those months may reach 50°C, which means the solar modules may have operation temperature over 75°C.

In general, current-voltage curve is the most informative curve for testing the performance of any PV module or array. **Fig.6** illustrates the effect of temperature on the I-V curve for the four modules. Two arbitrary selected temperatures showed great influence on the output voltage especially on open circuit voltage while small increase in the output current has been noticed. Another important characteristic curve is the P-V curve which is shown in **Fig.7**.

A scatter plot is used to analyze the data of the maximum power output, open circuit voltage and short circuit current against the operating module temperatures. The scatter plot shows that there is a linear relationship between them and the operating module temperature. The temperature coefficient (TCO) is defined as the amount of change in V_{oc} , I_{sc} or P_m with temperature. TCO considered to be equal to the slope of the linear equation as given in Eq.(2), the value of the slope of each straight line equation is provided by Microsoft Office/Excel using linear regression fitting option. the TCOs of P_m , I_{sc} or V_{oc} are symbolized as the following:

$$\mu_{V_{oc}} = \frac{\Delta V_{oc}}{\Delta T} \quad , \quad \mu_{I_{sc}} = \frac{\Delta I_{sc}}{\Delta T} \quad , \quad \mu_{P_m} = \frac{\Delta P_m}{\Delta T} \quad (2)$$

Temperature variation effects greatly on the output voltage as the open circuit voltage have a logarithmic relationship with the inverse of the reverse saturation current which is greatly influenced by temperature. In **Fig.8**, pc-Si module showed a decrease by -0.0912V/°C while both mc-Si and a-Si had nearly the same $\mu_{V_{oc}}$ with nearly -0.07V/°C and the CIGS has -0.0123V/°C. The voltage ratio which is the measured open circuit voltage to the value at STC decreased from 98% to 85% when the temperature increased from 22°C to 63°C for mc-Si as presented in **Fig.9** on the other hand the pc-Si, a-Si and CIGS lost 17%, 11.5% and 14% respectively. The difference in $\mu_{V_{oc}}$ between the four modules is due to the value of the band gap energy characterized for each semiconductor and the recombination rates which greatly increased with temperature level. Another factor influence the decrease in open circuit voltage is the impurities and the deformation in the semiconductors crystals which represents a source of recombination. That explains why the pc-Si has the largest $\mu_{V_{oc}}$.

A scatter plot illustrates the linear relationship represented by a linear regression equation with the positive slope which shows slightly increase in I_{sc} with temperature increasing and this effect can be neglected as shown in **Fig.10**. Both poly-crystalline silicon and amorphous silicon modules have larger $\mu_{I_{sc}}$ than the other two modules. This increasing of the output current is a result of the decrease in the band gap energy because the electrons gain thermal energy added to the electromagnetic radiation energy required to liberate the electrons from the valence band in the semiconductor material to the conduction band where the electrons are free to move and the current is generated. This increase is still relatively small and compensate slightly the drop in voltage which is clear in mc-Si module where the temperature effect I_{sc} on can be neglected.

In **Fig.11** the maximum power plotted against the module temperature. mc-Si showed a degradation of 0.1353W for each degree centigrade. pc-Si, a-Si and CIGS have μ_{P_m} of -0.0915, -0.0114 and -0.0276W/°C respectively.

For better representation of how much does the module temperature decreases the output power, change the temperature coefficient in the form of the performance ratio (PR) which is defined as the output power produced at any condition to the power produced at STC:

$$PR = \frac{P_m \text{ at any operation conditions}}{P_m \text{ at STC}} \quad (3)$$

Fig.12 shows the monthly average performance ratio (PR). In May, the mono-crystalline silicon module lost about 15% of its power in January and it's expected to reach more than 20% in June or July. While the Amorphous silicon lost only about 5.5% in May.

The relation of the fill factor with module temperature is important to understand the effect of temperature on the combination of series and shunt resistances. The results is shown in **Fig.13**.The results showed that the fill factor decrease with about 0.1-0.17%/°C for the different module. Which, means that the temperature does not have the great influence on the resistances.

Table 3 summarize the temperature coefficients of the aforementioned output parameters of the four PV module used in this work. **Table 4** introduces a comparison between the temperatures coefficients of maximum power obtained in this work with the a sample of other previous work such as **Radziemska, 2003, Virtuani et al., 2010, El-Shaer et al., 2014, Spataru et al., 2014, Dash and Gupta, 2015, Shaari et al., 2009, Makrides et al., 2009 and Buday, 2011**. Those works studied the temperature effect on the performance of different types of PV modules.

5. CONCLUSION

From the previous results, the following points can be concluded:

- Regardless the wind speed effect on the module temperature, the module temperature on the most is greater by 10-15°C than the ambient temperature.
- It is found from the analysis that a-Si and CIGS photovoltaic modules seem to be better option in hot climates considering the temperature loss to be minimum due to low temperature coefficient. However the choice still depend on the module efficiency, installation area and the capital cost.
- With temperature increasing, the reverse saturation current increases rapidly causes major drop in voltage rate. Also the photon generation slightly increases as a result of the reduction in band gap. Hence this leads to marginal changes in current.
- Fill Factor seemed to be has little dependence on the module temperature for tested modules. Therefore the temperature effect on the parasitic internal resistances can be neglected.

**REFERENCES**

- Buday, M. S., 2011, *Measuring Irradiance, Temperature and Angle of Incidence Effects on Photovoltaic Modules in Auburn Hills, Michigan*. Thesis for Master of Science/Sustainable Systems (Natural Resources and Environment) at the University of Michigan.
- Dash, P. K., Gupta, N. C. , 2015, *Effect of Temperature on Power Output from Different Commercially available Photovoltaic Modules*, Journal of Engineering Research and Applications, Vol. 5, Issue 1(Part 1), PP.148-151.
- Dincar, I., 2003, *The Role of Energy in Energy Policy Making*. Energy Policy Vol 30, PP. 137-149.
- El-Shaer, A., Tadros, M. T. Y., Khalifa, M. A., 2014, *Effect of Light intensity and Temperature on Crystalline Silicon Solar Modules Parameters*, International Journal of Emerging Technology and Advanced Engineering, Volume 4, Issue 8, PP. 311-326.
- Lim, J.L., Woo, S.C., Jung, T.H., Min, Y.K., Won, C.S., Ahn, H.K., 2013, *Analysis of Factor on The Temperature Effect on The Output of PV Module*. Transactions of the Korean Institute of Electrical Engineers, 62, PP. 365-70.
- Makrides, G., Bastian, Z., George, E.G., Markus, S., Jurgen, H.W., 2009, *Temperature Behaviour of Different Photovoltaic Systems Installed in Cyprus and Germany*. Solar Energy Materials and Solar Cells, 93: PP.1095-99.
- Makrides, G., Zinsser, B., Phinikarides, A., Schubert, M. and Georghiou, G.E., 2012, *Temperature and Thermal Annealing Effects on Different Photovoltaic Technologies*. Renewable Energy; 43: PP.407-17.
- Mattei, M., Notton, G., Cristofari, C., Muselli, M. and Poggi, P., 2006, *Calculation of The Polycrystalline PV Module Temperature Using a Simple Method Of Energy Balance*. Renewable Energy, Vol. 31, PP.553–567.
- Nelson, J., 2003, *The Physics of Solar Cells: Properties of Semiconductor Materials*. Imperial College Press, London.
- Radziemska, E. , 2003, *The Effect of Temperature on The Power Drop in Crystalline Silicon Solar Cells*, Renewable Energy, (28) PP. 1–12.
- Shaari, S., Sopian, K., Amin N. and Kassim M., 2009, “*The Temperature Dependence Coefficients of Amorphous Silicon and Crystalline Photovoltaic Modules Using Malaysian Field Test Investigation*”. American Journal of Applied Sciences 6 (4): PP.586-593.



- Spataru, S., Sera, D., Kerekes, T., 2014, Teodorescu, R., Cotfas, P. A., and Cotfas, D. T., *Experiment Based Teaching of Solar Cell Operation and Characterization Using the SolarLab Platform*. 7th International Workshop on Teaching in Photovoltaics.
- Virtuani, A., Pavanello, D., Friesen, G. , 2010, *Overview of Temperature Coefficients of Different Thin Film Photovoltaic Technologies*, Proc. 25th Europ. Photovolt. Solar Energy Conf, PP.4248–4252.
- Vokas, G., Christandonis N, Skittides F., 2006, *Hybrid Photovoltaic Thermal Systems for Domestic Heating and Cooling- Theoretical Approach*. Solar Energy; 80: PP.607–15.

NOMENCLATURE

A = diode ideality factor, dimensionless.

A_m = surface area of the solar module, m^2 .

AM = air mass, dimensionless.

I = output current of the solar module, A.

I_m = current at maximum power point, A.

I_{sc} = short circuit current, A.

N_s = number of solar cells connected in series.

P_m = power at maximum power point, W.

PR = performance ratio, dimensionless.

T = temperature, °C.

TCO = temperature coefficient, $X/^\circ\text{C}$ where $X=V$, A or W.

V = output voltage of the solar module, V.

V_m = voltage at maximum power point, V.

V_{oc} = open circuit voltage, V.

μ_X = temperature coefficient of X where X is P_m , V_{oc} or I_{sc} .

Table 1. Solar module specifications (available from the manufacturer datasheet).

	mc-Si	pc-Si	a-Si	CIGS
Area [m ²]	0.26	0.46	0.147	0.055
V _{oc} [V]	22	23	27	3.5
I _{sc} [A]	1.9	1.7	0.35	2.7
V _m [V]	17	17.45	18	2.8
I _m [A]	1.76	1.375	0.227	2.5
P _m [W]	30	26	5	7
Ns	36	40	18	6

Table 2. Measurement apparatus range, resolution and accuracy.

	Measuring range	Resolution	Accuracy
Solar module analyzer PROVA 200A			
DC voltage measurements	0-60 V	0.001-0.01 V	±1% ±(1% of Voc±0.09 V)
DC current measurements	0-6 A	0.1-1 A	±1% ±(1% of Isc±0.9 mA)
Solar power meter TES1333R			
Solar Radiation measurements	0-2000 W/m ²	0.1 W/m ²	±10 W/m ² or ±5%. higher temperature induced error of ±0.38 W/m ² /°C from 25°C
Digital thermometer TPM-10			
Temperature measurement	-50~70 °C	0.1 °C	±1 °C

Table 3. Temperature coefficients summary.

		mc-Si	pc-Si	a-Si	CIGS
$\mu_{V_{oc}}$	V/°C	-0.0734	-0.0912	-0.0727	-0.0123
	%/°C	-0.3336	-0.3965	-0.2693	-0.3514
$\mu_{I_{sc}}$	A/°C	0.0003	0.0044	0.0009	0.0009
	%/°C	1.58E-4	0.00251	0.00257	0.0003
μ_{P_m}	W/°C	-0.1353	-0.0915	-0.0114	-0.0276
	%/°C	-0.45	-0.352	-0.228	-0.39

Table 4. Maximum power degradation comparison with some previous studies.

	mc-Si		pc-Si		a-Si		CIGS	
	W/°C	%/°C	W/°C	%/°C	W/°C	%/°C	W/°C	%/°C
Our Results	0.1353	0.45	0.0915	0.352	0.0114	0.228	0.0276	0.39
Radziemska, 2003	-	0.65	-	-	-	-	-	-
Shaari et al., 2009	0.1742	-	0.2525	-	0.1036	-	-	-
Makrides et al., 2009	-	0.456	-	0.502	-	0.0461	-	-
Virtuani et al., 2010	-	-	-	-	-	0.13	-	0.36
Buday, 2011	-	0.5	-	-	-	0.0021	-	0.24
El-Shaer et al., 2014	-	0.25	-	0.14	-	-	-	-
Spataru et al., 2014	-	0.4546	-	-	-	0.04	-	-
Dash and Gupta, 2015	-	0.446	-	0.387	-	0.234	-	-

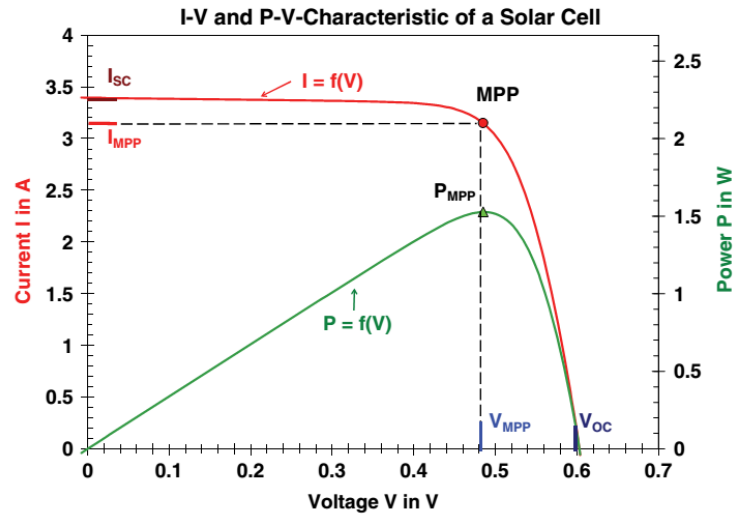


Figure 1. Characteristic curves I-V and P-V of a mono-crystalline silicon solar cell with a cell area of 102 cm^2 .

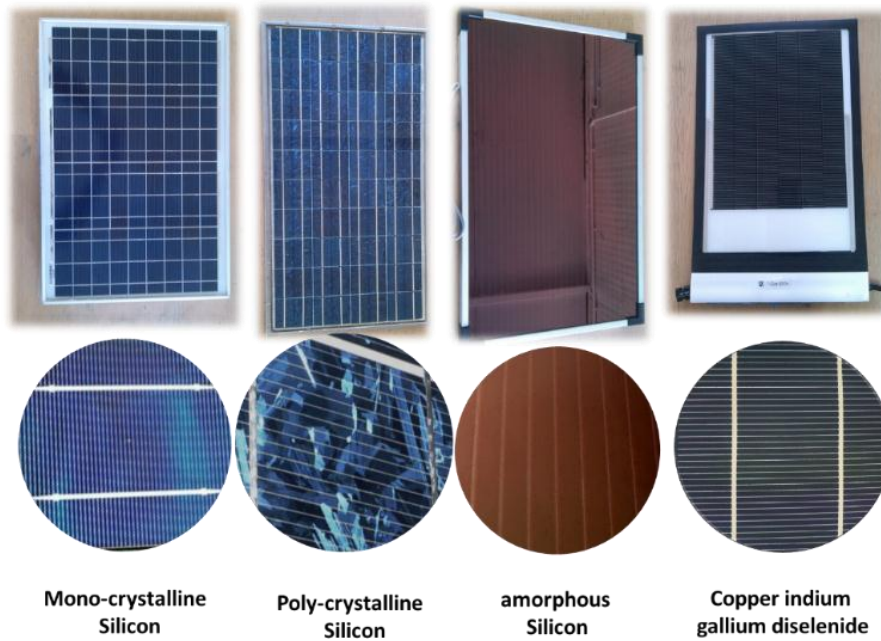


Figure 2. The four PV modules used in the test and close up views.

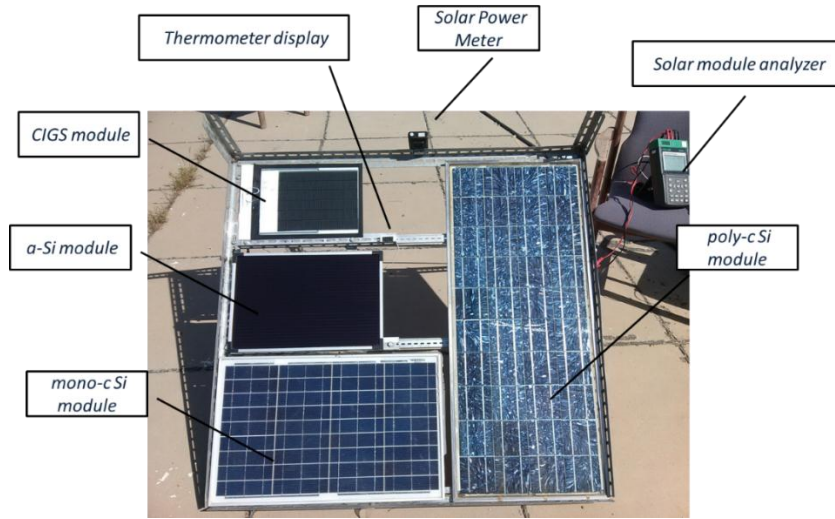


Figure 3. Experimental setup.



Figure 4. Measuring apparatus from left to right: solar module analyzer, Solar Power meter and digital thermometer.

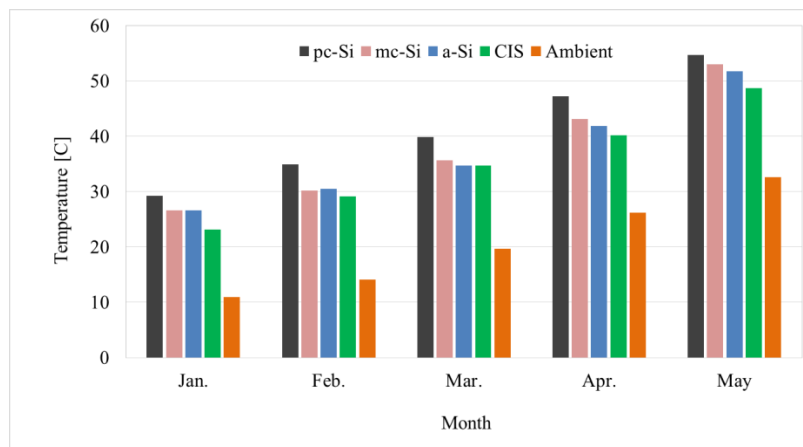


Figure 5. The monthly average temperature of the four modules and the ambient.

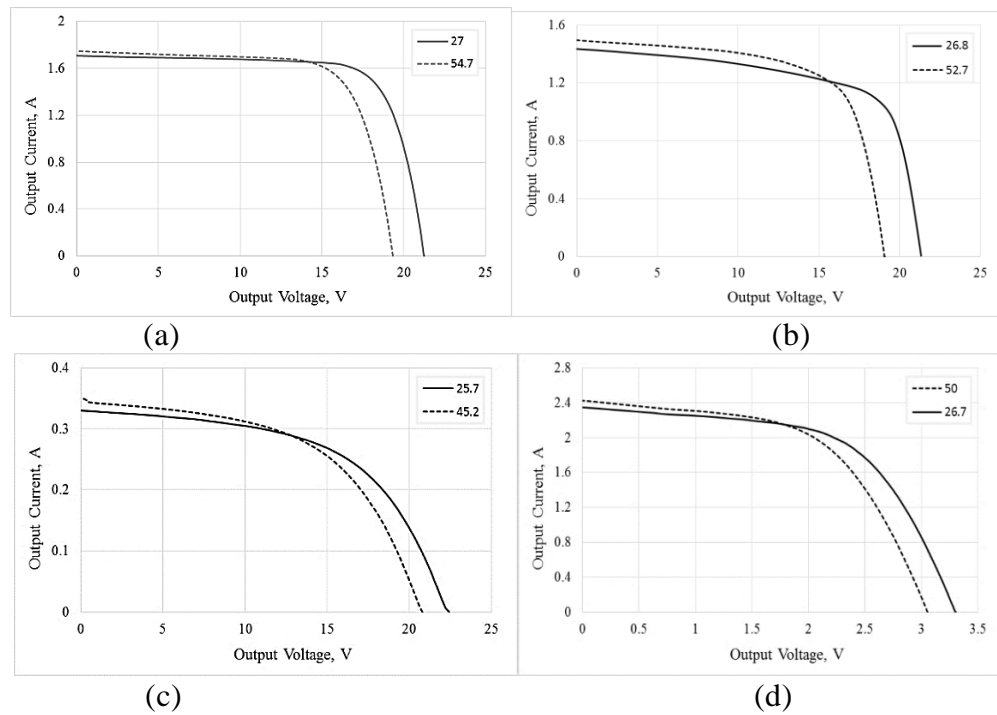


Figure 6. Current-Voltage curve at solar radiation of 1000W/m^2 and two different selected temperatures in $^{\circ}\text{C}$, for (a) mc-Si (b) pc-Si (c) a-Si (d) CIGS modules.

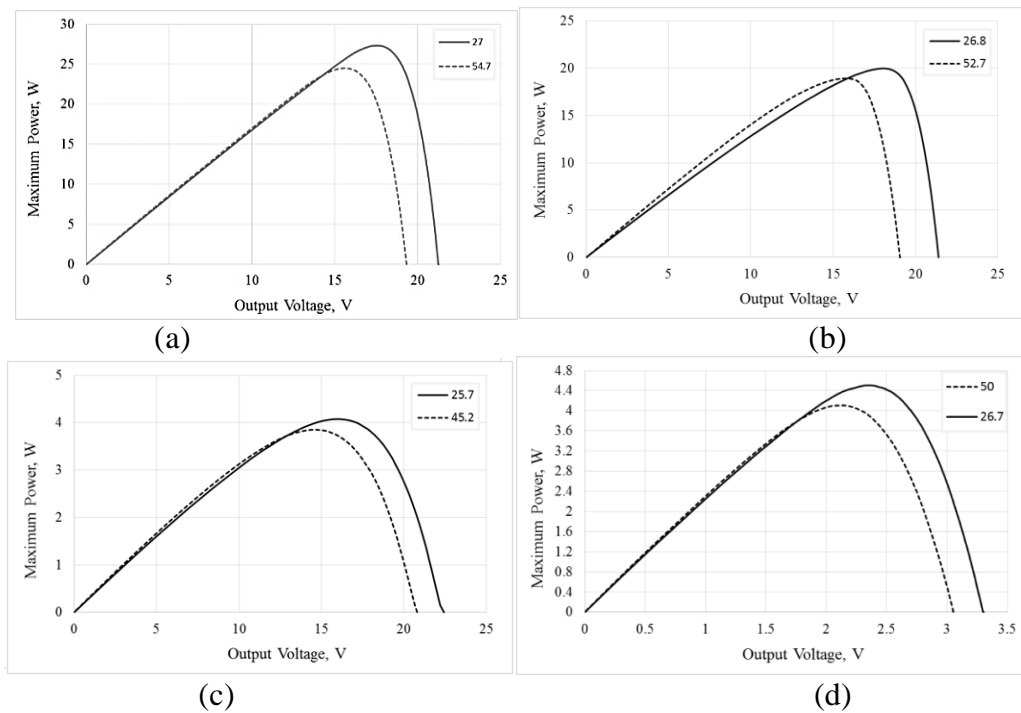


Figure 7. Power -Voltage curve at solar radiation of 1000W/m^2 and two different selected temperatures in $^{\circ}\text{C}$, for (a) mc-Si (b) pc-Si (c) a-Si (d) CIGS modules.

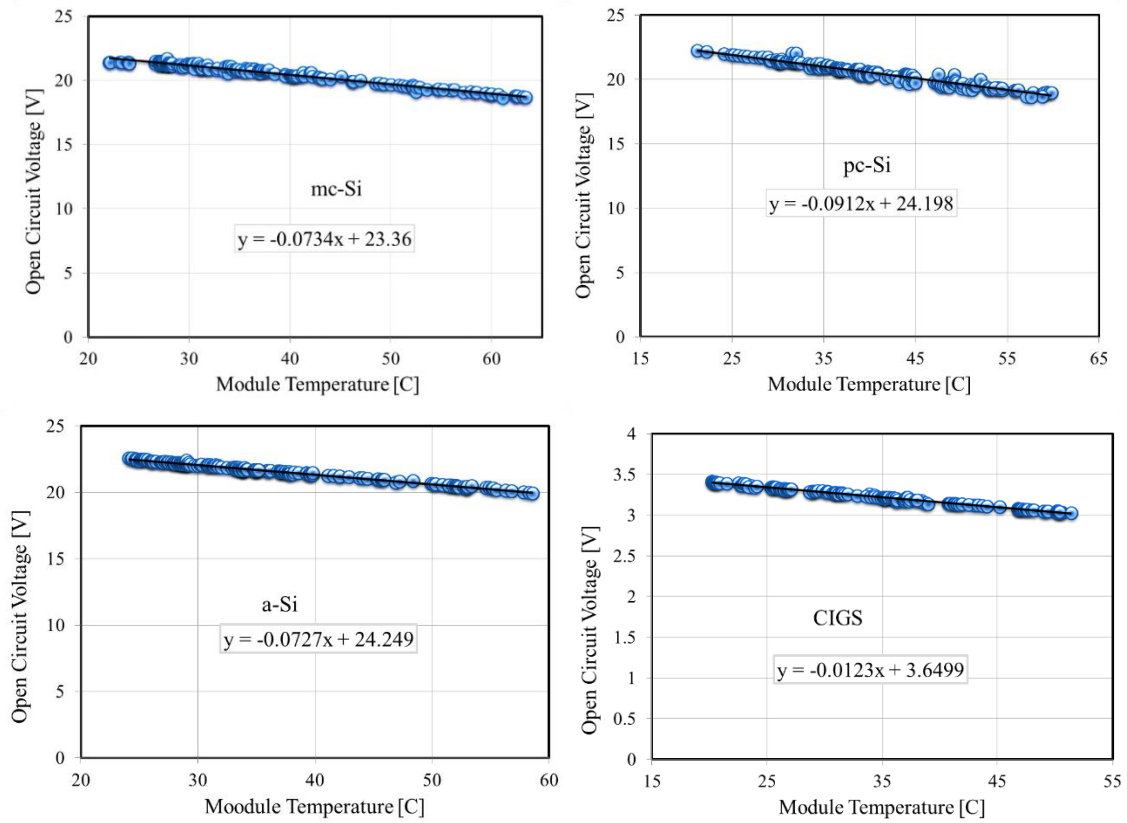


Figure 8. Experimental open circuit voltage vs. module temperature for the four modules.

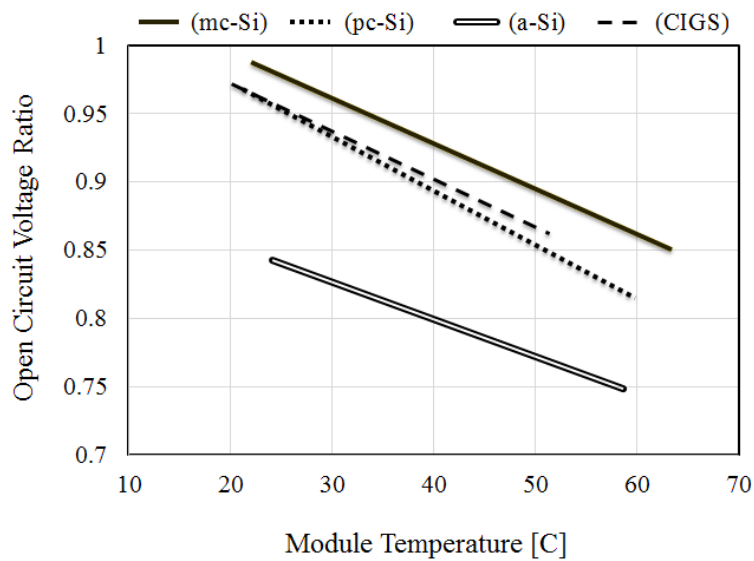


Figure 9. Open circuit voltage ratio vs. module temperature for the four modules.

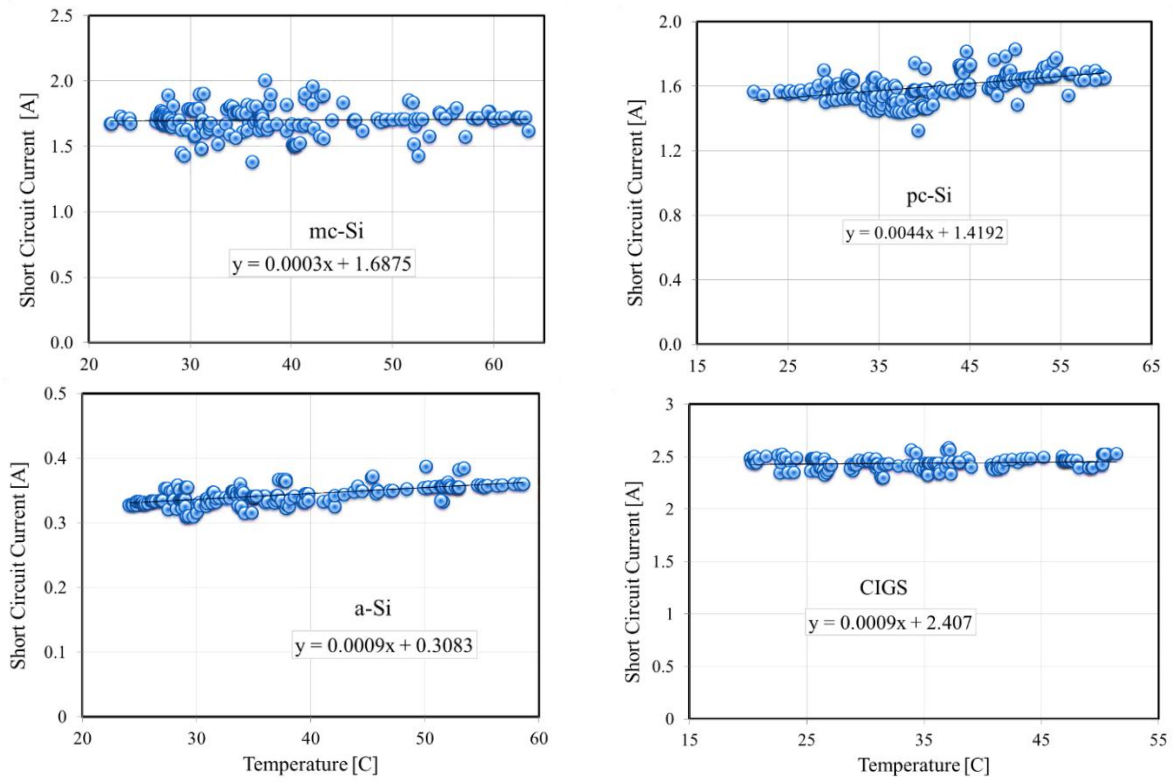


Figure 10. Experimental short circuit current vs. module temperature for the four modules.

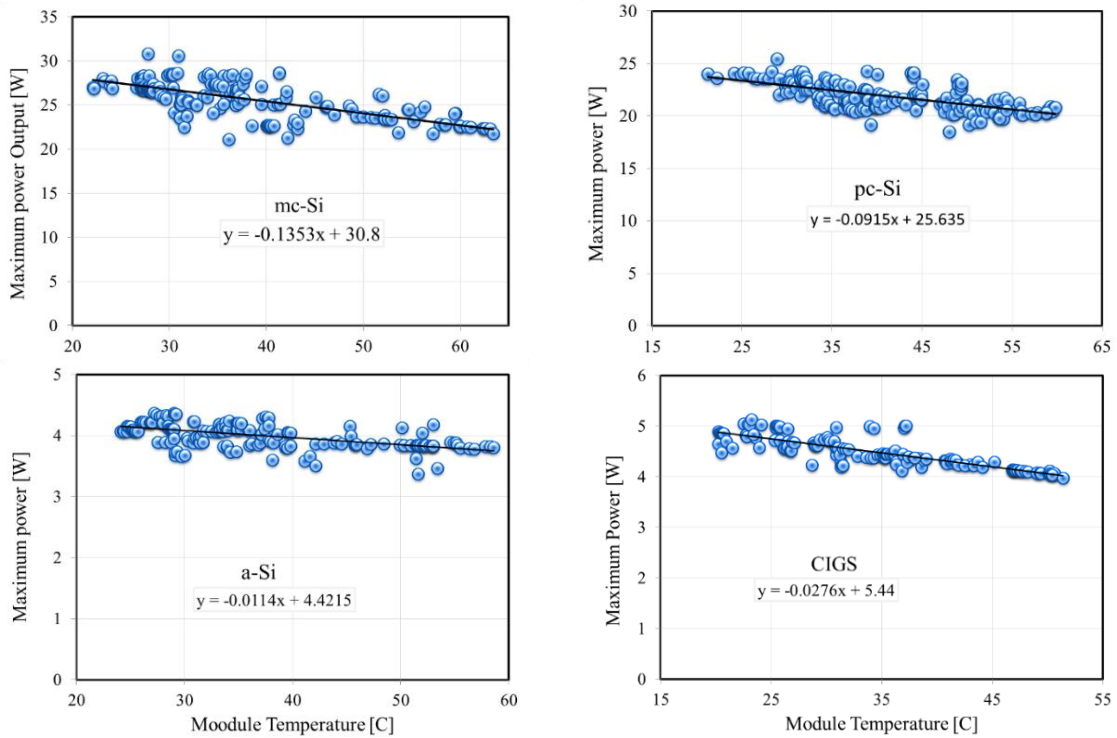


Figure 11. Maximum power output vs. module temperature for the four modules.

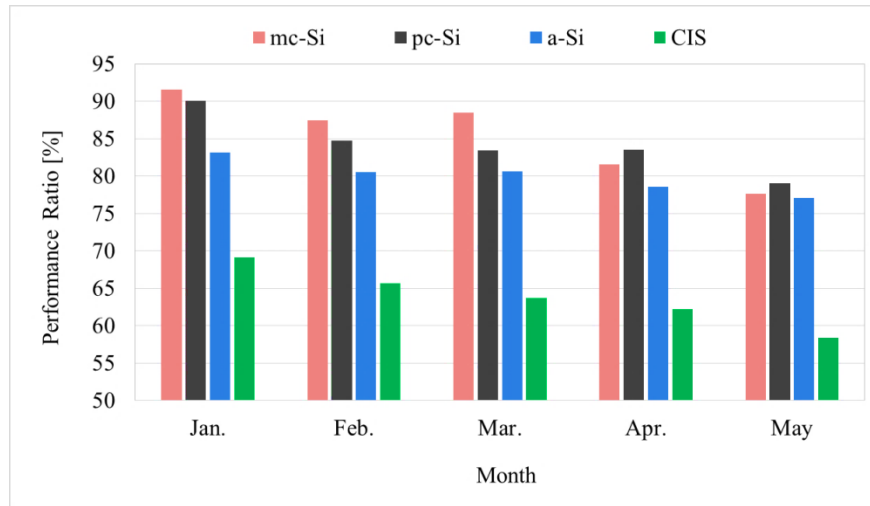


Figure 12. Monthly averaged performance ratio for the four modules.

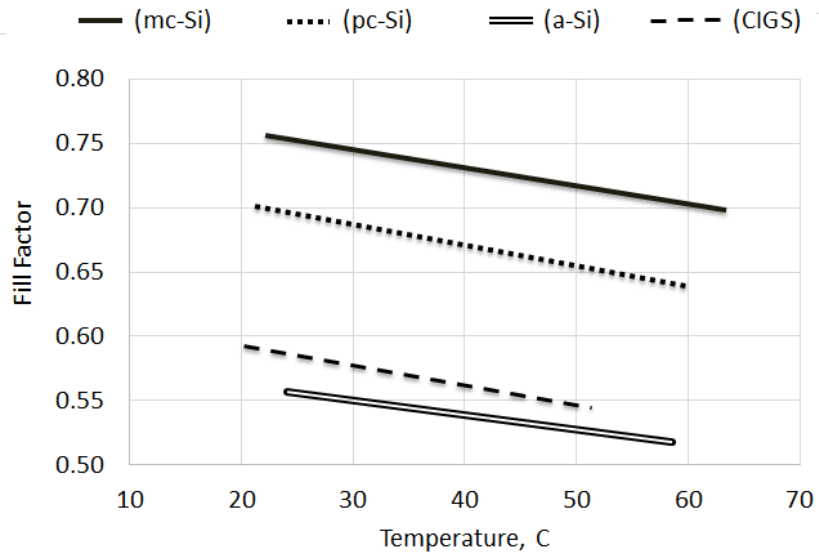


Figure 13. Temperature effect on the fill factor

Experimental Investigation of Convection Heat Transfer Enhancement in Horizontal Channel Provided with Metal Foam Blocks

Dr. Mohammed Abdulraouf Nima

Lecturer

Mechanical Engineering Department
College of Engineering- Baghdad University
E-mail: dralsafi@uobaghdad.edu.iq

Abbas Husain Hajeej

MSc. Student

Mechanical Engineering Department
College of Engineering- Baghdad University
E-mail: abbas_eng1@yahoo.com

ABSTRACT

Convection heat transfer in a horizontal channel provided with metal foam blocks of two numbers of pores per unit of length (10 and 40 PPI) and partially heated at a constant heat flux is experimentally investigated with air as the working fluid. A series of experiments have been carried out under steady state condition. The experimental investigations cover the Reynolds number range from 638 to 2168, heat fluxes varied from 453 to 4462 W/m², and Darcy number 1.77x10⁻⁵, 3.95x10⁻⁶. The measured data were collected and analyzed. Results show that the wall temperatures at each heated section are affected by the imposed heat flux variation, Darcy number, and Reynolds number variation. The variations of the local heat transfer coefficient and the mean Nusselt number are presented and analyzed. The mean Nusselt number enhancement was found to be more than 80% for all the studied cases.

Key words: convection heat transfer, metal foam, constant heat flux.

دراسة عملية لتحسين انتقال الحرارة بالحمل في قناة أفقية مزودة بكتل من رغوة معدنية

عباس حسين هجيج
قسم الهندسة الميكانيكية
كلية الهندسة- جامعة بغداد

المدرس الدكتور محمد عبد الرؤوف نعمة
قسم الهندسة الميكانيكية
كلية الهندسة- جامعة بغداد

الخلاصة

أنتقال الحرارة بالحمل في قناة أفقية مزودة بكتل ذات رغوة معدنية لعددين من المسامات لكل وحدة طول (10 و 40 ثقب لكل بوصة) وبتسخين جزئي بثبوت الفيض الحراري قد تم دراسته عملياً مع استخدام الهواء كمائع مشغل. تم إجراء عدد من التجارب العملية وعند الوصول لحالة الاستقرار تم جمع البيانات وتحليلها. شملت الدراسة العملية لمدى رقم رينولدز من 638 الى 2168 وفيض حراري متغير من 453 واط/م² الى 4462 واط/م² ورقم دارسي 1.77x10⁻⁵، 3.95x10⁻⁶. أظهرت النتائج تأثير درجات حرارة الجدار في كل جزء مسخن بتغير الفيض الحراري المسلط وتغير رقم رينولدز ودارسي. تغير معامل انتقال الحرارة الموضعي و متوسط رقم نسلت قد تم أظهارها وتحليلها. وجد أن التحسن في متوسط رقم نسلت أكثر من 80% لجميع الحالات التي تم دراستها.

الكلمات الرئيسية: انتقال الحرارة بالحمل، رغوه معدنية، فيض حراري ثابت.

1. INTRODUCTION

Convection heat transfer in a horizontal channel that provided with heated metal foam blocks of different PPI has a considerable technological interest. This is due to the wide range of applications such as electronic cooling, heat exchangers, nuclear power generation, filtration, and separation. A porous medium is considered as an effective enhancement method of heat transfer due to their intense mixing of the flow and their large surface area to volume ratio. Because of the random structures of porous mediums, they are different in their engineering, physical and thermal properties. Metal foams are class of porous materials with unique properties that are used in several structural and heat transfer applications. Metal foams are being produced as open-cell (functional) and closed-cell foams (structural). Open-cell metal foam consists of pores that are open to their neighboring pores and allow the fluid to pass through them. The closed-cell metal foams have a thin layer of metal dividing the individual pores. **Huang and Vafai, 1994** performed a numerical study of forced convection in a channel with four porous blocks. The Brinkman-Forchheimer-extended Darcy model was used to simulate the flow in the porous medium and the Navier-Stokes equation in the fluid region. They showed that a significant heat transfer augmentation can be achieved by adding the porous blocks. **Hadim, 1994** studied numerically the laminar forced convection in a fully or partially filled porous channel contains with discrete heat sources flush-mounted on the bottom wall. In the both cases, partial and fully porous channel, results show that the Nusselt number increased when the Darcy number was decreased. Results also show that the heat transfer in the both cases was almost the same increase (especially at low Darcy number), while the pressure drop was much lower in the partially filled channel. **Rachedi and Chick, 2001** investigated numerically the electronic cooling enhancement by insertion of foam materials. This technique based on inserting the porous or foam material between the components on a horizontal board. The Darcy -Brinkman-Forchheimer model was used to describe the fluid motion in the porous media. Results indicated that for a high thermal conductivity porous substrate, substantial enhancement is obtained compared to the fluid case even if the permeability is low. In the mixed convection case, inserting the foam between the blocks lead to a remarkable reduction in temperature of 50%. **Chikh et al., 1998** numerically studied force convection heat transfer in a parallel plate channel, with equally spaced porous blocks attached on the partially heated lower plate. The Darcy-Brinkman-Forchheimer equation was used to simulate the flow in the porous regions. Results show that for porous blocks with low permeability, recirculation zones appear between the blocks and prevent the fluid from going through the next blocks. The local Nusselt number was increased with a decreased in the wall temperature up to 90% by insertion of porous blocks. **Guerroudj and Kahalerras, 2010** studied numerically mixed convection in a channel provided with porous blocks of various shapes that subjected to constant heat flux from the lower plate. The considered shapes vary from the rectangular shape ($\gamma = 90^\circ$) to the triangular shape ($\gamma = 50.2^\circ$). Results indicated that when the mixed convection (Gr/Re^2) increased, the global Nusselt number increased, especially at small values of permeability for triangular shape. At small values of the Reynolds number, Darcy number, thermal conductivity ratio and porous blocks height, the triangular shape lead to high rate of heat transfer. The highest pressure drop was obtained with the rectangular shape due to its volume which the highest in comparison to the others shapes.

Kurtabas and Celik, 2009 investigated experimentally the mixed convective heat transfer in rectangular channel where the channel filled with open-cells aluminium foams with different number of pores per unit of length (PPI) with constant porosity ($\epsilon=0.93$). The channel was heated from the top and bottom by uniform heat flux. Results indicated that the average Nusselt number increased relative to the pore densities. Results also showed that at high values of the Reynolds number and Grashof number, the local Nusselt number increased rapidly.

To the best of the authors' knowledge, there is no existing experimental study on the convection heat transfer in a horizontal channel that provided with metal foam blocks of different number of pores per unit of length (PPI) and partially heated at constant heat flux. So the present study was proposed to cover this shortage in the understanding of the fluid flow and heat transfer characteristics in metal foam with convection effects.

In the present work, convection heat transfer in a horizontal channel that provided with metal foam (copper foam) blocks of different (PPI) and subjected to a constant heat flux, is experimentally examined with air as the working fluid. The main objective is to study the influence of convection heat transfer on the flow field and the associated heat transfer process in such system. The influence of heat flux, Darcy number, and Reynolds number variation on wall temperatures and Nusselt number are investigated and analysed.

2. EXPERIMENTAL APPARATUS AND PROCEDURE

2.1 Experimental Apparatus

The experimental investigation is carried out in the apparatus shown in **Fig.1**. The apparatus has been constructed in the Heat Transfer Lab, at the Mechanical Engineering Department, University of Baghdad to achieve the requirements of the present study and it consists of the following major assemblies:

1- The Wind Tunnel

A driven type, low speed wind tunnel with solid wood walls was used in the present work. The general arrangement of this tunnel is shown photographically in **Fig.2**. The wind tunnel has the following parts and features;

- A conical inlet section of 500 mm length. The conical section inlet diameter is 70 mm and its outlet is designed as a rectangular section (100 mm x 50 mm).
- A calming (entry) section of 150 mm length.
- The test section is made up from Perspex material (10 mm thickness) from three sides (left, right and top) while the bottom side is made up of solid wood. The left and right sides dimensions are (250 mm x 100mm), and the top and bottom sides dimensions are (250 mm x 50 mm) as sketched in **Fig.3**.
- Exit section of 1500 mm length.
- A blower that driven by a one phase A.C motor with a speed of 2800 RPM.
- The valve by which the flow rate of air can be controlled and bypass.

2- Heating System

Three heaters are used in the present study. Each heater is made from the zigzag coil with a 0.5mm diameter and length 1050 mm made from nickel-chrome wire, putting on a mica sheet of 0.4mm thick to ensure electrical insulation. The zigzag coils as shown in **Fig.3a** are covered from the top and bottom with mica sheets. Bottom side of the each heater was insulated by a Teflon plate (16 mm thickness) and the top side served as the heating surface unit that covered by copper plate (1.5mm thickness) to ensure a uniform distribution of the supplied heat flux. The Teflon was chosen because of its low thermal conductivity in order to reduce the heat loss from the heaters bottom. Then the test section is well insulated from bottom with a glass wool and kaowool layer of 20, 60 mm thickness respectively. The heaters are supplied with the AC-current in series from a two transformer (Variac), to control the incoming current according to the heat flux desired. Thermal grease is used between the heated section and the metal foam blocks to achieve better contact between them.

3- The Thermocouples Network

The temperature distribution of the enclosure test section was measured by twenty four K-type thermocouples. There are fifteen thermocouple used to measure the air bulk temperature distribution inside the test section and distributed within five sections along the test section as sketched in **Fig.4a**. Three thermocouples are positioned on each heater to measure the temperature distribution along the copper plate surface. The mean value of the measured air temperature is used as the air temperature at that section.

The thermocouples were fixed on the copper plate surface by drilling (V) holes of 1 mm in diameter and 0.5 mm deep. Then the thermocouples junctions were fixed by the solder. The excess solder was removed and the copper plate surface was cleaned carefully by fine grinding paper. All the thermocouples wires and heater terminals were taken out the test section through the Perspex material and the insulation material, respectively.

In the case of adding full length rectangular metal foam blocks, another seven K-type thermocouples are added for each block as shown in **Fig.4b**. Four thermocouples are used to measure the metal foam wall temperature distribution by soldering them with metal foam wall. The other three thermocouples are used to measure the air bulk temperature that flow through the metal foam block.

The outer covering shield is removed from each thermocouple in order to reduce the space it takes inside the metal foam block. The thermocouples are fixed on the metal foam surface by the solder.

Finally, the temperature distribution on the lower surface of the insulation shield was measured by employing two K-type thermocouples distributed in an equal pitch, to calculate the heat transfer lost during the experiment, which is found to be approximately 3% during the whole range of the imposed heat flux.

2.2 Measuring Systems

1- Temperature Measuring System

The thermocouples were connected to a data acquisition system, consisting of NI CompactDAQ chassis with three NI 9213 16-channel thermocouple input model, with LabVIEW 2009 software to record the temperature measurements.

2- Pressure Drop Measuring System

The measurement of pressure drop is interesting consideration to study in the metal foam as it related to the characteristics of the metal foam blocks.

3- Pressure Taps Positions

For pressure drop measurements, four pressure taps of inner diameter 3 mm were placed on four locations long the flow direction on the top side with a uniform spacing of 75 mm as sketched in **Fig.4a**. The pressure drop in the test section is measured by micromanometer.

4- Electrical Power Measurement

The constant heat flux is supplied by using electrical circuit of alternating current that includes:

- A) Voltage regulator.
- B) Transformer.
- C) Voltmeter.
- D) Clamp meter.

2.3 Experimental Procedure

The experiments are repeated with varying some parameters to study their effect on the temperature distribution, pressure drop and Nusselt number. These parameters are:

1. Porosity (90.302%) for 10 PPI and (89.81%) for 40 PPI.
2. Air flow rate range (3, 7, and 9 m³/hr.).
3. Heat flux range (453, 1862, 3007, and 4462 W/m²).

The experiments has been started by operating the blower and adjusting the required air flow rate by regulating valve, then the electrical power switched on and the heaters input voltage is adjusted by the transformer (Variac) to give the required voltage and current to calculate the electrical power in accordance to the heat flux required. The apparatus is left at least for two hours to reach the steady state condition. The thermocouples readings are recorded every half an hour by the data acquisition system until the reading became almost constant (temperature did not vary by more than 0.5°C in 30 min), a final reading is recorded at the steady state condition. During each test run, the following readings were recorded:

- a- Thermocouples reading in °C.
- b- Micro manometer reading (pressure drop) in Pa with the pressure of the metal foam.
- c- The heater voltage in volts.
- d- The heater current in amperes.

3. HEAT TRANSFER CALCULATIONS

The net heat flux that supplied at the copper plate is determined from recording the electrical power that supplied to the heater and applying the following equation;

$$P_o = I \times V_h \quad (1)$$

$$q = \frac{P_o}{3 \times A_h} \quad (2)$$

where P_o is the electrical power that consumed by the heaters, I is the current that flow through the heaters, V_h is the voltage across the heaters, and A_h surface area of each heated section.

The Reynolds Number and Darcy number are prescribed, following as;

$$Re = \frac{u_{in} D_h}{\nu} \quad (3)$$

$$Da = \frac{K}{D_h^2} \quad (4)$$

The local friction coefficient is given by:

$$f = \left(-\frac{dp}{dx}\right) \frac{D_h}{2\rho u^2} \quad (5)$$

The local heat transfer coefficient at the heated wall can be defined as:

$$h = \frac{q}{T_w - T_b} \quad (6)$$

Hence, the local and the mean Nusselt number can be calculated as, **Nield and Bejan, 2006**:

$$Nu = \frac{h D_h}{k} = \frac{q D_h}{k (T_w - T_b)} \quad (7)$$

$$Nu_m = \frac{1}{W} \int_{X_i}^{X_i+W} Nu dX \quad (8)$$

where X_i is the position of the block i from the channel entrance.

4. POROSITY AND DENSITY OF METAL FOAM

In general, porosity (ε) is the important property of metal foams, which depends on the volume of pores and the total volume of the sample that contains the copper foams. Measuring the volume of the copper foam sample was done after taken three readings for volume of three different samples for the same (PPI) and dimensions, and takes the average of these readings. Then porosity can be found from the equation;

$$\varepsilon = \left(1 - \frac{\rho_{cal.}}{\rho_{th.}}\right) \times 100 \% \quad (9)$$

where $\rho_{th.}$, theoretical density of pure copper (8933 kg/m^3), **Incropera et al. 2007**.

For the copper foams the average porosity was obtained at (90.302%) for 10 PPI and (89.81%) for 40 PPI. The average density of the copper foams was measured (866.301 kg/m³) for 10 PPI and (909.575 kg/m³) for 40 PPI.

5. PERMEABILITY OF THE METAL FOAM

The permeability can be found from a Darcy- Forchheimer relation:

$$\frac{\Delta P}{L} = \underbrace{\frac{\mu}{K}u}_{\text{Darcy term}} + \underbrace{\frac{\rho C}{\sqrt{K}}u^2}_{\text{Forchheimer term}} \quad (10)$$

$$\frac{\Delta P}{L} = A u + B u^2 \quad (11)$$

By comparing Eq. (10) with Eq. (11), permeability and inertial coefficient for each metal foam block can be written as:

$$K = \frac{\mu}{A} \quad (12)$$

$$C = \frac{B\sqrt{K}}{\rho} \quad (13)$$

The permeability (K) and inertial coefficient (C) of each metal foam block are experimentally determined by measuring the pressure drop across the test section at different air flow rate. To find permeability and inertial coefficient for each metal foam block, first A and B constants in Eq. (11) must be calculate by making a curve fitting (second order polynomial) for each curve in **Fig.5**. A and B values for each curve are listed in **Table 1**. **Table 2** lists the permeability and inertial coefficient for each metal foam block.

6. RESULTS AND DISCUSSION

A series of experiments have been carried out with a heat flux range from $q = 453 \text{ W/m}^2$ to 4462 W/m^2 and $Re = 638$ to 2168 . The temperature distribution along the three heaters surfaces is measured and presented. The influence of heat flux, Darcy number, and Reynolds number variation on the local heat transfer coefficient and the mean Nusselt number is discussed and analyzed.

6.1 Wall Temperature Distribution of the Heated Section

Figs. 6 and **7** show the effect of the imposed heat flux variation and Reynolds number variation on the distribution of the wall temperature at each heated section for the case of without metal foam blocks (fluid case) at $q=453, 1862$, and 3007 W/m^2 and $Re=638, 1594$, and 2168 . As expected, **Fig.6** shows that the wall temperature is increased at each heated section as the heat flux increased for the same Reynolds number value. When the imposed heat flux is increased (with a constant Reynolds number), the buoyancy effect increases and causes a faster growth in the thermal boundary layer along the surface at each heated section.

Fig.7 shows the influence of Reynolds number variation on the wall temperature distribution at each heated section for $q = 1862 \text{ W/m}^2$. It is obvious that the increasing of Reynolds number reduces the wall temperature at each heated section as heat flux is kept

constant. When the Reynolds number is increased the thermal boundary layer retreat along the heated wall at each heated section.

Another observation can be made from **Fig.7** that the difference between the temperature distribution values for different Reynolds number at the first heated section is maximum while this difference is minimum at the third heated section. This can be attributed to the fact that the thermal boundary layer thickness over the third heated section is greater than that over the first heated section and as a result the Reynolds number variation has a smaller effect on the temperature variation at the third heated section.

A general trend can be seen from **Figs.8-10** that the wall temperature values at the third heated section are higher than that at the first heated section due to the largest thickness of the thermal boundary layer over the third heated section. **Fig.8** shows the influence of the imposed heat flux variation on the the distribution of the wall temperature at each heated section for $Re=1594$, and $Da=1.77 \times 10^{-5}$. It can be seen that wall temperature is increased at each heated section as the heat flux increased for the same Reynolds number value. When the imposed heat flux is increased, the buoyancy effect increases and causes a faster growth in the thermal boundary layer along the surface at each heated section.

Fig.9 shows the effect of Reynolds number variation on the wall temperature distribution at each heated section for $q = 1862 \text{ W/m}^2$, and $Da=3.95 \times 10^{-6}$. It is obvious that the increasing of Reynolds number reduces the wall temperature at each heated section for the same heat flux value. When the Reynolds number is increased the thermal boundary layer retreat along the heated wall at each heated section.

Fig.10 shows the effect of insert metal foam blocks on the wall temperature distribution at each heated section for $q=1862 \text{ W/m}^2$, $Re=1594$, and $Da=1.77 \times 10^{-5}$, 3.95×10^{-6} . It can be seen that the wall temperature in the case of insert metal foam blocks is much lower than that in the case of without metal foam blocks (fluid case). The presence of the metal foam blocks caused part of heat to transfer from the heated section by mean of conduction through the metal foam blocks and the other part by mean of convection to the incoming fluid that passed over the heated section. The conducted heat through the metal foam block is then transferred to the incoming fluid by means of convection due to the high mixing that provided by the metal foam. The above mechanism that works in the case of metal foam presence increased the heat transfer from the heated section to the incoming fluid and increases the bulk temperature of air which means that air will gain more heat from the hot wall which leads to decrease the wall temperature at each heated section. The wall temperature at each heated section reduces more with a Darcy number decrease because of increasing in mixing which leads to increase in convected heat by air.

6.2 Local Heat Transfer Coefficient

A general behavior can be seen from the distribution of the local heat transfer coefficient in **Figs. 11-13** that the local heat transfer coefficient in all cases decreases with increase in the axial distance at each heated section. Since the heat transfer coefficient is based on the temperature difference with respect to the bulk temperature, this trend is expected as the largest temperature difference between the heated wall and the incoming cold fluid occurs at the leading edge of the heated section especially at higher Reynolds number. Therefore, the highest heat transfer rate

occurs at the leading edge of the heated section especially at first heated section which is nearest to the inlet.

Fig.11 shows the influence of the imposed heat flux variation on the distribution of the local heat transfer coefficient at each heated section for $Re = 2168$ and $Da = 1.77 \times 10^{-5}$. It can be seen that the local heat transfer coefficient is increased at each heated section as the heat flux increased for the same Reynolds number value. This can be attributed to the fact that for higher heat fluxes the buoyancy effect increases and the thermal boundary layer growth is more rapidly and causes a smaller temperature difference between the fluid bulk temperature and the heated wall temperature at each heated section.

Fig.12 shows the influence of Reynolds number variation on the distribution of the local heat transfer coefficient at each heated section for $q = 1862 \text{ W/m}^2$ and $Da = 3.95 \times 10^{-6}$. It can be seen that the local heat transfer coefficient is increased as the Reynolds number increased for the same heat flux value. When the Reynolds number is increased, a reduction in the thermal boundary layer thickness occurs with the domination of the incoming cold-fluid effect and this will cause a larger fluid mixing and higher local heat transfer coefficient values especially at first heated section which is nearest to the inlet.

Fig.13 shows the effect of Darcy number on the local heat transfer coefficient at each heated section for $q = 1862 \text{ W/m}^2$ and $Re = 1594$. It can be seen that the local heat transfer coefficient in the case of insert metal foam blocks is much higher than that in the case of without metal foam blocks (fluid case). **Fig.13** also shows that the local heat transfer coefficient for lower Darcy Number ($Da = 3.95 \times 10^{-6}$) is higher than that for higher Darcy Number ($Da = 1.77 \times 10^{-5}$). This can be attributed to the heat transfer enhancement that caused by the higher fluid mixing in the lower Darcy number metal foam block.

6.3 Mean Nusselt Number

A general behavior can be seen from **Figs.14-16** that the maximum mean Nusselt number value is located at the first block. This trend is expected as the largest temperature difference between the heated wall and the incoming cold fluid occurs at the first block. Therefore, the highest heat transfer rate occurs at the first heated section.

The variation of the mean Nusselt number with imposed heat flux along the heated wall at each block is presented in **Fig.14** for $Re = 1594$ and $Da = 1.77 \times 10^{-5}$. It can be noticed from **Fig.14** that the mean Nusselt number is increased as the heat flux increased at each block number for the same Reynolds number value.

Fig.15 shows the influence of Reynolds number variation on the mean Nusselt Number at each block for $q = 1862 \text{ W/m}^2$ and $Da = 3.95 \times 10^{-6}$. It can be seen that the mean Nusselt number is increased at each block as the Reynolds number increased for the same heat flux value. This can be attributed to the higher fluid mixing that associated with the domination of the incoming cold-fluid effect.

Fig.16 shows the effect of Darcy number on the mean Nusselt number at each block for $q = 1862 \text{ W/m}^2$ and $Re = 1594$. It can be seen that the mean Nusselt number in case insert of metal foam blocks enhanced the heat transfer from the heated sections compared with the pure fluid

case. **Fig.16** also indicate that the mean Nusselt number for $Da= 3.95 \times 10^{-6}$ is higher than that of $Da= 1.77 \times 10^{-5}$ due to the higher fluid mixing in the lower Darcy number. The adding of the metal foam blocks caused a remarkable enhancement in the mean Nusselt number from that in the fluid case as in case of $q=1862 \text{ W/m}^2$ and $Re=1594$ (95% first block, 93% second block, and 93% third block) for $Da=3.95 \times 10^{-6}$, (91% first block,89% second block,and 85% third block) for $Da=1.77 \times 10^{-5}$.

6.4 Temperature Distribution through the Metal Foam Blocks

Fig.17 shows the influence of Darcy number on the temperature distribution, through the metal foam blocks at each heated section. It can be seen that the temperature distribution is decreased at each heated section as the Darcy number decreased for the same Reynolds number and heat flux. This can be attributed to the fact that for higher surface area of the metal foam especially for lower Darcy number (3.95×10^{-6}).

6.5 Local Friction Coefficient

Fig.18 shows the effect of the local friction coefficient on the Reynolds number for different Darcy number. This figure shows that the local friction coefficient is affected by the Darcy number of the metal foam. It shows that the local friction coefficient increases with Darcy number decreasing because of the increase in the resistance to the axial flow. So the local friction coefficient also decreases with increase in Reynolds number.

7. COMPARISON WITH PREVIOUS EXPERIMENTAL RESULTS

Hadim, 1994 conducted a numerical study on the force convective heat transfer in a channel filled partially porous with discrete heat source. This work is the closest previous published work that found in the literature using the same setup with convection heat transfer except that it is a theoretical study and different properties such as $Pr=10$ and $\varepsilon=0.97$. Additionally, thermal conductivity ratio ($R_k= k_{eff} / k_f$) was set equal to 1 which means that the thermal conductivity of the porous medium is equal to the thermal conductivity of the fluid. But in our present work the thermal conductivity of the porous blocks material has great influence of the overall heat transfer and fluid flow characteristics.

It can be seen from **Fig.19** that the average Nusselt number increases when the Reynolds number is increased and when the Darcy number increased. The behavior shown in **Fig. 19** agrees with the present work results that shown in **Fig.15** (the mean Nusselt number increases as Reynolds number is increased for the same Darcy number value at each block) and in **Fig.16** (the mean Nusselt number is increased as Darcy number decreased for the same Reynolds number value at each heated section).

8. CONCLUSIONS

The main conclusions of the present work are:

- 1- The wall temperature at each heated section increases as the imposed heat flux is increased of two cases without (fluid case) and with metal foam blocks.



- 2- The wall temperature at each heated section decreases as the Reynolds number (the same heat flux value) is increased of two cases without (fluid case) and with metal foam blocks.
- 3- The local heat transfer coefficient and the mean Nusselt number increased with the increased of the imposed heat flux and Reynolds number.
- 4- The local heat transfer coefficient and the mean Nusselt number is increased with the decreased of the Darcy number.
- 5- The enhancement in the mean Nusselt number for all the studied cases is over 80 % from the fluid case.

REFERENCES

- Chikh S, Boumedien A, Bouhadek K, Lauriat G., 1998 , *Analysis of Fluid Flow and Heat Transfer in Channel with Intermittent Heated Porous Blocks*, Heat Mass Transfer, Vol. 33, pp.405–413.
- D. A. Nield, A. Bejan, 2006, *Convection in Porous Media*, New York, Springer.
- Guerroudj N. and Kahalerras H., 2010, *Mixed Convection in a Channel Provided with Heated Porous Blocks of Various Shapes*, Energy Conversion and Management, Vol. 51, pp. 505-517.
- Hadim A., 1994, *Forced Convection in a Porous Channel with Localized Heat Sources*, J Heat Transfer, Vol. 116, pp.465–471.
- Huang, P. C., and Vafai, K., 1994, *Analysis of Forced Convection Enhancements in a Channel Using Porous Blocks*, Journal of Thermophysics and Heat Transfer, Vol. 8, No. 3, pp. 563-573.
- Incropera, F. P., DeWitt, D. P., Bergman, T. L., and Lavine, A. S., 2007, *Fundamentals of Heat Mass Transfer*, Sixth Edition, John Wiley & Sons, U.S.A.
- Kurtbas, I. and Celik, N., 2009, *Experimental Investigation of Forced and Mixed Convection Heat Transfer in a Foam-Filled Horizontal Rectangular Channel*, Int. J. Heat Mass Transfer , Vol. 52 , pp.1313–1325.
- Rachedi R. and Chikh S., 2001, *Enhancement of Electronic Cooling by Insertion of Foam Materials*, Heat Mass Transf, Vol. 37, pp.371–378.

NOMENCLATURE

- C= inertia coefficient.
Da= Darcy number.
 D_h = hydraulic diameter, m.
 h = local heat transfer coefficient, $W/m^2.K$.
 k = thermal conductivity of fluid, $W/m.K$.
 k_{eff} = effective thermal conductivity , $W/m.K$.
L =thickness of metal foam block in flow direction, m.
 p = pressure, pa.
PPI= pores per inch.
 q = heat flux, W/m^2 .

Re= Reynolds number.

T = temperature, °C.

u_{in} = inlet velocity, m/s.

W= width of the copper foam block, m.

K = permeability, m^2 .

Nu = Nusselt number.

Pr = Prandtl Number.

ν = kinematic viscosity, m^2/s .

ϵ = porosity.

μ = dynamic viscosity, kg m/s.

ρ = density of air, kg/m^3 .

Subscript Meaning

b = bulk.

m = mean.

w = wall.

Table 1. The values of A, and B constants.

Pores per inch (PPI)	Porosity (ϵ) (%)	A	B
10	90.302	234.89	728
40	89.81	1052	1444

Table 2. Measured permeability and inertial coefficient of the metal foam.

Pores per inch (PPI)	Porosity (ϵ) (%)	Permeability † (K) (m^2)	Inertial coefficient (C)	Darcy number †† (Da)
10	90.302	7.859×10^{-8}	0.17	1.77×10^{-5}
40	89.81	1.75×10^{-8}	0.159	3.95×10^{-6}

† Calculated experimentally with the use of Eq. (12).

†† Calculated from Eq. (4).

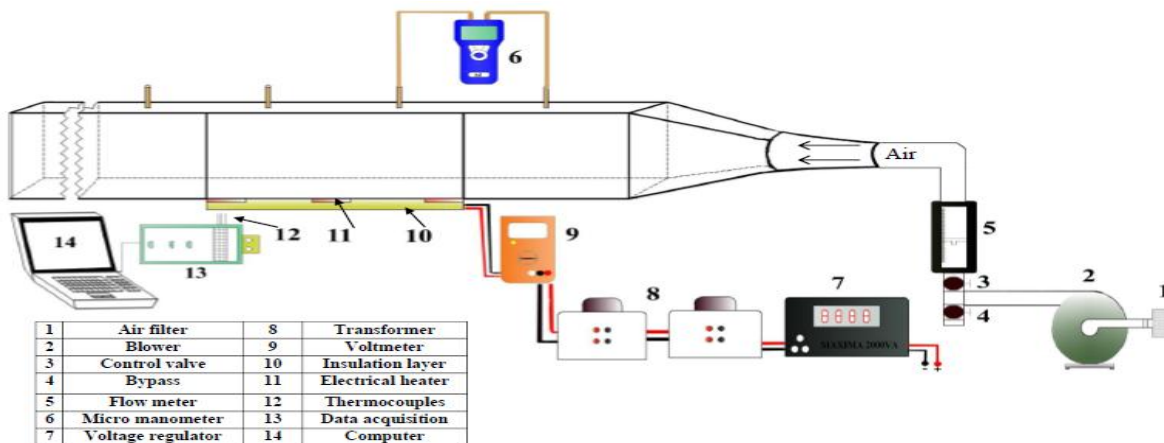
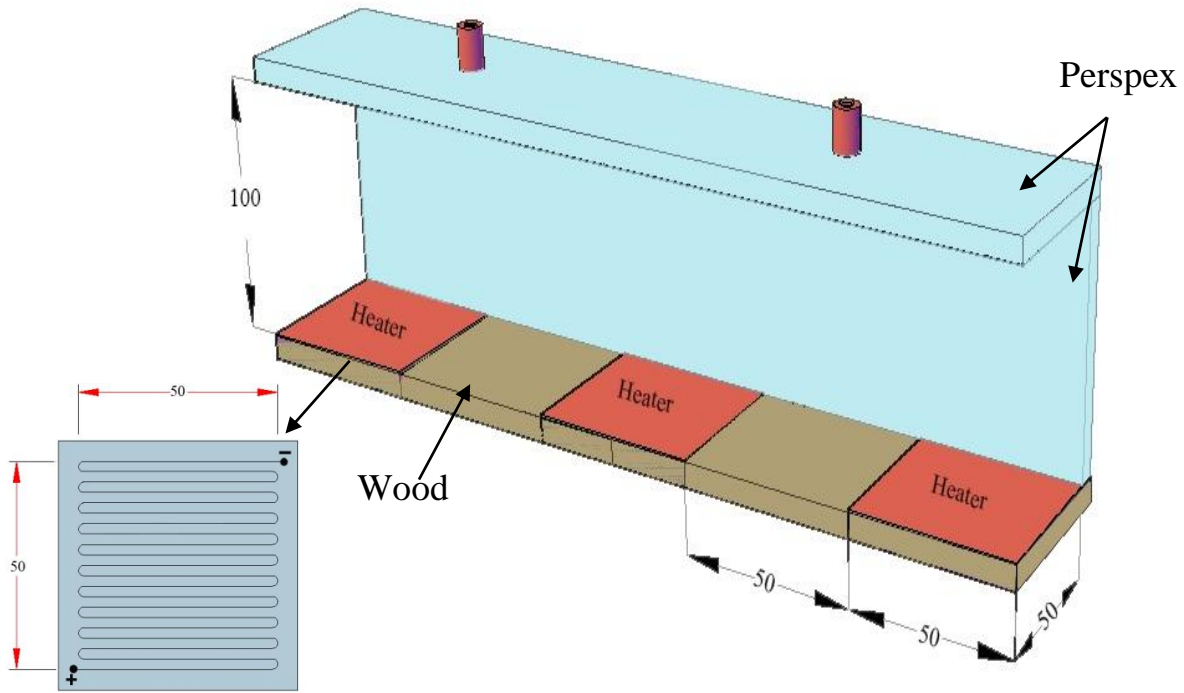
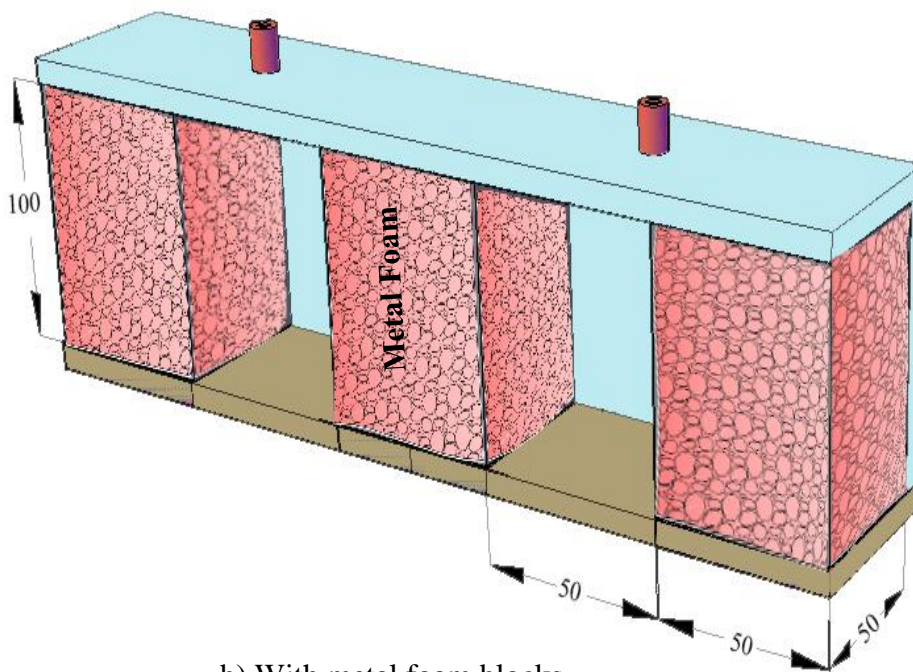


Figure 1. Schematic of the experimental apparatus.

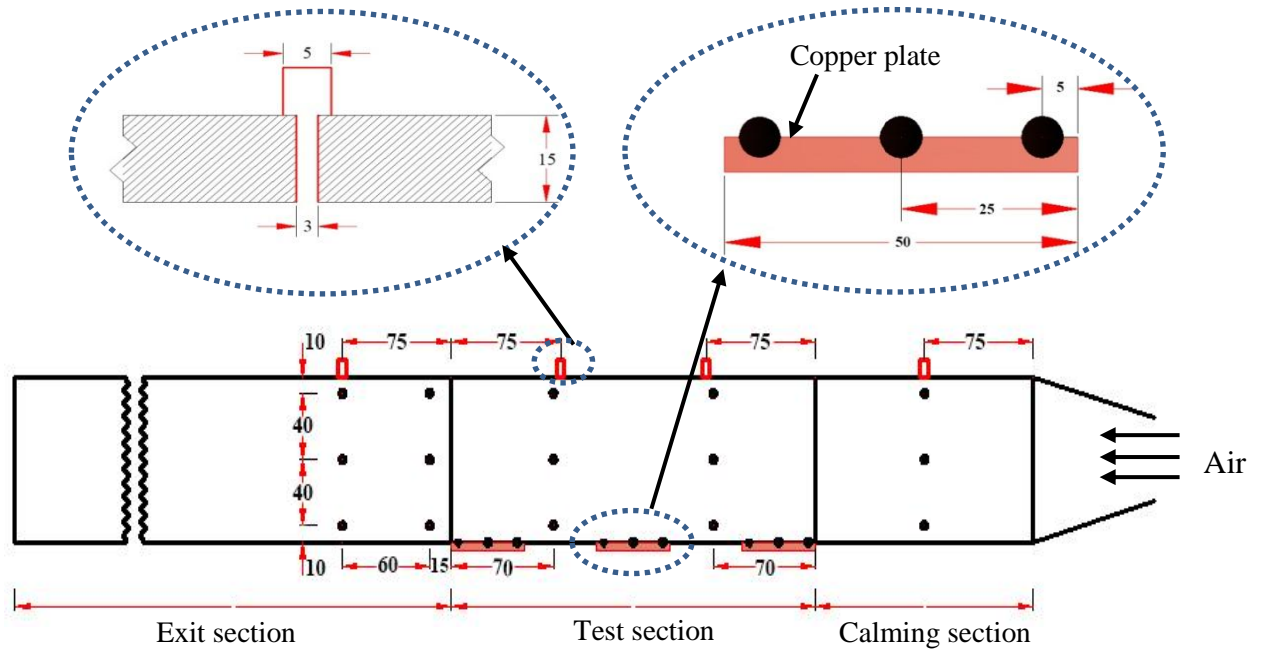


a) Without metal foam blocks.

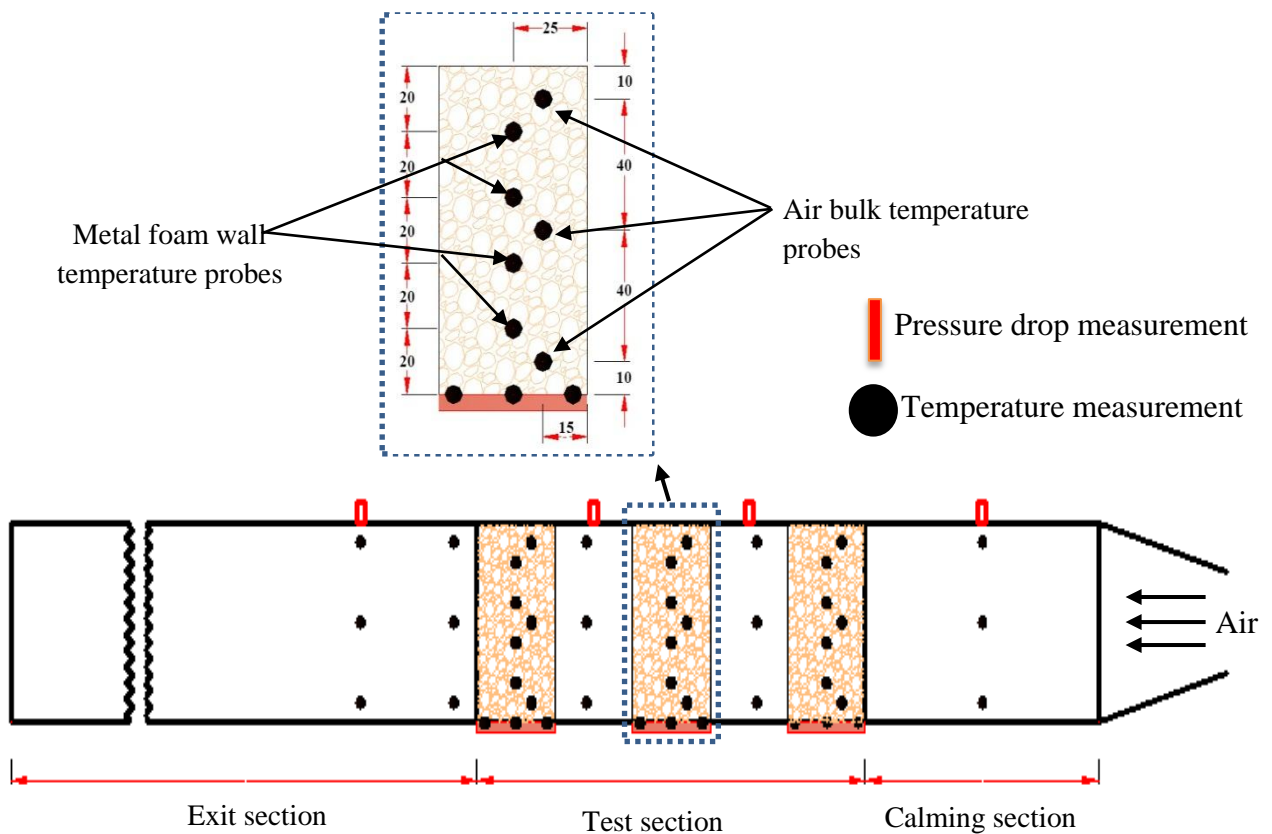


b) With metal foam blocks.

Figure 3. Schematic of the test section (All dimensions are in mm).



a) Without metal foam blocks.



b) With metal foam full rectangular block.

Figure 4. Thermocouples distribution and pressure taps. (All dimensions in mm).

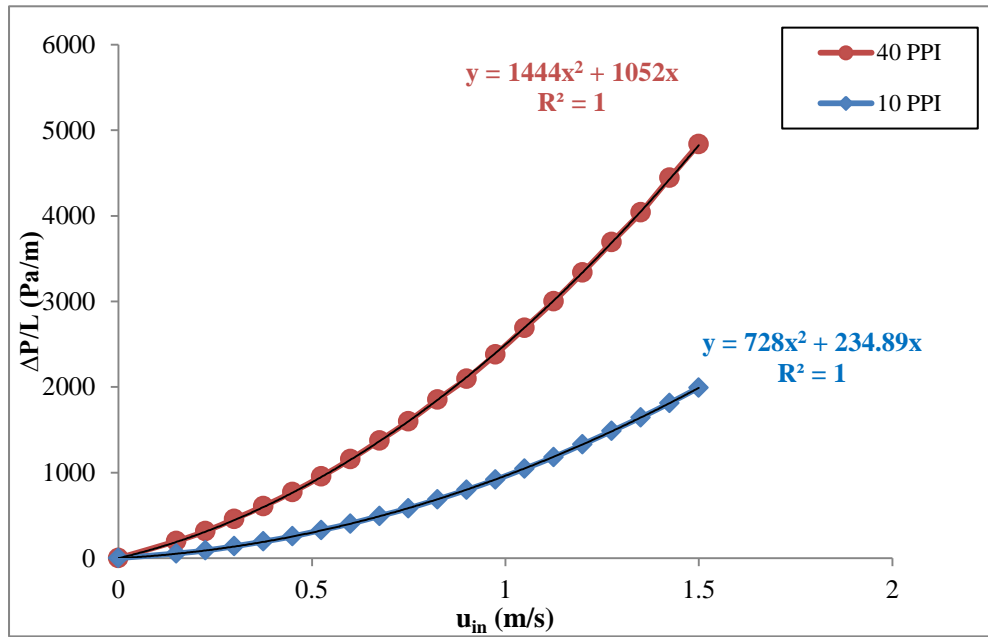


Figure 5. Variation of pressure drop across the metal foam with the velocity at the inlet.

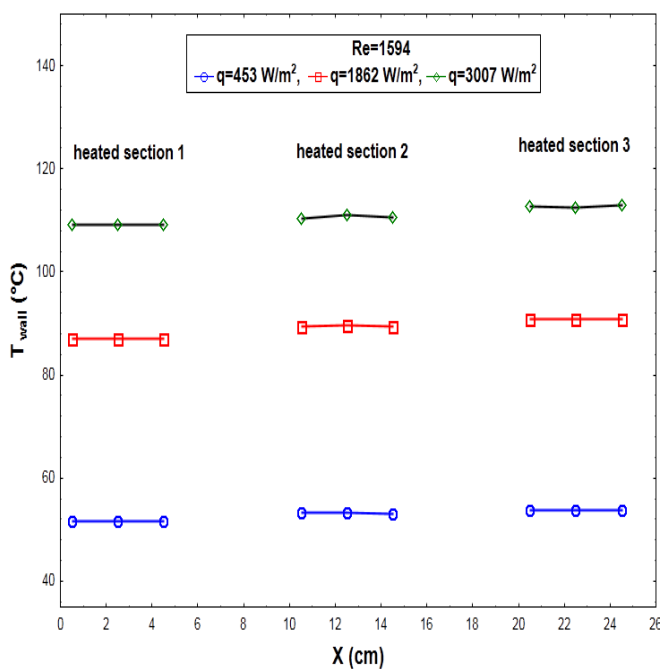


Figure 6. Variation of the wall temperature (fluid case) with the axial distance for different heat fluxes.

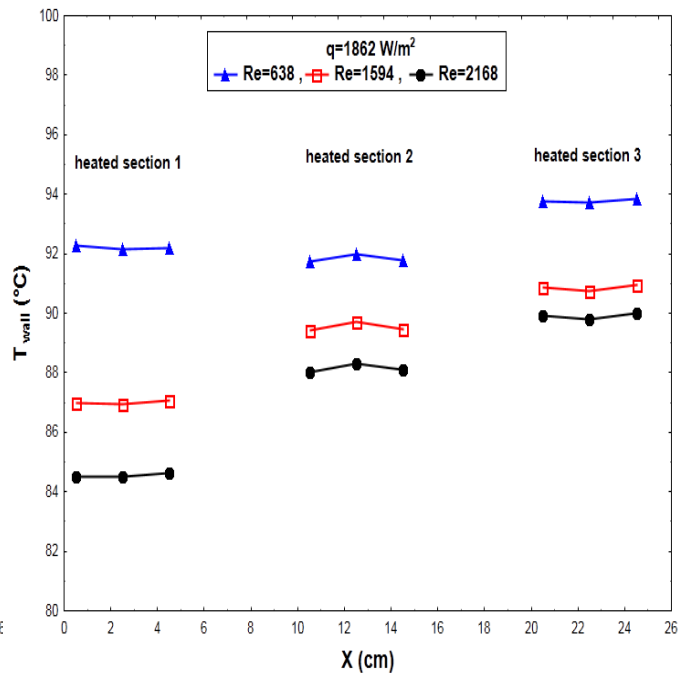


Figure 7. Variation of the wall temperature (fluid case) with the axial distance for different Reynolds numbers.

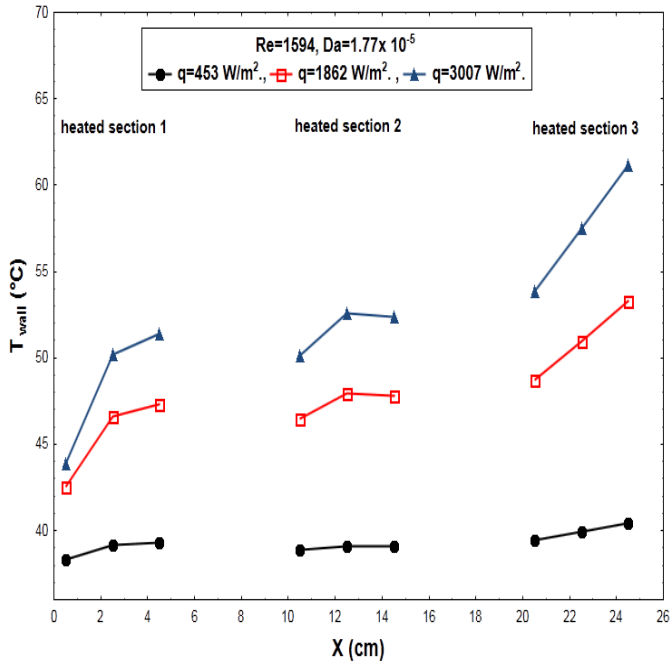


Figure 8. Variation of the wall temperature with the axial distance for different heat fluxes.

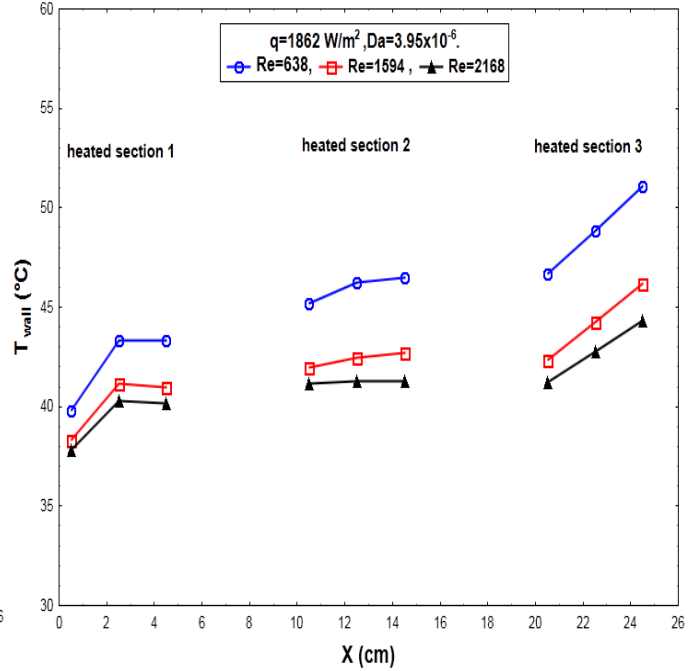


Figure 9. Variation of the wall temperature with the axial distance for different Reynolds numbers.

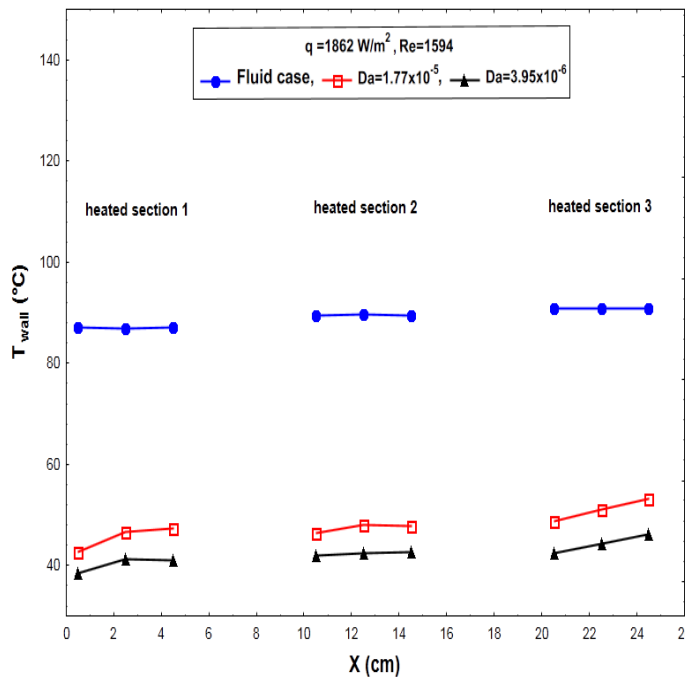


Figure 10. Variation of the wall Temperature with the axial distance for different Darcy number.

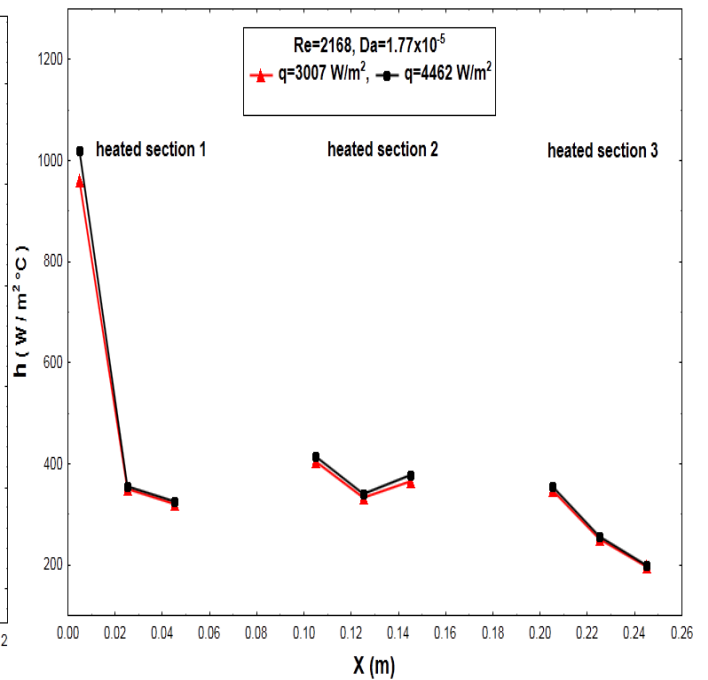


Figure 11. Local heat transfer coefficient with the axial distance for different heat fluxes.

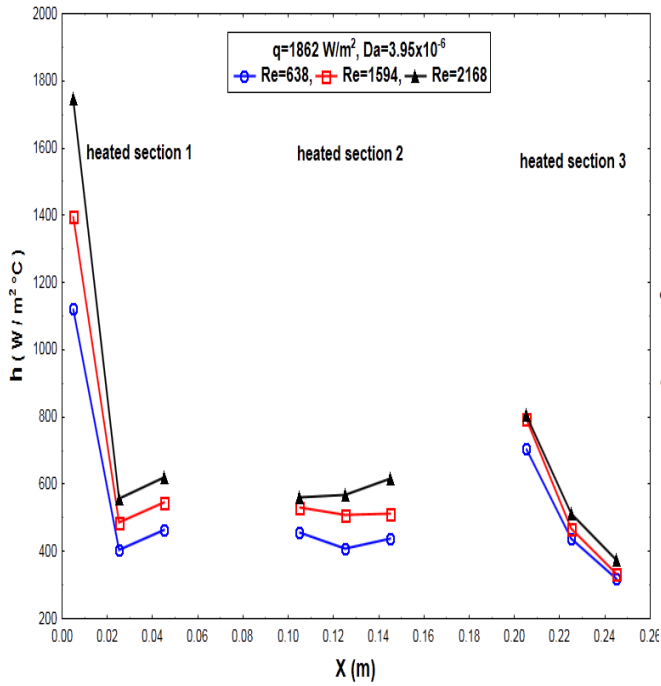


Figure 12. Local heat transfer coefficient with the axial distance for different Reynolds numbers.

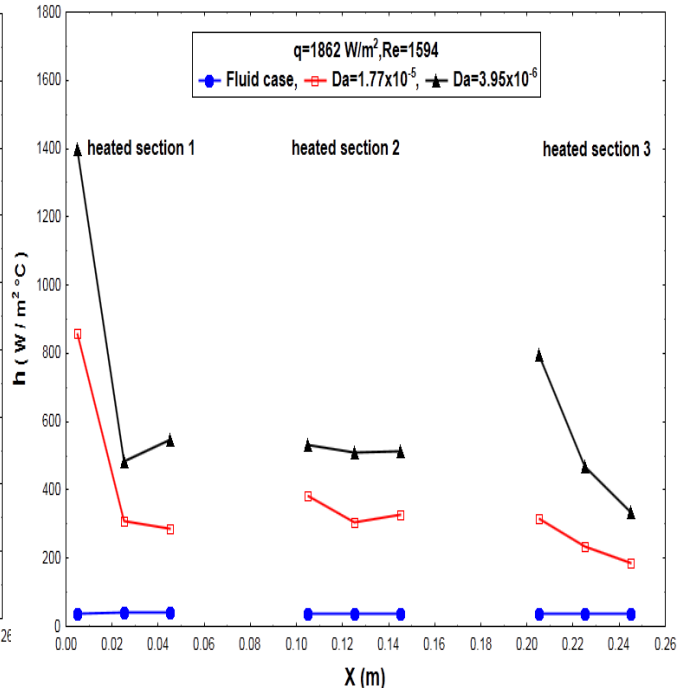


Figure 13. Local heat transfer coefficient with the axial distance for different Darcy number.

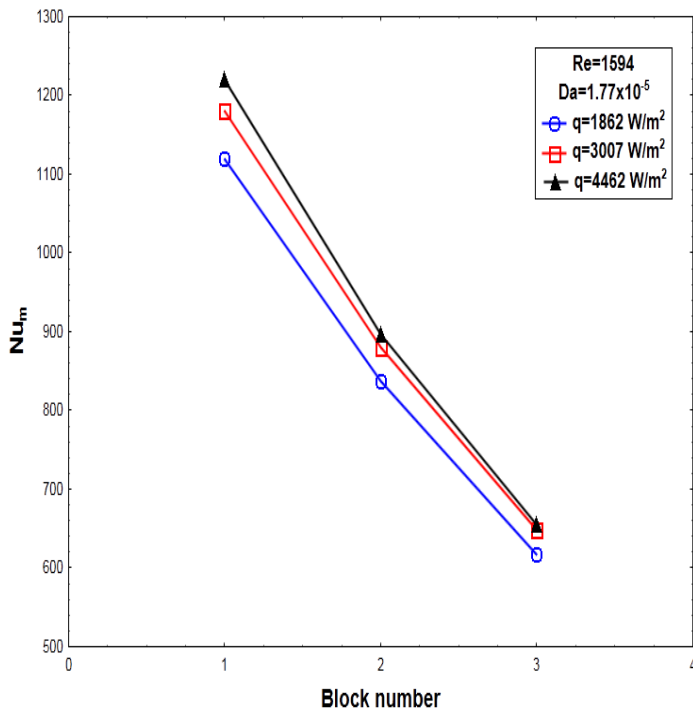


Figure 14. Mean Nusselt number with block number for different heat fluxes.

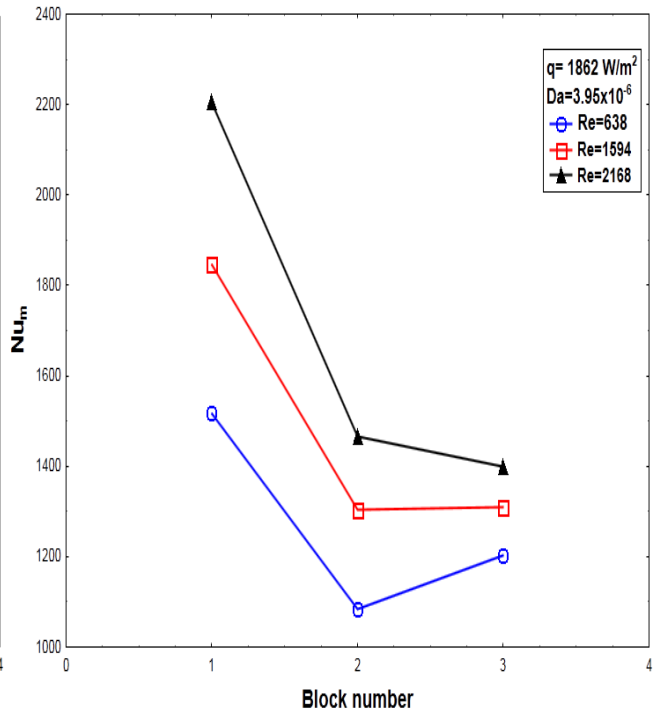


Figure 15. Mean Nusselt number with block number for different Reynolds numbers.

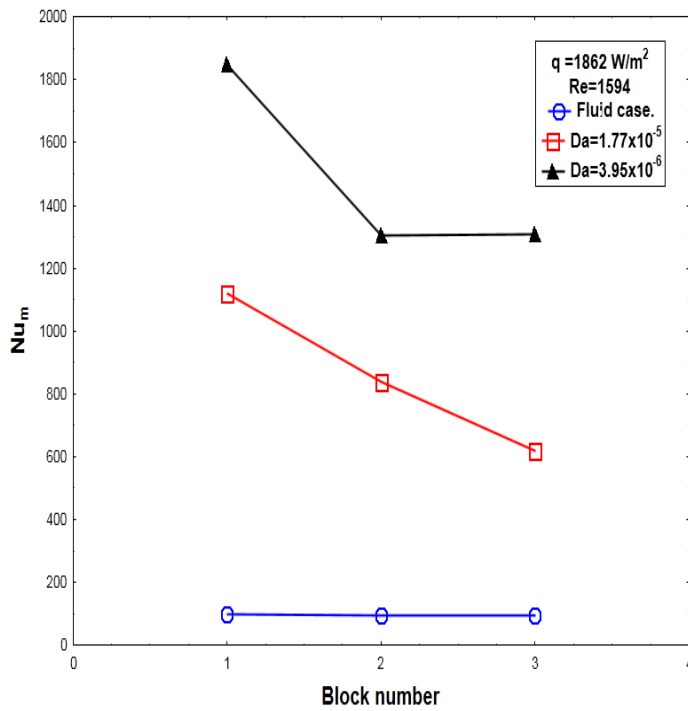


Figure 16. Mean Nusselt number with block number for different Darcy number.

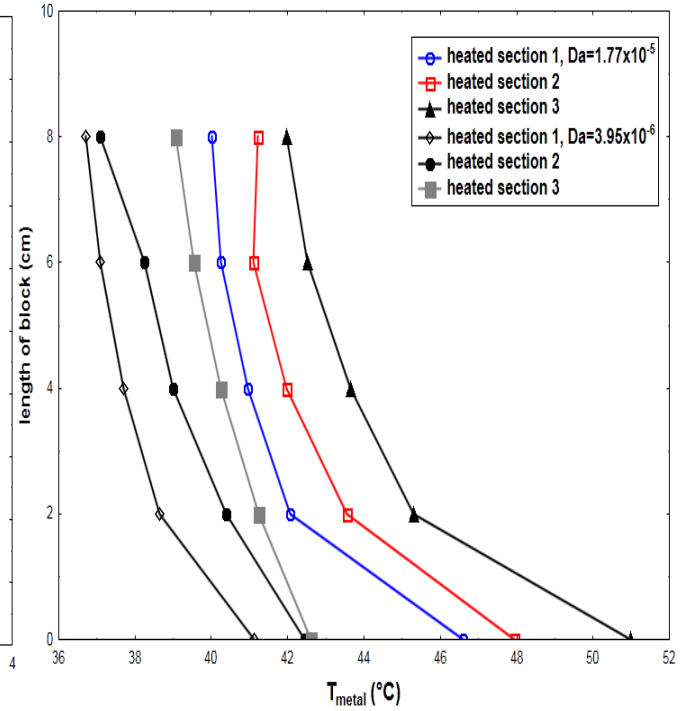


Figure 17. Variation of the metal foam temperature with the length of block for different Darcy Number.

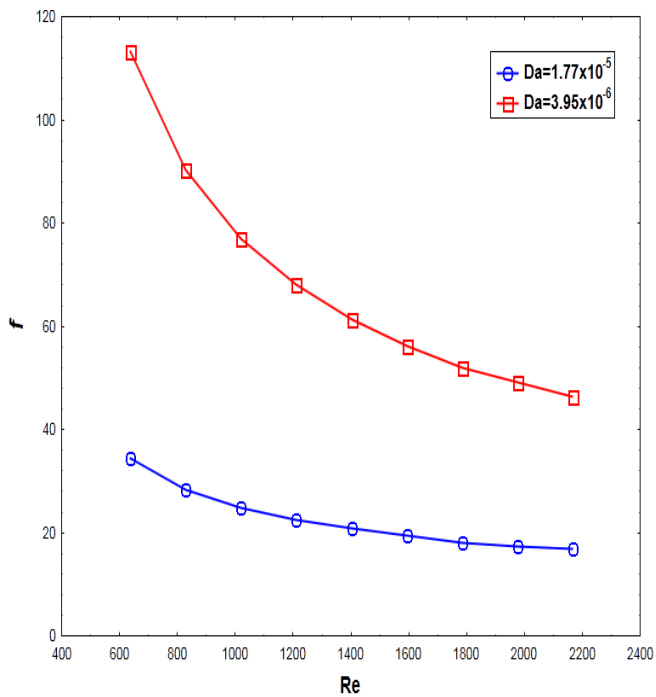


Figure 18. Local friction coefficient with the Reynolds numbers for different Darcy number.

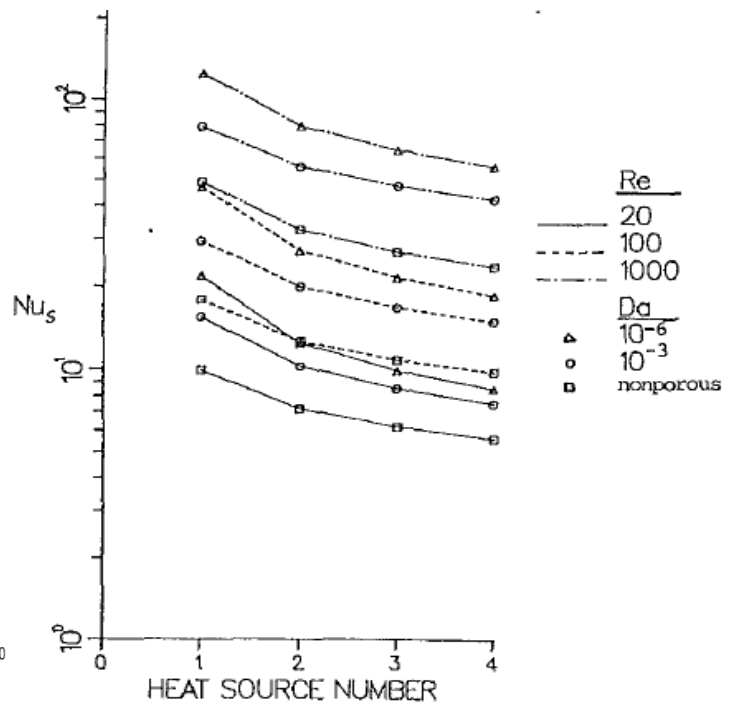


Figure 19. Variation of the average Nusselt Number over each heated section with Darcy and Reynolds numbers, Hadim, 1994.

Improving the Accuracy of Handheld GPS Receivers Based on NMEA File Generating and Least Squares Adjustment

Zahraa Ezzulddin Hussein

Assistant Lecturer

College of Engineering - University of Baghdad

E-mail: Zahraazeldeen@yahoo.com

ABSTRACT

This study aims to improve the quality of satellites signals in addition to increase accuracy level delivered from handheld GPS data by building up a program to read and decode data of handheld GPS. Where, the NMEA protocol file, which stands for the National Marine Electronics Association, was generated from handheld GPS receivers in real time using in-house design program. The NMEA protocol file provides ability to choose points positions with best status level of satellites such as number of visible satellite, satellite geometry, and GPS mode, which are defined as accuracy factors. In addition to fix signal quality, least squares technique was adopted in this study to minimize the residuals of GPS observations and enhance its accuracy. Moreover, one hundred reference control points were established using geodetic GPS receiver (GR5 receiver), and fixing them in a specified sites of the University of Baghdad, Al Jadriya campus, which selected as a study area, to evaluate positioning accuracy of handheld GPS before and after adjustment. The study findings showed significant decrease in root mean square error (RMSE) in both horizontal and vertical directions from 9.4 m to 3.2 m and 6.8 m to 2.4 m respectively.

Key words: handheld GPS, least square adjustment, accuracy, NMEA file.

تحسين دقة مواقع اجهزة الـ GPS المحمولة القائمة على توليد ملف NMEA وتقنية التصحيح بأقل المربعات

م.م زهراء عز الدين حسين

قسم هندسة المساحة

كلية الهندسة/جامعة بغداد

الخلاصة

تهدف هذه الدراسة إلى تحسين جودة إشارات الأقمار الصناعية بالإضافة إلى زيادة مستوى الدقة لاجهزة الـ GPS المحمولة من خلال تصميم برنامج لقراءة ومعالجة بيانات اجهزة الـ GPS المحمولة. حيث تم انشاء ملف بروتوكول NMEA، والتي تشير الى الجمعية الوطنية للإلكترونيات البحرية، من مستقبلات الـ GPS المحمولة في الوقت الحقيقي باستخدام البرنامج المصمم. يوفر هذا الملف امكانية اختيار مواقع النقاط مع أفضل مستوى من وضع الأقمار الصناعية مثل عدد الاقمار المرئية والهندسة الفضائية (GDOP، HDOP) وحالة اقمار الـ GPS، التي تعرف بأنها عوامل الدقة. ولقد تم الاعتماد على تقنية اقل المربعات في هذه الدراسة أضافة إلى تثبيت جودة الإشارة لتقليل الخطأ المتبقي من رصدات الـ GPS الى اقل ما يمكن و تعزيز دقتها. وعلاوة على ذلك، تم إنشاء مائة نقطة مرجعية باستخدام المستقبلات الجيوديسية (GR5 receiver) وتثبيتها في مواقع معينة من جامعة بغداد/ الجادرية / الحرم الجامعي التي اختبرت كمنطقة دراسة، لتقييم دقة مواقع اجهزة الـ GPS المحمولة (قبل وبعد إجراءات التصحيح). نتائج هذه الدراسة أظهرت انخفاضاً ملحوظاً بجذر متوسط مربع الخطأ (RMSE) في كلا المواقع الراسية والافقية للـ GPS من حوالي 6.8 متر إلى 2.4 متر ومن 9.4 متر الى 3.2 متر على التعاقب .

الكلمات الرئيسية: نظام تحديد المواقع المحمول، التصحيح بأقل المربعات، معاملات الدقة، ملف NMEA.



1. INTRODUCTION

In general, usage of handheld GPS for several applications is very economic; however it is limited because of its low accuracy. This is due to the fact that the handheld GPS suffers from lacking in generating raw data in real time, **Syedul Amin, et al., 2013**. National Marine Electronics Association produced uniform protocol, which defined as NMEA protocol, to exchange data between different marine electronics devices. NMEA protocol has special format, which was defined for all marine devices such as GPS. In this paper, the program was designed to read this special format in real time, using a pc as a collector of logging observation. The NMEA standard provides conforming devices those speak the same language, **Parmar, 2011**. This language can be interpreted by a PC program like the one designed in this study. The accuracy of handheld GPS is not homogeneous and they are ranging between 5-10 meters. Where, the accuracy of GPS devices is based on several factors such as a number of visible satellites, signal strength, period of observation and the geometry of satellites, which are determined by dilution of precision (DOP) or geometric dilution of precision (GDOP), **Meduri, and Bramhanadam, 2012**. Additionally, the DOP is determined for each of horizontal (HDOP), vertical (VDOP), 3D position (PDOP), and time dilution of precision (TDOP). Accuracy level of GPS observations can be improved by minimizing its residual using least square adjustment method, which provides the best fitting for all GPS track points. Thus, increasing accuracy of handheld GPS is an important factor to give possibility of using it in specific applications consistent with the resulting accuracy. Improving accuracy of low cost GPS was considered by some of researchers in previous studies. This accuracy may be enhanced by decoding the specific format of handheld GPS and generating the RINEX file depending on a developed program in addition to commercial software, **Schweiger, 2003**. Other hand, the Web services offers the ability to improve the accuracy of low cost GPS receivers a few centimeters or more by exchanging Continuously Operating Reference Stations (CORS) network data using wireless mobile devices, **Fraser, et al., 2004**. The differential relative positioning technique, which based on using two or more than one receiver in a same time, was applied to get a sub-metric accuracy level less than 5 meters, **Acosta, and Toloza, 2012**. Thus, the results of this study show best accuracy and simplest approach comparing with previous studies.

2. NMEA STRUCTURE

The National Marine Electronics Association (NMEA) has applied to define the interface between various marine electronic. Information of marine electronics can be sent to computers and to other marine equipment for post-processing. Communication for most GPS receiver is defined within standard of NMEA, **Sinivee, 2010**. The notion of NMEA is to transmit a line of data named a sentence that is fully autonomous. There are regular signal sentences for each device kind and there is also the capability to define proprietary sentences for usage by the specific company. All devices that use the standard sentences are defined by a two letter prefix in this sentence form, **Amin, et al., 2014**. Moreover, the NMEA standard relies on ASCII (American standard code for information interchange) format. Each sentence starts with the character of dollar, \$, and ends with a carriage return and a line feed. Identifier and data fields are between the beginning and the end, separated by commas. The first two characters following the \$ include the "talker" identifier, describing the type of instrument sending the data. For example \$ZA for atomic clock or \$GP for GPS receiver. A three letter code, which identifying the type of signal sentence, is followed the talker ID such as GSA referring to GNSS Satellites active, **Bosy, et al., 2007; Rajendran, 2010**. Additionally, message of NMEA contains information about position, time and velocity which identified as follow, **Adrdalan, and Awange, 2000 and Park, et al., 2013**.



- A. GNSS Fix Data (GGA) refers to position, time, and fix regarding data for a GPS receiver. The format of GGA sentences is illustrated in **Table 1**.
- B. Geographic Position – Latitude/Longitude (GLL) stands for longitude of vessel position, latitude, and time of position. The format of these elements is explained in **Table 2**.
- C. GNSS Satellites Active (GSA) refers to DOP values, satellites used in the navigation solution which mentioned by the GGA or GNS sentence and GPS receiver operating mode. This sentence is listed in **Table 3**.
- D. GNSS Satellites in View (GSV) represents each of satellite ID numbers, number of satellites (SV) in view, elevation, azimuth, and SNR value. Format of this sentence is explained in **Table 4**.
- E. Recommended Minimum Specific GNSS Data (RMC) stands for position, time, date, path and speed data determined by a GNSS navigation receiver. Format of RMC is decoded in **Table 5**.
- F. Course over Ground and Ground Speed (VTG) represent the elements of actual course and speed relative to the ground. The solution of this format is explained in **Table 6**.

3. METHODOLOGY

The positioning accuracy of handheld GPS is inhomogeneous along period of observation, because of the constant changing in both of number and geometry of satellites. Thus, the methodology of this study was considered to fix the quality of received GPS signal in addition to increase the level of accuracy. The main stages of this methodology are explained as following:

A. The designed program

Graphical user interface (GUI), using MATLAB Language, was employed and designed to read the NMEA file in addition to adjust the coordinates of GPS track points observed by handheld GPS, (illustrated in **Fig.1**). The program code includes two steps as follow:

1. In the first step, the designed program downloads NMEA data in real time for any period of observation time. Then, this data were processed depending on the quality of satellites signals to determine the positions for all GPS track points. For example, this program downloads the initial GGA sentence of NMEA file as following, **Ince, and Sahin, 2000 and Amin, et al., 2013**:

```
$GPGGA,090726,3316.4104,N,04422.6311,E,1,04,3.6,49.5,M,3.4,M,,*45
```

where:

\$GPGGA : Protocol header

090726 : UTC position which equals to 09h 07m 26s

3316.4104 : Latitude which equals to 33° 16.4104'

N : North

04422.6311: Longitude which equals to 044° 22.6311'

E : East



- 1 : Position Fix Indicator, where number 1 refers to GPS SPS Mode, fix valid
- 04 : Satellites used which range 0 to 12
- 3.6 : Horizontal Dilution of Precision (HDOP)
- 49.5 : Mean sea level
- M : Units in meters
- 3.4 : Geoid separation
- M : Units in meters
- *45 : Checksum (detect errors in the data)

While, the next GGA sentence for specific period of observations is shown as follow:

\$GPGGA,093112,3316.4079,N,04422.6435,E,1,07,1.9,32.1,M,3.4,M,,*4B

By comparing between the initial GGA sentence and the next sentence, we can find the following:

- Period of observation equals to 23^m 46.33^s which is computed by subtracting the UTC values between the next sentence of GGA and the initial sentence.
- Increasing number of observed satellite from 4 to 7 refers to improve the accuracy of positioning, **Meduri, and Bramhanadam, 2012.**
- Decreasing HDOP factor from 3.6 to 1.9 refers to increase the level of accuracy, see **Table 7.**
- Logging rate of this period of observation equals to 2^s, which is computed by subtracting the UTC values between two sequential sentences, see Appendix A.

2. Least square adjustment was applied in the second step to find the best fitting of GPS track points based on existence of two control points, which are often available from previous surveys with accuracy less than 1 cm derived from practical experiments of this study. In this program, baseline vectors were created between the reference points and the GPS track points to adjust their positions as shown in **Fig. 2.** Where, the least squares adjustment method is considered to minimize the residual of observations (coordinates of GPS track points) based on the following observational equations, **Witchayangkoon, 2000; Amiri-Simkooei, and Sharifi, 2004 :**

$$(x_p + v_{xp}) - x_R = dx_{Rp} + \Delta_x \tag{1}$$

$$(y_p + v_{yp}) - y_R = dy_{Rp} + \Delta_y \tag{2}$$

$$(z_p + v_{zp}) - z_R = dz_{Rp} + \Delta_z \tag{3}$$

where, $(x_p, y_p, \text{ and } z_p)$ are the coordinates of GPS track points, $(x_R, y_R, \text{ and } z_R)$ are the coordinates of reference control points, $(dx_{Rp}, dy_{Rp}, \text{ and } dz_{Rp})$ are the baseline vectors, $(v_{xp},$

v_{yp} , and v_{zp}) are the residual of observations, and (Δ_x , Δ_y , and Δ_z) are the correction of unknowns (baseline vectors).

B. The fieldwork

For accuracy assessment purpose of handheld GPS positions after adjustment, one hundred reference points (as shown in **Fig. 3.**), were established in Baghdad University campus using differential technique (DGPS), with period of observation equals to 25 minutes (static method). These reference points were observed by handheld GPS receiver (Garmin eTrex) to collect GPS track points using two methods of observation, which are observation with adjustment procedure (generating and processing NMEA file) and observation without adjustment. Firstly, GPS track points were collected without the adjustment procedures of this study. While, in the second method of observation, handheld GPS was connected with a PC using the serial port (RS232) to gather NMEA files of track points (for 10 minute period of observation) by the designed program as shown in **Fig. 4.** In later method, GPS track points were adjusted based on the best fitting tools, which is used in this study (processing of NMEA files and least squares technique). Consequently, the handheld positioning, which resulted from both methods, were evaluated by compare them with the reference points.

C. Accuracy assessment

Accuracy assessment of GPS track points can be applied based on computation of root mean square error (RMSE) for the delivered observations. For specific number of GPS track points (n) defined by geocentric coordinates ($X, Y, and Z$), the vertical and horizontal RMSE, in addition to the total 3D RMSE are explained as following, **Misra and Enge, 2001 and Diggelen, 2007**:

$$RMSE \text{ vertical error} = \sqrt{\frac{\sum \Delta Z^2}{n}} \quad (4)$$

$$RMSE \text{ horizontal error (2D RMSE)} = \sqrt{\frac{\sum \Delta X^2 + \Delta Y^2}{n}} \quad (5)$$

$$RMSE \text{ of three dimensional error (3D RMSE)} = \sqrt{\frac{\sum \Delta X^2 + \Delta Y^2 + \Delta Z^2}{n}} \quad (6)$$

where $\Delta X, \Delta Y, \Delta Z$ refers to the coordinates difference between GPS track points observed by handheld GPS and reference points measured by DGPS. Additionally, the distance error (D-error) between track and reference points can be calculated as following, **Boal, 1992**:

$$D - error = \sqrt{\Delta X^2 + \Delta Y^2 + \Delta Z^2} \quad (7)$$

4. RESULTS

The results delivered from this study refer to significant improvement of positioning accuracy for all GPS track points, which were adjusted based on the methodology suggested in this study. The results showed that the vertical accuracy of GPS track points, which was computed based on the RMSE values, decreased from 6.8 m to 2.4 m by applying the adjusted procedures. Additionally, both of horizontal accuracy and three dimensional accuracy values were reduced with a percentage reaches to 66% and 65% respectively as shown in **Table 8.** Thus, distance error were computed for all GPS track points (before and after adjustment technique), and summarized in **Fig. 5.** It is remarkable that a considerable improvement in the homogeneity of the resulting



coordinates, which was delivered by decreasing the standard deviation value from 4.3713 m to 1.0909 m. Thus, differences of coordinates values, which computed relative to the reference points, were summarized in **Table 9**, for some of GPS track points.

5. CONCLUSIONS

This study showed the ability to enhance the quality of handheld GPS signals using a designed program for receiving and processing NMEA files. Additionally, the accuracy of handheld GPS positioning were increased to about 3m based on least squares adjustment technique with existing two control points. Moreover, decreasing of standard deviation to around 75% refers to the homogeneity improvement regarding distribution of errors on all GPS track points. Therefore, this study give the facility to use the low cost GPS in certain applications compatible with accuracy of 3 meters such as for GIS applications.

REFERENCES

- Acosta, N., and Toloza, J., 2012, *Techniques to Improve the GPS Precision*, International Journal of Advanced Computer Science and Applications, Vol.3, No.8, PP.125-130.
- Adrdalan, A., and Awange, J.L., 2000, *Compatibility of NMEA GGA with GPS Receivers Implementation*, GPS Solutions journal, Vol.3, No.3, PP.1-3.
- Amin, M. S., Reaz, M. B. I., Bhuiyan, M. A. S., and Nasir, S. S., 2014, *Kalman Filtered GPS Accelerometer Based Accident Detection and Location System: A Low-Cost Approach*, Current Science, Vol.106, No.11, PP.1548-1554
- Amiri-Simkooei, A., and Sharifi, M., 2004, *Approach for Equivalent Accuracy Design of Different Types of Observations*, Journal of Surveying Engineering, Vol.130, No.1, PP.1-5.
- Boal, J. D., 1992, *Guidlines and Specifications for GPS Surveys*, Geodetic Survey Division, Canada.
- Bosy, J., Graszka, W., and Leończyk, M., 2007, *ASG-EUPOS. A Multifunctional Precise Satellite Positioning System in Poland*, European Journal of Navigation Vol.5, No.4, PP.2-6.
- Diggelen, F. v., 2007, *GNSS Accuracy: Lies, Damn Lies, and Statistics*, GPS World, Vol.18, No.1, PP.26-32.
- Fraser, R., Mowlam, A., and Collier, P., 2004, *Augmentation of Low-Cost GPS Receivers via Web Services and Wireless Mobile Devices*, Positioning, Vol.1, No.08, PP.85-94.
- Ince, C. D., and Sahin, M., 2000, *Real-time Deformation Monitoring with GPS and Kalman Filter*, Earth, planets and space, Vol.52, No.10, PP.837-840.
- Meduri, S.R, and Bramhanadam, P.S, 2012, *Comparison of Dilution of Precision (DOP) in Multipath and Error free Environment Using Single Frequency Global Positioning*



System, International Journal of Engineering and Advanced Technology (IJEAT), Vol.1, No.5, PP.445-448.

- Misra, P. and Enge, P., 2001, *Global Positioning System. Signals, Measurements and Performance*. Ganga-Jamuna Press, Massachusetts, U.S.
- Park, B., Lee, J., Kim, Y., Yun, H., and Kee, C., 2013, *DGPS Enhancement to GPS NMEA Output Data: DGPS by Correction Projection to Position-Domain*. Journal of Navigation, Vol.66, PP.249-264.
- Parmar, S. N., 2011, *Design and Implementation of GPS based Navigation System for Location based Services*, in International Conference on Technology Systems and Management (ICTSM) proceedings published by International Journal of Computer Applications (IJCA), PP.24-27.
- Rajendran, G., Arthanari, M., and Sivakumar, M., 2010, *A Simplified NMEA Sentence Generator for the Simulation of GPS Tracking*, Global Journal of Computer Science and Technology Vol.10, No.14, PP.19-26.
- Schwieger, V., 2003, *Using Handheld GPS Receivers for Precise Positioning*, 2nd FIG Regional Conference, Marrakech, Morocco, December 2-5, 2003.
- Sinivee, V., 2010, *Simple Yet Efficient NMEA Sentence Generator for testing GPS Reception Firmware and Hardware*, Novel Algorithms and Techniques in Telecommunications and Networking, Springer Netherlands, PP.207-210.
- Syedul Amin, Md., Bhuiyan, M.A.S., Reaz, M.B.I. and Nasir, S.S., 2013, *GPS and Map Matching Based Vehicle Accident Detection System*, IEEE Student Conference on Research and Development (SCORED), Putrajaya, 16-17 December 2013.
- Witchayangkoon, B., 2000, *Elements of GPS Precise Point Positioning*, Maine: University of Maine.

Table 1. Format of signal sentences regarding to GGA – GNSS Fix Data, Adrdalan, and Awange, 2000 and Park, et al., 2013.

Field	Name	Explanation
hhmmss.ss	UTC Time	UTC of position in hhmmss.sss format
llll.lll	Latitude	Latitude in ddm. mmmm format
A	N/S Indicator	‘N’ = North, ‘S’ = South
yyyyy.yyy	Longitude	Longitude in dddmm. mmmm format
A	E/W Indicator	‘E’ = East, ‘W’ = West
X	GPS quality indicator	GPS quality indicator
Uu	Satellites Used	Number of satellites in use, (00 ~ 24)
v.v	HDOP	Horizontal dilution of precision, (00.0 ~ 99.9)
w.w	Altitude	Mean sea level altitude in meter
x.x	Geoid separation	In meter



Zzzz	DGPS Station ID	Differential reference station ID, NULL when DGPS not used
Hh	Detect errors in the data	

Table 2. Format of GLL – Geographic Position – Latitude/Longitude, Adrdalan, and Awange, 2000; Park, et al., 2013 and Amin, et al., 2014.

Field	Name	Explanation
llll.lll	Latitude	Latitude in ddmm.mmmm arrangement
A	N/S Indicator	‘N’ = North, ‘S’ = South
yyyyy.yyy	Longitude	Longitude in dddmm.mmmm arrangement
B	E/W Indicator	‘E’ = East, ‘W’ = West
hhmmss.sss	UTC Time	UTC of position in hhmmss.sss arrangement
A	Status	A= data adequate, V= data not adequate
Hh	Detect errors in the data	

Table 3. Format of GSA – GNSS Satellites Active and DOP, Adrdalan, and Awange, 2000 and Park, et al., 2013.

Field	Name	Explanation
A	Mode	Mode ‘M’ = Manual, required to run in 2D or 3D style ‘A’ = Automatic, acceptable to mechanically shift
X	Mode	Fix form 1= Fix not accessible, 2= 2dimention, 3= 3dimention
xx’s	Satellite ID	In the best way 12 satellites are involved in each GSA sentence.
u.u	PDOP	Position dilution of precision (00.0 to 99.9)
v.v	HDOP	Horizontal dilution of precision (00.0 to 99.9)
z.z	VDOP	Vertical dilution of precision (00.0 to 99.9)
Hh	Detect errors in the data	

Table 4. Format of GSV – GNSS Satellites in View, Adrdalan, and Awange, 2000 and Park, et al., 2013 .

Field	Name	Explanation
X	Number of message	Whole number of GSV messages to be transferred (1-3)
U	Order number	Order number of current GSV message
Xx	Satellites in view	Total number of satellites in view (00 ~ 12)
Uu	Satellite ID	Greatly 4 satellites are included in each GSV sentence.
Vv	Elevation	Elevation of satellite in degrees, (00 ~ 90)
Zzz	Azimuth	Satellite azimuth angle in degrees, (000 ~ 359)
Ss	SNR	C/No in dB (00 ~ 99) Useless when not tracking
Hh	Detect errors in the data	



Table 5. Format of RMC – Recommended Minimum Specific GNSS Data, Adrdalan, and Awange, 2000; Park, et al., 2013 and Amin, et al., 2014.

Field	Name	Explanation
hhmmss.ss	UTC Time	UTC time in hhmmss.sss format
X	Situation	Situation 'A' = Data Suitable 'V' = Navigation receiver caution
llll.lll	Latitude	Latitude in dddmm.mmmm format.
A	N/S Indicator	North='N', South='S'
yyyyy.yyy	Longitude	Longitude in dddmm.mmmm arrangement
A	E/W Indicator	East='E', West='W'
x.x	Speed above ground	Speed above ground in knots (000.0 ~ 999.9)
u.u	Track above ground	Track above ground in degrees (000.0 ~ 359.9)
Xxxxxx	UTC Epoch	UTC epoch of position solution, ddmmyy
V	Style index	Style index 'N' = Files not adequate, 'A' = at large style 'D' = differed style, 'E' = Expected style
Hh	Detect errors in the data	

Table 6. Format of VTG – Course over Ground and Ground Speed, Awange, 2000 and Amin, et al., 2014.

Field	Name	Explanation
x.x	Course	Track above ground, degrees Right (000.0 ~ 359.9)
y.y	Course	Track above ground, degrees Magnetic (000.0 ~ 359.9)
u.u	Quickness	Quickness above ground in knots (000.0 ~ 999.9)
v.v	Quickness	Quickness above ground in kilometers per hour (0000.0 ~ 1800.0)
M	Style index	Style index 'N' = not adequate, 'A' = at large style, 'D' = = differed style, 's' = Expected style
Hh	Detect errors in the data	

Table 7. Values of dilution of precision, Awange, 2000 and Amin, et al., 2014.

DOP Value	Ranking	Explanation
< 20	Poor	Observations are inaccurate
10-20	Fair	Denotes a low confidence level. Positional observations should be used only to show a very irregular estimate of the current location.
5-10	Mild	Positional observations could be used for designs, however the fix quality could still be improved
2-5	Good	Positional observations could be used to make reliable in-route navigation plans to the user.
1-2	Excellent	For precise positional observations
< 1	Ideal	For peak possible confidence level



Table 8. Resulting errors of GPS track points.

GPS points	RMSE (vertical error)	RMSE (horizontal error)	RMSE (three dimensional error)	standard deviation
Before adjustment	6.8131	9.3847	11.5970	4.3713
After adjustment	2.4012	3.1667	3.9741	1.0909

Table 9. Difference of coordinates between reference points and GPS track points for arbitrary sample of points.

No.	Reference Control Points			GPS Track Points (before adjustment)			GPS Track Points (after adjustment)		
	X(m)	Y(m)	Z(m)	DX(m)	DY(m)	DZ(m)	DX(m)	DY(m)	DZ(m)
1	3681756.653	442080.126	37.055	11.801	10.756	10.388	1.5184	1.2763	3.9442
2	3681814.996	442074.611	37.173	9.6115	6.6597	5.0265	2.8727	1.6527	0.3945
3	3681817.526	442012.727	37.141	1.5255	7.8554	10.368	2.9382	2.5492	0.2954
4	3681819.211	441960.039	37.186	3.2952	10.082	0.84906	0.4820	3.9264	1.9872
5	3681881.184	441960.216	37.516	4.5455	3.218	1.8351	0.0897	0.2153	0.5635
6	3681930.842	441955.21	37.563	7.572	3.7965	11.509	3.5739	1.8633	2.2434
7	3681930.848	441955.224	37.552	5.9841	8.8633	0.15307	1.9778	0.2711	3.5906
8	3681987.892	441960.177	37.495	7.2642	6.9174	9.6885	1.1543	1.0762	2.3768
9	3682054.395	441961.244	37.476	7.8596	10.539	10.828	1.9035	1.4732	2.6224
10	3682052.282	442019.832	37.492	1.8268	2.311	9.4917	3.7528	2.4817	1.1314
11	3682010.698	442017.069	37.811	0.72846	4.6779	3.5996	0.8207	1.7565	0.1090
12	3681954.797	442014.695	38.057	8.8102	1.2505	9.5109	3.5047	2.4404	0.8144
13	3681882.434	442007.819	37.835	9.3927	6.3888	3.0402	2.0797	0.2153	3.4487
14	3681871.347	441911.405	38.302	0.85146	7.5096	0.29618	1.7717	2.1920	2.2674
15	3681857.675	441846.845	38.312	0.74451	1.5553	5.4074	2.7216	1.4855	0.3129
16	3681848.25	441795.361	38.224	8.068	10.273	5.9813	1.8254	0.1914	2.9530
17	3681858.177	441742.009	38.025	0.58541	3.766	7.6996	0.1520	3.8170	2.9695
18	3681867.205	441687.375	38.277	9.4366	3.4698	5.9744	3.7498	2.0535	0.9636
19	3681866.141	441626.473	37.76	9.8212	7.1415	6.4371	1.0399	3.0359	3.9734
20	3681932.233	441634.247	37.025	3.9705	4.9403	9.5281	1.4268	3.0114	0.4402
21	3681944.419	441677.567	37.735	4.1185	5.5513	4.4139	2.3882	1.7224	2.9229
22	3682021.664	441668.044	37.394	8.1548	6.8133	7.8213	1.0447	0.3792	1.8039
23	3682012.264	441608.496	37.133	5.8934	4.7815	5.7298	2.5603	0.5282	1.8113
24	3682036.929	441743.654	37.454	0.79905	4.9323	11.629	2.6088	3.3080	1.2323
25	3681988.463	441755.84	37.518	9.3687	8.7482	9.1878	1.6095	3.5369	2.8023
26	3682012.79	441805.479	37.993	9.079	10.119	9.2419	0.9675	3.0393	1.1637
27	3682055.342	441793.475	37.249	11.744	1.3363	4.7529	1.1098	0.0244	1.4988
28	3682055.827	441839.834	37.307	5.9047	3.0971	0.44359	1.7477	1.2172	1.1634
29	3682013.483	441859.114	37.814	11.693	8.7171	1.7756	0.9701	3.7467	3.4408

30	3681949.014	441882.158	38.02	1.7747	8.4579	4.5719	1.5889	1.9177	2.2600
31	3681936.117	441836.105	38.215	0.91694	4.9301	1.7159	1.9585	1.0792	3.9590
32	3681909.788	441784.371	38.321	9.587	11.163	0.056634	0.7347	3.4466	0.1305
33	3681791.576	441619.32	37.623	7.8005	8.1424	3.0435	1.3278	2.9950	2.1731
34	3681718.139	441620.216	37.704	10.118	3.5275	0.32232	0.6770	3.8088	3.6619
35	3681745.826	441734.395	37.71	1.1197	9.5746	8.5368	1.0057	2.3143	1.7710
36	3681798.809	441731.341	36.987	9.4009	7.4871	9.905	3.5824	1.9300	
37	3681737.609	441778.682	38.166	0.42027	4.8657	2.996	1.2470	0.2213	3.0152
38	3681728.833	441826.792	38.28	5.7708	10.57	3.3682	0.5278	1.4237	1.5835

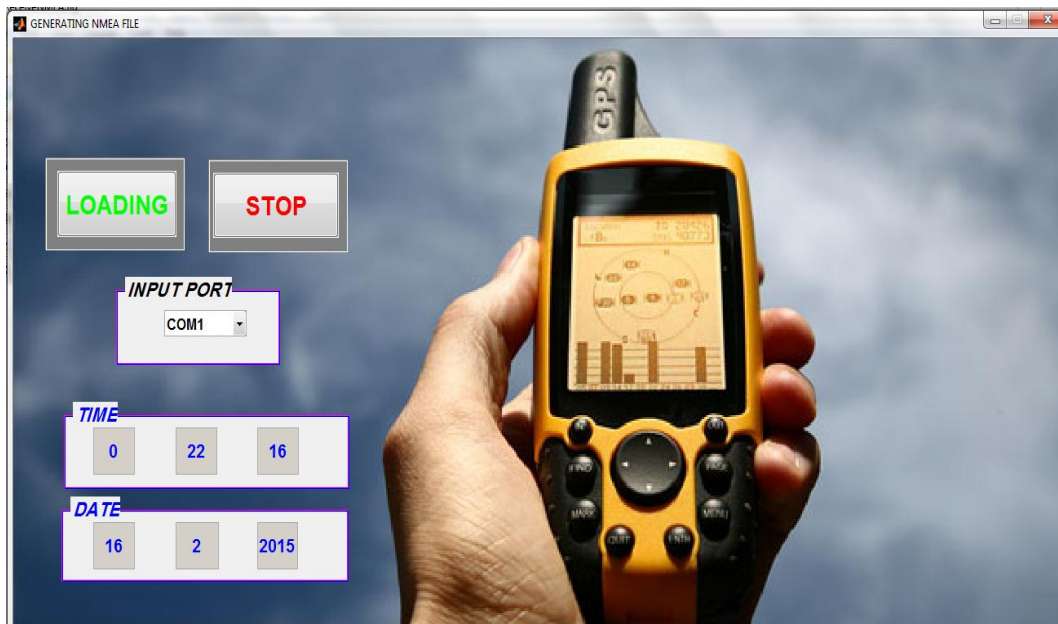


Figure 1. Designed program for loading and processing NMEA file.

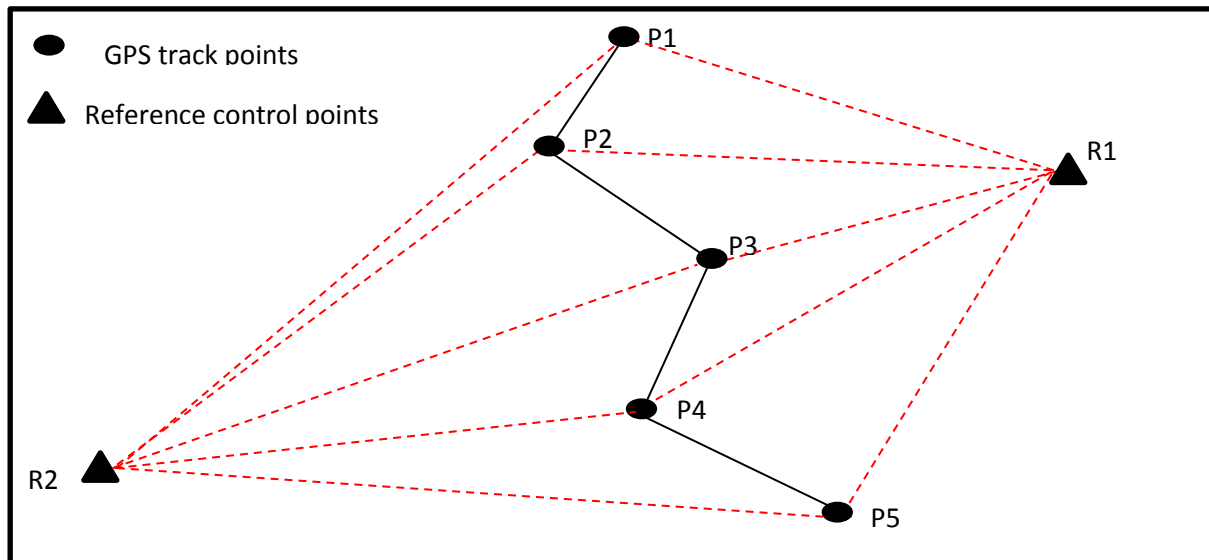


Figure 2. Illustrative sketch for the GPS baselines, which created between the GPS track points and the control points using the designed program.



Figure 3. Distribution of reference control points in the campus of the University of Baghdad.



Figure 4. The connection between a Pc and Garmin GPS for data post - processing.

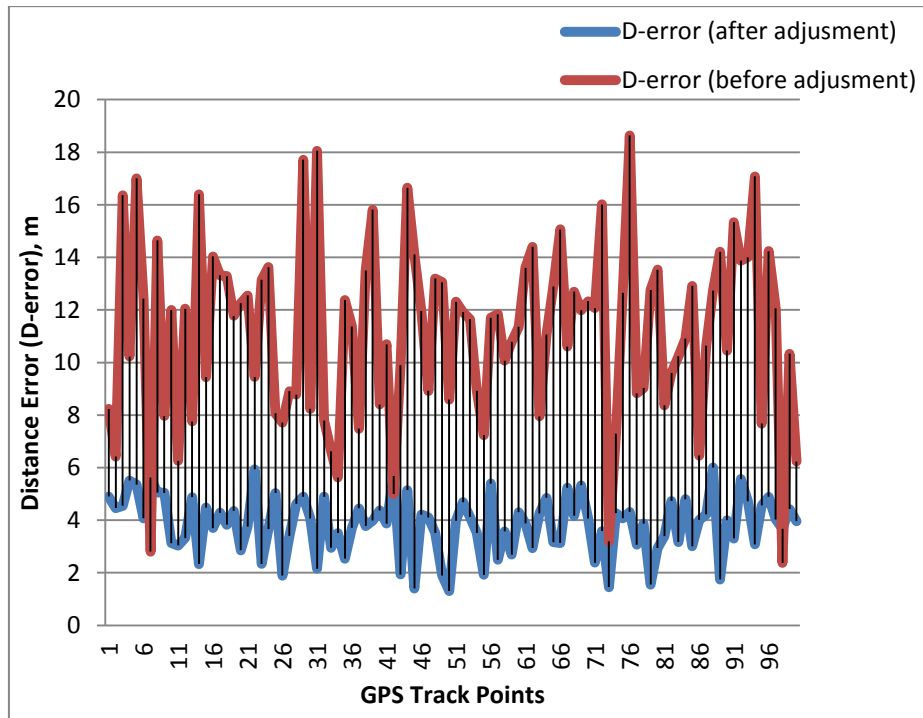


Figure 5. The histogram of distance error for all GPS track points before and after adjustment.